

Document Version

Final published version

Citation (APA)

Khalighi, S. (2026). *Field-Validated Aging Protocols for Paving Binders Using Chemo-Rheological and Data-Driven Analysis*. [Dissertation (TU Delft), Delft University of Technology]. <https://doi.org/10.4233/uuid:7d4d143f-d60d-41a9-906d-17eb8872a25d>

Important note

To cite this publication, please use the final published version (if applicable). Please check the document version above.

Copyright

In case the licence states "Dutch Copyright Act (Article 25fa)", this publication was made available Green Open Access via the TU Delft Institutional Repository pursuant to Dutch Copyright Act (Article 25fa, the Taverne amendment). This provision does not affect copyright ownership. Unless copyright is transferred by contract or statute, it remains with the copyright holder.

Sharing and reuse

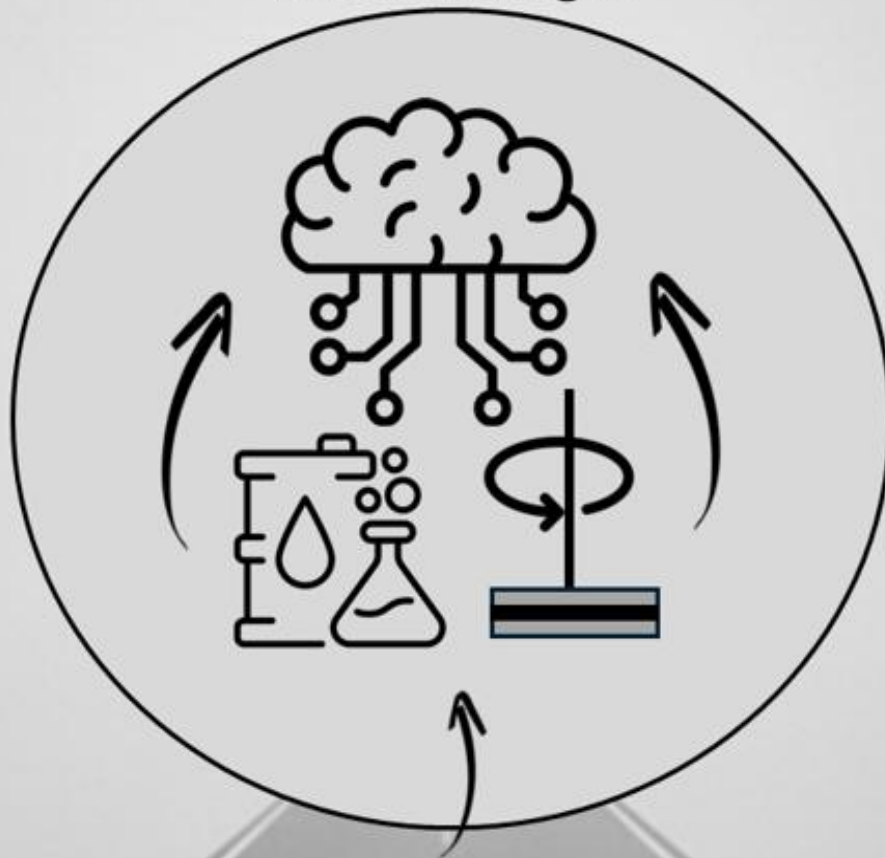
Other than for strictly personal use, it is not permitted to download, forward or distribute the text or part of it, without the consent of the author(s) and/or copyright holder(s), unless the work is under an open content license such as Creative Commons.

Takedown policy

Please contact us and provide details if you believe this document breaches copyrights. We will remove access to the work immediately and investigate your claim.

Field-Validated Aging Protocols for Paving Binders Using Chemo-Rheological and Data-Driven Analysis

Sadaf Khalighi



Field-Validated Aging Protocols for Paving Binders Using Chemo-Rheological and Data-Driven Analysis

Dissertation

for the purpose of obtaining the degree of doctor

at Delft University of Technology

by the authority of the Rector Magnificus, Prof. dr. ir. T. H. J. J. van der Hagen

chair of the Board for the Doctorates

to be defended publicly on

Tuesday, 24 February 2026 at 10:00

by

Sadaf Khalighi

This thesis is dedicated to my family: Maman, Baba, and Setareh.

Table of Contents

SUMMARY	8
SAMENVATTING	9
1 INTRODUCTION	11
1.1 BACKGROUND	12
1.2 RESEARCH OBJECTIVES.....	13
1.3 THESIS OUTLINE	14
1.4 REFERENCES.....	18
2 AGING OF PAVING BINDERS	21
2.1 BITUMEN CHEMISTRY AND AGING MECHANISMS	22
2.2 AGING FACTORS (TEMPERATURE, PRESSURE, TIME, HUMIDITY/WATER, UV, THICKNESS, OXIDATIVE AGENTS).....	24
2.3 EVALUATION OF EXISTING LONG-TERM BINDER AGING PROTOCOLS: ADVANTAGES VS DISADVANTAGES.....	30
2.4 CHARACTERIZATION METHODS TO EVALUATE BINDER AGING	35
2.4.1 <i>Chemical characterization methods</i>	35
2.4.2 <i>Surface characterization methods</i>	40
2.4.3 <i>Rheological characterization methods</i>	41
2.5 APPLICATION OF MULTIVARIATE ANALYSIS IN PAVING MATERIALS	45
2.6 KNOWLEDGE GAPS	50
2.7 REFERENCES.....	51
3 ATR-FTIR PRE-TREATMENT OF PAVING BINDERS	60
3.1 INTRODUCTION ON IMPORTANCE OF FTIR AND ITS PRE-TREATMENT FOR PAVING BINDER STUDIES	61
3.2 OBJECTIVES AND RESEARCH STRUCTURE	66
3.3 MATERIALS AND DATA COLLECTION (SAMPLE PREPARATION, AGING CONDITIONS, AND FTIR MEASUREMENT)	67
3.4 DATA PRE-PROCESSING (DP) METHODS	69
3.4.1 <i>Baseline correction methods</i>	69
3.4.2 <i>Normalization methods</i>	73
3.4.3 <i>Combined normalization and baseline-correction methods</i>	75
3.5 TRANSFORMATION OF SPECTRA TO PEAK AREAS AND INDICES	75
3.6 EVALUATION OF DP METHODS	77
3.6.1 <i>Partial least squares-discriminant analysis</i>	77
3.6.2 <i>Partial least squares-discriminant analysis model validation</i>	79
3.6.3 <i>Variable Importance in Projection Scores (VIP scores)</i>	80
3.6.4 <i>Hierarchical Cluster Analysis (HCA)</i>	81
3.7 METHODOLOGICAL APPROACH	82
3.8 RESULTS AND DISCUSSION	83
3.8.1 <i>IR spectra</i>	83
3.8.2 <i>Effect of DPs on aging classification</i>	84
3.8.3 <i>Influential spectral regions for aging classification of peak areas/indices</i>	93
3.8.4 <i>Effect of DPs on entire and first derivative spectra for aging classification</i>	96
3.9 CONCLUSIONS	98
3.10 REFERENCES.....	99
4 EFFECT OF AGING FACTORS ON CHEMICAL PROPERTIES OF PAVING BINDERS	104
4.1 BACKGROUND	105
4.2 OBJECTIVES AND RESEARCH STRUCTURE	105

4.3	MATERIALS AND SAMPLE PREPARATION	107
4.3.1	<i>Materials</i>	107
4.3.2	<i>Samples preparation</i>	108
4.3.3	<i>Laboratory long-term aging method</i>	108
4.3.4	<i>Field samples</i>	113
4.4	CHARACTERIZATION AND ANALYSIS METHODS	114
4.4.1	<i>Attenuated Total Reflectance-Fourier Transform Infrared (ATR-FTIR) spectroscopy</i>	114
4.4.2	<i>Cumulative chemical aging and aging rate</i>	115
4.4.3	<i>Deconvolution FTIR spectra</i>	115
4.4.4	<i>Dynamic time warping (DTW)</i>	117
4.5	ASSESSING CHANGES IN CHEMICAL PROPERTIES OF AGED BINDERS	118
4.5.1	<i>Effect of hygrothermal, thermo-oxidative, and aqueous-thermal aging on chemical properties of laboratory-aged binders</i>	118
4.5.2	<i>Effect of temperature, pressure, time, humidity, and thickness on chemical properties of laboratory-aged binders</i>	132
4.5.3	<i>Effect of ROS on chemical properties of laboratory-aged binders</i>	140
4.5.4	<i>Assessing changes in chemical properties of field-aged recovered binders</i>	147
4.6	COMPARISON OF AGING RATE FOR LAB-AGED SAMPLES BASED ON CHEMICAL PROPERTIES	147
4.7	DETAILED CHEMICAL COMPARISON OF FIELD- AND LAB-AGED SAMPLES USING FTIR DECONVOLUTION	148
4.8	UPA AGING MECHANISMS.....	153
4.9	CONCLUSIONS	155
4.10	REFERENCES.....	156
5	EFFECT OF AGING FACTORS ON RHEOLOGICAL PROPERTIES OF PAVING BINDERS.....	159
5.1	BACKGROUND	160
5.2	OBJECTIVES AND RESEARCH STRUCTURE	160
5.3	MATERIALS AND SAMPLE PREPARATION	162
5.4	CHARACTERIZATION AND ANALYSIS METHODS	162
5.4.1	<i>Dynamic Shear Rheometer (DSR) - Frequency sweep</i>	162
5.4.2	<i>Cumulative rheological aging and aging rate</i>	163
5.5	ASSESSING CHANGES IN RHEOLOGICAL PROPERTIES OF AGED BINDERS	164
5.5.1	<i>Effect of hygrothermal, thermo-oxidative, and aqueous-thermal aging on rheological properties of binders</i>	164
5.5.2	<i>Effect of temperature, pressure, time, humidity, and thickness on rheological properties of binders</i>	172
5.5.3	<i>Effect of reactive oxygen species (ROS) on rheological properties of binders</i>	175
5.5.4	<i>Assessing changes in rheological properties of field-aged recovered binders</i>	179
5.6	COMPARISON OF AGING RATE FOR LAB-AGED SAMPLES BASED ON RHEOLOGICAL PROPERTIES	181
5.7	5.7 DETAILED RHEOLOGICAL COMPARISON OF FIELD- AND LAB-AGED SAMPLES.....	182
5.8	CONCLUSIONS	185
5.9	REFERENCES.....	185
6	MULTIVARIATE CHEMO-RHEOLOGICAL FRAMEWORK FOR OPTIMIZING LABORATORY AGING PROTOCOLS OF PAVING BINDERS.....	188
6.1	BACKGROUND	189
6.2	OBJECTIVES AND RESEARCH STRUCTURE	189
6.3	MULTIVARIATE ANALYSIS METHODS	192
6.3.1	<i>Principle component analysis (PCA)</i>	195
6.3.2	<i>Multiple linear regression (MLR)</i>	196
6.3.3	<i>Support vector regression (SVR)</i>	198
6.3.4	<i>Deep artificial neural networks (DNNs)</i>	199
6.3.5	<i>Model validation</i>	202
6.4	RESULTS AND DISCUSSION	203

6.4.1	<i>Dataset construction</i>	203
6.4.2	<i>Chemical and rheological features importance for aging pattern recognition by PCA</i>	204
6.4.3	<i>Evaluating lab-field aging similarity based on Euclidean distance</i>	208
6.4.4	<i>Quantifying the impact of aging factors and back-calculation of field-aging conditions by MLR</i>	209
6.4.5	<i>Chemo-rheological relationships in aging studies</i>	214
6.4.6	<i>Prediction of G* master curve with FTIR indices using DNNs</i>	215
6.4.7	<i>Prediction of field aging for laboratory samples using SVR</i>	222
6.5	MODELLING LIMITATIONS	223
6.6	CONCLUSIONS	224
6.7	REFERENCES	225
7	CONCLUSIONS AND FUTURE PERSPECTIVES	228
7.1	CONCLUSIONS	229
7.2	RECOMMENDATIONS FOR FUTURE WORK	230
7.2.1	<i>Recommendations for future research</i>	230
7.2.2	<i>Recommendations for practice</i>	231
	APPENDIX OF CHAPTER 3	234
	APPENDIX OF CHAPTER 4	238
	APPENDIX OF CHAPTER 5	240
	APPENDIX OF CHAPTER 6	243
	ACKNOWLEDGMENT	250
	CURRICULUM VITAE	251
	LIST OF PUBLICATIONS	252

Summary

Road networks are a cornerstone of transportation infrastructure, yet their long-term performance is severely challenged by a complex phenomenon known as aging. The aging of bituminous binders, a key component of asphalt pavements, leads to a progressive loss of flexibility and durability, resulting in premature cracking and expensive maintenance. Existing laboratory aging protocols often fail to accurately replicate real-world conditions, creating a significant gap between simulated and actual pavement performance. This discrepancy complicates the development of more durable and sustainable paving materials.

The central objective of this thesis is to address this gap by developing a robust, data-driven methodology to establish field-validated laboratory aging protocols for paving binders. To achieve this, the research was guided by four key questions: investigating the chemo-rheological effects of diverse environmental factors, developing a novel accelerated aging protocol, employing multivariate and machine learning methods to integrate data, and optimizing data pre-processing for spectral analysis.

To achieve these objectives, the effect of key environmental factors like temperature, pressure, humidity, UV light, and reactive oxygen species (ROS) were studied. The research systematically analyzed chemical and rheological changes in binders aged under thermo-oxidative, hygrothermal, aqueous-thermal, and ROS-induced conditions. The effectiveness of the protocols was validated by comparing laboratory-aged samples against a 9-year field-aged benchmark. The study utilized Fourier-transform infrared spectroscopy (FTIR) for chemical characterization, with data pre-processed using an optimized framework developed in the thesis. Multivariate statistical methods, including Principal Component Analysis (PCA), were employed to identify key aging trends, while machine learning models linked chemical and rheological properties.

The findings demonstrate that a new UV-Peroxide Aging (UPA) protocol, particularly under conditions such as 33% H₂O₂ at 85°C for 3 hours, effectively replicates the chemo-rheological state of long-term field-aged binders. The study confirmed that carbonyl and sulfoxide indices, along with rheological crossover parameters, are critical indicators of aging. While regression models like Multiple Linear Regression (MLR) and Support Vector Regression (SVR) provided valuable insights, the research found that Deep Neural Networks (DNNs) were particularly effective in capturing the complex, nonlinear relationships between FTIR features and rheological properties, enabling robust predictive modeling. Furthermore, the systematic evaluation of data pre-processing techniques for FTIR established essential strategies for ensuring reliable chemical characterization.

In conclusion, this thesis provides a validated, practical framework for establishing field-relevant aging protocols, bridging the gap between laboratory simulations and real-world performance. The developed methodology, integrating advanced characterization and machine learning, offers a powerful tool for predicting the long-term behavior of bituminous materials. These findings provide valuable guidance for the design and selection of more durable paving binders, contributing directly to the development of sustainable and resilient road infrastructure. Future work should focus on

expanding the dataset to include extended field durations and on applying this framework to new materials like bio-binders and polymer-modified binders to ensure its broad applicability.

Samenvatting

Wegennetwerken zijn een hoeksteen van de transportinfrastructuur, maar hun prestaties op de lange termijn worden ernstig op de proef gesteld door een complex fenomeen dat veroudering wordt genoemd. De veroudering van bitumineuze bindmiddelen, een sleutelcomponent van asfaltverhardingen, leidt tot een geleidelijk verlies van flexibiliteit en duurzaamheid, wat resulteert in vroegtijdige scheurvorming en kostbaar onderhoud. Bestaande laboratoriumverouderingsprotocollen slagen er vaak niet in om de omstandigheden in de praktijk nauwkeurig na te bootsen, waardoor een aanzienlijke kloof ontstaat tussen gesimuleerde en werkelijke prestaties van de verharding. Deze discrepantie bemoeilijkt de ontwikkeling van duurzamere en bestendigere bestratingsmaterialen.

De centrale doelstelling van dit proefschrift is om deze kloof aan te pakken door een robuuste, datagestuurde methodologie te ontwikkelen om in de praktijk gevalideerde laboratoriumverouderingsprotocollen voor bestratingsbindmiddelen vast te stellen. Om dit te bereiken, werd het onderzoek geleid door vier kernvragen: het onderzoeken van de chemo-reologische effecten van diverse omgevingsfactoren, het ontwikkelen van een nieuw versneld verouderingsprotocol, het inzetten van multivariate en machinale leermethoden om gegevens te integreren, en het optimaliseren van de gegevensvoorverwerking voor spectrale analyse.

Om deze doelstellingen te bereiken, werden de effecten van belangrijke omgevingsfactoren zoals temperatuur, druk, vochtigheid, UV-licht en reactieve zuurstofsoorten (ROS) bestudeerd. Het onderzoek analyseerde systematisch chemische en reologische veranderingen in bindmiddelen die waren verouderd onder thermo-oxidatieve, hygrothermische, aquatisch-thermische en ROS-geïnduceerde omstandigheden. De effectiviteit van de protocollen werd gevalideerd door laboratoriumverouderde monsters te vergelijken met een referentiemonster dat 9 jaar in de praktijk was verouderd. Het onderzoek maakte gebruik van Fourier-transform infraroodspectroscopie (FTIR) voor chemische karakterisering, waarbij de gegevens werden voorverwerkt met een geoptimaliseerd kader dat in het proefschrift is ontwikkeld. Multivariate statistische methoden, waaronder Principal Component Analysis (PCA), werden gebruikt om belangrijke verouderingstrends te identificeren, terwijl machinale leermodellen chemische en reologische eigenschappen met elkaar in verband brachten.

De bevindingen tonen aan dat een nieuw UV-Peroxide Aging (UPA) protocol, met name onder omstandigheden zoals 33% H₂O₂ bij 85°C gedurende 3 uur, effectief de chemo-reologische toestand van langdurig in de praktijk verouderde bindmiddelen nabootst. De studie bevestigde dat carbonyl- en sulfoxide-indices, samen met reologische crossover-parameters, kritieke indicatoren van veroudering zijn. Hoewel regressiemodellen zoals Multiple Linear Regression (MLR) en Support Vector Regression (SVR) waardevolle inzichten opleverden, bleek uit het onderzoek dat Deep Neural Networks (DNN's) bijzonder effectief waren in het vastleggen van de complexe, niet-lineaire relaties tussen FTIR-kenmerken en reologische eigenschappen, waardoor robuuste voorspellende modellering mogelijk werd. Verder heeft de systematische evaluatie van gegevensvoorverwerkingstechnieken voor FTIR essentiële strategieën vastgesteld om een betrouwbare chemische karakterisering te waarborgen.

Concluderend biedt dit proefschrift een gevalideerd, praktisch kader voor het opstellen van praktijkrelevante verouderingsprotocollen, waardoor de kloof tussen laboratoriumsimulaties en de prestaties in de praktijk wordt overbrugd. De ontwikkelde methodologie, die geavanceerde karakterisering en machinaal leren integreert, biedt een krachtig hulpmiddel voor het voorspellen van het gedrag van bitumineuze materialen op de lange termijn. Deze bevindingen bieden een waardevolle leidraad voor het ontwerp en de selectie van duurzamere wegenbouwbindmiddelen en dragen rechtstreeks bij aan de ontwikkeling van duurzame en veerkrachtige weginfrastructuur. Toekomstig werk moet zich richten op het uitbreiden van de dataset met langere praktijkveroudering en op het toepassen van dit kader op nieuwe materialen zoals biobinders en polymeer-gemodificeerde bindmiddelen om de brede toepasbaarheid ervan te waarborgen.

1

Introduction

Environmental aging is a critical factor influencing the durability and performance of paving binders. This chapter provides an overview of the background and challenges associated with the environmental aging of bituminous materials. The significance of the thesis topic is highlighted, along with the research objectives aimed at advancing the understanding of aging mechanisms and improving aging protocols. Additionally, the chapter presents the overall structure and organization of the thesis.

1.1 Background

The durability and resource efficiency of road infrastructure have gained attention due to their indirect role in the overall environmental impact of transportation systems. Although the majority of emissions arise from vehicle use, the materials and construction practices associated with roads contribute to resource consumption and long-term maintenance demands. A key factor influencing the durability and maintenance frequency of asphalt pavements is the aging of bituminous binders, which significantly alters their mechanical performance and service life [1, 2]. Binder aging occurs at the material level, yet field aging takes place within the context of asphalt mixtures. The interaction between the binder and aggregates, as well as the surrounding environmental and traffic-related factors, adds layers of complexity to aging mechanisms [3]. Although studying aging at the binder level might appear to simplify these complex processes, binder-level research is indispensable for uncovering the fundamental chemical and rheological changes that govern material performance [4]. This focus is particularly justified because the binder, unlike aggregates or stones, undergoes significant property changes over time, making it the most critical component in determining asphalt behaviour and durability [4, 5]. By linking these changes to alterations observed at the mixture level, researchers can establish a scaled-down framework to simulate field conditions accurately. This approach provides a pathway to connect binder aging mechanisms with field aging phenomena, offering valuable insights into how binder properties influence the durability of the entire pavement structure. Therefore, the study of aging at the binder level is not only sufficient but also instrumental in bridging the gap between laboratory and field observations.

Binder aging, characterized by an increase in stiffness and susceptibility to cracking, is a progressive process that begins during the production and construction phase, known as short-term aging (STA), and continues throughout the service life of the pavement under environmental influences, referred to as long-term aging (LTA) [5, 6]. This degradation reduces the lifespan of roads and increases maintenance demands, emphasizing the need for innovative approaches to predict and manage the binder's mechanical and chemical properties after aging has occurred (e.g., its resistance to cracking or its ability to retain flexibility).

Accurate simulation of both STA and LTA effects is essential for durable and sustainable pavements design. Laboratory aging protocols are commonly employed for this purpose, using factors such as temperature, pressure, time, binder thickness, and moisture [7-10]. Despite their utility, these protocols face significant challenges in replicating the complexity of field conditions. For instance, real-world aging factors, such as visible light or ultraviolet (UV) radiation and reactive oxygen species (ROS), are often excluded, creating discrepancies between laboratory predictions and field performance [8, 9, 11]. Addressing this gap requires achieving a balance between accelerated aging processes and the true representation of field conditions.

The abovementioned challenges associated with binder aging are also compounded by evolving environmental and societal pressures. Climate change phenomena—such as extreme temperatures, intense precipitation, and fluctuating weather conditions—alongside increased traffic volumes and heavier vehicles, impose additional stresses on road networks, compromising their resilience and reliability. These factors are expected to escalate maintenance costs, further emphasizing the need for sustainable solutions [12-14].

Moreover, the integration of circular economy principles into infrastructure policy has reinforced the use of reclaimed asphalt (RA) in pavement construction. In the Netherlands, RA has been incorporated into binder and base layers since the 1980s, with typical contents reaching 50% by 2008. Recent targets, such as the national aim to reduce primary raw material consumption by 50%

by 2030 and to achieve a fully circular economy by 2050, have accelerated these developments. Current practices allow up to 60–65% RA in binder and base layers, while porous asphalt (PA) applications with 25–35% RA have been technically validated and are permitted under Rijkswaterstaat (RWS) guidelines. Nevertheless, constraints persist under the standard for certain surface applications, reflecting ongoing concerns related to the environmental aging and long-term durability of RA-containing mixtures [15-20].

Looking ahead, the continued recycling of asphalt raises open questions regarding the long-term mechanical performance and durability of mixtures potentially containing material in its second or third lifecycle. While asphalt recycling has been practiced since the 1980s—making it likely that some reclaimed material has already undergone multiple reuse cycles—this is not systematically monitored. As a result, it remains unclear whether repeated recycling has a negligible effect or whether it contributes to cases of premature or unexpected pavement deterioration. These concerns are further compounded by recent developments in the bitumen supply chain, notably changes in refinery operations resulting from the International Maritime Organization’s (IMO) 2020 regulations on low-sulfur marine fuels, which have altered residue streams and, consequently, bitumen production [21]. Additionally, fluctuations in crude oil sourcing due to geopolitical instability [22, 23], along with increasingly stringent environmental regulations on refinery emissions and process efficiency [24], have contributed to observable variations in bitumen quality across markets. Emerging alternative binders, such as RAP binders with regenerators and bio-binders, offer sustainable options but introduce considerable variability in pavement performance and durability due to their diverse compositions and modifiers.

To address the above challenges and achieve the desired goals robust testing protocols are required which are lacking in the pavement community both in the Netherlands and globally. These protocols are critical for addressing the variability in binder characteristics introduced by recycled materials, regenerators, and non-traditional binders. Developing reliable tools and methods to assess long-term performance is necessary to ensure the sustainability and resilience of road networks in an era of increasing environmental and societal challenges. Utilizing these developed tools and protocols at the material level, it is possible to advance sustainable practices in pavement engineering, ensuring the durability, reliability, and environmental compatibility of road networks amidst evolving global demands.

1.2 Research objectives

The primary challenge addressed in this thesis is the lack of robust, reliable, and comprehensive protocols to evaluate the long-term aging of bituminous materials under complex and interacting environmental conditions. This gap hinders the pavement engineering community from effectively understanding and predicting the durability of paving binders, particularly in the context of increasing adoption of recycled materials, regenerators, and non-traditional binders.

To address this challenge, this research is structured around four overarching questions. Questions 1 and 2 focus on the fundamental understanding and experimental replication of aging processes, while Questions 3 and 4 address the development of analytical and data-driven tools needed to interpret chemical and rheological changes more effectively. Together, these questions span both the physical phenomena of aging and the methodological advancements necessary for their evaluation:

1. What are the chemical and rheological consequences of aging under diverse environmental factors, and how do these conditions compare to field aging?

2. Can novel accelerated aging protocols replicate field aging more effectively than existing laboratory methods?
3. How can multivariate statistical and machine learning methods be employed to integrate chemical and rheological data for a deeper understanding of the aging process?
4. How can data pre-processing techniques for ATR-FTIR spectral analysis of bituminous binders be optimized to ensure reliable chemical characterization?

Beyond the development of field-representative protocols, a key objective of this thesis is to establish a multivariate framework that integrates spectral data preprocessing, chemical and rheological analyses, and multivariate chemo-rheological modelling to optimize laboratory aging protocols. By systematically addressing the aforementioned questions, the thesis aims to enhance our understanding of aging mechanisms at the binder level and improve the predictive capabilities of laboratory aging tests.

This thesis advances pavement engineering by addressing critical gaps in the evaluation of paving binder aging (Figure 1.1). Specifically, it evaluates the effects of multiple aging factors on binder performance and introduces a novel aging protocol to more accurately simulate real-world conditions. A multivariate machine learning framework is developed for evaluating binder aging and optimizing aging protocols, enabling more precise predictions of binder behaviour under various aging scenarios. Additionally, the research assesses a range of preprocessing and post-processing methods for the chemical evaluation of binders and their aging, providing a comprehensive approach to binder characterization. The outcomes of this work contribute to the development of sustainable, durable pavements by offering enhanced tools for predicting long-term binder performance and optimizing laboratory aging protocols, thus supporting more resilient and environmentally responsible infrastructure.

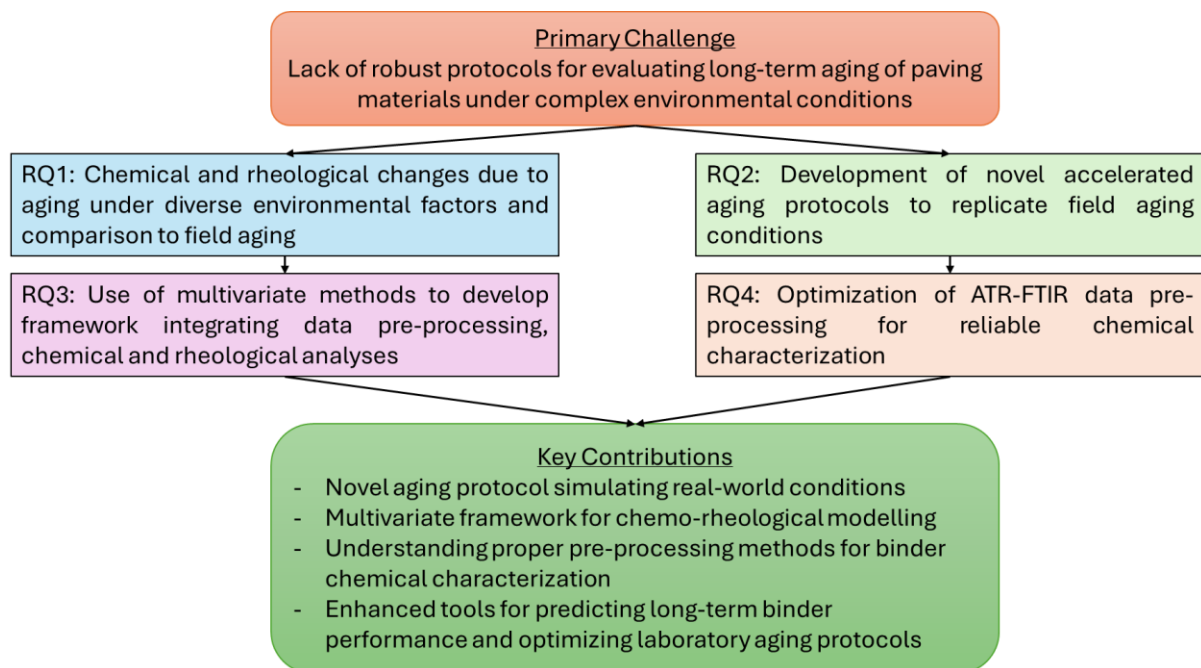


Figure 1.1 Research scope and schematic flow diagram of thesis structure

1.3 Thesis outline

This dissertation consists of seven chapters. It explores the complex aspects of aging and environmental effects on bituminous binders. The primary focus is on developing novel laboratory aging protocols to replicate field aging conditions accurately. This introductory chapter addresses the overarching challenges in studying oxidative and moisture-induced degradation in bituminous materials, emphasizing the critical need to investigate these phenomena to predict pavement performance effectively. It sets the basis for the research by delineating key research questions and objectives while providing a comprehensive background on the subject. The chapter highlights the necessity of integrating chemical, rheological, and multivariate analytical techniques to achieve a holistic understanding of aging mechanisms in bituminous binders. Furthermore, the thesis structure is outlined in Figure 1.2, guiding the reader through the interconnected research themes explored in subsequent chapters.

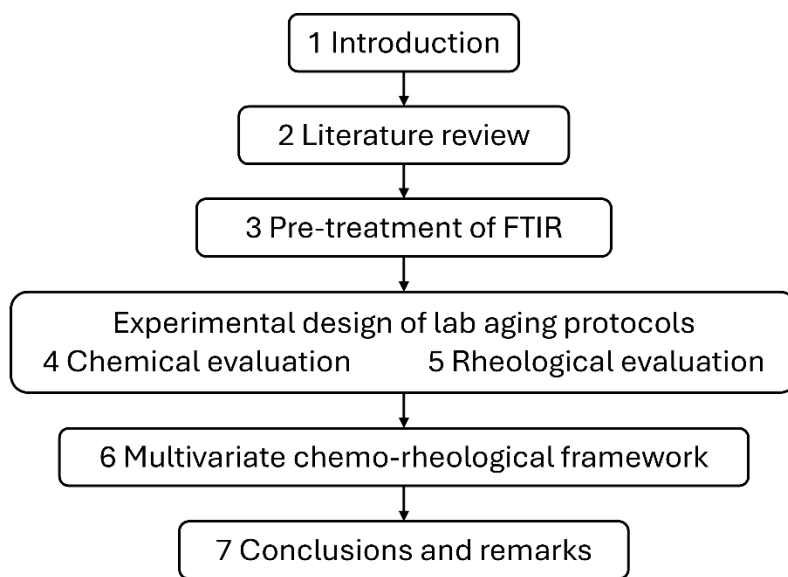


Figure 1.2 Schematic diagram of thesis outline

Chapter 2 reviews the scientific and technical literature on environmental aging in bituminous materials. It begins with an overview of paving binder chemistry, establishing the material's susceptibility to aging. Key environmental factors such as temperature, pressure, time, humidity, UV exposure, thickness, and oxidative agents are examined for their roles in bitumen degradation. A comparative analysis of long-term aging protocols highlights their strengths and limitations in simulating real-world conditions. The chapter also explores characterization techniques like attenuated Total Reflectance Fourier Transform Infrared Spectroscopy (ATR-FTIR) and Dynamic Shear Rheometry (DSR), emphasizing their importance in analysing chemical and rheological changes in aged bitumen. Multivariate analysis and chemometric methods are discussed as tools for interpreting complex datasets and revealing interdependencies in aging processes. The chapter concludes by identifying knowledge gaps in aging mechanisms and laboratory protocols, linking these to the research questions in Chapter 1 and providing a ground for the subsequent investigations.

The third chapter begins with the optimization of data pre-processing (DP) techniques for ATR-FTIR spectral analysis (Chapter 3). Figure 1.3 provides an overview of Chapters 3 to 6, detailing their goals and methodologies, to help the reader follow the steps more effectively. Spectroscopic data are fundamental to characterizing chemical changes during binder aging, yet existing approaches often suffer from non-informative spectral regions, inconsistent baselines, and lack of standardization. This

chapter establishes a unified framework for evaluating DP methods, comparing various normalization and baseline correction strategies. Using Partial Least Squares-Discriminant Analysis (PLS-DA), the impact of these methods on classification accuracy is assessed across diverse binder types, aging states, and modifications. This step provides a robust foundation for spectral analysis in subsequent chapters and ensures reliable chemometric evaluation of aging effects.

The chemical effects of aging under various environmental conditions are then analysed using ATR-FTIR in Chapter 4. This chapter examines the roles of temperature, pressure, humidity, sample thickness, UV light, and reactive oxygen species (ROS) in accelerating binder oxidation. A novel accelerated aging protocol— UV-Peroxide Aging (UPA) Protocol—is introduced, leveraging hydroxyl radicals as potent oxidizing agents. This chapter evaluates the changes in the chemical composition of paving binders induced by individual and combined aging factors. These chemical changes are subsequently used to calculate the relative aging rates under different conditions, allowing for the quantification of the acceleration aging effect of each factor. Moreover, field-aged samples are integrated into the analysis to establish a comparative framework, ensuring that laboratory protocols replicate field conditions as closely as possible. The outcomes of this chapter provide critical insights into how environmental factors influence chemical aging and help identify efficient aging protocols.

Building on the chemical analysis, Chapter 5 focuses on the rheological changes due to aging. Rheological parameters such as complex shear modulus, phase angle, and crossover frequency are evaluated under identical aging conditions to those examined chemically in Chapter 4. The observed variations in rheology are then utilized to determine relative aging rates across different conditions, enabling the assessment of acceleration aging effects. Additionally, field-aged samples are incorporated to provide a comparative basis, ensuring that laboratory aging procedures closely reflect real-world aging conditions. Moreover, the aim is to link chemical changes to alterations in the viscoelastic behaviour of binders, providing a holistic perspective on aging effects. This integration of chemical and rheological data facilitates a deeper understanding of the material-level changes that dictate binder performance.

Chapter 6 develops a multivariate chemo-rheological framework to optimize laboratory aging protocols. Principal Component Analysis (PCA) is employed to identify critical chemical and rheological factors differentiating aging states. Regression models, including Multiple Linear Regression (MLR), are utilized to quantify the effects of environmental variables such as temperature, pressure, and moisture on aging rates and to back-calculate laboratory conditions that simulate field aging. Support Vector Regression (SVR) is applied to predict equivalent field aging durations for various laboratory protocols and to model the relationship between chemical properties and rheological behaviour. While SVR provided valuable insights, its limitations in accurately predicting sigmoidal model parameters and other critical rheological properties necessitated the use of Artificial Neural Networks (ANNs). ANNs demonstrated superior performance in capturing the complex, nonlinear relationships between FTIR indices and rheological parameters, providing robust predictive models for sigmoidal parameters and crossover values. By integrating PCA, regression models, SVR, and ANNs, this chapter establishes a comprehensive, data-driven approach to align laboratory tests with real-world aging processes.

Finally, Chapter 7 summarizes the key findings of this thesis and offers recommendations for further research in this field.

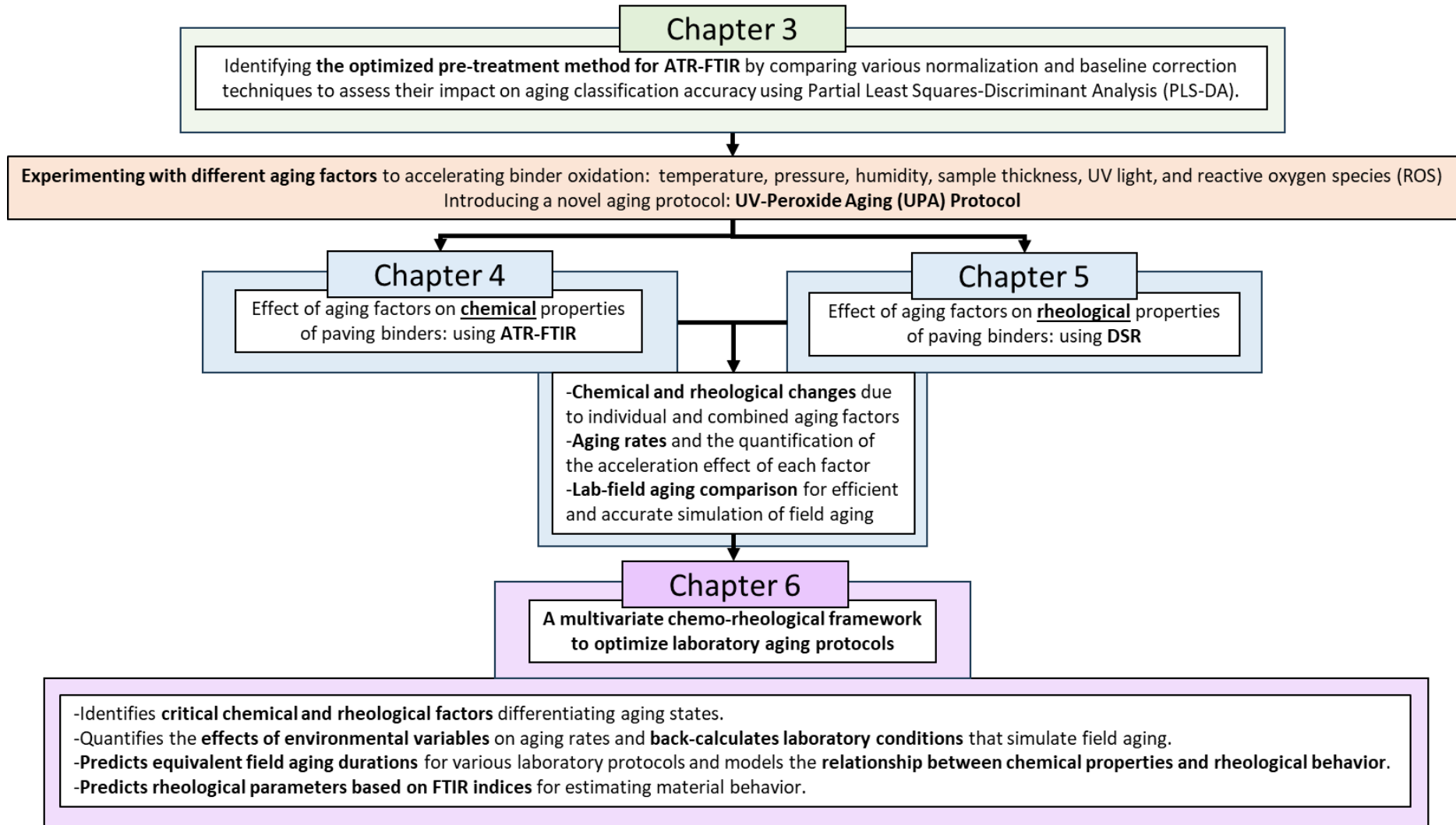


Figure 1.3 Detailed Flow of Chapters 3-6: Objectives and Methodologies

1.4 References

1. Salehi, S., et al., *Sustainable pavement construction: A systematic literature review of environmental and economic analysis of recycled materials*. Journal of Cleaner Production, 2021. **313**: p. 127936.
2. Lyu, L., et al., *Aging evolution and sustainability implications of crumb rubberized asphalt binder: a state-of-the-art*. Journal of Cleaner Production, 2024. **434**: p. 140202.
3. Saleh, N.F., et al., *Effects of aging on asphalt mixture and pavement performance*. Construction and Building Materials, 2020. **258**: p. 120309.
4. Hu, Y., et al., *State of the art: Multiscale evaluation of bitumen ageing behaviour*. Fuel, 2022. **326**: p. 125045.
5. Tauste, R., et al., *Understanding the bitumen ageing phenomenon: A review*. Construction and Building Materials, 2018. **192**: p. 593-609.
6. Ahmad, M., et al., *Aging characterization of asphalt binders through multi-aspect analyses: A critical review*. Fuel, 2024. **376**: p. 132679.
7. Airey, G.D., *State of the art report on ageing test methods for bituminous pavement materials*. International Journal of Pavement Engineering, 2003. **4**(3): p. 165-176.
8. Khalighi, S., S. Erkens, and A. Varveri, *Exploring the impact of humidity and water on bituminous binder aging: a multivariate analysis approach (TI CAB)*. Road Materials and Pavement Design, 2024: p. 1-25.
9. Khalighi, S., et al., *Multivariate chemo-rheological framework for optimizing laboratory aging protocols of paving binders*. Materials & Design, 2024: p. 113520.
10. Petersen, J.C., *A review of the fundamentals of asphalt oxidation: chemical, physicochemical, physical property, and durability relationships*. Transportation research circular, 2009(E-C140).
11. da Silva Lopes, A.M., et al., *Impact of aging protocols on asphalt binder behavior: a laboratory and field study*. Case Studies in Construction Materials, 2023. **19**: p. e02629.
12. Underwood, B.S., et al., *Increased costs to US pavement infrastructure from future temperature rise*. Nature Climate Change, 2017. **7**(10): p. 704-707.
13. Jeekel, H., *Adaptation to climate change*. 2012.
14. Axelsen, C., et al., *Implementing climate change adaptation for European road administrations*. Transportation Research Procedia, 2016. **14**: p. 51-57.
15. An, E., *action plan for the Circular Economy*. Communication from the Commission to the European Parliament, the Council, the European economic and social committee and the Committee of the regions closing the loop. Brussels, 2015. **2**.
16. Aurangzeb, Q., et al., *Achieving desired volumetrics and performance for mixtures with high percentage of reclaimed asphalt pavement*. Transportation research record, 2012. **2294**(1): p. 34-42.
17. Hajj, E.Y., P.E. Sebaaly, and R. Shrestha, *Laboratory evaluation of mixes containing recycled asphalt pavement (RAP)*. Road Materials and Pavement Design, 2009. **10**(3): p. 495-517.
18. He, G.-P. and W.-G. Wong, *Effects of moisture on strength and permanent deformation of foamed asphalt mix incorporating RAP materials*. Construction and Building Materials, 2008. **22**(1): p. 30-40.
19. West, R.C., J.R. Willis, and M.O. Marasteanu, *Improved mix design, evaluation, and materials management practices for hot mix asphalt with high reclaimed asphalt pavement content*. Vol. 752. 2013: Transportation Research Board.
20. Varveri, A., S. Avgerinopoulos, and A.T. Scarpas. *Durability of European Asphalt Mixtures Containing Reclaimed Asphalt and Warm-Mix Additives*. in *Transportation Research Board 95th annual meeting*. 2016.
21. Organization, I.M. *IMO 2020 - cleaner shipping for cleaner air*. 2019 [cited 2025 15 April]; Available from: <https://www.imo.org/en/MediaCentre/PressBriefings/pages/34-IMO-2020-sulphur-limit->

[.aspx#:~:text=%E2%80%8BFrom%201%20January%202020,the%20limit%20is%20already%200.10%25.](#)

22. Massimo Ferrari Minesso, M.-S.L., Denise Rößler. *Geopolitical risk and oil prices*. 2023 [cited 2025 15 April]; Available from: https://www.ecb.europa.eu/press/economic-bulletin/focus/2024/html/ecb.ebbox202308_02~ed883ebf56.en.html.
23. Cappelli, F., G. Carnazza, and P. Vellucci, *Crude oil, international trade and political stability: Do network relations matter?* *Energy Policy*, 2023. **176**: p. 113479.
24. Zhao, F., Y. Fan, and S. Zhang, *Assessment of efficiency improvement and emission mitigation potentials in China's petroleum refining industry*. *Journal of cleaner production*, 2021. **280**: p. 124482.

2

Aging of paving binders

Mechanisms, accelerated aging protocols, experimental characterization, and multivariate analysis

Laboratory simulation of paving binder aging has long been a challenge in pavement engineering. To improve binder aging simulations in the laboratory and achieve a more accurate representation of field aging, it is essential to understand key aspects, including binder aging mechanisms and field aging factors. It is also critical to have the experimental and computational capabilities available for replication and analysis, respectively.

This chapter begins with a brief introduction to paving binder chemistry and aging mechanisms in Section 2.1. Section 2.2 provides a comprehensive review of various aging factors—temperature, pressure, time, humidity, UV exposure, thickness, and oxidative agents—highlighting their roles in the degradation of binder. Section 2.3 presents a comparative analysis of existing long-term aging protocols, discussing their advantages and limitations to assess their effectiveness in simulating real-world conditions. Section 2.4 explores post-aging characterization techniques, with a focus on Fourier Transform Infrared Spectroscopy (FTIR) and Dynamic Shear Rheometry (DSR), examining how these methods capture changes in paving binder properties. Section 2.5 discusses the application of multivariate analysis and chemometric methods in bitumen research, emphasizing their role in enhancing data interpretation. Finally, Section 2.6 identifies knowledge gaps in each discussed area, linking them to the research questions outlined in Chapter 1, thus framing the context for subsequent investigations.

This comprehensive review aims to highlight the critical factors and methodologies that contribute to a deeper understanding of bitumen performance and long-term durability.

2.1 Bitumen chemistry and aging mechanisms

Bitumen is classified as a viscoelastic material primarily composed of hydrocarbons and their derivatives. It is produced through the removal of lighter fractions, such as liquefied petroleum gas, gasoline, and diesel, from crude oil during the refining process [1]. Bitumen represents a complex mixture of approximately 300 to 2000 chemical compounds, including polar heteroatoms such as sulfides, thiols, sulfoxides, ketones, phenols, carboxylic acids, pyrrolic and pyridinic compounds, and metal complexes like metalloporphyrins. This complexity complicates detailed chemical analysis [2]. Consequently, bitumen composition is categorized into two main fractions:

- a) Asphaltenes
- b) Maltenes

Maltenes can be further divided into three subcategories: saturates, aromatics, and resins. Collectively, these four fractions are referred to as the SARA (Saturate, Aromatic, Resin, Asphaltene) fractions (Figure 2.1) [2]. This classification is based on the solubility of each fraction in specific solvents.

Bitumen ageing is divided into short-term and long-term ageing. Short-term ageing refers to the changes occurring during asphalt production and road construction processes, such as mixing, storage, transportation, and compaction at elevated temperatures. In contrast, long-term ageing takes place during the service life of the mixture under various environmental conditions. The generally accepted ageing mechanism, irrespective of its stage, includes oxidation, evaporation of lighter components, and physical (steric) hardening [3, 4].

Reversible physical hardening refers to a time-dependent stiffening of bitumen that can be reversed upon reheating. This phenomenon is primarily attributed to the formation of ordered structures by alkyl aromatics within the maltenes phase, which are responsible for steric-hardening[5, 6]. It becomes more pronounced at lower temperatures and is associated with the internal rearrangement of binder components. While its overall impact on performance is moderate, it can still affect the rheological properties of bitumen [7].

Evaporation of volatile compounds, influenced by temperature, primarily occurs during mixing, laying, and exposure. Oil refineries are increasingly focused on separating these volatile compounds from bitumen, as they can be both valuable and toxic; thus, their effect on ageing is considered less significant than that of oxidation [1].

The most critical aging mechanism in bitumen is oxidation, an irreversible thermal reaction between atmospheric oxygen and bitumen fractions. This process involves two interconnected stages: oxygen diffusion into the bitumen and subsequent oxidative chemical reactions[8]. Oxygen present in the atmospheric air, and consequently in the voids of bituminous mixtures, diffuses into the bitumen, supplying the oxygen necessary for the oxidative reactions [9]. As the active bitumen components react with oxygen, they undergo molecular agglomeration and structural rearrangement, leading to hardening and embrittlement of the material [10].

The extent of oxygen diffusion and the exposed surface area of bitumen are influenced by factors such as void content in the mixture, the depth of various road layers, bitumen content, and the presence of cracks [1]. Moreover, the oxidative reaction in bitumen is influenced by various factors, including the microstructure, chemical composition, temperature, pressure, and UV exposure [11]. The diffusion-reaction coupling process plays a critical role in determining the kinetics of oxidation[8]. The oxidative reaction continuously consumes diffused oxygen, creating a concentration gradient that drives further diffusion of oxygen into the material [12]. Over time, the disturbed microstructure and increased polarity of the bitumen can impede further oxygen diffusion due to denser molecular packing, resulting in a non-Fickian diffusion process[8]. The system reaches a terminal state when no reactants remain, and no oxygen concentration gradient persists.

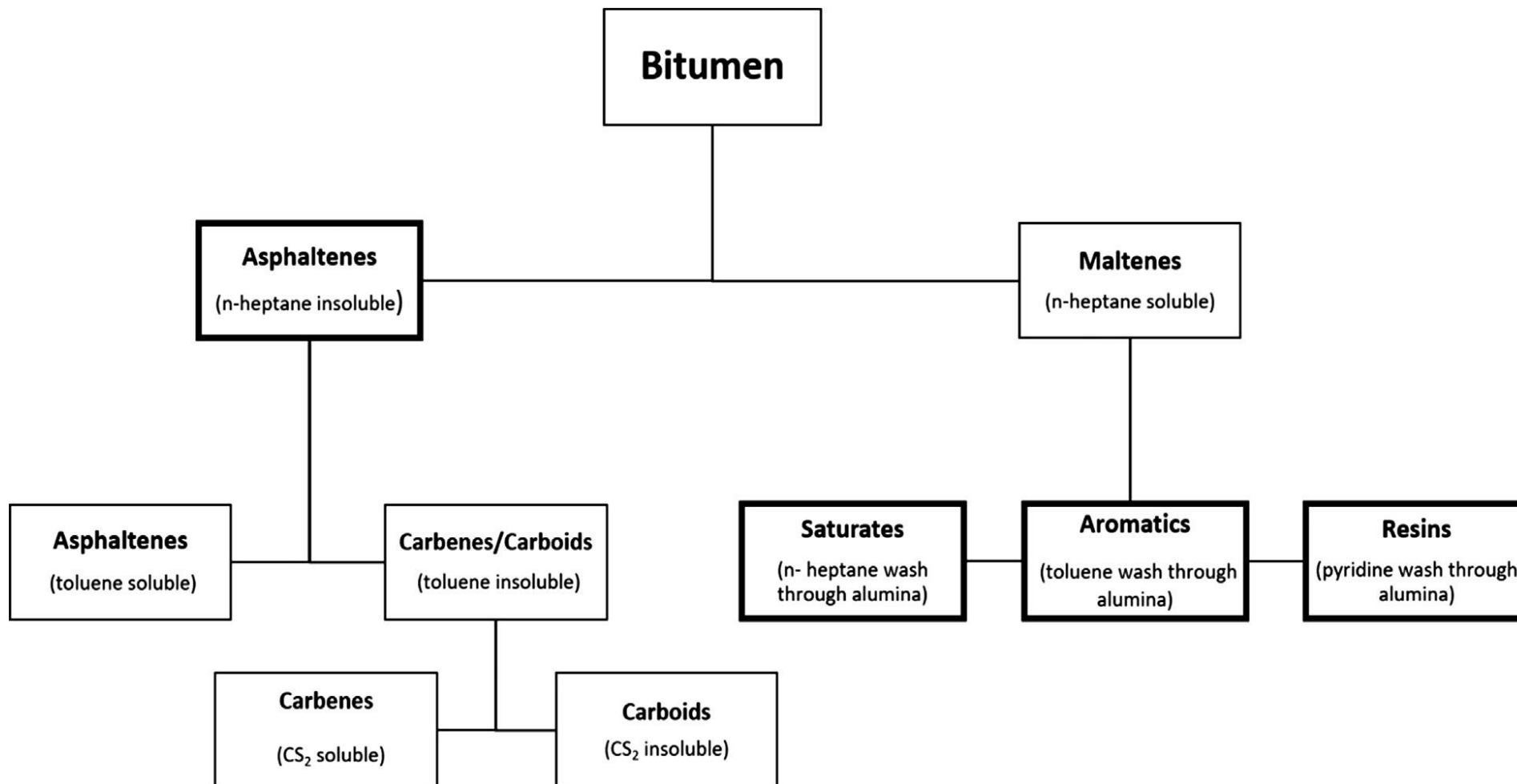


Figure 2.1- Separation of bitumen into its various fractions, highlighting the SARA fractions [13].

During oxidation, oxygen removes hydrogen atoms from carbon atoms (Figure 2.2a), converting benzyl carbons into ketones and subsequently into carboxylic acids (Figure 2.2b, c, d, f), while transforming alkyl sulfur into sulfoxides (Figure 2.2b, e, g). These reactions lead to an increase in the asphaltene fraction and a decrease in resins and aromatic compounds. Such transformations render bitumen more polar, acidic, and susceptible to molecular condensation. The kinetics of the oxidation reaction and volatilization are significantly affected by temperature; consequently, these processes occur at higher rates during manufacturing and continue at reduced rates throughout the service life. A commonly cited rule of thumb indicates that for every 10 °C increase in temperature above 100 °C, the reaction rate approximately doubles [2].

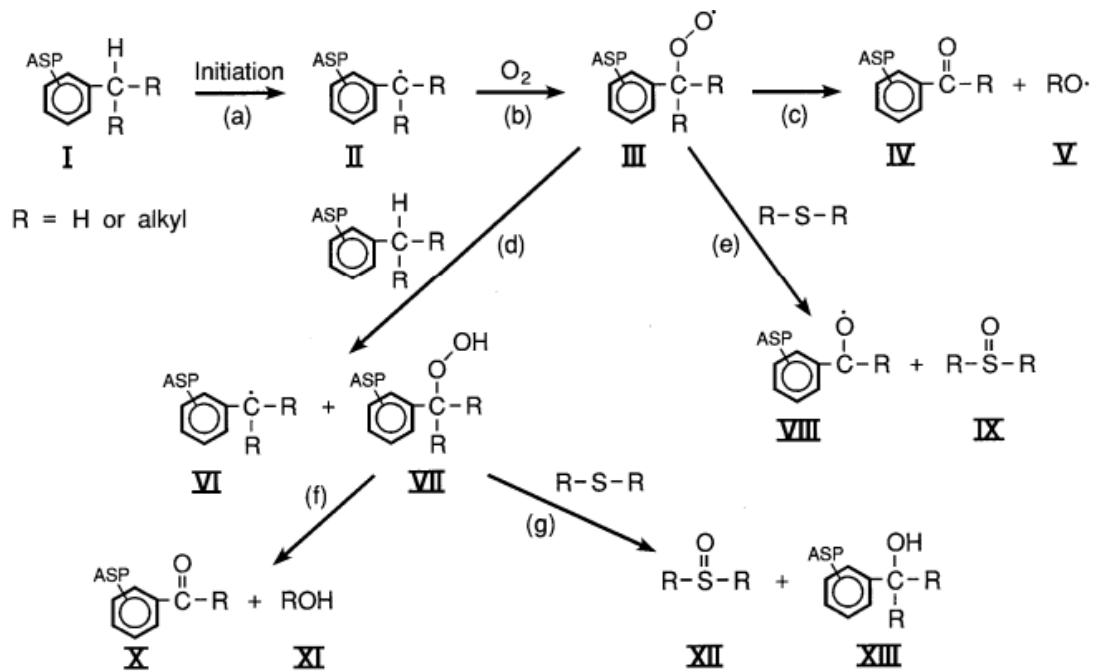


Figure 2.2- Schematic illustration of benzylic carbon oxidation reaction and ketone and sulfoxide formation [9].

2.2 Aging factors (temperature, pressure, time, humidity/water, UV, thickness, oxidative agents)

To optimize the performance and durability of asphalt pavements, a detailed evaluation of binder aging under laboratory conditions is required to approximate field aging accurately [14]. In real-world applications, bituminous binders are subject to diverse environmental stresses, including moisture, temperature fluctuations, and traffic loads, which are often underrepresented in traditional aging protocols. A comprehensive aging protocol should encompass these factors and accelerate their effects to closely emulate actual field aging conditions. Before implementing these factors within laboratory protocols, it is essential to analyse their individual impacts on binder properties.

Temperature

Temperature plays a critical role in the aging of paving binders, as oxidation reactions in binders proceed more rapidly at higher temperatures. Temperature significantly influences the oxidation kinetics of bitumen [15]. The aging behaviour of bitumen varies with temperature, as some types exhibit distinct oxidation rates depending on the thermal conditions. This variability can be attributed to temperature-induced changes in the colloidal structure of bitumen, which affect the diffusion rate of oxygen. Consequently, the oxidation kinetics become inconsistent as the diffusion process adjusts to the structural changes [15] (Figure 2.3).

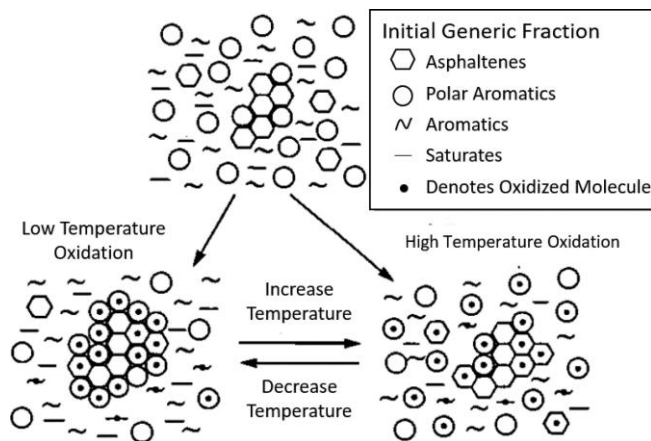


Figure 2.3- The Petersen model illustrating bitumen oxidation as a function of temperature, with variations in kinetics attributed to the availability of oxidation sites at specific temperatures[15].

Temperature plays a significant role in lab-aging protocols, such as the PAV method, which employs elevated temperatures to simulate aging. However, these temperatures are higher than those encountered by pavements during their service life. Elevated temperatures not only accelerate the rate of reaction but can also influence the pathways of the reaction, deviating from natural field aging, particularly at temperatures exceeding 90-100 °C [9]. In the Netherlands, maximum air temperatures generally reach only 30-35 °C (Figure 2.4) [16]. Though pavement temperatures are not commonly measured directly, they are known to exceed air temperatures by 27-50 °C on sunny days, which implies potential pavement surface temperatures between 60 °C and 85 °C [17]. The upper temperature of 85 °C chosen for this study accounts for this air-pavement temperature difference, making it suitable not only for the Netherlands but also for regions with higher average temperatures [18]. Moreover, several recent long-term aging protocols have adopted similar maximum temperatures, such as 80 °C, to maintain reaction pathways that closely mimic natural field aging while accelerating aging rates [19, 20]. Other protocols, by contrast, use a lower temperature, around 60 °C, to avoid excessive reaction deviations [20, 21].

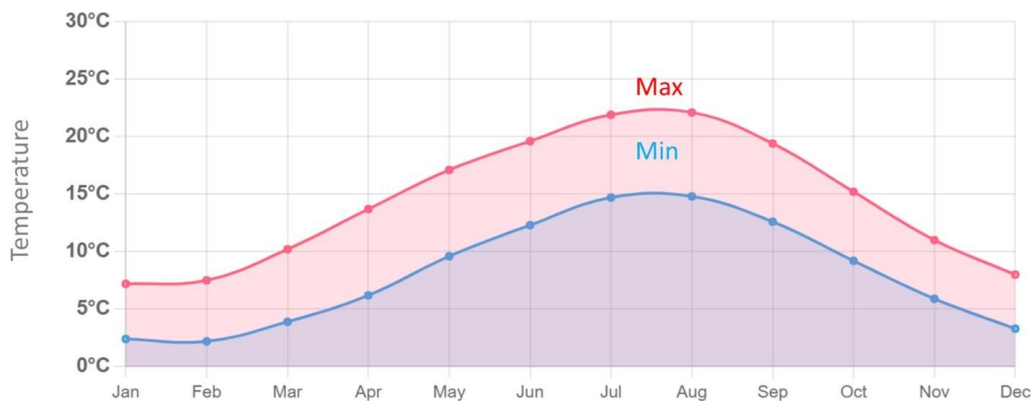


Figure 2.4- Average minimum and maximum temperature in Amsterdam, Netherlands during Jan. 2021 to Dec. 2021, from weather-and-climate.com [22].

Pressure

An important factor contributing to binder aging in the field is the diffusion of oxygen molecules. During long-term aging, oxygen has sufficient time to diffuse into the binder and participate in oxidation reactions. However, replicating such extended exposure periods in laboratory conditions is not feasible. To address this, elevated pressure is introduced in laboratory simulations to accelerate oxygen diffusion and, consequently, the oxidative aging process. Although pressure variation in the field is minimal and does not significantly influence aging, in the laboratory, increased pressure

enhances the solubility of oxygen in the binder, thereby increasing the availability of oxygen molecules for reaction [16]. This elevated concentration of diffused oxygen accelerates the formation of oxygenated compounds [9, 16], contributing to the hardening and embrittlement of bitumen [23].

Furthermore, the coupling of pressure with other factors such as temperature can amplify its impact [9, 23]. At higher temperatures, the enhanced mobility of oxygen molecules combined with increased pressure intensifies the diffusion-reaction process [8]. This synergistic effect can accelerate the oxidative degradation of bitumen in laboratory simulations, particularly in thicker binder films, where pressure-induced oxygen availability counteracts the natural decline in diffusion rates associated with limited exposure depth. Therefore, understanding the effect of pressure and oxygen diffusion is crucial for accurately predicting oxidation kinetics of bitumen aging. In this thesis, laboratory experiments were conducted over a pressure range from 1 bar to 150 bar.

Film thickness

Selecting an appropriate binder film thickness is a critical aspect of developing an effective aging protocol. In actual pavement structures, the asphalt binder film thickness varies considerably. Around filler particles within the mastic, it ranges from approximately 0.5 to 2.5 μm , as observed through image analysis, and from 9 to 13 μm based on analytical estimations. In contrast, the binder film thickness around coarse aggregates is significantly greater and plays a critical role in resisting stripping. Depending on the binder content and mix design, thicknesses around coarse aggregates have been reported to reach up to several hundred micrometers [24-26]. Research on polymer-modified mixtures indicates that binder films that are too thin compromise aggregate bonding and overall pavement performance, while excessive thickness reduces mixture stiffness and lowers resistance to cracking and fatigue under load [27]. However, replicating submicron thicknesses in the lab is challenging, as factors like substrate and application method influence film uniformity and aging behaviour. To develop a practical aging protocol, it is necessary to select a film thickness that realistically represents the binder thickness in actual pavements, while also being feasible to produce consistently with standard laboratory equipment. Importantly, the chosen thickness should allow sufficient material for post-aging rheological and chemical characterization. Various studies have demonstrated that changes in film thickness lead to different aging effects [20]. For instance, studies have shown that reducing film thickness from 3.2 mm to 1 mm leads to a significant increase in oxidized molecules, as well as higher complex shear modulus and lower phase angle after aging, indicating increased stiffness and reduced viscoelasticity [28]. These effects result from enhanced oxygen accessibility in thinner layers and the limited oxygen diffusion in thicker layers, which slows the aging process at greater depths. Different binder aging protocols utilize specific film thicknesses based on these considerations. For example, the Viennese Binder Aging (VBA) protocol employs a film thickness of 0.5 mm to enhance aging efficiency [19], while the widely-used Pressure Aging Vessel (PAV) protocol typically employs a 3.2 mm film thickness [28]. However, the authors' own experience has shown that producing consistent 0.5 mm films in petri dishes is time-consuming and challenging. Consequently, this study evaluates a range of thicknesses, beginning with 1 mm and extending to 3.2 mm, with an intermediate thickness of 2 mm. This range was selected to examine how varying film thickness influences aging behaviour and to identify a practical balance between accelerated aging effects and experimental feasibility.

Moisture

Moisture's impact on bitumen degradation is well-documented through both experimental and molecular dynamics studies. This factor is particularly crucial for countries like the Netherlands, which experience high humidity levels year-round (Figure 2.5). For instance, Ma et al. demonstrated that hydrogen bonding and water clustering affect bitumen properties, including viscosity and cohesive energy, through molecular dynamics simulations under various temperature and water conditions [29]. Experimental studies show that moisture exposure, combined with mechanical stress, leads to debonding and adhesive or cohesive failure in bitumen, reducing asphalt durability

[30-33]. Omar et al. reported that water infiltration reduces adhesive strength between aggregate surfaces and bitumen, leading to surface issues such as spalling and pothole formation [34]. Khalighi et al. showed that combined thermal and moisture aging, or hygrothermal aging, accelerates aging more significantly than oxidative aging alone [22]. Moreover, the interaction of bitumen with salt solutions, as highlighted by Zou et al., accelerates erosion and alters surface characteristics [35]. While some studies suggest minimal effects of moisture on bitumen aging [36] or variability in moisture susceptibility among binder types [37], further exploration of moisture impacts is warranted. In this thesis, two humidity levels were selected based on the limitations of the laboratory equipment: below 10% and above 90% relative humidity.

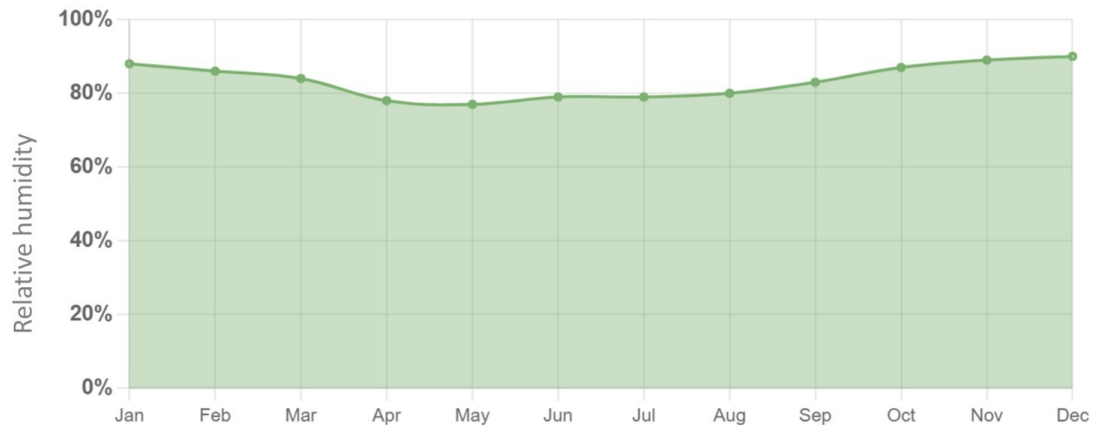


Figure 2.5- Average relative humidity (%) in Amsterdam, Netherlands during Jan. 2021 to Dec. 2021, from weather-and-climate.com [19].

Time

Time is a critical factor in binder aging protocols. Extended aging durations generally result in more pronounced changes in binder properties [9]. However, aging procedures must balance the need to replicate field aging realistically with practical constraints; excessively long durations may be impractical for laboratory studies. Accelerating the aging process through increased temperature, pressure, or the use of catalysts can reduce the required time while aiming to maintain representative aging mechanisms. Although shorter protocols are often preferred for convenience, they must still produce aging effects consistent with those observed in the field to remain valid for research purposes. In practical applications, it is not always necessary to simulate exact field aging durations. Instead, protocols should accelerate the aging process sufficiently to induce the expected chemical and physical changes, allowing classification of materials by their relative sensitivity to aging alongside their initial properties. In this study, PAV-aging durations between 5 and 80 hours were tested to evaluate these effects.

Reactive oxygen species (ROS)

In addition to temperature and moisture, atmospheric conditions and reactive oxygen species (ROS) play significant roles in binder aging. Ozone (O_3) and nitrogen oxides (NO_x), formed through hydrocarbon and carbon monoxide oxidation and emitted by vehicular traffic [38, 39], affect asphalt pavements. However, studies investigating the combined effects of realistic aging conditions, including ROS, are limited. The Viennese Binder Aging (VBA) method (Figure 2.6), developed by Mirwald et al., incorporates O_3 and NO_x exposure in binder aging, surpassing the aging levels of RTFOT + PAV within three days at 80 °C [19]. Hofko et al. investigated the effect of O_3 solely and in combination with NO_x on bitumen recovered from aged asphalt specimens [40]. Their results reveal that significant aging occurred only in the presence of NO_x . Primerano et al. further showed that NO_2 -aged samples exhibit chemical characteristics more similar to field-aged samples, highlighting the importance of ROS in simulating real-world aging [41]. VBA-induced aging resulted in a 110% increase in ketone formation compared to a 42% increase in PAV-aged samples, indicating enhanced

oxidative reaction rates with VBA [14]. Additionally, the presence of sulphurous oxidation products in NO₂-aged samples underscored the complexity of chemical transformations during aging. Notably, the field-aged sample consistently shows the highest absorbance across all investigated bands, underscoring that neither laboratory method fully replicates the extensive aging experienced in real-world conditions. However, the VBA method provided a better approximation compared to the standard aging procedure, enabling a more accurate qualitative simulation of the chemical properties of the investigated field samples.

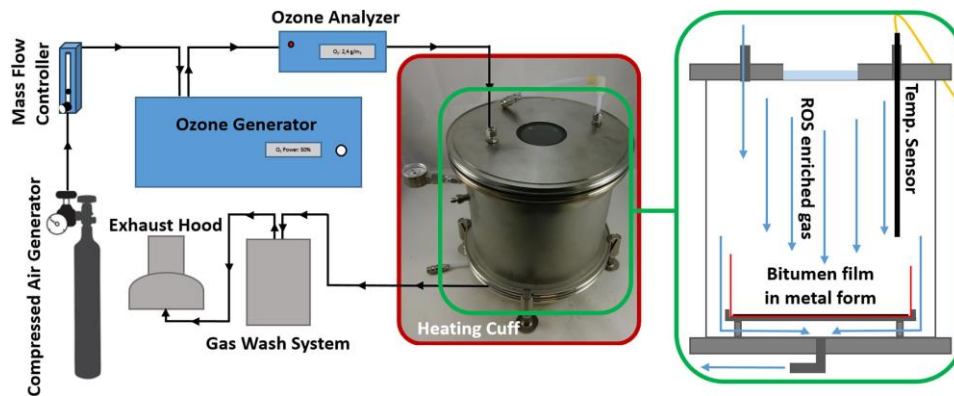


Figure 2.6- Scheme of the VBA aging setup[19].

light

Photo-oxidative ageing, resulting from exposure to UV light and oxygen (Figure 2.7), is a key factor in the long-term ageing of asphalt pavement, which also significantly influences asphalt binder properties [42]. Menapace et al. reported extensive chemical changes in binders under UV exposure (0.89 W/m²/nm at 340 nm) over 388 days, especially under dry conditions, where oxidized groups accumulated [43]. Crucho et al. observed increases in binder stiffness and reduced fatigue life under simulated UV exposure with water/dry cycling for 30 days[44]. Similarly, Hu et al. demonstrated that UV aging gradually decreases with depth, primarily affecting the surface layers of the binder and thus influencing the rheological properties and the overall durability [45]. The effects of UV radiation are wavelength-dependent, with wavelengths between 300 and 350 nm having the greatest impact on binder aging. Mirwald et al. investigated light-induced aging using wavelengths ranging from 365 to 770 nm, covering both UV-A and the visible spectrum, with particular focus on the blue-green range (approximately 405 and 525 nm). They observed that exposure to these wavelengths initiated photo-oxidation in bitumen, leading to the formation of carbonyl and sulfoxide groups, key indicators of oxidative aging. Aging was quantified using Fourier Transform Infrared (FTIR) spectroscopy by monitoring the increase in absorption at characteristic wavenumbers for carbonyl (~1700 cm⁻¹) and sulfoxide (~1030 cm⁻¹) functional groups. Their results demonstrated that even visible light, especially in the blue-green spectrum, contributes significantly to oxidative aging through photochemically induced reactions [46]. UV aging effects, however, are often restricted to surface layers due to limited penetration, forming an impermeable layer that reduces oxygen diffusion and thereby diminishes aging severity compared to thermal aging [47].

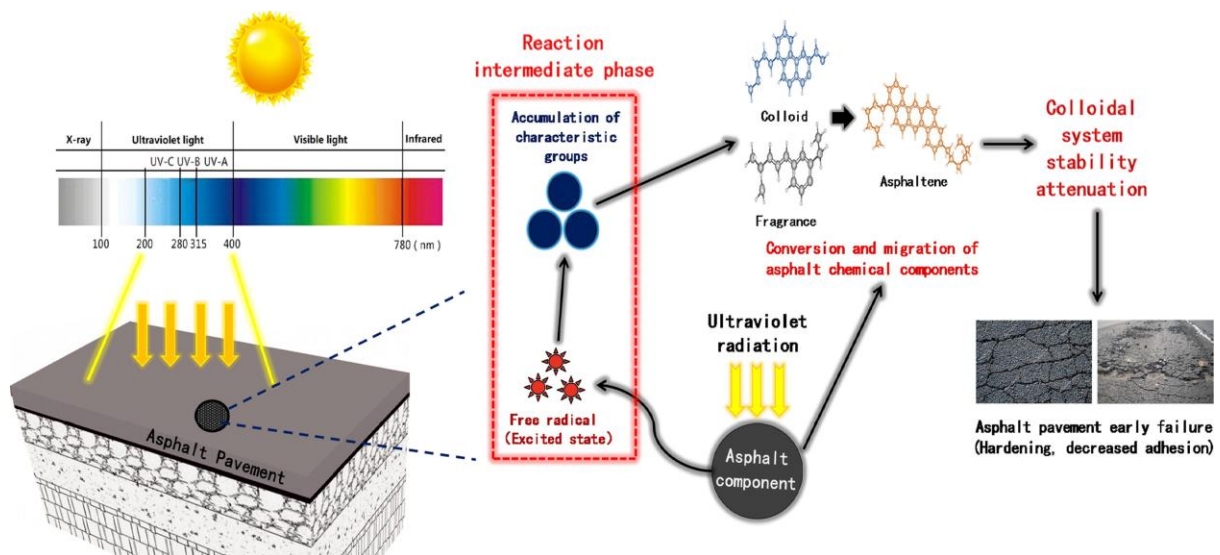


Figure 2.7 The process of UV ageing in asphalt pavement formation [42].

Summary of aging factors in paving binder studies and their ranges in this thesis

Previous research has established the influence of individual aging factors, such as temperature, pressure, moisture, and radiation, on the evolution of binder properties. However, these studies often focus on isolated parameters under simplified or idealized laboratory conditions. While this has yielded valuable insights, it limits understanding of how multiple aging factors interact under realistic exposure scenarios. Furthermore, the absence of systematic evaluations combining these factors within experimentally feasible and field-relevant boundaries constrains the development of reliable and representative laboratory aging protocols.

A central challenge in simulating long-term field aging in the laboratory is the need to accelerate aging processes while preserving the mechanisms that govern property changes under field conditions. This requires applying conditions that increase the rate of aging, such as elevated temperature, pressure, or reactive species, without inducing chemical pathways that diverge from those active in situ. Existing literature suggests that excessively elevated temperatures may alter reaction mechanisms in bitumen oxidation [9], whereas such boundary conditions are less well understood for other factors such as pressure or moisture. Accordingly, this thesis adopts an approach in which each aging factor is examined within a range that balances experimental acceleration with mechanistic realism. The aim is not only to replicate observed field behaviour but also to assess whether increased intensities of these factors can be used to reliably accelerate aging without introducing artificial effects.

This study evaluates the following factors:

- Temperature: Temperatures above 100 °C are commonly used in laboratory aging protocols but may introduce chemical changes not observed in the field. This study therefore investigates temperatures of 60 °C, 70 °C, and 85 °C to assess whether accelerated oxidation can be achieved while preserving field-relevant reaction mechanisms.
- Pressure: Elevated oxygen pressure enhances oxygen solubility and diffusion, offering a potential means for accelerating aging. However, the extent to which high pressure affects oxidation pathways remains underexplored. Pressures of 5, 10, 20, and 150 bar are applied to investigate whether such conditions can be used to accelerate aging without altering its chemistry.

- **Film Thickness:** Binder film thickness controls oxygen accessibility and aging kinetics. The selected thicknesses (1 mm, 2 mm, and 3.2 mm) reflect a range suitable for experimental analysis while enabling the study of diffusion effects relevant to in-service binder layers.
- **Moisture:** While moisture is recognized as a key factor in bitumen degradation, especially under combined oxidative conditions, its role is often underrepresented in laboratory protocols. The extreme humidity conditions, below 10%, 20%, and above 90% relative humidity, and immersion under liquid water are applied here to better understand moisture-induced effects. These conditions are not representative of typical field exposure but are chosen to define mechanistic boundaries and assess whether extreme humidity accelerates relevant degradation pathways.
- **Time:** Aging duration influences the extent and type of binder modification. Rather than seeking to simulate fixed field exposure periods, this study explores durations from 5 hours to 3 weeks. A 9-year field-aged sample is used as a benchmark to evaluate whether specific combinations of laboratory conditions approximate the chemical and rheological changes observed in practice.
- **Reactive Oxygen Species (ROS):** ROS such as ozone and nitrogen oxides are present in the environment and contribute to binder oxidation. Due to their reactive nature, direct inclusion in laboratory protocols is difficult. This study introduces hydroxyl radicals via a controlled liquid-phase reaction to accelerate oxidation in a way that mimics environmental ROS activity. The choice of ROS is based on their relevance in atmospheric chemistry and their potential to accelerate aging; care is taken to evaluate whether this approach results in aging products comparable to those observed under natural conditions.
- **UV Radiation:** UV aging is primarily a surface phenomenon, with intensity decreasing rapidly with depth. This study incorporates UV radiation (300-400 nm) in combination with temperature and ROS to explore synergistic effects and assess whether photo-oxidative mechanisms can be meaningfully simulated in layered or composite exposures. While UV is not unique in its interactions with other factors, it is singled out here due to its spatially localized impact, which requires special consideration when designing accelerated protocols.

By examining these parameters (Figure 2.8) in controlled combinations and assessing their chemical and rheological effects on bitumen, this thesis aims to define the operational limits within which laboratory aging can be both accelerated and mechanistically representative. This framework supports the development of more robust and predictive protocols for evaluating long-term binder performance under diverse environmental conditions.

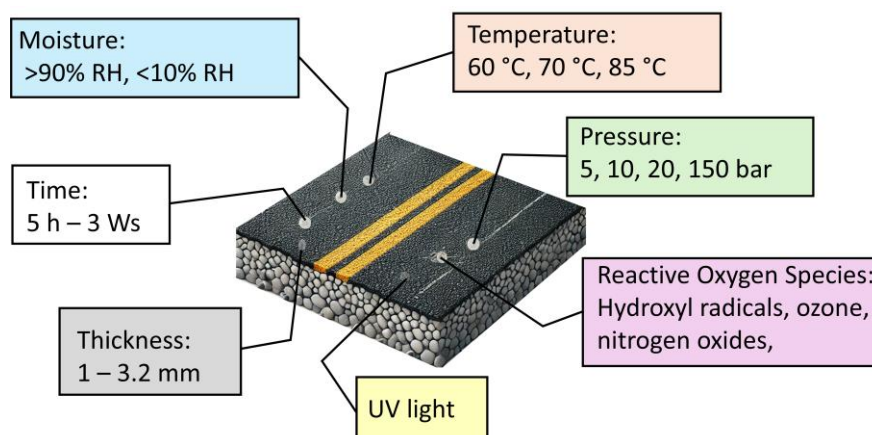


Figure 2.8 Summary of Aging Factors in this thesis. Temperature (°C), Pressure (bar), Film Thickness (mm), Moisture (RH%), Time (hours, weeks), Reactive Oxygen Species (ROS: Ozone, NO_x, liquid-phase method), UV Light.

2.3 Evaluation of existing long-term binder aging protocols: advantages vs disadvantages

Understanding and characterizing the long-term aging (LTA) of paving binders remains essential for improving predictions of pavement performance and enhancing durability assessments. While it is not feasible to replicate field conditions exactly in a laboratory setting, given the inherent variability in production practices, construction quality, climate, and traffic loadings, it is still necessary to approximate field-relevant aging processes as closely as possible. A universal laboratory aging protocol that suits all technologies, pavement designs, and climatic zones is unlikely to be attainable. However, a detailed understanding of the mechanisms and factors influencing binder aging enables the development of more targeted and adaptable protocols. By studying individual and combined effects of key variables, such as temperature, pressure, oxygen availability, moisture, and UV exposure, this work aims to establish a framework that can inform the tailoring of laboratory aging procedures to different field scenarios.

Binder aging protocols play a significant role in simulating oxidative and thermal degradation processes that occur over a pavement's service life. While aging in the field occurs at the mixture level, this thesis focuses specifically on binder aging protocols, as they provide fundamental insights into the chemical and rheological changes of the binder itself. Evaluating the advantages and limitations of existing protocols is essential for identifying gaps and improving their ability to represent real-world aging conditions effectively.

Conventional laboratory aging protocols, such as the Rotating Thin-Film Oven Test (RTFOT), Pressure Aging Vessel (PAV), and Rotating Cylinder Aging Test (RCAT), often fail to replicate the full complexity of field aging [9]. While these methods provide standardized procedures, growing evidence shows that their outcomes may diverge significantly from those observed in field-aged materials. Lu et al. reported notable differences in the extent of oxidation, quantified by changes in carbonyl and sulfoxide functional groups, between binders aged in the laboratory and those recovered from the field [4]. However, it is important to note that their study involved comparisons with field-aged cores of unknown binder origin, making it difficult to isolate aging effects from variations in initial composition. Thus, while the study supports the general observation of a mismatch between laboratory and field aging, its conclusions must be interpreted in the context of these limitations.

Jing et al., by contrast, conducted a more controlled study using the same binder for both laboratory and field experiments on porous asphalt in the Netherlands. They found that three years of field aging resulted in more pronounced oxidative changes than those achieved through standard RTFOT and PAV protocols [48,49]. This supports the view that conventional lab methods may underpredict aging severity under certain conditions. The same group further demonstrated that porous asphalt exhibited more substantial field-induced aging than dense asphalt, underscoring the role of mixture design in aging susceptibility [50].

In other contexts, field aging has been found to outpace lab aging in some cases and lag behind in others. For instance, Qin et al. showed that the combined RTFOT+PAV procedure corresponded approximately to the aging profile of only the lower portion (~75 mm) of 8-year-old pavement cores, suggesting that surface aging processes were not well captured [51]. Conversely, Singhvi et al. reported that a double PAV treatment could approximate 8-12 years of field aging in Illinois pavements, although differences in aging pathways between lab and field remained evident [52].

Together, these studies demonstrate that laboratory aging protocols do not consistently replicate field conditions, whether in terms of severity, aging gradient, or mechanism. While discrepancies in severity (more or less oxidative change) can vary depending on environmental exposure, asphalt type, and test duration, the broader concern is the lack of consistency and the inability of standard procedures to capture the full spectrum of aging behaviour. This reinforces the need for more targeted and mechanistically informed aging protocols that account for both the specific binder properties and the environmental context.

In 2003, Airey conducted a comprehensive review of binder and paving mixture aging methods, detailing established aging protocols and their respective conditioning parameters, advantages, and limitations [20]. Among the most widely adopted methods are the Rolling Thin Film Oven Test (RTFOT) and Pressure Aging Vessel (PAV) protocols [53-55]. The RTFOT method involves subjecting binder films to controlled airflow at 163 °C for 75 minutes, targeting short-term aging (STA) (EN 12607-1, 2014) [56]. For long-term aging (LTA), the PAV method ages bitumen films in a pressurized vessel at 2.07 MPa and temperatures between 90 and 110 °C over a 20-hour period (EN 14769, 2012) [57]. These protocols, while prevalent, continue to show limitations in closely replicating field aging, underscoring the need for improved methods that approximate key aspects of field conditions more reliably by accounting for the combined and variable environmental stresses encountered in real pavement applications.

Table 2.1 summarizes the key protocols for short-term aging (STA), long-term aging (LTA), and combined LTA with UV exposure, providing a comparative evaluation of their conditions, advantages, limitations, and the aging factors they address.

Table 2.1- Overview of aging protocols for short-term aging (STA), long-term aging (LTA), and combined long-term aging with UV exposure (LTA+UV), highlighting their conditions, advantages, disadvantages, and considered aging factors.

Aging Type	Name of Protocol	Conditions	Advantages	Disadvantages	Considered Aging Factors
Short-Term	Thin Film Oven Test (TFOT) [58]	163°C for 5 hours; 3.2 mm film thickness	Standardized; effective in simulating construction conditions	Limited simulation of field conditions; lacks UV and humidity influence	Temperature, Time, Thickness
	Rolling Thin Film Oven Test (RTFOT) [56]	163°C for 85 minutes; rotating thin film with air flow	Improves on TFOT by including air flow; better at simulating construction aging	Higher volatile loss; limited oxidative simulation compared to actual field conditions	Temperature, Time, Pressure, Thickness
Long-Term	Pressure Aging Vessel (PAV) [57]	100°C, 2.07 MPa pressure, typically 20 hours	Widely accepted for long-term aging; effective oxidative aging simulation	High temperature cause deviation from field aging, High pressure can induce binder segregation in polymer-modified bitumen	Temperature, Pressure, Time
	High Pressure Aging Test (HiPAT) [59]	85°C at 2.07 MPa pressure for 65 hours	Low temperature reduces non-representative binder hardening	Potential overestimation of long-term field aging effects	Temperature, Pressure, Time
	Rotating Cylinder Aging Test (RCAT)[60]	85°C, oxygen at 75 ml/min, rotation creates ~2mm film	Designed based on kinetic approach; simulates realistic oxidative aging over extended times	Limited UV or humidity influence; not as widely standardized, large amount of material needed (500 grams)	Temperature, Oxygen flow, Thickness, Time
	Viennese Binder Aging (VBA) [19]	80°C, ozone (O ₃) and nitrogen oxides (NO _x), 0.5 mm film, 72 hours	Including ROS, low temperature and pressure	Long aging time compared to PAV, needs pre-VBA as STA, no humidity and UV effect	Temperature, ROS, Thickness, Time
Long-Term Aging Combined UV	UV Aging Chamber [61]	Mercury gas lamp (180-315 nm), 140°C, 1.5 mm film on glass plates, aged for 450 days, equivalent to ~2000 solar days	Provides long-term UV aging simulation; comprehensive testing for polymerization, volatilization, and oxidation	Limited to surface simulation; lacks humidity and pressure controls	Temperature, UV Exposure, Thickness

	UV Aging Method [62]	UVA, UVB, and UVC light, 30 g bitumen sample, heated to 1 mm thickness, duration between 12 and 35 days based on lamp position, accumulating 360,000 Wh/m ²	Simulates UV radiation exposure up to ~14.5 years; consistent UV energy density for standardized results	UV only; photochemical effects not replicable by oxidative methods alone	UV Exposure, Temperature, Thickness
	UV Weatherometer [63]	UV treatment at 65°C on 100 mm films, 2-hour cycle (102 mins UV, 18 mins water spray at 300 kPa), test durations up to 14 days	Combines UV radiation with humidity; realistic field simulation of photochemical aging effects	Limited to upper surface layer; difficult to generalize effects across binder depths	UV Exposure, Temperature, Humidity
	Climate Chamber [64]	UV exposure with simulated rain and drying cycles over 24 h (16.25 h UV at 50°C, 4 h NaCl rain at 40°C, 1 h water at 20°C, 2.75 h dry at 22°C)	Integrates UV exposure with water damage; repeated cycles allow for cumulative aging simulation	Poor correlation with field performance; lacks control over air flow and pressure	UV Exposure, Temperature, Humidity, Water Damage

2.4 Characterization methods to evaluate binder aging

Aging impacts both the chemical composition and rheological properties of bitumen, necessitating diverse assessment methods beyond standard tests such as penetration (EN 1426 [65]), softening point (EN 1427 [66]), and viscosity (commonly evaluated via Brookfield or rotational viscosity tests – EN 13302 [67]). Advanced techniques such as thin-layer chromatography-flame ionization detector (TLC-FID), Fourier-transform infrared spectroscopy (FTIR), nuclear magnetic resonance (NMR), gel permeation chromatography (GPC), and differential scanning calorimetry (DSC) have enabled detailed analysis of chemical components, functional groups, molecular weights, and thermal properties of bitumen before and after aging [10, 68]. Recently, advancements in microscale characterization methods, including fluorescence spectroscopy (FS) and atomic force microscopy (AFM), have further expanded the understanding of bitumen aging by exploring its microscale properties [68]. The following paragraphs offer a brief overview of each method, including their application in aging studies of paving binders, along with their respective advantages and disadvantages.

2.4.1 Chemical characterization methods

Thin-Layer Chromatography-Flame Ionization Detector (TLC-FID)

TLC-FID is a chromatographic technique that separates bitumen into four fractions: saturates, aromatics, resins, and asphaltenes, leveraging differences in molecular polarity [10, 69, 70]. This method quantifies the content of these fractions by burning them and measuring the resulting ionization. When applied to binder aging, TLC-FID is typically used by comparing aged samples to their unaged counterparts to evaluate shifts in chemical composition due to oxidation and thermal effects. These changes commonly manifest as an increase in asphaltene content and a reduction in saturates and aromatics (Figure 2.9) [68, 71]. Previous studies have demonstrated its utility in characterizing oxidative aging, correlating the asphaltene increase with enhanced stiffness and brittleness of the aged binder [72]. While providing rapid results, the high cost of TLC-FID instrumentation limits its accessibility in routine testing [68].

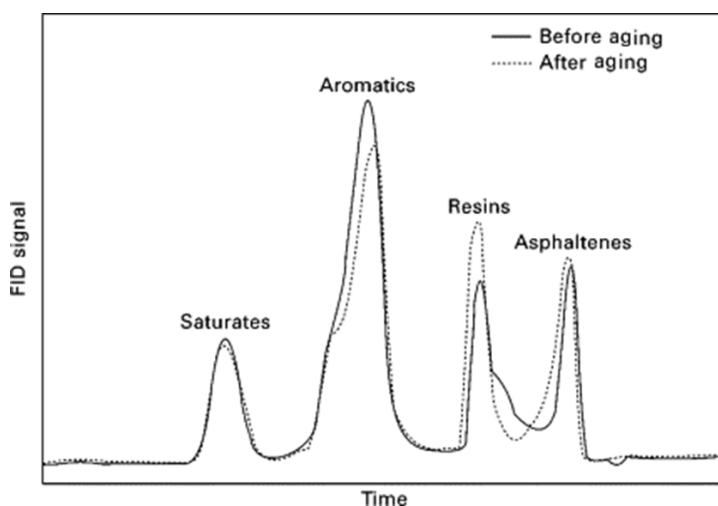


Figure 2.9 Aging effect on bitumen TLC-FID chromatogram [71].

Gel Permeation Chromatography (GPC)

GPC is a chromatographic technique that separates bitumen molecules based on their molecular size, offering insights into the molecular weight distribution [10, 68]. Aging typically induces polymerization of smaller molecules into larger ones, which is observable through a shift in GPC peaks when comparing aged samples to their unaged counterparts. As illustrated in Figure 2.10, the chromatogram area is divided into three fractions: large molecular size (LMS) corresponding to slices 1–5, medium molecular size (MMS) covering slices 6–9, and small molecular size (SMS) including slices 10–13 [73]. Earlier research revealed that as the ageing process progressed, the molecular structure shifted from smaller to larger sizes. Significant correlations have been identified between sulfoxide content, LMS proportion, and viscosity variations [74, 75]. This method is particularly effective in associating chemical changes with macroscopic performance alterations [68]. Additionally, the polydispersity index (PDI), which represents the molecular weight distribution of a polymer and is calculated as the ratio of weight-average molecular weight to number-average molecular weight, exhibited a strong correlation with rheological properties [76-78]. However, GPC analysis alone does not provide a comprehensive understanding of the mechanisms underlying aging-related changes and is mainly employed for qualitative assessments or in combination with other analytical techniques [79]. Another limitation of GPC in bitumen studies is its inability to fully resolve complex molecular weight distributions due to the highly diverse and heterogeneous nature of bitumen.

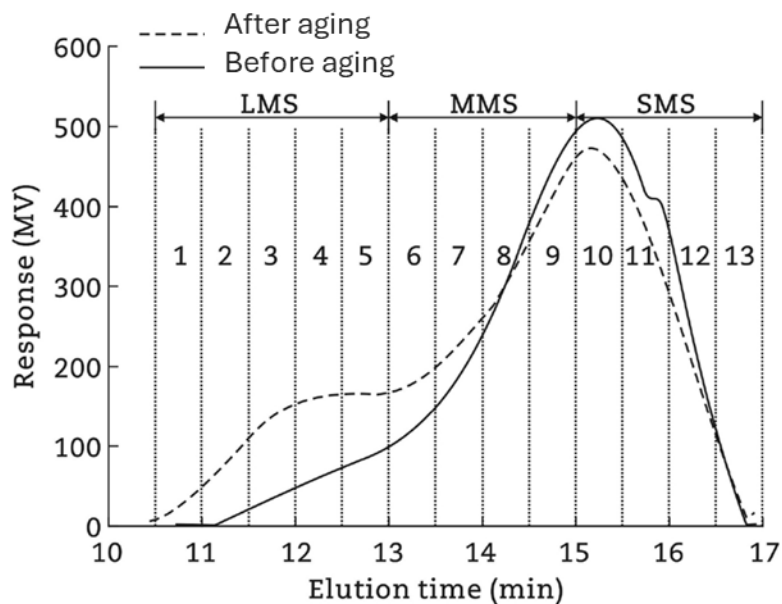


Figure 2.10 GPC profiles of paving binder before and after aging, displaying three segments: LMS, MMS, and SMS [73].

Nuclear magnetic resonance (NMR)

NMR Nuclear Magnetic Resonance (NMR) is a spectroscopy technique that exploits the magnetic properties of atomic nuclei (e.g., ^1H , ^{13}C , ^{31}P) to provide detailed information about molecular structures and dynamics. In the context of bitumen, NMR is utilized to investigate the complex mixture of molecules, offering insights into the distribution of functional groups, molecular weight, and structural features of the different polarity-based fractions (saturates, aromatics, resins, and asphaltenes). By comparing aged samples to their unaged counterparts, NMR can capture the aging process of bitumen by revealing structural transformations such as oxidation and the formation of new functional groups. Figure 2.11 presents examples of ^1H NMR spectra for a binder sample in different ageing states, along with the normalised per sample mass area integrations [80], while

Table 2.2 lists typical proton groups in bitumen along with their corresponding chemical shift ranges. Using spectroscopic ^1H NMR, shifts in functional groups, including increases in methyl and methylene and decreases in aromatic and α -alkyl protons, are observed during aging, reflecting molecular changes in the material [81-83]. However, a significant limitation of NMR in bitumen analysis is the overlapping signals produced by the diverse range of molecular species present, which complicates data interpretation[84]. Additionally, the technique's effectiveness can be constrained by the need for well-defined samples, as the complexity of bitumen means that no single analysis can provide a complete picture of its chemical characteristics[84].

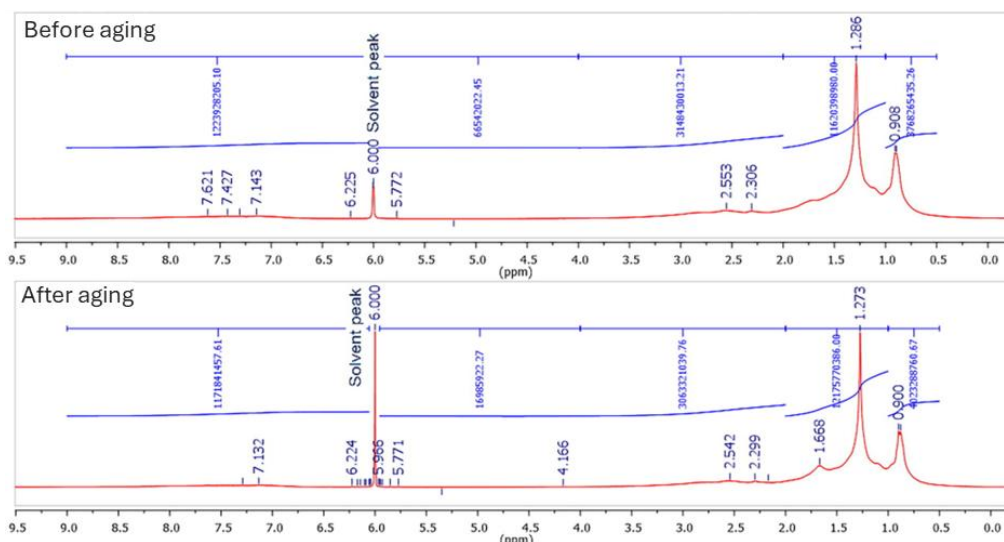


Figure 2.11 Example of ^1H NMR spectra for bitumen A in all ageing states, highlighting the main proton peaks.

Table 2.2 Typical groups of protons in bitumen [80].

Designation	Chemical shift range	Type of protons	Major proton peak in this region
H_{methyl}	0.5–1.0	Aliphatic hydrogen on C_γ^* and the CH_3 beyond the C_γ to aromatic rings	Methyl
$\text{H}_{\text{methylene}}$	1.0–2.0	Aliphatic hydrogen on C_β^* and the CH_2 beyond the C_β to aromatic rings	Methylene
$\text{H}_{\alpha\text{-alkyl}}$	2.0–4.0	Aliphatic hydrogen on C_α^* to aromatic rings	–
$\text{H}_{\text{olefinic}}$	4.0–6.0	Olefinic hydrogen	–
$\text{H}_{\text{aromatic}}$	6.0–9.0	Aromatic hydrogen	–

C_γ , C_β , and C_α refer to the first, second, and third carbon atoms, respectively, in a carbon chain relative to a reference group or functional moiety (e.g., an aromatic ring). This notation is commonly used to describe the position of atoms in aliphatic chains with respect to a central functional group.

Differential Scanning Calorimetry (DSC)

DSC is a thermal analysis method that measures the heat flow associated with phase transitions in bitumen, such as the glass transition temperature (T_g)[68]. The T_g defines the phase behaviour of amorphous materials or the amorphous fraction of semi-crystalline materials. Below T_g , the

molecular chains in bitumen are "frozen", and the bitumen is in a brittle, glassy state. As the temperature rises, bitumen progressively shifts to a more viscous state[85]. T_g is observed over a temperature range with an onset, endpoint, and midpoint. The onset marks the start of the glass transition, the endpoint indicates its completion, and the midpoint represents T_g , where the heat flow difference is halved. The heat capacity difference (ΔC_p) between onset and endpoint reflects the energy needed for molecular motion in the glassy and viscous states (Figure 2.12). Aging elevates T_g due to the accumulation of asphaltenes and the loss of lighter fractions, signalling a shift toward brittleness[86, 87]. Studies using DSC have shown consistent increases in T_g with aging time, highlighting its utility in monitoring thermal properties. Additionally, the method captures changes in specific heat capacity, indicative of reduced molecular mobility in aged binders[87]. Moreover, crystallization and dissolution in bitumen are observed through endothermic peaks during heating, indicating decrystallization, and exothermic peaks during cooling, representing crystallization. The enthalpies of these processes are quantified by integrating the areas under the respective peaks. The interpretation of crystallization and decrystallization in bitumen varies regarding the mechanisms involved, such as the role of primary and secondary crystals and the impact of aging on these processes, with no consensus on the underlying behaviour [85]. The limitation of DSC in bitumen studies is its low sensitivity to subtle phase transitions and the overlapping thermal events in complex paving materials.

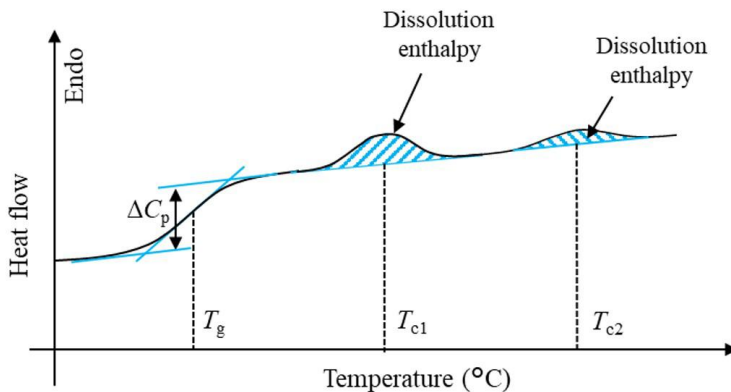


Figure 2.12 Measurement of glass transition temperature, crystallization temperature, and crystallization-related enthalpy from heat flow data obtained through DSC analysis [85].

Fluorescence Spectroscopy (FS)

FS utilizes fluorescence emission to examine the microscale morphology of bitumen[68]. Changes in fluorescence intensity and particle distribution provide indirect evidence of chemical alterations during aging. Mirwald et al. observed a decline in fluorescence intensity and shifts in excitation-emission spectra across aging conditions (Figure 2.13), correlating these changes with the depletion of aromatic compounds and increased particle aggregation [88]. FS is particularly suited for visualizing microstructural evolution in modified and aged binders. The limitation of FS in bitumen studies is its inability to detect non-fluorescent components and its sensitivity to sample preparation and environmental factors, which can affect reproducibility.

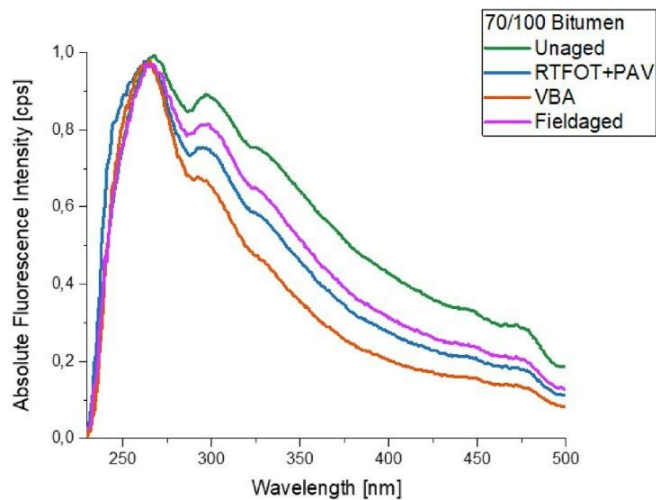


Figure 2.13 Excitation spectra of unaged and three LTA bitumen samples (RTFOT+PAV, VBA as shown in Table 2.1, and field-aged), displayed with their normalized intensity.

Attenuated total reflectance Fourier-transform infrared spectroscopy (ATR-FTIR)

ATR-FTIR is a widely utilized technique to probe the chemical complexity of paving binders, valued for its cost-effectiveness, accessibility, and non-destructive nature [95-97]. ATR-FTIR is particularly useful in detecting changes in functional groups due to oxidative aging or the incorporation of new materials, such as polymers or regenerators, typically by comparing spectra of aged and unaged binder samples [98-100]. The technique captures these chemical modifications in the ATR-FTIR spectra, enabling direct comparisons between aged and unaged samples (Figure 2.14)[49, 101]. Infrared spectroscopy provides detailed insight into functional group composition, which is especially valuable in aged bitumen analysis. Using this method, researchers can quantify carbonyl compounds (e.g., ketones, dicarboxylic anhydrides, carboxylic acids) and sulfoxides within bitumen samples [22, 95, 102, 103]. FTIR analysis in bitumen studies requires data pre-processing (DP) techniques such as normalization and baseline correction to ensure accurate spectral interpretation; however, there are no standardized protocols for these methods. The details of these challenges and their implications will be discussed in Chapter 3.

While FTIR allows for a chemical perspective on aging, relying solely on this technique may yield incomplete conclusions, as each analytical approach has limitations and results can vary across binders based on their intrinsic properties or aging conditions. Therefore, a comprehensive understanding of a specific binder's aging behaviour necessitates coupling FTIR with a rheological evaluation.

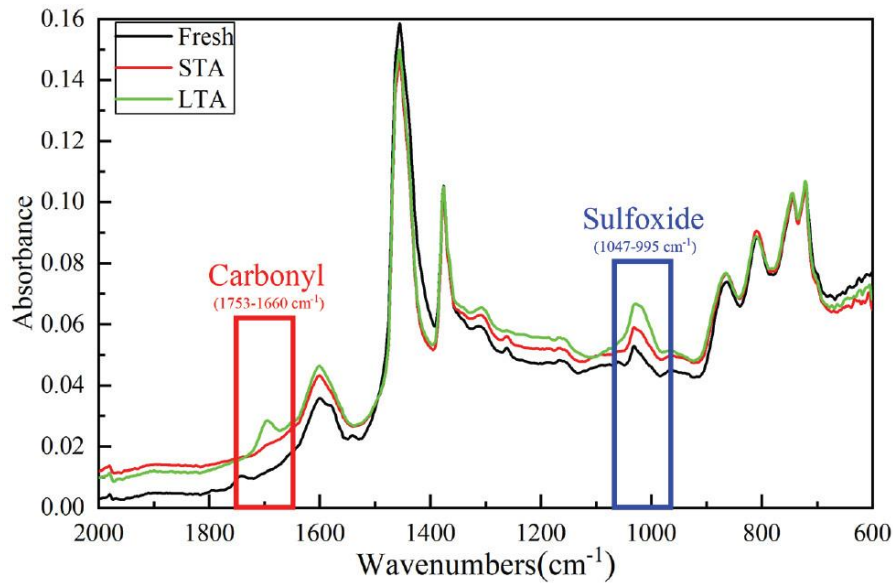


Figure 2.14 FTIR spectra of laboratory-aged bitumen: STA and LTA, using RTFO and PAV tests, respectively [49].

2.4.2 Surface characterization methods

Atomic Force Microscopy (AFM)

AFM provides nanoscale topographical property data of bitumen. Aging changes distinct "bee-like" structures on the bitumen surface (Figure 2.15) [89, 90], which are often attributed to asphaltene aggregation or microphase separation, though their exact origin remains under discussion. Quantitative parameters like surface roughness and "bee-like" structure percentage derived from AFM have been correlated with binder stiffness and oxidative aging severity [91]. Researchers suggest that microscopic characteristics link the chemical components and macroscopic properties of bitumen. Analysing these characteristics before and after ageing helps assess bitumen's ageing mechanism. The correlation between micro and macro-level changes has been explored in various studies [92-94]. The limitations of AFM in bitumen studies include its focus on surface imaging, which does not capture subsurface structures or bulk rheology, slow scanning speed limiting high-volume sample analysis, and the need for contact with the sample, making it unsuitable for imaging high-temperature bitumen in its sticky liquid state. Additionally, as a primarily visual technique, AFM remains challenging to quantify in a standardized and reproducible manner.

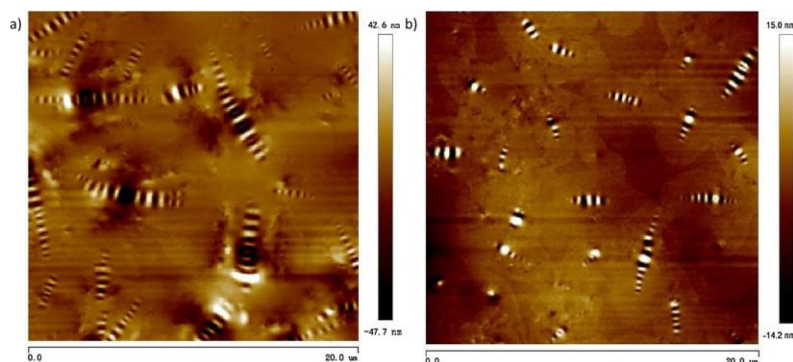


Figure 2.15 Topographic maps of binder: (a) Unaged. (b) Aged [90].

2.4.3 Rheological characterization methods

Dynamic Shear Rheometer (DSR)

DSR - Complex modulus (G^) and phase angle (δ)*

Rheological characterization is central to aging studies of bitumen, as it provides insights into material behaviour at specified temperatures while accounting for chemical composition and molecular structure [10]. The Dynamic Shear Rheometer (DSR) is typically employed to monitor changes in complex modulus (G^*) and phase angle (δ) across temperature or frequency sweeps, generally by comparing aged binders to their unaged counterparts to assess the effects of aging. Researchers commonly assess these rheological parameters before and after aging processes. Results typically reveal that aging leads to an increase in complex modulus and decrease in phase angle and crossover values, indicating a progression toward more solid-like mechanical properties. The magnitude of these changes depends on the binder type and testing conditions. Generally, aged bitumen demonstrates a higher complex modulus at low frequencies (or medium-high temperatures) compared to (the same) unaged bitumen, while aging has limited influence on the complex modulus at high frequencies (or low temperatures) (Figure 2.16) [100, 104].

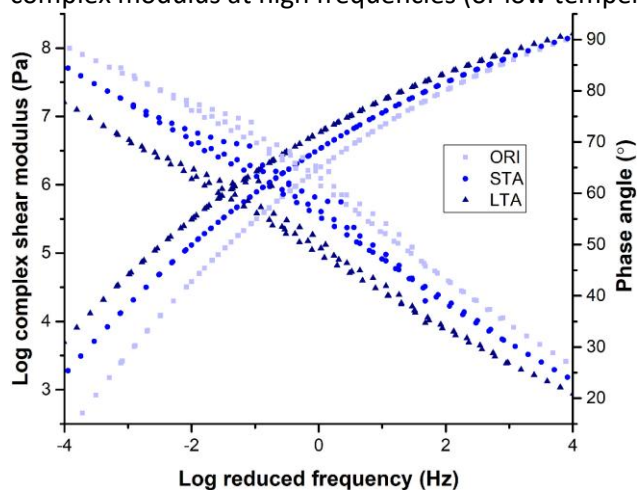


Figure 2.16 Master curves of the 70/100 bitumen at different ageing levels, ORI stands for unaged binder, STA and LTA, using RTFO and PAV tests, respectively [104].

DSR - Crossover values

Parameters such as crossover frequency and crossover modulus are also analysed, corresponding to the frequency and complex modulus where the phase angle reaches 45° and storage modulus equals the loss modulus, respectively [22, 105]. These indicators highlight transitions in bitumen's viscoelastic behaviour, marking the shift from liquid-like to solid-like states. Both parameters decrease with oxidative aging [106].

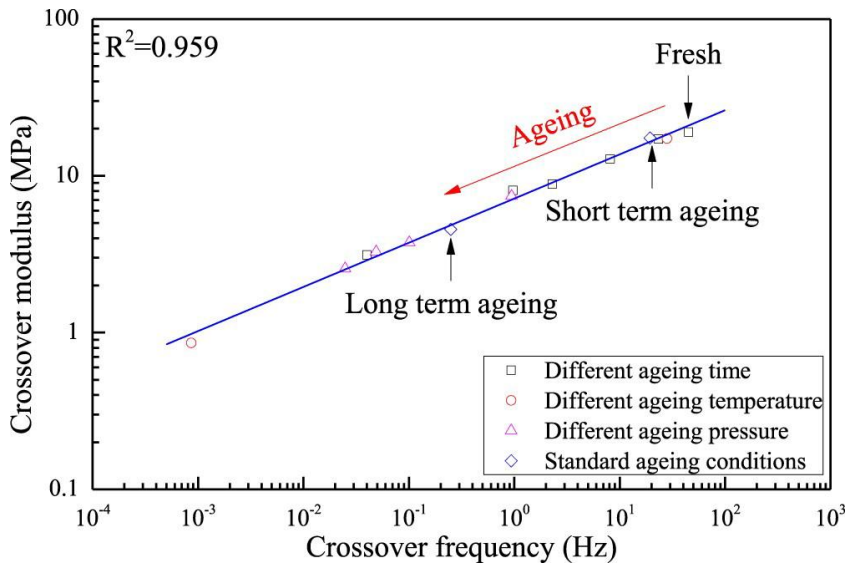


Figure 2.17 Comparison of crossover modulus and crossover frequency of bitumen under various aging conditions [106].

DSR - Rutting factor and fatigue factor

Parameters such as the rutting factor ($G^*/\sin \delta$) and fatigue factors ($G^* \cdot \sin \delta$ and $G^* \cdot \cos^2 \delta / \sin \delta$) provide additional insights into high-temperature rutting resistance and low-temperature durability [68]. The rutting factor generally increases with aging, reflecting enhanced stiffness and resistance to deformation (Figure 2.18). However, fatigue factors show material-dependent trends. In contrast, fatigue factors exhibit material-dependent trends. This variation arises because aging affects not only stiffness but also brittleness; the interplay between increased stiffness and the material's reduced ability to dissipate strain determines its fatigue performance. Consequently, depending on the balance between these two effects, fatigue resistance may improve, deteriorate, or remain relatively unchanged across different binder types.

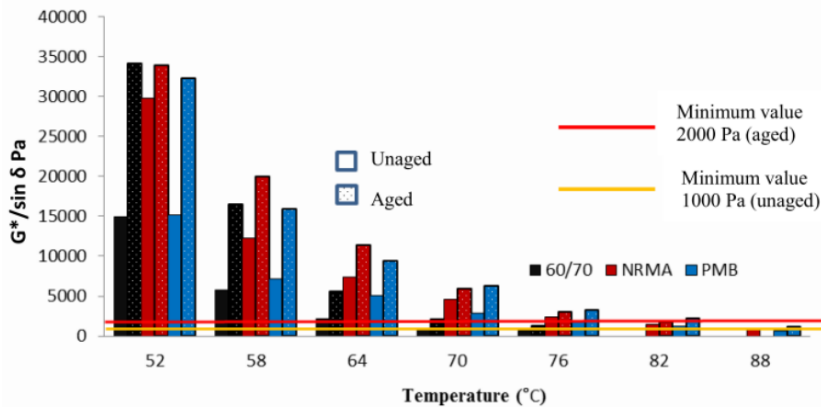


Figure 2.18 Rutting factor ($G^*/\sin \delta$) (kPa) of unaged and aged RTFO bitumen binder, natural rubber-modified asphalt (NRMA), and polymer-modified binder (PMB)[107].

DSR - Glover-Rowe

Newer indicators like the Glover-Rowe (G-R) parameter have proven effective in correlating viscoelastic properties with durability [108, 109]. The G-R parameter reflects the binder's resistance to cracking, with higher values indicating increased stiffness and a higher potential for cracking, especially as aging progresses. As asphalt materials age, the G-R value increases, suggesting reduced flexibility and greater susceptibility to durability cracking (Figure 2.19)[110, 111].

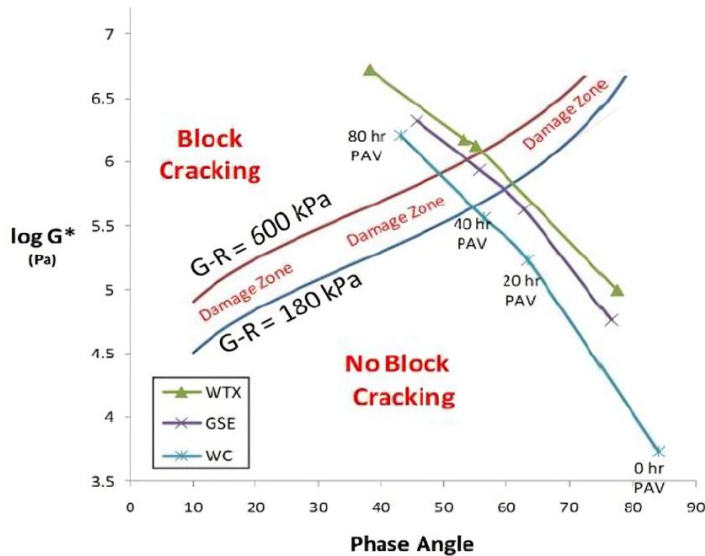


Figure 2.19 Black space diagram showing G-R parameter limits for various binders at different aging stages [110].

DSR - Creep stiffness and m-value

For low-temperature performance, the bending beam rheometer (BBR) and dynamic shear rheometer (DSR) with smaller geometry (4 mm) are used to measure creep stiffness (S) and m -value, critical for predicting cracking[68]. Aging elevates stiffness while reducing relaxation capacity, impairing low-temperature resistance [112, 113].

DSR - Stress-strain curves in linear amplitude sweep

The Linear Amplitude Sweep (LAS) test evaluates the damage tolerance of bitumen by applying oscillatory loading with linearly increasing strain [114]. The resulting stress-strain curves (Figure 2.20) reveal that binders initially exhibit linear stress increase within their Linear Viscoelastic (LVE) region[115]. As the strain increases, stress reaches a peak, indicating binder damage, followed by a decrease in stress as strain continues to rise. Aged binders generally exhibit higher peak stresses, with more severe aging leading to progressively higher stress levels. Notably, short-term aged binders demonstrate the highest strain at peak stress compared to fresh and long-term aged binders, suggesting that short-term aging may enhance damage tolerance by increasing stiffness and elasticity. In contrast, long-term aging leads to increased brittleness, reducing strain tolerance. Overall, the LAS test shows that while short-term aging marginally improves damage tolerance, long-term aging significantly weakens it by lowering the strain at peak stress. However, this reduction occurs alongside an increase in stiffness, indicating a mixed effect similar to fatigue behaviour, where the balance between increased modulus and reduced ductility governs the net damage resistance.

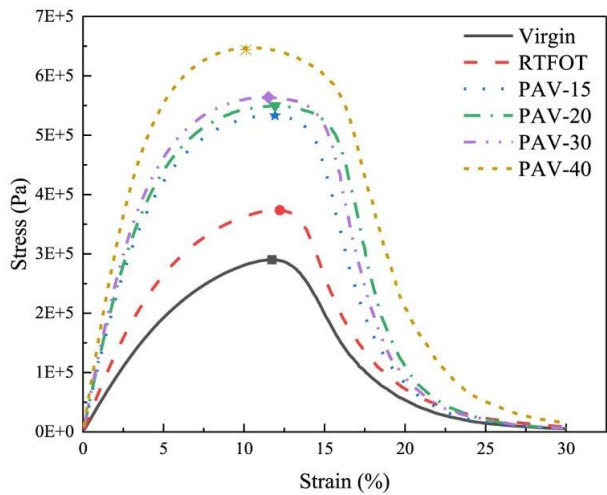


Figure 2.20 Stress-strain curves for the 70/100 binder in the LAS test at various aging stages.

DSR - Nonrecoverable creep compliance and percent recovery

The Multiple Stress Creep Recovery (MSCR) test is considered a key method for assessing the high-temperature performance of paving materials. It provides two critical parameters: nonrecoverable creep compliance (J_{nr}), which indicates rutting susceptibility, and percent recovery (%R), reflecting the binder's elastic response and stress dependence [116]. Aging significantly affects both parameters (Figure 2.21), with aging reducing bitumen strain, thus enhancing deformation resistance. Short-term aging causes a notable decrease in strain, while long-term aging further reduces strain, though with diminishing effects over time. The J_{nr} value decreases as aging progresses, with a sharp drop after short-term aging and another significant decline after long-term aging. However, as aging continues, the rate of decline in J_{nr} becomes less pronounced, due to the stabilization of heavy fractions like asphaltenes [116, 117]. Similarly, the %R value increases with aging, indicating improved elasticity and recovery as the binder hardens. Overall, MSCR results demonstrate that while short-term aging enhances binder stiffness and recovery, long-term aging continues to harden the binder, reducing its ability to recover but improving its rutting resistance.

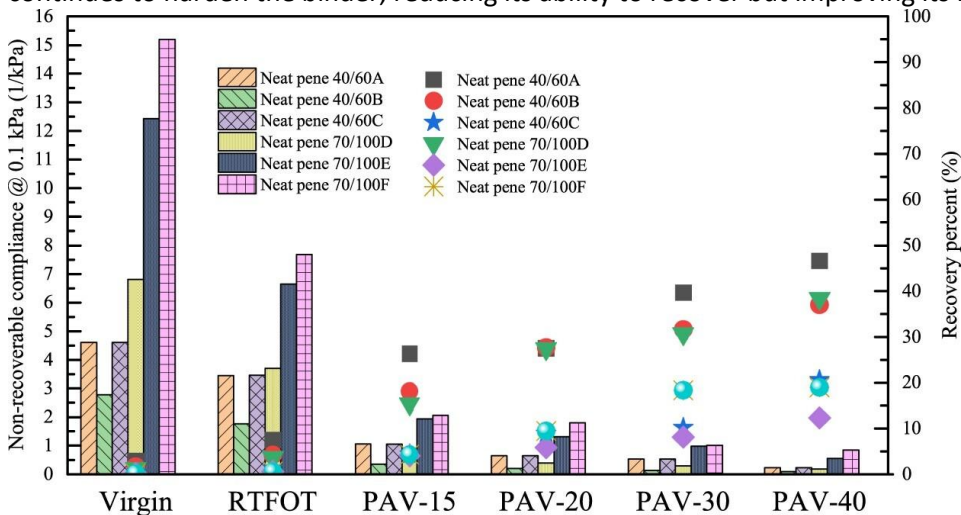


Figure 2.21 J_{nr} and %R values of binders under different aging conditions [116].

For this thesis, a combined approach of attenuated total reflectance Fourier-transform infrared spectroscopy (ATR-FTIR) and frequency sweep rheological testing has been selected to facilitate a detailed investigation of bitumen aging. ATR-FTIR was chosen due to its ability to provide precise chemical information by detecting changes in functional groups, such as carbonyl and sulfoxide, which are critical markers of oxidative aging. This method is non-destructive, requires minimal

sample preparation, and offers high sensitivity to chemical changes, making it ideal for analysing bitumen aging mechanisms. Moreover, frequency sweep rheological testing complements this by offering a detailed assessment of viscoelastic properties across a range of temperatures and frequencies, capturing mechanical changes like stiffness and elasticity caused by aging. Together, these methods enable a comprehensive evaluation by linking chemical transformations with corresponding changes in mechanical performance, surpassing the capabilities of other techniques that typically focus on either chemical or physical properties in isolation. A more detailed explanation of these methods, along with a literature review, can be found in Chapters 3, 4, and 5.

2.5 Application of multivariate analysis in paving materials

Advancements in technology now enable the rapid acquisition of high-dimensional data, though its analysis can be challenging. Multivariate analysis methods address this complexity by revealing intricate relationships between variables, thus aiding decision-making in pavement engineering and material selection. Multivariate analysis methods play a crucial role in paving binder aging studies, offering effective tools for analysing complex, high-dimensional datasets. Techniques such as Principal Component Analysis (PCA), Hierarchical Cluster Analysis (HCA), Linear Discriminant Analysis (LDA), Partial Least Squares Regression (PLSR), Support Vector Regression (SVR), and Artificial Neural Networks (ANNs) are widely applied in pavement engineering. These methods can process diverse types of input data, including FTIR spectra and DSR results, to evaluate binder properties and aging behaviour.

Principal Component Analysis and Hierarchical Cluster Analysis

To study different aging stages and binder types, Siroma et al. applied PCA, a dimensionality reduction technique that identifies key patterns in datasets by transforming variables into a set of orthogonal components, alongside HCA, a method that groups data based on similarities, to analyse phase angle master curves and assess aging conditions [118]. This combination provided a clear distinction between binders at various aging stages, showcasing the effectiveness of these techniques in evaluating binder performance comprehensively. The integration of PCA allowed for the identification of critical variations in rheological properties across aging stages, while HCA effectively clustered the binders based on their performance attributes. PCA effectively identified key variations in rheological properties across aging stages, while HCA clustered binders based on performance attributes. However, PCA does not inherently provide class separability, and HCA's results can be sensitive to distance metrics and linkage methods, potentially leading to variations in clustering outcomes. These limitations necessitate careful preprocessing and validation when using these techniques.

Principal Component Analysis and Linear Discriminant Analysis

Similarly, Ma et al. used PCA combined with LDA, a method for classifying data into predefined categories, to analyse FTIR spectra (Figure 2.22) [119]. This approach effectively identified aging-induced changes in aliphatic and aromatic bonds, underscoring the chemical changes that occur during oxidation. LDA enhanced the interpretability of PCA by classifying binders into predefined aging categories, thereby reinforcing the link between chemical transformations and oxidation. However, LDA assumes normality and homoscedasticity (homogeneity of variances) of data distributions, which may not always hold in complex chemical datasets. The combined approach of PCA-LDA effectively improved aging classification accuracy.

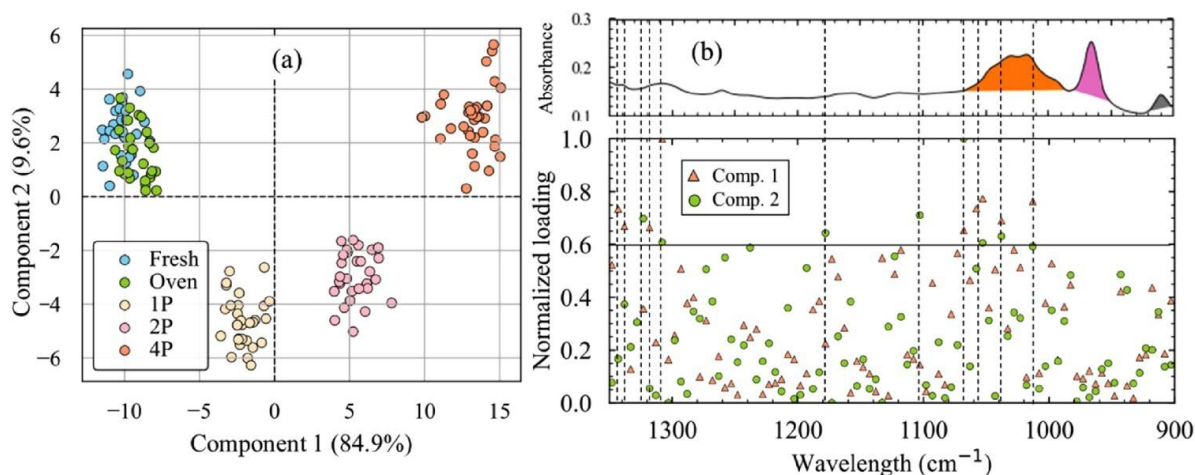


Figure 2.22 Classification of aging states: (a) score plot and (b) loading plot of the PCA-LDA model. The variables selected for this analysis are based on the highest prediction accuracy, specifically the band range from 1350 to 900 cm^{-1} [120].

Partial Least Squares Regression

Partial Least Squares Regression (PLSR), a method that relates predictor variables to response variables by maximizing their covariance, has been widely used for predicting binder properties. Unlike PCA, which prioritizes variance maximization, PLSR relates predictor and response variables by maximizing covariance, making it more suitable for regression tasks. Weigel and Stephan [121] explored the use of FTIR spectra and its first derivative for LDA and PLS regression, demonstrating that paving binder samples, despite differences in grade and aging state, could be accurately distinguished based on refinery origin. They also developed PLS regression models based on FTIR peak areas to predict parameters such as penetration, complex shear modulus, phase angle, and asphaltene content [122]. However, PLSR can be prone to overfitting, particularly when using a large number of latent variables, necessitating proper model validation. Primerano et al. further improved PLSR by integrating it with random forest analysis to classify FTIR spectra, identifying key wavenumbers associated with distinct aging states [123]. This approach combined the interpretability of PLSR with the robustness of ensemble learning, enhancing predictive performance. Moreover, Motevalizadeh et al. expanded the application of PLSR by integrating it with LDA to analyse FTIR data (Figure 2.23a), using Variable Importance in Projection (VIP) scores to highlight key chemical indicators of aging, such as carbonyl and sulfoxide indices (Figure 2.23b). These findings were further enhanced by CatBoost regression analysis, a gradient boosting algorithm designed to handle categorical and numerical data, which effectively captured the non-linear relationships between chemical composition and rheological properties [124]. Additionally, multivariate clustering approaches, combining PLSR for dimensionality reduction and HCA for clustering, have revealed how mineral fillers influence aging [125]. For instance, limestone fillers were shown to mitigate aging effects in foamed bitumen mastics, offering practical implications for binder design. This advanced chemometric approach enabled a more detailed characterization of binder aging behaviour. However, the increased complexity of such models requires careful selection of preprocessing steps, latent variables, and distance metrics. To enhance reproducibility and objectivity, it is essential to standardize these parameters and document them transparently, so that others using the same techniques on the same data can reproduce the results reliably.

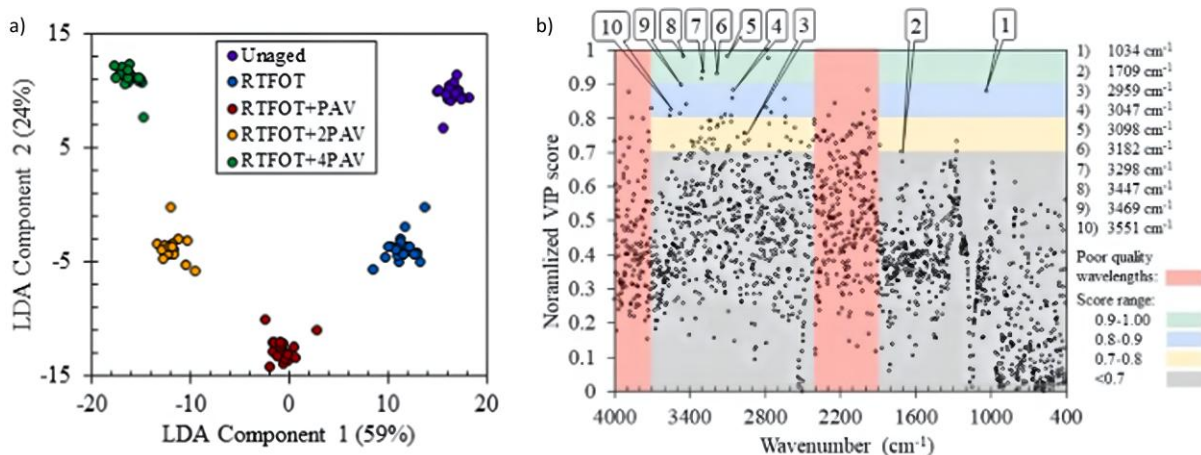


Figure 2.23 a) Classification of paving mastics by aging states using PLSR-LDA, plotted along component 1 vs. component 2. b) Normalized VIP scores highlighting key wavenumbers for distinguishing different aging states [124].

Support Vector Regression

Furthermore, other machine learning methods such as Support Vector Regression (SVR) that models non-linear and complex relationships by mapping input data into higher-dimensional spaces using kernel functions, has also shown promise in predicting rheological properties from FTIR data. Ma et al. demonstrated that SVR outperformed traditional PLSR models in capturing the intricate chemical-rheological relationships inherent to bitumen [126]. While SVR does not itself provide mechanistic insight, its improved predictive capacity can support the identification of relevant variables and trends, thereby facilitating a more informed interpretation of aging behaviour when used alongside domain knowledge. Unlike ordinary linear regression, SVR employs kernel functions to handle non-linear relationships, offering improved predictive performance in cases where conventional linear models fall short. While non-linear regression techniques can also model such complexity, SVR provides a flexible framework that is particularly well-suited for high-dimensional and multicollinear data, although requiring careful parameter selection and validation. However, SVR requires careful selection of kernel parameters and is computationally more intensive than PLSR. Despite these challenges, SVR's ability to handle high-dimensional data makes it a valuable tool for analysing binder properties.

Multiple linear regression

Additionally, to model relationships between a dependent variable and multiple independent variables Multiple linear regression (MLR) is commonly used by fitting a linear equation to the data. Giri et al. successfully applied MLR to predict optimal binder content [127], and Tusar et al. identified key factors impacting asphalt mix properties using this method. MLR models have also shown higher predictive accuracy than PLS model in similar applications [128]. MLR provides a straightforward interpretation of variable relationships; however, it assumes linearity, independence, and minimal multicollinearity among predictors, which may not always be valid in complex aging studies. The validity of these assumptions must be checked before applying MLR, for example by using Pearson correlation coefficients or other diagnostic tests, since in aging studies the measured parameters are usually deliberately chosen to reflect interrelated aspects of material transformation. Khalighi et al. employed MLR to examine the impact of variables such as temperature, pressure, and time on a combined chemical-rheological index, identifying optimal aging conditions for simulating nine years of field aging in porous and stone mastic asphalt [129]. Similarly, Weigel and Stephan utilized MLR to

construct a model describing the rheological and aging behaviour of bitumen based on its chemical properties. By considering the contents and average molecular weights (M_n) of the SARA fractions, they derived linear combinations (Figure 2.24) that allowed the prediction of conventional and rheological parameters such as the softening point ($T_{R\&B}$), needle penetration (PEN), G^* , and δ at different temperatures [130]. The simplicity and interpretability of MLR make it a useful tool for identifying general trends and relationships; however, its predictive performance may be limited in comparison to more flexible non-linear models such as SVR and ANN, which can better capture the complex, non-linear behaviour often observed in aging-related data.

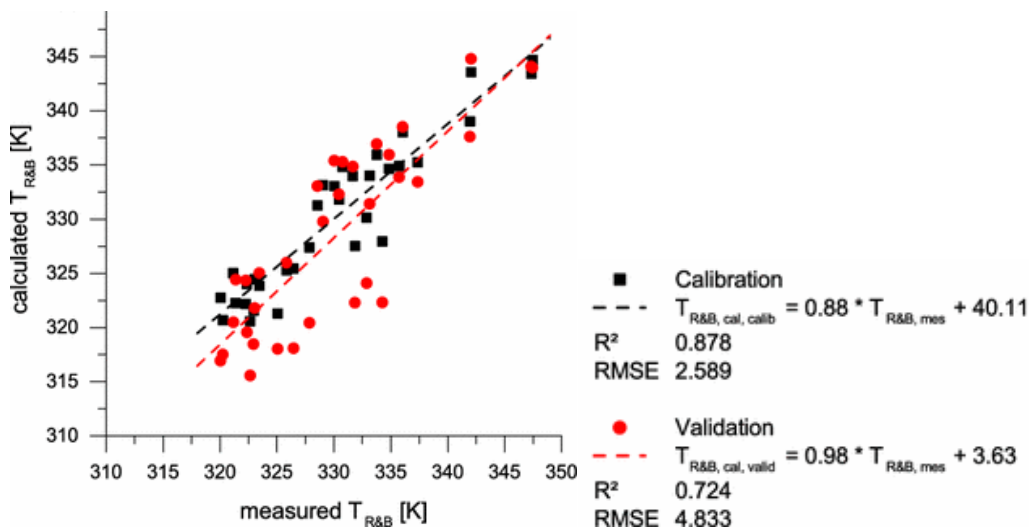


Figure 2.24 Comparison between the experimentally measured softening point and the MLR-predicted values based on the linear combination of $T_{R\&B}$ and SARA fractions ($n = 33$) [130].

Artificial Neural Networks

Artificial Neural Networks (ANNs), a machine learning method capable of modelling complex and non-linear relationships, have emerged as a powerful tool for predicting the behaviour and properties of asphalt binders, addressing the limitations of traditional analytical (Figure 2.25) [131]. Unlike traditional statistical methods, ANNs can model complex and non-linear interactions between multiple parameters, such as temperature, aging, and composition. [131, 132]. ANNs, with their robust ability to identify patterns within large datasets, have been widely employed to model such intricate relationships [132]. Various studies have utilized ANNs to predict key binder properties critical for pavement performance [132, 133]. For instance, ANN models have been developed to predict recovery and nonrecoverable compliance of asphalt binders under high stress conditions, using inputs such as test temperature, frequency, storage modulus, loss modulus, and viscosity [134]. These models have demonstrated high predictive accuracy, underscoring their potential in optimizing binder performance across diverse conditions. ANN models were employed to predict asphalt mixture aging characteristics, using asphaltene content as a fundamental performance parameter, demonstrating robust correlations with dynamic modulus ($|E^*|$) values [135]. Another study applied ANNs to predict the complex shear modulus of geopolymer-modified bitumen, incorporating parameters such as temperature, different geopolymer concentration, and frequency as inputs [136]. The study concluded that ANNs could reliably model the complex modulus.

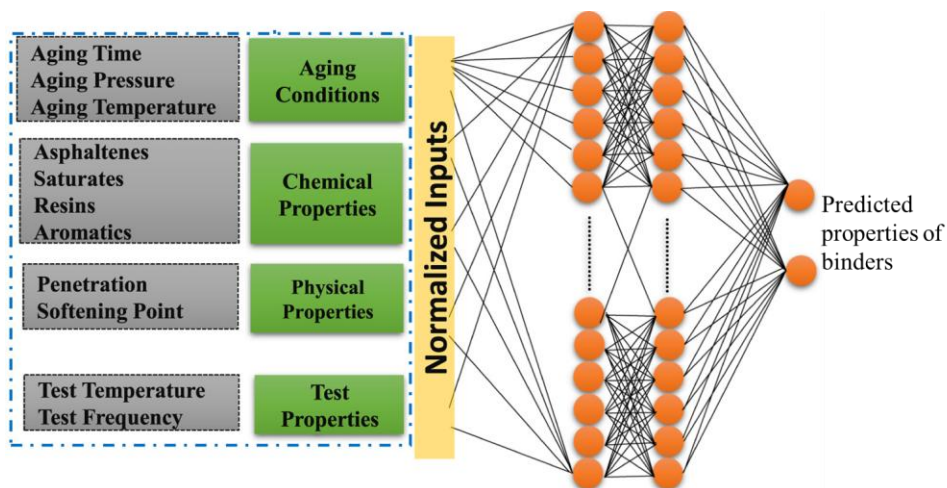


Figure 2.25 Schematic representation of an ANN model used for predicting asphalt binder properties. The input layer could consist of normalized features categorized into four groups: aging conditions (aging time, pressure, and temperature), chemical properties (asphaltenes, saturates, resins, and aromatics), physical properties (penetration and softening point), and test properties (test temperature and frequency). These inputs are processed through multiple hidden layers to capture complex relationships and predict asphalt binder performance [131].

Despite their high predictive capability, artificial neural networks (ANNs), like many advanced machine learning models, require large datasets for effective training and are often considered black-box approaches due to their limited interpretability compared to simpler statistical models. Additionally, hyperparameter tuning and computational demand can be significant challenges. Nonetheless, ANNs have proven valuable for predicting rutting performance parameters of binders using gradation components, base binder viscosity, and test conditions as inputs [137]. These studies highlight the ability of ANNs to model complex, nonlinear behaviours of asphalt binders effectively, offering valuable insights into the design and evaluation of binders under a range of service conditions. Moreover, one study developed an ANN model to predict the degree of binder activity in reclaimed asphalt pavement (RAP) samples using a reduced set of input variables, namely compaction temperature, air voids, and indirect tensile strength (ITS). This study highlighted the utility of ANNs in streamlining data analysis and accurately predicting binder activity for RAP applications [138, 139]. Similarly, ANNs have been applied to Styrene Butadiene Styrene (SBS) modified asphalt to model its performance parameters, including SBS content, needle penetration, and softening point. Using infrared spectral data as inputs, an ANN model achieved high accuracy, for SBS content, softening point, and penetration prediction, respectively. These results underscore the efficacy of ANNs in predicting SBS-modified asphalt properties, providing reliable regression models between spectral data and performance characteristics.

Overall, multivariate analysis provides a robust framework for evaluating binder aging by integrating chemical and rheological data. These techniques facilitate a comprehensive understanding of aging, enabling the identification of key chemical transformations and rheological properties associated with specific aging conditions and supporting the development of accurate aging protocols. Each method presents distinct advantages and limitations: PCA and HCA effectively reduce dimensionality and reveal structural patterns but may lack direct interpretability for regression tasks. PLSR and SVR offer strong predictive capabilities, though they differ in handling linear versus non-linear relationships. MLR provides a simple and interpretable approach but is constrained by its assumptions. ANNs, while highly flexible, require extensive data and computational resources. Understanding these strengths and weaknesses allows for the strategic selection of methods in

pavement engineering research. In later chapters, such as chapter 6, each method will be used for a specific goal aligned with its properties.

2.6 Knowledge gaps

The aging of paving binders under real-world conditions is a multifaceted process influenced by various environmental factors, including ultraviolet radiation, moisture exposure, ROS, and temperature fluctuations[47]. While laboratory aging protocols aim to simulate the effects of environmental exposure under controlled conditions, they cannot comprehensively replicate the variability and complexity of field aging. Existing aging procedures, such as RTFOT and PAV, primarily focus on accelerated oxidative aging, while often neglecting other critical mechanisms such as UV-induced degradation, moisture effects, and the contribution of reactive oxygen species (ROS) to binder deterioration. As such, current protocols may fail to represent the full spectrum of aging phenomena observed in service conditions. As a result, significant discrepancies persist between laboratory-aged and field-aged paving samples, raising concerns about the reliability of current laboratory protocols for pavement performance[20, 48, 49, 51, 140-146].

One fundamental limitation in existing research is the tendency to examine aging factors in isolation. Studies have predominantly focused on individual environmental stressors, such as thermal oxidation, UV radiation, or moisture damage, without adequately considering their combined effects. In real-world conditions, these aging mechanisms interact in complex and nonlinear ways, influencing the chemical and rheological properties of paving binders. The absence of a systematic framework to assess the combined influence of aging factors is likely a contributing reason for the limited development of protocols that more closely reflect field conditions.

Another critical gap pertains to the characterization of binder chemistry using ATR-FTIR. Although ATR-FTIR is widely employed for chemical characterization, its application in bitumen aging studies remains hindered by inconsistencies in spectral pre-processing techniques. The absence of standardized protocols for data pre-processing, such as baseline correction, normalization, and spectral smoothing, leads to variability in extracted chemical information and undermines the reproducibility of findings. Given that ATR-FTIR plays a central role in assessing oxidation and molecular changes in paving binders, the lack of well-defined pre-processing strategies constitutes a major obstacle to accurate spectral interpretation.

Furthermore, although both chemical and rheological properties are essential for understanding bitumen aging, most studies analyse these datasets separately rather than integrating them. Multivariate analytical techniques, such as PCA, PLSR, and ANNs, have typically been applied to either chemical or rheological data alone, without combining both types of information. This separation limits the development of predictive models capable of capturing the comprehensive relationship between molecular changes and mechanical performance, thereby hindering a holistic understanding of binder aging under complex environmental conditions.

Additionally, there is a lack of a standardized framework for evaluating the comparability of laboratory-aged and field-aged binders. The absence of a robust metric to assess the fidelity of aging protocols in replicating real-world conditions hinders efforts to refine existing methods. Without such a framework, it remains challenging to establish whether current aging protocols yield binders with properties representative of long-term field performance.

To address these gaps, this research systematically investigates the combined effects of multiple environmental aging factors, including liquid water, gaseous humidity, UV radiation, temperature, pressure, and ROS in both gaseous and liquid forms, on the chemical and rheological properties of paving binders. The study aims to refine laboratory aging protocols by incorporating these factors in a controlled and measurable manner. Additionally, it seeks to establish a standardized ATR-FTIR data pre-processing framework to enhance the accuracy and reproducibility of chemical characterization. A key aspect of this research is the integration of multivariate statistical methods to simultaneously analyse chemical and rheological data, enabling a more comprehensive understanding of the aging

process. By bridging the gap between binder chemistry and mechanical performance, this approach will facilitate the development of predictive models with greater reliability. Furthermore, this study will introduce an evaluation framework for comparing laboratory-aged and field-aged binders, providing a basis for validating and improving aging simulation techniques.

Ultimately, this thesis aims to develop a more accurate and efficient laboratory aging protocol for binders that better simulates real-world conditions. This research addresses the broader challenge of understanding how environmental aging factors collectively influence the chemical and rheological evolution of paving binders. A central hypothesis is that chemical changes induced by aging govern rheological changes, and that establishing consistent links between these domains, using data obtained under controlled and comparable conditions, can enhance our understanding of bitumen behaviour. Although most existing studies treat chemical and mechanical aspects independently, this work explores their integration through multivariate techniques, aiming to reveal meaningful correlations between molecular changes and macroscopic properties. To support this aim, selected analytical tools such as ATR-FTIR and chemometric methods were refined where necessary to ensure their suitability for integrated aging assessment. Methodological decisions and specific hypotheses are further developed within the respective chapters, each contributing to a more comprehensive framework for laboratory aging simulations. By doing so, this research ultimately contributes to the longer-term goal of supporting the design of more durable and sustainable asphalt materials.

2.7 References

1. Tauste, R., et al., *Understanding the bitumen ageing phenomenon: A review*. Construction and Building Materials, 2018. **192**: p. 593-609.
2. Porto, M., et al., *Bitumen and bitumen modification: A review on latest advances*. Applied Sciences, 2019. **9**(4): p. 742.
3. Zaidullin, I., et al., *Variation of the composition of asphaltenes in the course of bitumen aging in the presence of antioxidants*. Russian Journal of Applied Chemistry, 2013. **86**(7): p. 1070-1075.
4. Lu, X., Y. Talon, and P. Redelius. *Aging of bituminous binders—laboratory tests and field data*. in *Proceedings of the 4th Eurasphalt & Eurobitume Congress, Copenhagen*. 2008.
5. Collins, P., J. Masson, and G. Polomark, *Ordering and steric-hardening in SBS-modified bitumen*. Energy & fuels, 2006. **20**(3): p. 1266-1268.
6. Masson, J., P. Collins, and G. Polomark, *Steric hardening and the ordering of asphaltenes in bitumen*. Energy & fuels, 2005. **19**(1): p. 120-122.
7. Dessouky, S., et al., *Influence of antioxidant-enhanced polymers in bitumen rheology and bituminous concrete mixtures mechanical performance*. Advances in Materials Science and Engineering, 2015. **2015**.
8. Ma, L., et al., *Comprehensive review on the transport and reaction of oxygen and moisture towards coupled oxidative ageing and moisture damage of bitumen*. Construction and Building Materials, 2021. **283**: p. 122632.
9. Petersen, J.C., *A review of the fundamentals of asphalt oxidation: chemical, physicochemical, physical property, and durability relationships*. Transportation research circular, 2009(E-C140).
10. Tauste, R., et al., *Understanding the bitumen ageing phenomenon: A review*. Construction and Building Materials, 2018. **192**: p. 593-609.
11. Khalighi, S., et al., *Multivariate chemo-rheological framework for optimizing laboratory aging protocols of paving binders*. Materials & Design, 2024: p. 113520.
12. Herrington, P.R., *Diffusion and reaction of oxygen in bitumen films*. Fuel, 2012. **94**: p. 86-92.
13. Speight, J., *Petroleum Asphaltenes-Part 1: Asphaltenes, resins and the structure of petroleum*. Oil & gas science and technology, 2004. **59**(5): p. 467-477.

14. Hofer, K., et al., *Chemical and mechanical analysis of field and laboratory aged bitumen*. Road Materials and Pavement Design, 2023. **24**(sup1): p. 160-175.
15. Petersen, J.C., *Asphalt oxidation--AH overview including a new model for oxidation proposing that physicochemical factors dominate the oxidation kinetics*. Fuel science & technology international, 1993. **11**(1): p. 57-87.
16. Jing, R., *Ageing of bituminous materials: Experimental and numerical characterization*. 2019.
17. *Climate Atlas of Canada. (n.d.) Urban Heat Island Effect*. [cited 2024 11/14/2024]; Available from: <https://climateatlas.ca/urban-heat-island-effect>.
18. Zheng, Y., P. Zhang, and H. Liu, *Correlation between pavement temperature and deflection basin form factors of asphalt pavement*. International Journal of Pavement Engineering, 2019. **20**(8): p. 874-883.
19. Mirwald, J., et al., *Impact of reactive oxygen species on bitumen aging--The Viennese binder aging method*. Construction and Building Materials, 2020. **257**: p. 119495.
20. Airey, G.D., *State of the art report on ageing test methods for bituminous pavement materials*. International Journal of Pavement Engineering, 2003. **4**(3): p. 165-176.
21. Maschauer, D., et al. *Viennese Aging Procedure (VAPro): adaption for low-temperature testing*. in *Proceedings of the RILEM International Symposium on Bituminous Materials: ISBM Lyon 2020 1*. 2022. Springer.
22. Khalighi, S., S. Erkens, and A. Varveri, *Exploring the impact of humidity and water on bituminous binder aging: a multivariate analysis approach (TI CAB)*. Road Materials and Pavement Design, 2024: p. 1-25.
23. Bahia¹, H.U. and D.A. Anderson, *The Pressure Aging Vessel (PAV): a test to simulate rheological changes due to field aging*. Physical properties of asphalt cement binders, 1995. **1241**: p. 67.
24. Karim, F., J. Hussain, and I. Hafeez, *Estimating the asphalt binder film thickness using scanning electron microscope and energy dispersive X-Ray spectroscopy*. Advances in Materials Science and Engineering, 2021. **2021**: p. 1-16.
25. Karim, F. and J. Hussain, *Assessing the asphalt binder film thickness in recycled asphalt mixtures using micro-level techniques*. Materials, 2021. **14**(24): p. 7891.
26. AlKofahi, N. and T. Khedaywi, *Evaluation the effect of asphalt film thickness on stripping resistance*. International Journal of Applied Engineering Research, 2019. **14**(2): p. 560-570.
27. Lin, P., et al., *Effects of bitumen thickness on the aging behavior of high-content polymer-modified asphalt mixture*. Polymers, 2023. **15**(10): p. 2325.
28. Khalighi, S., et al., *Exploring the significance of exposed surface area in the aging of bitumen films with equal thickness*, in *Bituminous Mixtures and Pavements VIII*. 2024, CRC Press. p. 71-79.
29. Ma, L., et al., *Water diffusion mechanisms in bitumen studied through molecular dynamics simulations*. Construction and Building Materials, 2023. **409**: p. 133828.
30. Valentin, J., et al., *A comprehensive study on adhesion between modified bituminous binders and mineral aggregates*. Construction and Building Materials, 2021. **305**: p. 124686.
31. Cong, P., X. Guo, and W. Ge, *Effects of moisture on the bonding performance of asphalt-aggregate system*. Construction and Building Materials, 2021. **295**: p. 123667.
32. Valentová, T., J. Altman, and J. Valentin, *Impact of asphalt ageing on the activity of adhesion promoters and the moisture susceptibility*. Transportation Research Procedia, 2016. **14**: p. 768-777.
33. Airey, G., et al., *The influence of aggregate, filler and bitumen on asphalt mixture moisture damage*. Construction and building materials, 2008. **22**(9): p. 2015-2024.
34. Omar, H.A., et al., *Effects of moisture damage on asphalt mixtures*. Journal of Traffic and Transportation Engineering (English Edition), 2020. **7**(5): p. 600-628.
35. Zou, Y., et al., *Effect of different aqueous solutions on physicochemical properties of asphalt binder*. Construction and Building Materials, 2021. **286**: p. 122810.

36. López-Montero, T. and R. Miró, *Differences in cracking resistance of asphalt mixtures due to ageing and moisture damage*. Construction and Building Materials, 2016. **112**: p. 299-306.
37. HUANG, S.-C., T. Turner, and K. Thomas. *The influence of moisture on the aging characteristics of bitumen*. in *PROCEEDINGS OF THE 4TH EURASPHALT AND EUROBITUME CONGRESS HELD MAY 2008, COPENHAGEN, DENMARK*. 2008.
38. Jacob, D.J., *Heterogeneous chemistry and tropospheric ozone*. Atmospheric Environment, 2000. **34**(12-14): p. 2131-2159.
39. Singh, C.V., et al., *Formation of functionally graded hybrid composite materials with Al₂O₃ and RHA reinforcements using friction stir process*. Australian Journal of Mechanical Engineering, 2022. **20**(1): p. 141-154.
40. Hofko, B., et al., *Bitumen ageing—Impact of reactive oxygen species*. Case Studies in Construction Materials, 2020. **13**: p. e00390.
41. Hofer, K., et al., *Influence of selected reactive oxygen species on the long-term aging of bitumen*. Materials and Structures, 2022. **55**(5): p. 133.
42. Sun, X., et al., *New preparation method of bitumen samples for UV aging behavior investigation*. Construction and Building Materials, 2020. **233**: p. 117278.
43. Menapace, I., W. Yiming, and E. Masad, *Effects of environmental factors on the chemical composition of asphalt binders*. Energy & Fuels, 2018. **33**(4): p. 2614-2624.
44. Crucho, J., et al., *Tecnico accelerated ageing (TEAGE)—a new laboratory approach for bituminous mixture ageing simulation*. International Journal of Pavement Engineering, 2020. **21**(6): p. 753-765.
45. Hu, J., et al., *Effect of ultraviolet radiation in different wavebands on bitumen*. Construction and Building Materials, 2018. **159**: p. 479-485.
46. Mirwald, J., et al., *Impact of UV–Vis light on the oxidation of bitumen in correlation to solar spectral irradiance data*. Construction and Building Materials, 2022. **316**: p. 125816.
47. da Silva Lopes, A.M., et al., *Impact of aging protocols on asphalt binder behavior: a laboratory and field study*. Case Studies in Construction Materials, 2023. **19**: p. e02629.
48. Jing, R., et al., *Laboratory and field aging effect on bitumen chemistry and rheology in porous asphalt mixture*. Transportation Research Record, 2019. **2673**(3): p. 365-374.
49. Jing, R., et al., *Differences in the ageing behavior of asphalt pavements with porous and stone mastic asphalt mixtures*. Transportation Research Record, 2021. **2675**(12): p. 1138-1149.
50. Jing, R., et al. *Ageing Behavior of Porous and Dense Asphalt Mixtures in the Field*. in *RILEM International Symposium on Bituminous Materials*. 2020. Springer.
51. Qin, Q., et al., *Field aging effect on chemistry and rheology of asphalt binders and rheological predictions for field aging*. Fuel, 2014. **121**: p. 86-94.
52. Singhvi, P., et al., *Impacts of Field and Laboratory Long-Term Aging on Asphalt Binders*. Transportation Research Record, 2022: p. 03611981221083614.
53. Hofko, B. and M. Hospodka, *Rolling thin film oven test and pressure aging vessel conditioning parameters: Effect on viscoelastic behavior and binder performance grade*. Transportation Research Record, 2016. **2574**(1): p. 111-116.
54. Koyun, A., et al., *Rheological, spectroscopic and microscopic assessment of asphalt binder ageing*. Road Materials and Pavement Design, 2022. **23**(1): p. 80-97.
55. Nagabhushanarao, S.S. and A. Vijayakumar, *Chemical and rheological characteristics of accelerate aged asphalt binders using rolling thin film oven*. Construction and Building Materials, 2021. **272**: p. 121995.
56. EN 12607-1, C., *12607-1: Bitumen and Bituminous Binders—Determination of the Resistance to Hardening under Influence of Heat and Air—Part 1: RTFOT Method*. European Committee for Standardization: Brussels, Belgium, 2014.

57. EN 14769, C., *14769: Bitumen and Bituminous Binders—Accelerated Long-Term Ageing Conditioning by a Pressure Ageing Vessel (PAV)*. European Committee for Standardization: Brussels, Belgium, 2012.
58. EN 12607-2, C., *12607-2: Bitumen and Bituminous Binders—Determination of the Resistance to Hardening under Influence of Heat and Air—Part 2: TFOT Method*. European Committee for Standardization: Brussels, Belgium, 2014, 2014.
59. Hayton, B., et al. (1999) *Long term ageing of bituminous binders. Proc. Eurobitume Workshop 99, Paper No. 126(Luxembourg)*. in *Proc. Eurobitume Workshop 99*. 1999.
60. Verhasselt, A. *The UV/VIS characterisation of bitumens and their generic fractions*. in *International Symposium Chemistry of Bitumens*. 1991.
61. Montepara, A., E. Santagata, and G. Tosi. *Photochemical degradation of pure bitumen by UV radiation*. in *EURASPHALT & EUROBITUME CONGRESS, STRASBOURG, 7-10 MAY 1996. VOLUME 3. PAPER E&E. 5.133*. 1996.
62. Bocci, M. and G. Cerni. *The ultraviolet radiation in short-and long-term aging of bitumen*. in *2nd Euraspalt & Eurobitume Congress*. 2000. Foundation euraspalt.
63. Edler, A., et al. *USE OF AGING TESTS TO DETERMINE THE EFFICACY OF HYDRATED LIME ADDITIONS TO ASPHALT IN RETARDING ITS OXIDATIVE HARDENING (WITH DISCUSSION)*. in *Association of Asphalt Paving Technologists Proc.* 1985.
64. Li, Y., et al., *Negative impacts of environmental factors (UV radiation, water and different solutions) on bitumen and its mechanism*. *Construction and Building Materials*, 2020. **265**: p. 120288.
65. EN, B., *1427: 2007 BS 2000–58: 2007: Bitumen and bituminous binders—Determination of the softening point—Ring and Ball method*. 2007, BSI.
66. En, B., *1426,(2007). Bitumen and Bituminous Binders. Determination of needle Penetration*. British Standard, London, United Kingdom, 2007.
67. EN, C., *13302: 2018; Bitumen and bituminous Binders—Determination of Dynamic Viscosity of Bituminous Binder Using a Rotating Spindle Apparatus*. European Committee for Standardization: Brussels, Belgium, 2018: p. 16.
68. Hu, Y., et al., *State of the art: Multiscale evaluation of bitumen ageing behaviour*. *Fuel*, 2022. **326**: p. 125045.
69. Zhou, X., et al., *Effects of biochar on the chemical changes and phase separation of bio-asphalt under different aging conditions*. *Journal of Cleaner Production*, 2020. **263**: p. 121532.
70. Margaritis, A., et al., *Identification of ageing state clusters of reclaimed asphalt binders using principal component analysis (PCA) and hierarchical cluster analysis (HCA) based on chemorheological parameters*. *Construction and Building Materials*, 2020. **244**: p. 118276.
71. Lu, X. and U. Isacson, *Effect of ageing on bitumen chemistry and rheology*. *Construction and Building materials*, 2002. **16**(1): p. 15-22.
72. Oldham, D., et al., *Investigating change of polydispersity and rheology of crude oil and bitumen due to asphaltene oxidation*. *Energy & Fuels*, 2020. **34**(8): p. 10299-10305.
73. Huang, W., et al., *Chemical and rheological characteristics of rejuvenated bitumen with typical rejuvenators*. *Construction and Building Materials*, 2021. **273**: p. 121525.
74. Bowers, B.F., et al., *Investigation of reclaimed asphalt pavement blending efficiency through GPC and FTIR*. *Construction and building materials*, 2014. **50**: p. 517-523.
75. Cao, X., et al., *Investigation of rheological and chemical properties asphalt binder rejuvenated with waste vegetable oil*. *Construction and building materials*, 2018. **180**: p. 455-463.
76. Soenen, H., X. Lu, and O.-V. Laukkanen, *Oxidation of bitumen: Molecular characterization and influence on rheological properties*. *Rheologica acta*, 2016. **55**: p. 315-326.
77. Ye, W., et al., *Analysis of mechanism and time-temperature equivalent effects of asphalt binder in short-term aging*. *Construction and Building Materials*, 2019. **215**: p. 823-838.

78. Qin, Y., et al., *Study on the microscopic characteristics and rheological properties of thermal-oxidative aged and virgin-old recycled asphalts*. European Polymer Journal, 2021. **154**: p. 110499.
79. Shen, J., S.N. Amirkhanian, and S.-J. Lee, *HP-GPC characterization of rejuvenated aged CRM binders*. Journal of Materials in Civil Engineering, 2007. **19**(6): p. 515-522.
80. Pipintakos, G., et al., *Exploring the oxidative mechanisms of bitumen after laboratory short- and long-term ageing*. Construction and Building Materials, 2021. **289**: p. 123182.
81. Lu, X., et al., *Analysis of asphaltenes and maltenes before and after long-term aging of bitumen*. Fuel, 2021. **304**: p. 121426.
82. Khavandi Khiavi, A., A. Ghanbari, and E. Ahmadi, *Evaluation of poly 2-hydroxyethyl methacrylate—Modified bitumen aging using NMR and FTIR techniques*. Journal of Transportation Engineering, Part B: Pavements, 2021. **147**(1): p. 04020087.
83. Loise, V., et al., *Unravelling the role of a green rejuvenator agent in contrasting the aging effect on bitumen: A dynamics rheology, nuclear magnetic relaxometry and self-diffusion study*. Colloids and Surfaces A: Physicochemical and Engineering Aspects, 2020. **603**: p. 125182.
84. Werkovits, S., et al., *Multi-spectroscopic characterization of bitumen and its polarity-based fractions*. Construction and Building Materials, 2022. **352**: p. 128992.
85. Ma, L., *Interactions of moisture and oxidative ageing mechanisms in paving binders: Towards improving durability of pavements*. 2024.
86. Caputo, P. and C. Oliviero Rossi, *Differential scanning calorimetry as a new method to evaluate the effectiveness of rejuvenating agents in bitumens*. Applied Sciences, 2021. **11**(14): p. 6528.
87. Kaya, D., et al., *Aging effects on the composition and thermal properties of styrene-butadiene-styrene (SBS) modified bitumen*. Construction and Building Materials, 2020. **235**: p. 117450.
88. Mirwald, J., B. Hofko, and H. Grothe, *Utilising fluorescence spectroscopy and optical microscopy to investigate bitumen long-term ageing*. Road Materials and Pavement Design, 2021. **22**(sup1): p. S23-S36.
89. Loeber, L., et al., *New direct observations of asphalts and asphalt binders by scanning electron microscopy and atomic force microscopy*. Journal of microscopy, 1996. **182**(1): p. 32-39.
90. Xu, M., et al., *Generation and evolution mechanisms of pavement asphalt aging based on variations in surface structure and micromechanical characteristics with AFM*. Materials Today Communications, 2017. **12**: p. 106-118.
91. Hong, H., H. Zhang, and S. Zhang, *Effect of multi-dimensional nanomaterials on the aging behavior of asphalt by atomic force microscope*. Construction and Building Materials, 2020. **260**: p. 120389.
92. Yang, Z., *Study on Multi-scale Behavioral characteristics of Asphalt before and after Aging*. South China University of Technology: Guangzhou, China, 2018.
93. Xu, J., et al., *Microstructural, chemical and rheological evaluation on oxidative aging effect of SBS polymer modified asphalt*. Construction and Building Materials, 2021. **267**: p. 121028.
94. Pipintakos, G., et al., *Application of atomic force (AFM), environmental scanning electron (ESEM) and confocal laser scanning microscopy (CLSM) in bitumen: A review of the ageing effect*. Micron, 2021. **147**: p. 103083.
95. Hofko, B., et al., *Repeatability and sensitivity of FTIR ATR spectral analysis methods for bituminous binders*. Materials and Structures, 2017. **50**: p. 1-15.
96. Brereton, R.G., *Chemometrics for pattern recognition*. 2009: John Wiley & Sons.
97. Fringeli, U., *ATR and reflectance IR spectroscopy, applications*. Encyclopedia of spectroscopy and spectrometry, 2000: p. 115-129.

98. Hofko, B., et al. *Alternative approach toward aging of bitumen and asphalt mixes*. in *Proceedings of the Transport Research Board 94th Annual Meeting*. 2015.
99. Eberhardsteiner, L., et al., *Towards a microstructural model of bitumen ageing behaviour*. *International Journal of Pavement Engineering*, 2015. **16**(10): p. 939-949.
100. Pipintakos, G., et al., *Engineering bitumen for future asphalt pavements: A review of chemistry, structure and rheology*. *Materials & Design*, 2024: p. 113157.
101. Lamontagne, J., et al., *Comparison by Fourier transform infrared (FTIR) spectroscopy of different ageing techniques: application to road bitumens*. *Fuel*, 2001. **80**(4): p. 483-488.
102. Mirwald, J., D. Nura, and B. Hofko, *Recommendations for handling bitumen prior to FTIR spectroscopy*. *Materials and Structures*, 2022. **55**(2): p. 26.
103. Khalighi, S., et al., *The Impact of Reactive Oxygen Species Coupled with Moisture on Bitumen Long-Term Aging*. 2024.
104. Xu, S., et al., *The role of rejuvenators in embedded damage healing for asphalt pavement*. *Materials & Design*, 2021. **202**: p. 109564.
105. Zhang, Y., et al., *Chemical and rheological evaluation of aged lignin-modified bitumen*. *Materials*, 2019. **12**(24): p. 4176.
106. Jing, R., et al., *Ageing effect on chemo-mechanics of bitumen*. *Road Materials and Pavement Design*, 2021. **22**(5): p. 1044-1059.
107. Kamal, M.M., K.A. Hadithon, and R.A. Bakar. *Natural rubber modified asphalt*. in *IOP conference series: Earth and Environmental Science*. 2020. IOP Publishing.
108. Rowe, G., G. King, and M. Anderson, *The influence of binder rheology on the cracking of asphalt mixes in airport and highway projects*. *Journal of Testing and Evaluation*, 2014. **42**(5): p. 1-10.
109. Wang, H., et al., *Fatigue performance of long-term aged crumb rubber modified bitumen containing warm-mix additives*. *Construction and Building Materials*, 2020. **239**: p. 117824.
110. Rowe, G. *The development of the Delta Tc and Glover-Rowe parameters for the control of non-load associated cracking*. in *12th Conference on Asphalt Pavements for southern Africa*. 2019.
111. Airey, G., et al. *An overview of Black space evaluation of performance and distress mechanisms in asphalt materials*. in *Proceedings of the RILEM International Symposium on Bituminous Materials: ISBM Lyon 2020 1*. 2022. Springer.
112. ASTM, A., *D6648: Standard Test Method for Determining the Flexural creep STIFFNESS of Asphalt Binder Using the Bending Beam Rheometer (BBR)*. ASTM West Conshohocken, PA, USA, 2016.
113. McDaniel, R.S. and R.M. Anderson, *Recommended use of reclaimed asphalt pavement in the Superpave mix design method: technician's manual*. 2001, National Research Council (US). Transportation Research Board.
114. Test, F.O., *Estimating damage tolerance of asphalt binders using the linear amplitude sweep*. AASHTO TP, 2010: p. 101-14.
115. Hu, Y., et al., *Assessing correlations between two linear amplitude sweep (LAS) standards for evaluating the fatigue properties of aged bitumen*. *International Journal of Pavement Engineering*, 2024. **25**(1): p. 2375419.
116. Hu, Y., et al., *Evaluating the ageing degrees of bitumen by rheological and chemical indices*. *Road Materials and Pavement Design*, 2023. **24**(sup1): p. 19-36.
117. Cuciniello, G., et al., *Microstructure and rheological response of laboratory-aged SBS-modified bitumens*. *Road Materials and Pavement Design*, 2021. **22**(2): p. 372-396.
118. Siroma, R.S., et al., *Clustering aged bitumens through multivariate statistical analyses using phase angle master curve*. *Road Materials and Pavement Design*, 2021. **22**(sup1): p. S51-S68.
119. Ma, L., et al., *Chemical characterisation of bitumen type and ageing state based on FTIR spectroscopy and discriminant analysis integrated with variable selection methods*. *Road Materials and Pavement Design*, 2023: p. 1-15.

120. Ma, L., et al., *Chemical characterisation of bitumen type and ageing state based on FTIR spectroscopy and discriminant analysis integrated with variable selection methods*. Road Materials and Pavement Design, 2023. **24**(sup1): p. 506-520.
121. Weigel, S. and D. Stephan, *The prediction of bitumen properties based on FTIR and multivariate analysis methods*. Fuel, 2017. **208**: p. 655-661.
122. Weigel, S. and D. Stephan, *Bitumen characterization with Fourier transform infrared spectroscopy and multivariate evaluation: prediction of various physical and chemical parameters*. Energy & fuels, 2018. **32**(10): p. 10437-10442.
123. Primerano, K., et al., *Characterization of long-term aged bitumen with FTIR spectroscopy and multivariate analysis methods*. Construction and Building Materials, 2023. **409**: p. 133956.
124. Motevalizadeh, S.M. and K. Mollenhauer, *Exploration of chemical changes in bituminous mastics induced by aging: insights from FTIR spectroscopy, DSR measurements, and machine learning*. International Journal of Pavement Engineering, 2024. **25**(1): p. 2418927.
125. Motevalizadeh, S.M. and K. Mollenhauer, *Use of multivariate clustering analysis to investigate the physicochemical interactions in bitumen mastics using micromechanical modeling and FTIR spectroscopy*. Construction and Building Materials, 2024. **448**: p. 138230.
126. Ma, L., *Interactions of moisture and oxidative ageing mechanisms in paving binders: Towards improving durability of pavements*. 2025.
127. Giri, M.R. and G.B.S. Tamrakar, *Evaluating Multiple Linear Regression Prediction Model for Optimum Bitumen Content in Marshall Mix Design*. 2024.
128. Tušar, M. and M. Novič, *Data exploration on standard asphalt mix analyses*. Journal of Chemometrics: A Journal of the Chemometrics Society, 2009. **23**(6): p. 283-293.
129. Khalighi, S., L. Ma, and A. Varveri, *Accelerated laboratory simulations to mimic field aging of bituminous binders and mixtures: A multivariate analysis on environmental aging effects*. Available at SSRN: <https://ssrn.com/abstract=4995141>, 2024.
130. Weigel, S. and D. Stephan, *Modelling of rheological and ageing properties of bitumen based on its chemical structure*. Materials and structures, 2017. **50**: p. 1-15.
131. Khadijeh, M., et al., *Exploring the roles of numerical simulations and machine learning in multiscale paving materials analysis: Applications, challenges, best practices*. Computer Methods in Applied Mechanics and Engineering, 2025. **433**: p. 117462.
132. Yang, X., et al., *Research and applications of artificial neural network in pavement engineering: a state-of-the-art review*. Journal of Traffic and Transportation Engineering (English Edition), 2021. **8**(6): p. 1000-1021.
133. Useche-Castelblanco, J.S., O.J. Reyes-Ortiz, and A.E. Alvarez, *Application of machine learning models for prediction of rheological properties of wax-modified asphalt binders*. Construction and Building Materials, 2023. **395**: p. 132352.
134. Hamid, A., H. Baaj, and M. El-Hakim, *Predicting the recovery and nonrecoverable compliance behaviour of asphalt binders using artificial neural networks*. Processes, 2022. **10**(12): p. 2633.
135. Seitllari, A., et al., *A soft computing approach to predict and evaluate asphalt mixture aging characteristics using asphaltene as a performance indicator*. Materials and Structures, 2019. **52**(5): p. 100.
136. Alas, M. and S.I.A. Ali. *PREDICTION OF HIGH-TEMPERATURE PERFORMANCE OF GEOPOLYMER MODIFIED ASPHALT BINDER USING ARTIFICIAL NEURAL NETWORKS*. in SETSCI-Conference Proceedings. 2018. SETSCI-Conference Proceedings.
137. Venudharan, V. and K.P. Biligiri, *Heuristic principles to predict the effect of crumb rubber gradation on asphalt binder rutting performance*. Journal of Materials in Civil Engineering, 2017. **29**(8): p. 04017050.
138. Botella, R., et al., *Machine learning techniques to estimate the degree of binder activity of reclaimed asphalt pavement*. Materials and Structures, 2022. **55**(4): p. 112.

139. Zhong, K., et al., *Artificial Neural Network (ANN) modeling for predicting performance of SBS modified asphalt*. *Materials*, 2022. **15**(23): p. 8695.
140. Jing, R., et al. *Ageing Behavior of Porous and Dense Asphalt Mixtures in the Field*. in *Proceedings of the RILEM International Symposium on Bituminous Materials: ISBM Lyon 2020 1*. 2022. Springer.
141. Jing, R., et al., *Rheological, fatigue and relaxation properties of aged bitumen*. *International journal of pavement engineering*, 2020. **21**(8): p. 1024-1033.
142. Singhvi, P., et al., *Impacts of field and laboratory long-term aging on asphalt binders*. *Transportation Research Record*, 2022. **2676**(8): p. 336-353.
143. Qian, Y., et al., *Simulation of the field aging of asphalt binders in different reclaimed asphalt pavement (RAP) materials in Hong Kong through laboratory tests*. *Construction and Building Materials*, 2020. **265**: p. 120651.
144. Lu, X., Y. Talon, and P. Redelius. *406-001 Aging of bituminous binders—Laboratory tests and field data*. in *4th Eurasphalt Eurobitume Congress*. 2008.
145. Besamusca, J., et al. *Simulating ageing of EN 12591 70/100 bitumen at laboratory conditioning compared to porous asphalt*. in *5th Eurasphalt and Eurobitume congress, Istanbul*. 2012.
146. Erskine, J., S. Hesp, and F. Kaveh. *Another look at accelerated aging of asphalt cements in the pressure aging vessel*. in *Proceedings, Fifth Eurasphalt and Eurobitumen Congress, Istanbul, Turkey*. 2012.

3

ATR-FTIR pre-treatment of paving binders

This chapter presents a comprehensive evaluation of data pre-processing methods for ATR-FTIR spectral analysis of paving binders. This step is essential for a thorough evaluation of the ATR-FTIR results in the subsequent chapters. It addresses challenges such as non-informative spectral regions and inconsistent baselines by assessing various pre-processing strategies, including baseline correction and normalization techniques, through partial least squares-discriminant analysis (PLSDA). Key findings highlight the impact of these methods on aging classification accuracy and provide practical recommendations for optimizing spectral analysis. While the focus is on ATR-FTIR, the approaches discussed are broadly applicable to other spectroscopic techniques, enhancing the reliability of spectral data interpretation beyond the study of bituminous binders.

This chapter is structured as follows: Section 3.1 introduces the importance of ATR-FTIR and pre-treatment for paving binder studies. Section 3.2 outlines the objectives and research structure. Section 3.3 details materials and data collection, including sample preparation, aging conditions, and FTIR measurements. Section 3.4 presents data pre-processing (DP) methods, covering baseline correction, normalization, and their combinations. Section 3.5 describes the transformation of spectra into peak areas and indices. Section 3.6 evaluates DP methods using PLS-DA. Section 3.7 discusses the methodological approach, followed by results and discussion in Section 3.8.

Part of this chapter contains published material from " Khalighi, S., et al., Evaluating the impact of data pre-processing methods on classification of ATR-FTIR spectra of bituminous binders. Fuel, 2024. 376: p. 132701."

3.1 Introduction on importance of FTIR and its pre-treatment for paving binder studies

Bituminous binders, a crucial constituent in asphalt concrete pavements, are complex organic materials derived from crude oil residues. Mechanically, these binders exhibit viscoelastic behaviour, with their response to applied stress or strain being highly dependent on temperature and time and rate of loading [1, 2]. Chemically, the bituminous binder consists of carbon (C), hydrogen (H), oxygen (O), nitrogen (N), sulfur (S), and other trace elements. The elements present in bituminous binder form a chemical composition rich in functional groups, with a notable prevalence of aromatic and aliphatic hydrocarbons. Aromatic structures, characterized by conjugated double bonds, dominate, giving stability and adhesive properties to bituminous binder. Sulfur-containing functional groups, such as thiophenes, are known to influence the rheological properties of bituminous binders by contributing to their stiffness, particularly at elevated temperatures. Although typically present in low concentrations, these sulfur functionalities can have a measurable stiffening effect, especially when comparing binders with otherwise similar compositions. Oxygen-containing groups, including sulfoxides and carbonyls, are also present in bitumen, influencing reactivity and contributing to the overall complexity of the composition[3]. Understanding these functional groups is crucial, as they directly affect the binder's mechanical performance, aging behaviour, and resistance to environmental factors. Their influence on viscoelastic properties determines the material's suitability for specific applications, such as pavement durability and waterproofing efficiency. A detailed characterization of these groups allows for improved formulation strategies, ensuring optimal performance and longevity in practical engineering applications.

To understand the chemical complexity of bituminous binder one widely employed method is attenuated total reflectance Fourier-transform infrared spectroscopy (ATR-FTIR) [2]. ATR-FTIR proves valuable in analysing binder composition changes due to its cost-effectiveness, user-friendly nature, and non-destructive traits [4, 5].

Several factors can alter the chemical composition of bituminous binders, both during production and throughout their service life. These include exposure to environmental conditions such as oxidation, as well as the incorporation of additional materials like polymers or regenerators (Figure 3.1). The functional groups in bitumen may undergo transformation due to oxidative aging, while new functional groups may also appear as a result of the addition of such modifiers. Although these additives do not always chemically react with the native functional groups in bitumen, they can still influence the overall chemical composition through physical interactions or changes in phase behaviour [6, 7].

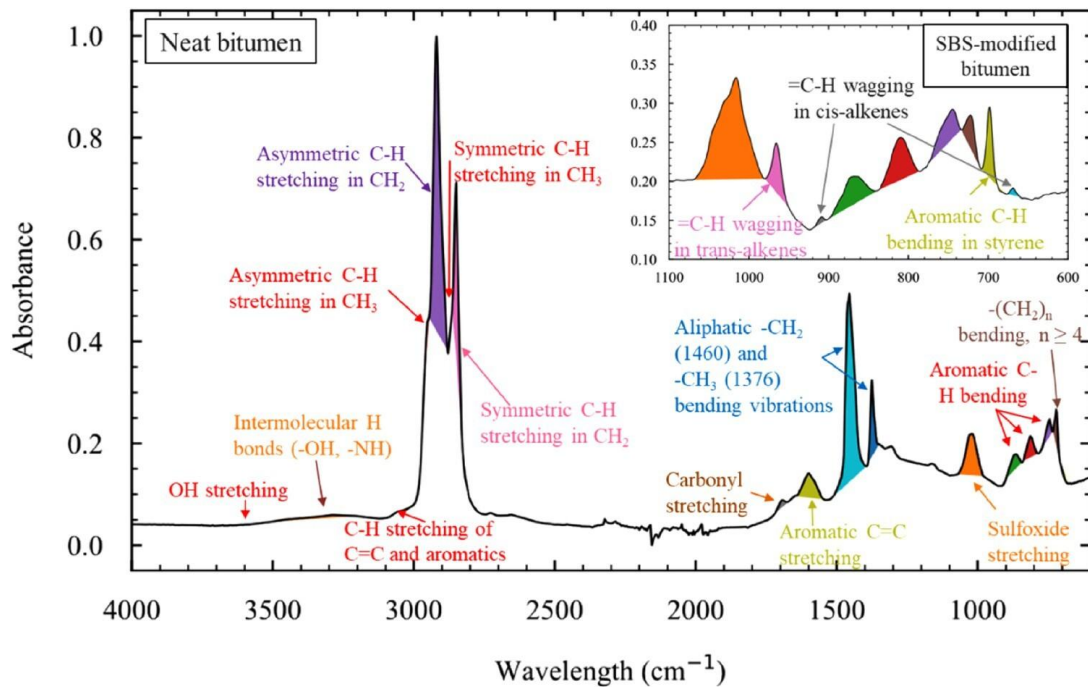


Figure 3.1 FTIR spectra of unmodified bitumen (4000–600 cm^{-1}) and SBS-modified bitumen (1100–600 cm^{-1}) [6].

These changes can occur during short-term conditions, such as storage and hot-mix production, or over the long term, particularly under field conditions. For example, oxidative aging promotes the formation of oxygen-containing functional groups, leading to an increase in binder polarity. These chemical modifications contribute to increased stiffness and brittleness, thereby affecting the viscoelastic properties of the binder and reducing its resistance to cracking and deformation. ATR-FTIR spectroscopy can capture these chemical transformations, offering insight into binder aging and performance over time. Understanding these changes is crucial for optimizing binder formulations and improving the durability and sustainability of asphalt pavements [8].

The ATR-FTIR spectrum is generated through the interaction of infrared (IR) light with the chemical composition of samples, specifically with those chemicals located near the sample's surface. For a more in-depth understanding of the theory behind IR spectroscopy, refer to [9, 10]. While ATR-FTIR offers several advantages and can quickly produce extensive data, there are still challenges, especially when applied to bituminous binders.

One important challenge in spectral analysis is the presence of both informative and uninformative regions within the spectra, which can reduce the effectiveness of subsequent post-processing steps [11]. In addition, systematic variations often arise due to inconsistent baselines and instrumental noise (Figure 3.2) [5, 11]. These variations may be introduced by factors such as sample preparation conditions, particle size distribution, chemical interferences, and the specifics of data acquisition protocols, all of which can alter the intensity of both relevant and irrelevant spectral features [12].

Sources of unwanted variation can originate from the instrument itself, for example, through detector drift, fluctuations in light source intensity, or optical misalignment, as well as from the samples. In particular, heterogeneity in particle size can lead to light scattering effects or uneven absorption, causing intensity distortions across the spectrum. Furthermore, differences in the physical amount of sample used, referred to here as *sample quantity*, not to be confused with *sample size* as in the number of replicates, can influence path length and optical density. This is especially critical in the case of solid samples, where variation in thickness or packing density can significantly impact absorbance values, leading to non-linear or non-reproducible spectral responses [12, 13].

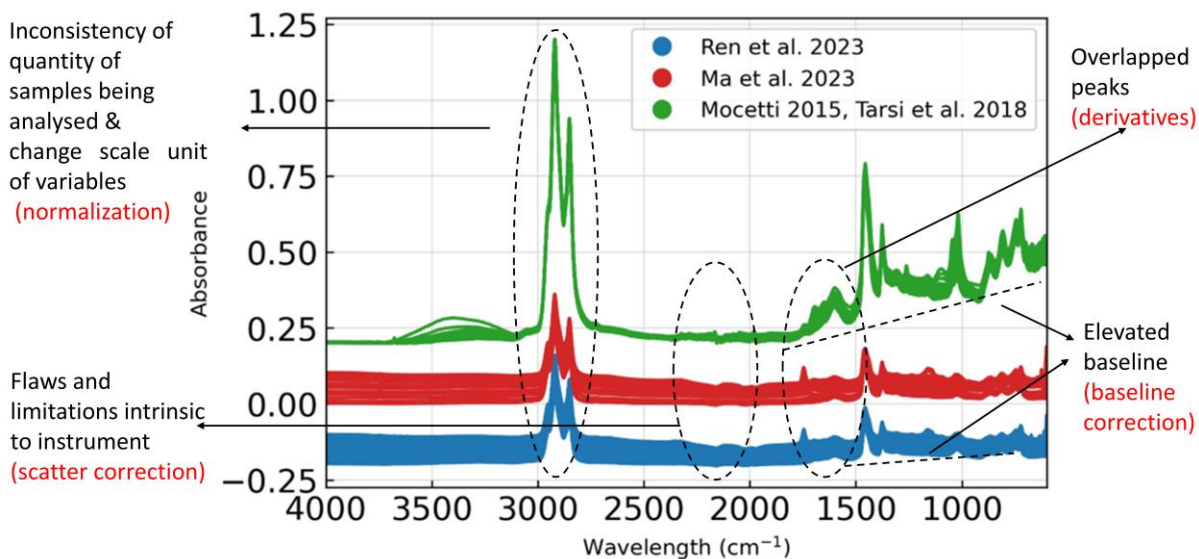


Figure 3.2 Typical characteristics of ATR-FTIR spectrum as exemplified with IR spectra collected from binders [14]. Each type of interference or noise could be resolved by different categories of data pre-processing methods.

Furthermore, another specific challenge is the complexity in analysing the spectra results of paving binders. Generally, values like the area under spectral curves or indices are used to characterize samples and compare various samples with different degrees of modifications and aging [2, 15]. Unfortunately, the lack of a standardized analysis method makes it difficult to compare findings across different studies.

To address this issue, various data pre-processing (DP) methods have been developed to enhance spectral quality and improve the robustness of downstream analyses [16]. These techniques aim to reduce systematic noise, correct baseline shifts, and account for sample-related variability that can obscure meaningful spectral information. Examples of such methods include normalization approaches, which standardize spectral intensity across samples, and baseline correction techniques, which remove background distortions and offset effects.

In the present investigation, the focus is placed exclusively on DP methods. Approaches involving variable or wavenumber selection, which are sometimes employed in parallel, are beyond the scope of this work and are discussed in detail elsewhere [16]. The DP techniques considered here are broadly divided into two categories: normalization data pre-processing (NDP) and baseline-correction data pre-processing (BDP).

NDP techniques are designed to mitigate the influence of sample-related and instrumental variability in spectral data. These methods address issues such as variations in sample quantity, instrumental limitations like low signal intensity or scattering, and differences in spectral scaling due to changes in mean or standard deviation. One basic NDP approach involves transforming the absorbance values of each spectrum relative to a pre-defined constant, for example, normalizing to the most intense absorption band or to the total absorbance. These strategies aim to standardize the magnitude of spectra across samples, reducing variability unrelated to chemical differences.

Additional NDP methods include scatter correction algorithms such as standard normal variate (SNV), which removes multiplicative and additive effects by centering and scaling each spectrum independently, and mean centering (MC) or autoscaling (AS), which adjust the data to have zero

mean or unit variance, respectively. These approaches improve comparability between spectra and are especially useful when multivariate analysis is applied [10, 11].

In addition to normalization, baseline-correction data pre-processing (BDP) techniques are essential for minimizing distortions caused by elevated baselines. Such distortions often arise in FTIR spectra due to reduced reflectance at lower wavenumbers, leading to background trends that obscure meaningful absorbance features. BDP methods remove or correct for these background effects, thereby enhancing the reliability of spectral interpretation [10, 11].

Whether normalization or baseline correction is applied, the choice of pre-processing method must be guided by the specific characteristics of the dataset and the objectives of the analysis. For readers unfamiliar with these techniques, further methodological details can be found in references [10, 11].

When using ATR-FTIR to evaluate bituminous binders, analyses typically fall into two categories: those based on the full spectral range and those focusing on specific peak areas or indices (Figure 3.3). In both approaches, the application and reporting of DP methods are often inconsistent or insufficiently described in the literature. This lack of transparency complicates the comparison of results across studies and raises concerns about the reproducibility and interpretability of spectral analyses. Given that DP methods can significantly influence the spectral output and the conclusions drawn, clearly reporting and justifying their use is essential for methodological rigor.

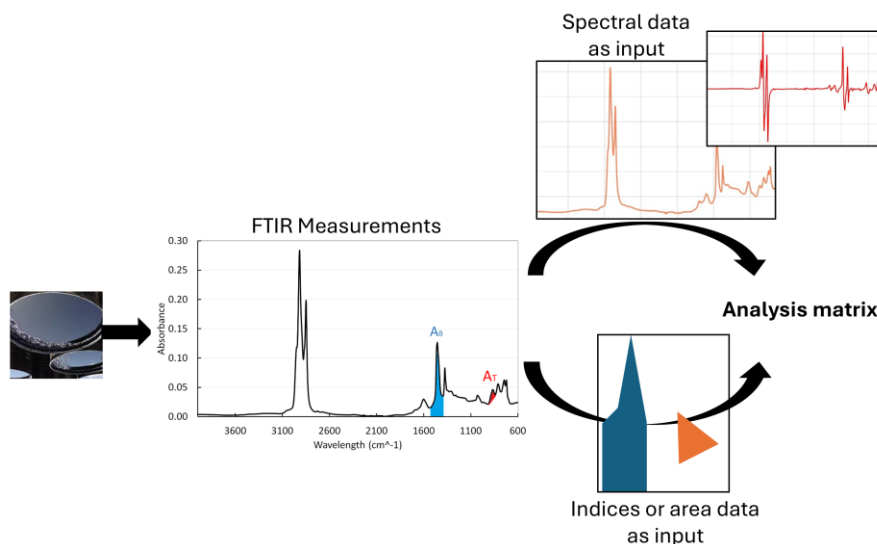


Figure 3.3 Schematic representation of ATR-FTIR analysis of bituminous binders, highlighting two primary approaches: using the entire spectral data or focusing on peak areas and indices.

Several recent studies in pavement engineering demonstrate the variety of DP techniques applied to ATR-FTIR spectral data, particularly in aging-related analyses. These examples are relevant to the present investigation as they reflect the lack of standardization in DP application and illustrate the performance implications of different choices. The studies discussed below encompass both full-spectrum analyses and those based on peak areas or indices, thereby covering the two primary approaches to FTIR interpretation.

In full-spectrum approaches, Ma et al. [17] employed standard normal variate (SNV) and Savitzky–Golay (SG) smoothing to reduce scattering and noise before applying PCA- linear discriminant analysis (LDA), demonstrating improved differentiation of binders at various aging stages. Primerano et al. [18] used standardized scaling with PCA, random forest, and PLSDA to distinguish between light aging, Pressure Aging Vessel (PAV), and Viennese Binder Aging (VBA) aged samples. Garmarudi et al.

[19] applied mean centering (MC) before PCA, hierarchical cluster analysis (HCA), and soft independent modelling of class analogies (SIMCA), showing that normalization can influence classification accuracy in petroleum-based materials. Similarly, Weigel and Stephan [20] combined standard normal variate (SNV) and first derivative processing prior to LDA and PLSR, achieving robust classification of bituminous binders from different refineries and aging states.

In contrast in literature focusing on peak areas and indices instead of entire spectra, the DP methods utilized are limited. Hofko et al. [2] evaluated eight combinations involving original vs. normalized spectra, absolute vs. tangential baselines, and band maximum vs. integrated indices. Their results supported the use of normalized spectra, absolute baselines, and integration-based indices, although no baseline correction methods were explicitly tested. Weigel and Stephan [21], drawing on Kessler's earlier work [22], used standard normal variate (SNV) prior to peak area calculations for subsequent PLS modeling of rheological parameters. Wieser et al. [23] attempted to optimize DP methods to improve the analysis of bituminous binder aging solely based on the carboxyl peak. They considered Vector-1, Vector-2, and SNV as normalization methods, and baseline corrections were done based on $\Delta y = a + b/x$, $\Delta y = a + b \exp[-xc]$ where y is the absorbance values and x represents the wavenumbers, and the one-point correction. Peak area Consideration Methods involved baseline integration, tangential integration, and peak-fit approach using Lorentzian-profile fitting. Based on their results, exponential baseline correction, vector 2 normalization, and peak-fit integration were identified as the best methods for aging studies.

Taken together, existing studies highlight both the diversity of DP methods employed in ATR-FTIR-based aging analyses and the absence of a standardized protocol. Many of these studies do not explicitly justify their choice of DP techniques, often adopting previously used methods without evaluating their effectiveness relative to raw spectral data or alternative approaches. This uncritical adoption limits the opportunity to explore DP methods better suited to specific datasets or analytical objectives. Lee et al. [11] underscored this issue in their review of forensic ATR-FTIR applications, noting that both experienced and inexperienced researchers tend to rely on a narrow range of familiar techniques. Their work, which applied PLSDA to pen ink classification, demonstrated how DP selection can markedly influence spectral interpretation. These observations underscore the need for a systematic assessment of DP methods in ATR-FTIR applications, particularly in bituminous binder studies, where such methodological choices can significantly affect classification outcomes [2, 23]. Accordingly, the present chapter compares multiple DP techniques using PLSDA, with the aim of identifying those that yield the most reliable differentiation of binder aging states.

To address these concerns, different approaches have been proposed to systematically assess the effectiveness of DP methods. Three main strategies are recognized: spectrum-comparison, clustering of samples projected on a PCA score plot, and evaluating modelling accuracy/error [24]. The spectrum-comparison method is qualitative and labour-intensive, relying on subjective visual assessment. Clustering on a PCA score plot provides a semi-quantitative means of evaluating DP methods but still involves subjective interpretation. In contrast, assessing modelling accuracy/error is an objective and goal-oriented approach, though it requires significant computational resources.

Assessing the impact of different DP methods on modelling accuracy/error requires robust analytical techniques capable of handling high-dimensional spectral data effectively. One such method is Partial Least Squares Discriminant Analysis (PLSDA) [11, 25], which integrates dimensionality reduction and classification into a single algorithm. This makes it particularly useful for spectral datasets, where variables (wavenumbers) are often collinear and traditional discriminant methods like Linear Discriminant Analysis (LDA) may not perform well [25, 26]. Unlike LDA, PLSDA does not assume a specific data distribution, allowing it to be more adaptable to complex spectral variations. While Principal Component Analysis (PCA) can address some of the limitations of LDA, studies have shown

that PLSDA often provides superior classification performance compared to PCA-LDA [27, 28]. Given that the effectiveness of DP methods is best evaluated using quantitative approaches such as modelling accuracy/error assessment, PLSDA is particularly suitable for this purpose. Therefore, in this research, PLSDA will be employed to systematically examine how different DP methods influence spectral classification outcomes.

Therefore, in this research, PLSDA will be employed to systematically examine how different DP methods influence spectral classification outcomes, with the aim of identifying the most suitable pre-processing strategy for aging studies of paving binders.

3.2 Objectives and research structure

In this chapter, the motivation to evaluate the effects of different DP methods on ATR-FTIR spectra analysis in bituminous binder research stems from the lack of comprehensive references guiding DP method selection. The aim is to incorporate all pre-treatment methods from the literature into a unified framework and compare various binder aging conditions, crucial for future laboratory aging protocols, with a detailed explanation of the different aging conditions provided in the Materials and Methods section.

To ensure both dataset diversity and sufficient representation, samples were selected from various bituminous binder types, sources, and aging conditions. These included unmodified binders from different sources, polymer-modified binders, and regenerated binders, both before and after aging. Additionally, the dataset size was designed to be large enough to allow meaningful statistical analysis while maintaining balance across different binder categories. This research utilizes the partial least squares-discriminant analysis (PLSDA) algorithm to evaluate the impact of pre-treatment methods on the classification of FTIR spectral data. The classification objectives include grouping samples based on binder source, modification type, or aging state. While binder modification and source significantly influence FTIR spectra, aging conditions result in less pronounced differences. Consequently, the focus is on aging studies to determine whether optimized DP methods can identify minor differences effectively.

Specifically, aging under PAV and humid conditions was examined, ensuring the findings are applicable to various aging protocols. As a result, our findings become more reliable and are capable of distinguishing between fresh samples and those aged under different conditions.

This chapter aims to address the following research sub-questions (RSQ):

- 1- Can pre-treatment methods, such as normalization, baseline correction, or a combination of both, enhance classification accuracy compared to using raw input data? (RQ4)¹
- 2- Which pre-treatment method is most effective for the aging classification of bituminous binders? (RQ4)
- 3- What is the most suitable pre-treatment method for calculating areas or aging indices in aging studies? (RQ4)
- 4- What region of FTIR spectra are more important for aging classification? Does the importance of regions change with pre-treatment of spectra? (RQ4)
- 5- When considering either the entire spectra or their first derivatives instead of using peak areas or indices, which approach yields better performance for aging-related classification in chemometric analysis? (RQ3, RQ4)

By addressing these questions, this chapter aims to provide guidelines for selecting DP methods, thereby enhancing the accuracy and reliability of ATR-FTIR spectral analysis for bituminous binders.

¹ The references in parentheses show the link to the main Research Questions (RQ) of this thesis, as outlined in Chapter 1.

3.3 Materials and Data collection (sample preparation, aging conditions, and FTIR measurement)

A well-structured and diverse dataset is essential for ensuring the reliability and applicability of spectral analysis methods, particularly in ATR-FTIR studies. The accuracy of classification models and chemometric analyses heavily depends on the quality and representativeness of the collected data. In FTIR-based investigations, data can be acquired through various approaches, including direct measurements of raw materials and controlled laboratory experiments with predefined conditions. Additionally, sample preparation techniques, aging protocols, and instrument settings play a crucial role in capturing relevant spectral features. This section outlines the procedures followed for sample preparation, aging conditions, and FTIR measurements to establish a comprehensive dataset for analysis.

The first set of data in this research was extracted from a study conducted by Ren et al. [29] (Table 3.1). For the investigation of regenerated binders, a 70/100 virgin bituminous binder was utilized. The study encompassed four types of regenerators: bio-oil (BO), engine-oil (EO), naphthenic-oil (NO), and aromatic-oil (AO). The regenerated binders comprised 20 hours-PAV aged samples mixed with 10 % of regenerators, 40 hours-PAV aged samples mixed with 5 %, 10 %, 15 % of regenerators, and 80 hours-PAV aged samples mixed with 10 % of regenerators. These samples were collectively treated as a fresh group. All these regenerated samples were then conditioned by 1PAV aging, which were considered as the aged group. All PAV aging procedures were conducted at 100 °C. An ATR-FTIR device (Waltham, MA, USA) was used to detect the distribution of functional groups in the samples, within the wavenumber range of 600-4000 cm^{-1} , with a scanning resolution of 4 cm^{-1} and 12 scans conducted for each sample. To ensure data reliability, a minimum of three parallel tests were conducted for each specimen. In total, 120 samples were measured at room temperature for this dataset.

The second set of data was obtained from the study by Ma et al. [17] (Table 3.1). They aimed to explore the chemical properties of bituminous binder derived from diverse crude oil sources, exhibiting various penetration grades, polymer modifiers (Styrene-butadiene-styrene (SBS)), and aging states. A total of 16 binder samples, representing eight different types, were prepared at two aging states—fresh and PAV aged. These samples included bituminous binder sourced from Q, featuring penetration grades 40/60, 70/100, and SBS modifier (using 70/100 as the base bituminous binder). Additionally, bituminous binder from source T included penetration grades 70/100, 100/150, and 160/220. Another variation was bituminous binder from source V, with penetration grade 70/100 and SBS modifier (using 70/100 as the base bituminous binder). The long-term aged samples were produced through a combination of short-term aging simulated by the thin-film oven test (TFOT) at 163 °C for five hours, followed by extended aging in the 1PAV. The ATR-mode FTIR spectroscopy was utilized, with a wavelength range of 4000–600 cm^{-1} , a resolution of 1 cm^{-1} and 32 scans. Three independent measurements were conducted for each sample, resulting in a total of 48 spectra (16 samples \times 3 repetitions) measured at room temperature for this group.

The final section of our input data set was sourced from the works by Tarsi [30] and Mocetti [31] (Table 3.1). Three types of bituminous binder were employed, including two unmodified binders and one polymer-modified bituminous binder. The two pure binders have penetration grades of 40/60 and 70/100, respectively, both derived from source Q. The polymer-modified bituminous binder was achieved through the addition of SBS polymers into a Q-sourced bituminous binder. The binder films had a diameter of 27.50 mm, and a thickness of 2 mm. Five aging methods were applied to these binders, namely aging at room temperature, oven aging, aging through the Pressure Aging Vessel (PAV), a protocol combining Rolling Thin Film Oven Test (RTFOT) and PAV aging, and moisture aging. Room temperature aging lasting for 5, 15, and 25 days were performed, with an average room temperature of 24.6 °C. Oven aging was conducted at 135 °C for three durations, namely, 60 hours, 10 days, and 15 days. The PAV test adhered to standard conditions, aging samples at a temperature

of 100 °C and a pressure of 2.1 MPa for 20 h, following the NEN-EN 14769:2005 European Standard. PAV testing was also conducted at the same temperature and pressure but for twice the standard aging time (40 h). The combined short-term and long-term aging procedures involved initial RTFOT aging according to the NEN-EN 12607-1:2014 European Standard [32], followed by PAV aging under the standard condition [33]. For moisture aging, all bituminous binder types underwent two different conditions, i.e., liquid water and water vapor with a RH = 88%, at temperatures of 20 and 40 °C for 5 and 15 days. The FTIR spectrum was obtained in the spectral range between 4000 and 600 cm⁻¹, with a scanning resolution of 4 cm⁻¹. Five scans were obtained and averaged for each measurement, and four repetitions were conducted for each sample. In total, 216 FTIR spectra were obtained.

These three groups were combined and examined collectively to determine the optimal pre-treatment method. The spectra from all groups were gathered, resulting in a comprehensive data frame comprising 384 spectra.

Table 3.1 Summary of datasets used in this study, including binder types and modifiers, aging conditions, and FTIR test parameters. Datasets are from three different references: dataset 1 is produced by Ren et. al. [30], dataset 2 is produced by Ma et al. [17], and dataset 3 is produced by Tarsi [31] and Mocetti [32].

Dataset number	Bituminous binder Type	Modifier	Aging Conditions (PAV)	FTIR Parameters	Test
1 (120 spectra)	T binder, 70/100	Bio-oil (BO), 10 %	20 hours PAV aged	ATR-FTIR: 600-4000 cm ⁻¹ , 12 scans/sample	
		Engine-oil (EO), 5,10, 15 %	40 hours PAV aged		
		Naphthenic-oil (NO), 10 %	40 hours PAV aged		
		Aromatic-oil (AO), 10 %	80 hours PAV aged		
2 (48 spectra)	Q binder, 40/60, 70/100	None	Fresh, TFOT + PAV Aged	ATR-FTIR: 4000–600 cm ⁻¹ , 32 scans/sample	
	Q binder, 70/100	SBS	Fresh, TFOT + PAV Aged		
	T binder, 70/100, 100/150, 160/220	None	Fresh, TFOT + PAV Aged		
	V binder, 70/100	SBS	Fresh, TFOT + PAV Aged		
3 (216 spectra)	Q binder, 40/60	None	Room Temperature Aging: 5, 15, 25 days at 24.6 °C	ATR-FTIR: 4000–600 cm ⁻¹ , 4 cm ⁻¹ resolution, 5 scans	
	Q binder, 70/100	None	Oven aging: 60 hours, 10 and 15 days at 135 °C		
	Q binder, 70/100	SBS, None	Standard RTFOT + PAV: 100 °C, 2.1 MPa, 20 and 40 h		
	Q binder, 70/100	None	Moisture Aging - Liquid Water: 20°C and 40 °C, 5 and 15		

			days	
	Q binder, 70/100	None	Moisture Aging - Water Vapor (RH=88 %): 20 °C and 40 °C, 5 and 15 days	

3.4 Data pre-processing (DP) methods

3.4.1 Baseline correction methods

The BDPs are crucial for minimizing irrelevant variations linked to elevated baselines which are created due to reduction of reflection with decrease of the wavenumbers [10, 11]. In this research, nine different data pre-processing techniques for baseline correction (BDP) were chosen from past bituminous binder studies [34] and the pybaselines python library [35]. The selection from pybaselines was guided by the compatibility of these methods with the spectral characteristics of bituminous binders. Compatibility, in this context, refers to the ability of a baseline correction method to effectively handle the inherent nonlinear baseline distortions present in ATR-FTIR spectra of binders. These distortions arise from scattering effects, absorbance flattening at high wavenumbers, and gradual baseline shifts. The pybaselines library provides algorithms specifically designed to address these spectral distortions, ensuring that the corrected spectra retain chemically relevant information while minimizing artificial alterations. The descriptions and relevant equations for these BDP methods are provided in Table 3.2.

Whittaker-smoothing-based (WSB) algorithms, also referred to as weighted least squares, Penalized Least Squares, or Asymmetric Least Squares, aim to fit a smooth baseline to measured spectral data while penalizing its roughness. The general function minimized to determine the baseline is presented in Table 3.2. Variants such as Asymmetric Least Squares (asls), Adaptive Iteratively Reweighted Penalized Least Squares (airpls), and Adaptive Smoothness Penalized Least Squares (aspls) are based on the same fundamental principle of iteratively refining a linear system to isolate the baseline. The iterative procedure involves solving for the baseline, updating the weights, and repeating the process until convergence criteria are met. The distinction among these WSB algorithms primarily lies in the strategy used to update the weights. In most cases, the weights are chosen based on the residuals between the observed spectrum and the current baseline estimate. For example, in asls, smaller weights are assigned to points above the baseline to emphasize fitting the lower envelope of the spectrum[36]. These weights are typically computed algorithmically, based on predefined criteria, rather than being manually set by the user. However, the user may influence the outcome by adjusting hyperparameters, such as the smoothing parameter or asymmetry coefficient, which indirectly affect the weighting behaviour. To ensure consistency and avoid bias introduced by manual tuning, default parameter values were used for all WSB algorithms in the present chapter.

Additionally, three approaches based on polynomial fitting were employed for baseline correction: regular polynomial (poly), modified polynomial (modpoly), and improved modified polynomial (imodpoly). These methods aim to mathematically approximate and subtract baseline distortions from spectra. Firstly, regular polynomial fitting applies least-squares regression with a custom weighting scheme: a weight array is introduced with values set to 0 in regions assumed to contain peaks and 1 elsewhere, effectively isolating the baseline regions for polynomial fitting. Secondly, the modified polynomial method iteratively applies thresholding to refine the baseline: each iteration fits a polynomial to the spectrum and updates the input by replacing values above the current fit with the fit itself, gradually excluding peaks. Thirdly, the improved modified polynomial extends modpoly

by incorporating the standard deviation of the residuals (difference between spectrum and estimated baseline) into the thresholding process, making it more robust to noise [36].

Although these methods are not physically motivated in the same way as models derived from radiative transfer or scattering theory, they are commonly used due to their computational efficiency and adaptability to varying spectral profiles. Their objectivity is ensured through reproducible, algorithmically defined fitting procedures, with no user intervention required once parameters such as polynomial order and iteration limits are set. In this study, default parameters were applied for all polynomial-based methods to maintain consistency and prevent subjective influence from manual tuning. While these algorithms are not mechanistically grounded, their empirical performance in spectral baseline correction has been well-documented across different domains, including ATR-FTIR analysis [36].

Another approach for baseline correction involves using splines, which are flexible, piecewise polynomial functions. Among these, basis splines (B-splines) are particularly useful due to their ability to model complex baseline variations without overfitting. Their implementation in the pybaselines library is not only widespread but also well-suited for FTIR spectral correction because they provide a balance between flexibility and smoothness. Unlike simple polynomial fitting, which can introduce artificial curvature, B-splines allow local adjustments without distorting the overall spectral shape. To further control the smoothness of the fitting function, a penalty is applied to the finite-difference between spline coefficients, resulting in penalized B-splines (P-splines). This penalty helps prevent excessive oscillations while preserving meaningful spectral features, making P-splines particularly effective for handling the gradual baseline shifts commonly observed in ATR-FTIR spectra of bituminous binders. These meaningful features are recognized and validated through domain knowledge, such as the expected absorbance positions of known functional groups (e.g., carbonyl, sulfoxide, or aromatic C=C bonds) or characteristic regions associated with specific chemical components, as established in prior studies or chemical spectral libraries.

P-splines share similarities with Whittaker smoothing; setting the number of basic functions, (M , Table 3.2), equal to the number of data points, (N , Table 3.2), and the spline degree to 0 makes the identity matrix, rendering the equation identical to that used for Whittaker smoothing. Consequently, Penalized Spline Asymmetric Least Squares (pspline_asls) and Penalized Spline Asymmetric Least Squares (pspline_airpls) are penalized versions of Asymmetric Least Squares (asls) and Adaptive Iteratively Reweighted Penalized Least Squares (airpls) [36]. The final method is the eight-point baseline correction (8points)[34]. Eight-Point baseline correction method was implemented based on recommendations from the RILEM consortium [34]. It involves defining eight reference valleys at wavenumber positions of 600, 680, 930, 1800, 2400, 3100, 3600, and 4000 cm^{-1} . A linear interpolation was performed between these fixed points to approximate the spectral baseline, which was subsequently subtracted from the raw absorbance spectrum. This approach is computationally simple and reproducible, making it suitable for standardization across laboratories.

Table 3.2 Mathematical expressions representing the baseline-correction methods (BDPs) along with their corresponding abbreviations.

Name	Abbreviation	Formula	Parameters
Asymmetric least squares	Asls	Minimized function: $\sum_i^N w_i (y_i - z_i)^2 + \lambda \sum_i^{N-d} (\Delta^d z_i)^2$ Linear system:	Measured data (y_i), estimated baseline (z_i), penalty scale factor

		$(W + \lambda D_d^T D_d)z = W_y$ <p>Weighting:</p> $W_i = \begin{cases} p & y_i > z_i \\ 1-p & y_i \leq z_i \end{cases}$	(λ) , weighting (wi), finite-difference operator of order d (Δ^d), diagonal matrix of the weights (W), and D_d matrix version of Δ^d .
Adaptive Iteratively Reweighted Penalized Least Squares	airpls	<p>Minimized function:</p> $\sum_i^N w_i (y_i - z_i)^2 + \lambda \sum_i^{N-d} (\Delta^d z_i)^2$ <p>Linear system:</p> $(W + \lambda D_d^T D_d)z = W_y$ <p>Weighting:</p> $W_i = \begin{cases} 0 & y_i \geq z_i \\ \exp\left(\frac{t(y_i - z_i)}{ r^- }\right) & y_i < z_i \end{cases}$ <p>t is the iteration number and r^- is the L1 norm of the negative values in the residual vector r, ie. $\sum_{y_i - z_i < 0} y_i - z_i$.</p>	
Adaptive Smoothness Penalized Least Squares	aspls	<p>Minimized function:</p> $\sum_i^N w_i (y_i - z_i)^2 + \lambda \sum_i^{N-d} \alpha_i (\Delta^d z_i)^2$ $\alpha_i = \frac{abs(r_i)}{\max(abs(r))}$ <p>Linear system:</p> $(W + \lambda \alpha D_d^T D_d)z = W_y$ <p>Weighting:</p> $W_i = \frac{1}{1 + \exp\left(\frac{0.5(r_i - \sigma^-)}{\sigma^-}\right)}$ <p>where $r_i = y_i - z_i$ and σ^- is the standard deviation of the negative values in the residual vector r.</p>	
Regular Polynomial	poly	$p(x) = \beta_0 x^0 + \beta_1 x^1 + \dots + \beta_m x^m = \sum_{j=0}^m \beta_j x^j$ <p>Minimized function:</p> $\sum_i^N w_i^2 (y_i - p(x_i))^2$	y_i and x_i represent the measured data, $p(x_i)$ denotes the polynomial estimate at x_i , w_i is the weighting,

		It uses selective masking.	and β is the array of coefficients for the polynomial.
Modified Polynomial	modpoly	$p(x) = \beta_0 x^0 + \beta_1 x^1 + \dots + \beta_m x^m = \sum_{j=0}^m \beta_j x^j$ <p>Minimized function:</p> $\sum_i^N w_i^2 (y_i - p(x_i))^2$ <p>It uses thresholding.</p>	
Improved Modified Polynomial	imodpoly	$p(x) = \beta_0 x^0 + \beta_1 x^1 + \dots + \beta_m x^m = \sum_{j=0}^m \beta_j x^j$ <p>Minimized function:</p> $\sum_i^N w_i^2 (y_i - p(x_i))^2$ <p>It uses thresholding with the standard deviation of the residual (data - baseline).</p>	
Penalized Spline Asymmetric Least Squares	pspline_asls	<p>B-splines:</p> $z(x) = \sum_i^N \sum_j^M B_j(x_i) c_j$ <p>Minimized function:</p> $\sum_i^N w_i (y_i - \sum_j^M \beta_j(x_i) c_j)^2 + \lambda \sum_i^{M-d} (\Delta^d c_i)^2$ <p>where λ is the penalty scale factor, and Δ^d is the finite-difference operator of order d.</p> <p>Linear system:</p> $(B^T W B + \lambda D_d^T D_d) c = B^T W y$ <p>Weighting:</p> $W_i = \begin{cases} p & y_i > z_i \\ 1 - p & y_i \leq z_i \end{cases}$	<p>N represents the number of points in x,</p> <p>M is the number of spline basis functions, $B_j(x_i)$ denotes the j-th basis function evaluated at x_i,</p> <p>c_j is the coefficient for the j-th basis,</p> <p>and B is the matrix containing all spline basis functions.</p>

Penalized Spline Adaptive Iteratively Reweighted Penalized Least Squares	pspline_ airpls	<p>B-splines:</p> $z(x) = \sum_i^N \sum_j^M B_j(x_i) c_j$ <p>Minimized function:</p> $\sum_i^N w_i (y_i - \sum_j^M \beta_j(x_i) c_j)^2 + \lambda \sum_i^{M-d} (\Delta^d c_i)^2$ <p>Linear system:</p> $(B^T W B + \lambda D_d^T D_d) c = B^T W y$ <p>Weighting:</p> $W_i = \begin{cases} 0 & y_i \geq z_i \\ \exp\left(\frac{t(y_i - z_i)}{ r^- }\right) & y_i < z_i \end{cases}$ <p>t is the iteration number and r⁻ is the L1 norm of the negative values in the residual vector r, ie. $\sum_{y_i - z_i < 0} y_i - z_i$.</p>	
Eight points baseline correction	8points	<p>8 valleys were considered at wavelength numbers of 600, 680, 930, 1800, 2400, 3100, 3600, and 4000 cm⁻¹</p> $y_i^* = y_i - (y_i + \left(\frac{y_{i+1} - y_i}{x_{i+1} - x_i}\right) \times (x - x_i))$ <p>y_i and x_i being the absorption intensity and the wavelength number respectively. i and i+1 are the two consecutive adjustment points.</p>	<p>y_{ij} and y_{ij}* represent the initial and new values of the j-th variable (i.e., absorbance) in the i-th spectrum (i.e., sample).</p>

3.4.2 Normalization methods

NDPs can address challenges related to varying sample size or quantity, flaws or limitations intrinsic to the instrument, for instance, low signal intensity or scattering, and variations caused by different mean or standard deviations (Figure 3.2). In this chapter, the impacts of nine distinct normalization data pre-processing techniques on ATR-FTIR spectra were explored, as these represent the full range of approaches identified in the existing literature.. Namely, the NDP methods include Normalization to sum (NTS), Normalization to constant vector length (NCV), Normalization to a maximum to 1 (NMO), Mean centring (MC), Autoscaling (AS), Pareto scaling (PS), Robust scaling (RS), Standard normal variate (SNV), Multiplicative scatter correction (MSC) [16, 37]. Table 3.3 lists these NDP methods alongside related equations. In this chapter, the reference spectrum required for MSC is set as the average spectral value of the entire dataset, as this approach minimizes bias by representing the central tendency of all spectra and helps ensure consistent correction across the dataset. Regarding the NMO method, the minimum point of the curve in the range 2800–3200 cm⁻¹ is set at zero, and the maximum point is adjusted to 1. This range was selected because it typically encompasses prominent C–H stretching vibrations in bituminous binders; aligning the extremes of this region facilitates comparability between samples while preserving relevant spectral information. Additionally, this spectral region exhibits relatively low noise, and focusing on it helps to avoid inconsistent minima that may occur in noisier regions of the spectrum.

Among the selected NDP methods, normalization to sum (NTS), normalization to constant vector (NCV), and standard normal variate (SNV) are referred to as one-way methods, where each spectrum is pre-processed individually. In these methods, the normalized result of a given spectrum is based solely on its own internal characteristics. In contrast, the other NDP methods applied in this study are considered two-way methods, in which the normalization outcome for a given spectrum is influenced by the entire dataset, as they rely on statistical parameters (e.g., global mean or standard deviation) computed from all spectra.

Reviews by Rinnan et al. [16] and Lasch [38] provide detailed theoretical overviews of these methods. Key conclusions from these reviews emphasize that while one-way methods offer robustness and are less prone to introducing inter-sample bias, two-way methods can provide better alignment across samples, especially when the dataset is consistent and homogeneous. However, they also caution that applying two-way normalization to test samples using parameters derived from the training set can lead to information leakage, thus biasing classification results.

To avoid such confounding effects, this study implemented independent pre-processing of the test set and training set. Specifically, the normalization parameters (e.g., mean, standard deviation, or vector norms) used for the test set were calculated solely from the test spectra, without reference to the training data. This approach ensures a strict separation between training and evaluation phases, preserving the objectivity of model performance assessments, particularly in the context of supervised classification techniques such as PLSDA [37, 39].

Table 3.3 Mathematical expressions representing the normalization methods (NDPs) along with their corresponding abbreviations.

Name	Abbreviation	Formula
Normalization to sum	NTS	$y_{ij}^* = \frac{y_{ij}}{\sum y_i}$
Normalization to constant vector length	NCV	$y_{ij}^* = \frac{y_{ij}}{\sqrt{\sum y_i^2}}$
Normalization to a maximum to one	NMO	$y_{ij}^* = \frac{y_{ij} - \min(y_i)}{\max(y_i)}$
Mean centring	MC	$y_{ij}^* = y_{ij} - \bar{y}_j$
Autoscaling	AS	$y_{ij}^* = \frac{y_{ij} - \bar{y}_j}{\sigma_j}$
Pareto scaling	PS	$y_{ij}^* = \frac{y_{ij} - \bar{y}_j}{\sqrt{\sigma_j}}$
Robust scaling	RS	$y_{ij}^* = \frac{y_{ij} - y_{median.j}}{y_{MAD.j}}$
Standard normal variate	SNV	$y_{ij}^* = \frac{y_{ij} - \bar{y}_i}{\sigma_i}$
Multiplicative scatter correction	MSC	$y_{ij}^* = \frac{y_{ij} - a_i}{b_i}$

Here, y_{ij} and y_{ij}^* denote the initial and normalized values of the j -th variable (absorbance) in the i -th spectrum (sample). Meanwhile, \bar{y}_i , σ_i , and $\sum y_i$ signify the mean, standard deviation, and sum of all variables for the i -th spectrum, respectively. Additionally, σ_j , $y_{MAD.j}$, and $y_{median.j}$ represent the standard deviation, median absolute deviation, and median of the j -th variable across all spectra in the dataset, respectively. For the multiplicative scatter correction (MSC), a_i and b_i refer to the additive and multiplicative effects of a sample spectrum, which can be estimated through least-squares regression from a reference spectrum [30].

3.4.3 Combined normalization and baseline-correction methods

It remains uncertain whether normalization, baseline-correction, or a combination of both is optimal for analysing FTIR spectra in bituminous binder-related studies. In this chapter, baseline correction was applied before normalization, following the common practice in FTIR spectral analysis of bituminous binders. This sequence is logical because baseline irregularities can distort the overall spectral shape, leading to misleading normalization results. By first correcting the baseline, the spectral data retains its true structural features, ensuring that the subsequent normalization process accurately adjusts for variations in intensity without being influenced by artifacts. If normalization were applied before baseline correction, unwanted fluctuations in the baseline could interfere with the scaling process, potentially amplifying or diminishing spectral features in an inconsistent manner [23, 34].

Following this rationale, the combined data pre-processing (CDP) strategy implemented in this study involved a sequential application of one of nine baseline correction methods, followed by one of nine normalization techniques. This procedure was applied uniformly across the entire dataset, which consisted of ATR-FTIR spectra from three independent sources, covering various binder types and aging conditions. Each individual spectrum was thus processed using all 81 possible combinations of baseline correction and normalization methods. In addition to these 81 combinations, the spectra were also processed using each of the nine baseline correction and nine normalization methods individually, without combination, leading to a total of 99 distinct pre-processing variants per spectrum. The raw, unprocessed spectra were retained as a reference, resulting in 100 versions of each original spectrum. This comprehensive pre-processing scheme was designed to enable a systematic assessment of how different data pre-processing strategies influence classification outcomes in aging-related chemometric analysis.

3.5 Transformation of spectra to peak areas and indices

In a FTIR spectrum of a bituminous binder sample, informative peaks describing the carbonyl, sulfoxide, aromaticity, aliphatic, sulfone, long chain, and hydroxyl groups can be observed, with their wavenumber ranges detailed in Table 3.4. Two common approaches employed in pavement engineering and bituminous binder studies, peak area calculation and index calculation, were used to characterize these functional groups following the pre-processing of the input data. Two peak area calculation methods were utilized, i.e., area-to-base, and tangential area (see Figure 3.4). For index calculation, Equation 3.1 was applied for each functional group, using the vertical limits outlined in Table 3.4. Four distinct types of indices were derived by varying the methods for peak area calculation and the selection of reference area. The definitions and applications of these indices and peak areas are presented in Table 3.5.

Table 3.4 Main functional groups of bituminous binder in FTIR spectra with their respective vertical bands and their molecular information [40].

Peak area	Vertical band limit(cm^{-1})	Functional groups
A810	710-734 734-783 783-833 833-912	Hydrocarbon chain, $(\text{CH}_2)_n$, C-H in isolated/two/four adjacent hydrogen aromatic rings or C- CH_2 rocking in alkyl side chains with more than four carbons
A1030	984-1047	Oxygenated function-sulfoxide, S=O
A1200	1100-1180 1280-1330	Tertiary alcohol C-C-O, C-O in carboxylic acid, C-C-C in diaryl ketones, C-N secondary amides, O=S=O in sulfone
A1376	1350-1395	Branched aliphatic structures bending, CH_3

A1460	1395-1525	Aliphatic structures bending, CH ₃ and CH ₂
A1600	1535-1670	Aromatic structure, C=C
A1700	1660-1800	Oxygenated function-carbonyl, C=O
A2953	2820-2880 2880-2990	Aliphatic structures, Symmetric, Asymmetric stretching, CH
A3400	3100-3800	Hydroxyl stretching, OH, NH
$A_{TOTAL} = A_{810} + A_{1030} + A_{1376} + A_{1460} + A_{1600} + A_{1700} + A_{2953} + A_{3400}$		
$A_{ALI} = A_{1376} + A_{1460}$		

The computation of indices followed this equation:

$$\text{index} = A_x / A_{\text{ref}} \quad (3.1)$$

The symbol A_x denotes the peak area under the curve within specific ranges outlined in Table 3.4. A_{ref} represents either the sum of all peak areas (A_{TOTAL}) or exclusively the aliphatic peak areas (A_{ALI}).

The calculation can be performed in two distinct manners: either as peak area to the baseline (A_B) or tangential peak area (A_T), as illustrated in Figure 3.4.

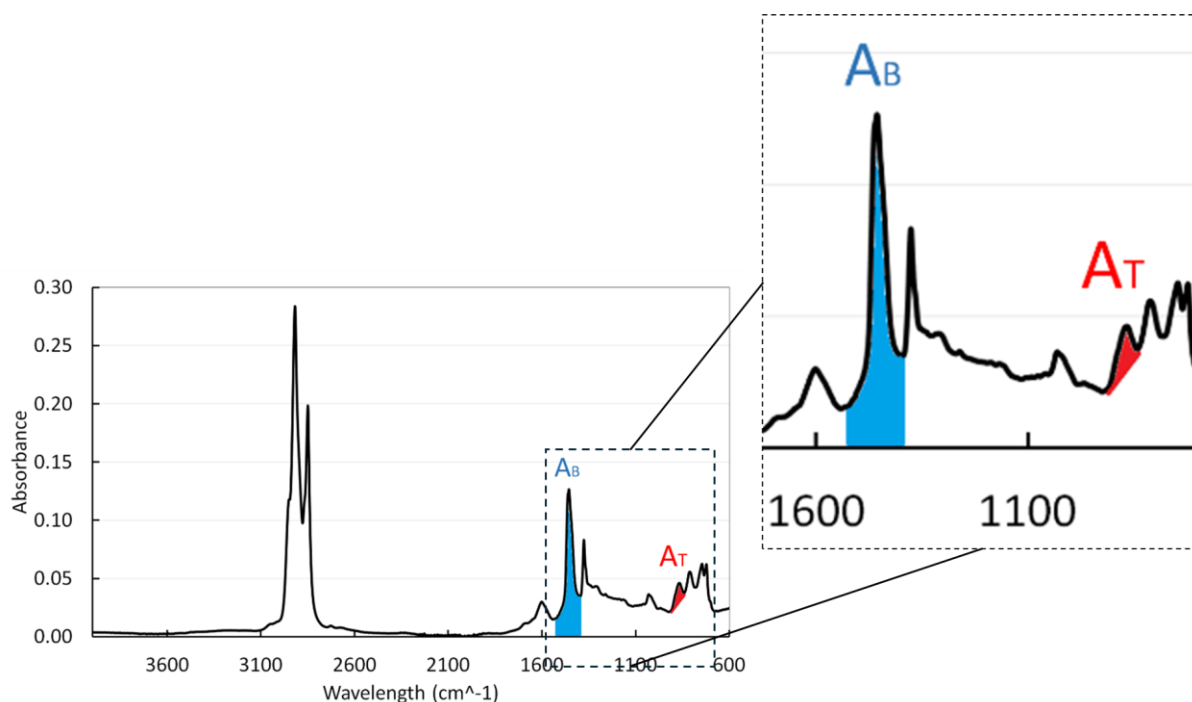


Figure 3.4 A typical ATR-FTIR spectrum with corresponding peak area considerations. A_B denotes the peak area beneath the curve to the baseline, while A_T represents the tangential peak area.

The methods for calculating peak areas and indices in ATR-FTIR spectra analysis are varied and defined by specific criteria in Table 3.5. The "Peak area to base" method (A_B) calculates the peak area underneath the curve and above the x-axis in the specified range, without computing any indices. The "Tangential peak area" method (A_T) also calculates the peak area underneath the curve but above a tangential line in the specified range, similarly without indices. The "Peak area to base-all peak area" method (A_B / A_{TOTAL}) involves calculating the peak area to base and then dividing each calculated peak area by the summation of all the calculated peak areas (A_{TOTAL}) to form indices. The "Peak area to base-aliphatic peak areas" method (A_B / A_{ALI}) follows a similar approach but the indices are formed by dividing each calculated peak area by the summation of all the calculated peak areas specifically for aliphatic groups (A_{ALI}). The "Tangential peak area-all peak areas" method (A_T / A_{TOTAL}) calculates the tangential peak area and then divides each by the summation of all peak areas to

create indices. Lastly, the "Tangential peak area-aliphatic peak areas" method (A_T/A_{ALI}) calculates the tangential peak area and forms indices by dividing each peak area by the summation of all peak areas for aliphatic groups ($A_{aliphatic}$). The details of peak areas and indices calculation are presented in Table 3.5.

Table 3.5 Specifics of calculations for peak areas and indices along with their respective abbreviations.

Name of method	Abbreviation	How to calculate peak area	How to calculate indices
Peak area to base	A_B	Peak area underneath the curve and above x-axis in the specified range	No index calculated
Tangential peak area	A_T	Peak area underneath the curve and above the tangential line in the specified range	No index calculated
Peak area to base-all peak area	A_B/A_{TOTAL}	Peak area underneath the curve and above x-axis in the specified range	Dividing each calculated peak area by the summation of all the calculated peak areas, A_{total}
Peak area to base-aliphatic peak areas	A_B/A_{ALI}	Peak area underneath the curve and above x-axis in the specified range	Dividing each calculated peak area by the summation of all the calculated peak areas for aliphatic groups, $A_{aliphatic}$
Tangential peak area-all peak areas	A_T/A_{TOTAL}	Peak area underneath the curve and above the tangential line in the specified range	Dividing each calculated peak area by the summation of all the calculated peak areas, A_{total}
Tangential peak area- aliphatic peak areas	A_T/A_{ALI}	Peak area underneath the curve and above the tangential line in the specified range	Dividing each calculated peak area by the summation of all the calculated peak areas for aliphatic groups, $A_{aliphatic}$

3.6 Evaluation of DP methods

3.6.1 Partial least squares-discriminant analysis

To determine the most effective data pre-processing (DP) methods for studying FTIR spectral data of bituminous binders, it is essential to evaluate their impact on the classification of performance. Without systematic evaluation, the choice of DP methods remains arbitrary, potentially leading to misleading interpretations.

Three commonly recognized approaches for evaluating data pre-processing (DP) methods are spectrum comparison, clustering of samples projected onto a PCA score plot, and assessment of modelling accuracy or error [24]. Spectrum comparison involves direct visual evaluation of the pre-processed spectra, but this method is inherently qualitative and subjective, requiring manual inspection and interpretation. Clustering of samples in PCA score plots adds a degree of quantitative evaluation, yet it remains dependent on visual interpretation and lacks a direct link to classification or prediction performance. In contrast, evaluating modelling accuracy, typically using chemometric techniques such as Partial Least Squares Discriminant Analysis (PLSDA), provides a more goal-oriented and performance-based metric. However, it is not entirely free from subjectivity either. Modelling outcomes can be influenced by choices related to class definitions, data partitioning (e.g.,

training vs test sets), and the selection of spectral regions or indices used as model inputs. For instance, emphasizing certain peaks over others may optimize classification accuracy for a particular target variable while overlooking spectral features relevant to alternative interpretations or secondary effects.

To address this, in the present chapter, all parameters that could introduce subjectivity, such as training/test splits, class definitions, and model structure, were held constant across all experimental conditions. This ensured that the observed differences in classification performance were attributable solely to the applied pre-processing strategies, rather than confounding factors related to model setup or data handling. Thus, while model-based evaluation is more quantitative and linked to analytical goals, it also requires careful control of procedural variables to enable fair and meaningful comparison. In this study, PLSDA was chosen as the primary tool for evaluating DP methods due to its widespread use in spectral classification tasks and its ability to generate clear performance metrics, such as classification accuracy, that facilitate comparison across DP strategies [11, 25].

Over the last two decades, the PLSDA has become widely acknowledged and extensively utilized in previous research [41-43]. Theoretically, PLSDA combines two processes – dimensionality reduction and discriminant analysis – into a single algorithm, which is particularly effective for handling complex, high-dimensional (HD) data [44]. Importantly, PLSDA does not assume that the data follows a specific distribution, making it more adaptable compared to other discriminant algorithms, such as Fisher’s linear discriminant analysis [25]. Spectral data usually have high dimensionality, and the variables (like wavenumbers) are often interconnected (collinear). As a result, traditional discriminant methods like LDA are not suitable for spectral data [25, 26]. Additionally, while PCA could address the challenges associated with LDA in HD data, PLSDA has frequently exhibited superior performance compared to PCA-LDA [27, 28]. The combination of spectral data and PLSDA has exhibited notable success across various domains, such as food analysis [45] and forensic science [46]. Therefore, in this chapter, PLSDA will be employed to assess the impact of different pre-processing methods.

PLSDA relies on Partial Least Squares (PLS) multivariate calibration, enabling the simultaneous decomposition of the data matrix X (of dimensions $n \times m$, with n samples and m variables, typically spectral intensities, or indices) and the response vector y , which contains numerical labels for each sample based on its class (e.g., fresh vs. aged bituminous binder). This decomposition introduces a new set of orthogonal axes called latent variables (LVs), which define a reduced coordinate system that captures the most relevant variance in X with respect to the response y . The method projects both the input variables and the response into this new latent space, allowing for a supervised dimensionality reduction that facilitates class separation. The mathematical form of the decomposition is given in Equations 3.2 and 3.3 [27, 47, 48]:

$$X = \sum_{a=1}^A t_a p_a^T + E \quad (3.2)$$

$$y = \sum_{a=1}^A t_a q_a^T + f \quad (3.3)$$

In these equations:

- t_a (the *scores*) represent the projections of the original samples onto the a -th latent variable. They describe the sample distribution along directions that are most relevant for class discrimination.
- p_a and q_a (the *loadings*) describe how the original X variables and the response y , respectively, contribute to the latent variable space. In essence, they reflect the weight or importance of each original variable in defining the new latent structure.

- **E** and **f** denote the residuals, i.e., the portion of the data in **X** and **y** not captured by the model (i.e., the variance not explained by the selected latent variables).
- **A** is the total number of latent variables included in the model, determined based on cross-validation or other performance-based criteria to avoid overfitting.

Thus, in the context of ATR-FTIR analysis, the scores can be interpreted as compressed representations of spectra, optimized for classification, while the loadings highlight which spectral regions (or indices) are most influential in distinguishing classes.

The decision rule for classification in this PLSDA analysis employs a fixed point-based approach, where the model's predicted continuous values of the response variable **y** (typically between 0 and 1) are converted into binary class labels. A fixed threshold of 0.5 is used as the cut-off point: samples with predicted **y** values greater than or equal to 0.5 are classified into one group (e.g., aged), while those with values below 0.5 are classified into the other group (e.g., fresh). This threshold is commonly used in binary classification tasks based on regression-type outputs, as it represents the midpoint between the two extremes of class encoding (0 and 1).

While this cut-off is widely accepted for balanced datasets, it is important to note that its suitability depends on the distribution of classes and the specific application. In this chapter, the 0.5 threshold is retained consistently across all pre-processing methods to ensure comparability and to avoid introducing additional subjectivity.

For more advanced applications or imbalanced data, alternative decision rules, such as using Receiver Operating Characteristic (ROC) curve analysis to optimize the threshold, may be warranted [27, 48]. However, such adaptations were deliberately avoided here to maintain methodological consistency and allow for fair comparison across the 100 pre-processed datasets.

3.6.2 Partial least squares-discriminant analysis model validation

In practical terms, the selection of a model validation method is influenced by the size of the dataset. For smaller datasets, internal validation techniques such as cross-validation (CV) are commonly employed because they allow the use of the entire dataset for both training and testing without requiring a separate test set. In *v*-fold CV, the dataset is randomly partitioned into *v* subsets (folds) of approximately equal size. The model is trained on *v*−1 folds and tested on the remaining one. This process is repeated *v* times, with each fold used once as the validation set. The average performance across all *v* iterations provides an estimate of the model's generalization ability. CV is especially advantageous for small datasets because it reduces the risk of overfitting that might arise if the dataset were split into separate training and test sets, leaving too few samples for either.

However, the choice of *v* in *v*-fold CV involves a trade-off. A lower *v* (e.g., 5-fold) decreases computational load and variance in the validation estimate but can increase bias due to the smaller training subsets. Conversely, a higher *v* (e.g., leave-one-out) reduces bias but increases variance and computational cost [25]. In this study, a 10-fold CV strategy was chosen as a balance between bias, variance, and computational feasibility. This choice is commonly adopted in chemometric and statistical studies as a robust compromise and has been shown to provide reliable estimates of model performance [49-51].

While the reference [25][49] provides methodological justification for this approach, the selection is also supported by its widespread use in comparative studies and methodological reviews in the field of spectral analysis and chemometrics [49-51].

In this investigation, a 10-fold cross-validation strategy was applied to conduct PLSDA. This approach entails dividing the dataset into 10 equal segments, employing 9 segments for model training and reserving one segment for testing. The process iterated 10 times, using a different segment for testing each time, and the accuracy outcomes were averaged to yield a robust evaluation of the

model's effectiveness. Given the uneven distribution of 282 aged samples and 102 fresh samples in the input data-frame, a potential bias could arise from simple random sampling [37]. To address this, stratified k-fold cross-validation was employed instead of the standard random k-fold method. This ensures that the class distribution in each data split aligns with the distribution in the complete training dataset and the target variable (y), thus controlling the sampling process [52] and preventing such a bias.

In multilabel classification, the accuracy score provides the subset accuracy. A subset accuracy of 1.0 is achieved when the entire set of predicted labels for a sample exactly matches the true set of labels; otherwise, it is 0.0. The accuracy score is calculated based on Equation 3.4. If \bar{y}_i represents the predicted value for the i -th sample and y_i is the corresponding true value, the fraction of correct predictions over $n_{samples}$ is defined as equation 3.4:

$$accuracy(y, \bar{y}) = \frac{1}{n_{samples}} \sum_{i=0}^{n_{samples}-1} 1(\bar{y}_i = y_i) \quad (3.4)$$

where $1(x)$ is the indicator function, returning 1 if the condition is true and 0 otherwise.

This strict metric for binary classification ('fresh' vs 'aged') counts only fully correct assignments as accurate, offering a robust assessment of performance. The 'true' value refers to the known class label of each spectrum, determined experimentally (e.g., PAV aging), and not to spectral values. These labels are fixed and independent of preprocessing.

Each preprocessing method is evaluated by training a model on a training set and testing it on an independent test set, with preprocessing applied separately to prevent data leakage. The model's classification accuracy on the test set reflects how well the preprocessing preserves or enhances class-relevant information.

Although dataset-specific variation may exist, methods that consistently perform well here are likely to generalize. Still, no technique is claimed to be universally optimal. The results offer empirically supported starting points, but validation on new datasets remains essential.

3.6.3 Variable Importance in Projection Scores (VIP scores)

Variable Importance in Projection (VIP) scores in PLSDA quantify the importance of each predictor variable in distinguishing between predefined classes [53]. These scores are calculated by evaluating the contribution of each variable to the PLS components and the explained variance in the classification model, involving a weighted sum of the PLS weights, adjusted for the discriminative power of each variable. Specifically, the calculation involves a weighted sum of squared correlations between the PLSDA components and the original variable, with the weights representing the percentage of variation explained by the respective PLSDA component. The formula for calculating the VIP score for a variable j can be expressed as Equation 3.5.

$$VIP_j = \sqrt{\frac{p \cdot \sum_{a=1}^A (w_{ja}^2 \cdot SS_{Y_a})}{\sum_{j=1}^p SS_{Y_a}}} \quad (3.5)$$

where p is the number of predictor variables, A is the total number of PLS components, w_{ja} is the weight of the j -th variable on the a -th component, and SS_{Y_a} is the sum of squares explained by the a -th component [54].

Variables with VIP scores greater than 1 are typically considered significant contributors to the classification model, while those with scores below 1 are generally regarded as less influential [54]. In some cases, thresholds of 1 and 0.7 are applied to categorize features into high, moderate, and

low importance. In this study, VIP scores were computed only for the pre-processing combinations that produced the highest classification accuracy in each evaluation category. The rationale for this selective application is to focus the interpretation on pre-processing strategies that were demonstrated to be most effective, thereby avoiding the confounding effect of suboptimal methods. The “best results” were determined based on classification accuracy obtained via 10-fold cross-validation.

VIP analysis was conducted on the latent variables of the PLS-DA model trained with these best-performing pre-processed datasets, with the objective of identifying which spectral variables contributed most to correct classification. This allows the evaluation of whether certain spectral regions, such as aging-sensitive peaks, consistently show high importance across the most effective pre-processing methods.

3.6.4 Hierarchical Cluster Analysis (HCA)

HCA utilizes two main strategies: agglomerative and divisive. In the agglomerative approach, each sample starts as an independent cluster. The algorithm progressively merges pairs of clusters based on a predefined metric describing sample distance (commonly Euclidean, Mahalanobis, or Manhattan distance) and the selected linkage criterion (single, complete, average, and Ward's linkage). These linkage criteria offer different ways to define the distance between clusters, contributing to cluster formation. In this research, an agglomerative approach was adopted, utilizing Euclidean distance and Ward's linkage criterion. Agglomerative approach is often computationally more efficient and allows for the flexibility of choosing different linkage methods. Ward's linkage minimizes variance within each cluster and is chosen for its effectiveness in optimizing a specific target function. HCA results are typically depicted as dendrograms, providing a visual representation of sample organization within a hierarchical tree-like structure [55].

In a dendrogram (Figure 3.5), each branch is referred to as a clade, and the end of each clade is called a leaf. The arrangement of these clades communicates the level of similarity among individual leaves. The point where branches intersect indicates the extent of likeness or dissimilarity, with higher intersections signifying more significant differences. Dendrograms can be interpreted in two ways: firstly, concerning broad-scale groupings, starting from the top and emphasizing high-level branch points (forming cluster X and cluster Y). Secondly, to identify the most similar components, the dendrogram was examined from the bottom up, focusing on the earliest converging clades. The length of the vertical lines in the dendrogram reflects the degree of divergence between branches, where longer lines denote greater distinctions. The horizontal alignment of dendrograms is not crucial, seeing it as a flexible structure where the arms may shift while maintaining consistent vertical height and subgroup arrangement [56].

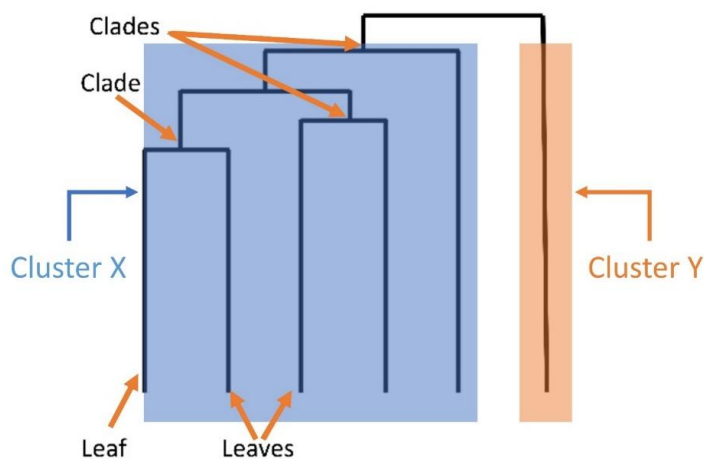


Figure 3.5 Illustration of a dendrogram depicting the hierarchy of leaves and clades.

3.7 Methodological Approach

This section outlines the analysis steps undertaken in this research, as illustrated in Figure 3.6. Initially, pre-processing was applied to a data frame containing 384 raw FTIR spectra measured at 3400 wavenumbers. Using the the 9 baseline corrections (Section 3.4.1) both separate and in combination with nine normalization techniques (Section 3.4.2) this resulted in 100 pre-processed data frames of size 384×3400. These frames included 9 normalized, 9 baseline-corrected, 81 combined-methods (BDPs + NDPs), and 1 raw data frame. For each pre-processed frame, 6 new frames of indices and peak areas (Table 3.5) were generated, yielding a total of 600 (6×100) data frames of size 384×14. The number 14 corresponds to spectral features extracted from 14 different FTIR regions associated with distinct functional groups, as outlined in Table 3.4. Additionally, the entire spectra and their first derivatives were considered, resulting in 200 frames of (each of the 100 pre-processed frames times 1 entire spectrum and 1 first derivative) size 384×3400 (same as the original spectra) after applying the Savitzky–Golay (SG) method for derivative calculation.

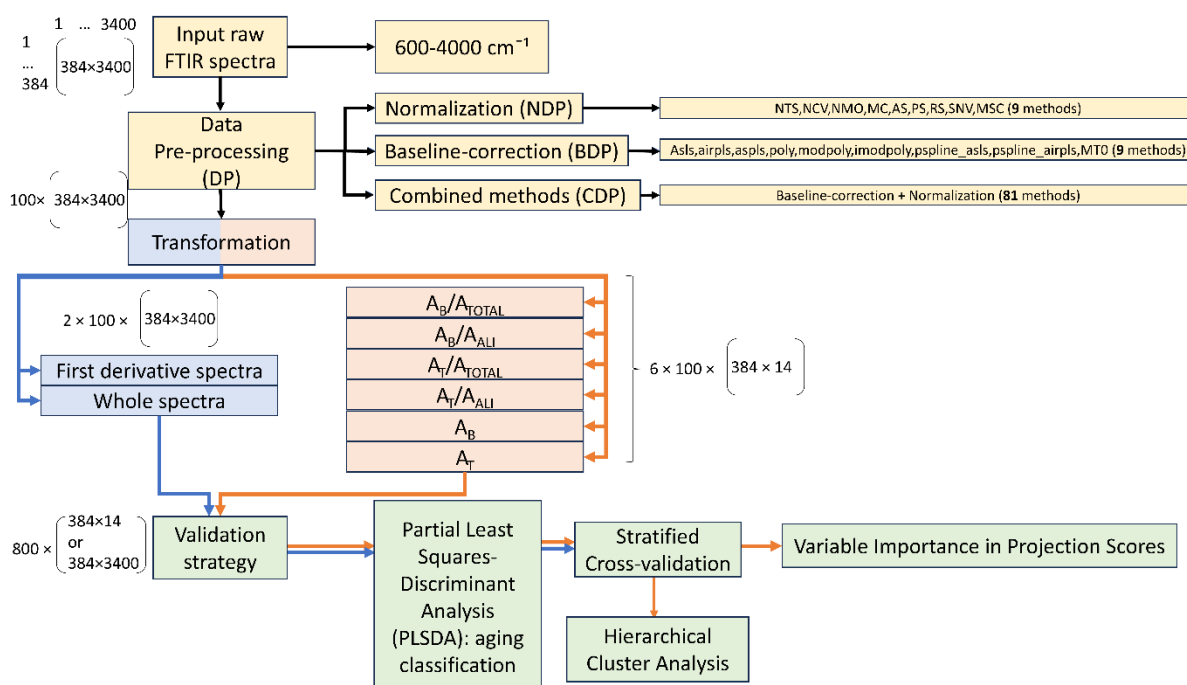


Figure 3.6 The schematic diagram depicts the sequential steps involved in the pre-processing and post-processing analysis conducted in this research. It offers a comprehensive overview of each stage, including details about the size and quantity of the data frames considered. The process begins with reading the data, applying pre-processing methods, and transforming the pre-processed data into area, indices, entire spectra, or first derivative spectra. This is followed by applying PLSDA classification with stratified cross-validation and HCA. Additionally, VIP scores were analyzed.

Subsequently, for PLSDA analysis (Figure 3.6), 600 frames of size 384×14 and 200 frames of size 384×3400 were considered. The primary focus has been on aging classification. This task is considered more complex than identifying or classifying materials such as regenerators or polymers, based on the assumption that aging introduces fewer alterations to FTIR spectra compared to the introduction of new substances. The idea is to optimize the selection of DP methods for the more challenging scenario, namely, the classification of fresh and aging states. For aging classification, the dataset was split into fresh and aged samples of various binder types. For aging classification, the

following steps were undertaken and discussed individually, and subsequently, the results were compared.

As discussed above, each data frame was divided into 10 parts, with 9 parts used for PLSDA training and 1 part reserved for testing. This process iterated 10 times, using a different segment for testing each time, and accuracy outcomes were averaged and presented in the result and discussion section. Subsequently, HCA was conducted on the accuracies of classification for DP modified spectra's indices and peak areas. This was undertaken to assess the similarities and differences among these methods for calculating peak areas and indices.

In the Results and Discussion section, classification accuracies for NDP and BDP modified peak areas/indices were visualized in a heatmap with an HCA clustering (cluster map). Classification accuracies for combined methods and entire spectra with their first derivatives were presented in separate tables. For methods with the highest accuracy, VIP scores, which are indicators of the most influential predictors in the aging classification process, were obtained to identify important regions.

The PLSDA and HCA implementation used Python programming libraries, and the entire statistical analysis process is outlined in Figure 3.6. The Python code for the entire procedure, covering normalization, baseline correction, combined methods, and PLSDA classification is available at 4TU repository [doi].

3.8 Results and discussion

3.8.1 IR spectra

The complete dataset utilized in this research is compiled from three distinct investigations, detailed in the materials and methods section. Figure 3.7 illustrates the spectra for all samples, measured in the wavenumber range of 600 to 4000 cm^{-1} through ATR-FTIR spectroscopy. While the spectra in Figure 3.7 exhibit similarities, characterized by peaks in the regions specified in Table 3.4, variations in absorbance intensity are evident due to differences in binder type, source, and aging level. This difference is particularly noticeable in the carbonyl and hydroxyl regions upon visual examination.

The variations observed in the carbonyl and hydroxyl regions can be attributed to the differing aging conditions and environmental factors affecting the bituminous binders. The carbonyl region differences arise due to the varying degrees of oxidative aging experienced by the binders. More severe aging conditions, such as extended Pressure Aging Vessel (PAV) treatment or exposure to high temperatures, promote the oxidation of binder components, leading to increased carbonyl absorbance. On the other hand, variations in the hydroxyl region are likely due to the presence of moisture during the aging process. Certain aging protocols, particularly those involving exposure to humid environments or water conditioning, can introduce or retain hydroxyl-containing species, contributing to differences in absorbance intensity in this region. These spectral variations emphasize the impact of aging severity and environmental exposure on the chemical composition of bituminous binders.

The differently coloured spectrum groups consist of both fresh samples and their corresponding aged counterparts, as explained in section 3.3. Additionally, all spectra display a slope in the lower wavelength region, though the slope varies across groups, with the last part of the data showing the highest rise. It is important to emphasize that these observations are solely based on visual inspection of the spectra. The classification potential of the spectra will be further assessed through PLSDA modelling, as discussed in the subsequent sections.

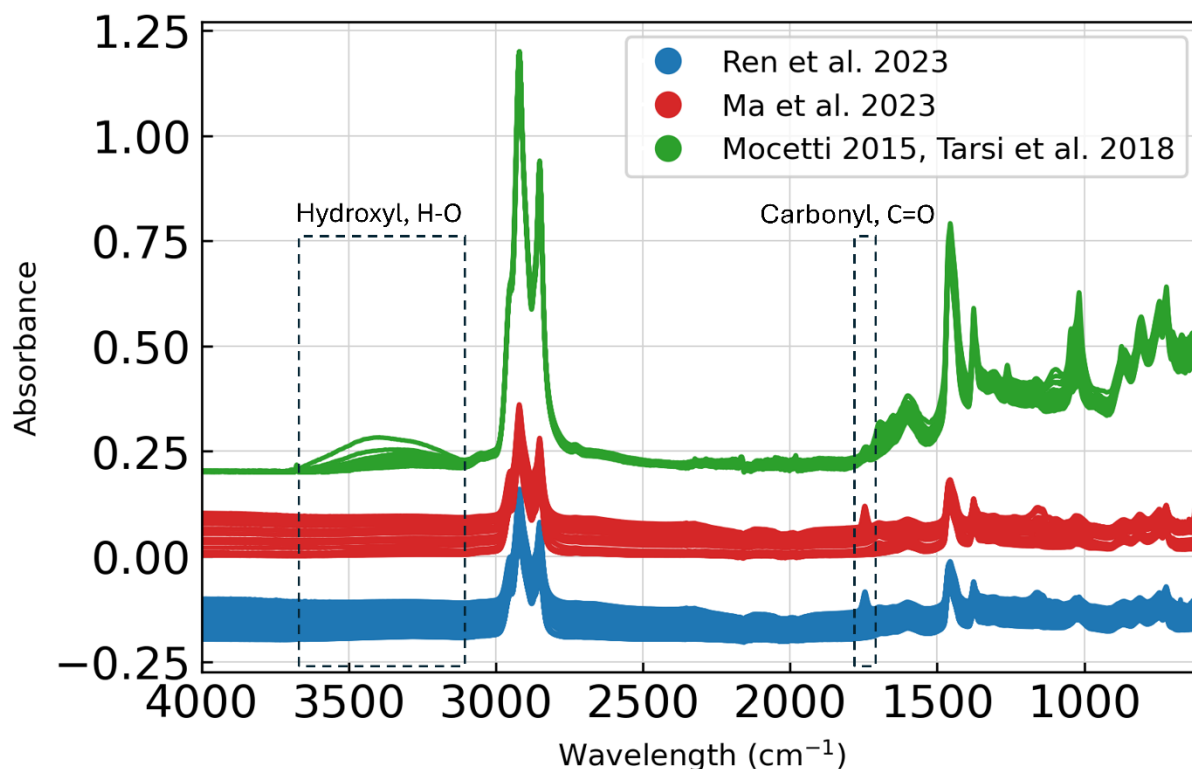


Figure 3.7 ATR-FTIR spectra derived from three distinct studies: the initial section sourced from [29], the second portion from [17], and the final segment obtained from [30, 31]. Details of each study are presented in Table 3.1. For better visualization, the data from the Ren et al. (2023) study and the Mocetti (2015) and Tarsi (2018) studies are shifted by -0.25 and $+0.25$ in their absorbance, respectively.

3.8.2 Effect of DPs on aging classification

This section examines the effects of nine normalization methods, nine baseline correction methods, and 81 combinations of both methods in comparison to the raw data through binary classification of fresh and aged samples using PLSDA.

Effect of different baseline correction data pre-processing methods on aging classification of peak areas/indices

Figure 3.8 presents the FTIR spectra before and after applying 9 different baseline correction pre-processing methods. The baseline-corrected spectra exhibit variations depending on the correction formula employed in Table 3.2. The original spectra (gray) are plotted against the baseline-corrected spectra (coral), revealing variations across different correction techniques. Some methods, such as airPLS (Figure 3.8c), result in more pronounced corrections, particularly in the lower wavenumber region. These differences arise from the varying mathematical approaches each method employs to estimate and subtract the baseline.

One key observation is that the corrected absorbance values differ across the subplots. This variation occurs because each baseline correction technique makes different assumptions about the spectral baseline, leading to differing extents of correction. For instance, polynomial-based methods (Figure 3.8d-f) adjust the baseline differently compared to spline-based methods (Figure 3.8g-h), which employ smooth piecewise functions. The choice of method impacts how much of the original spectral structure is retained after correction. It is advantageous to display the spectra in their adjusted scales rather than fixing them to a common absorbance range. This approach allows a clearer comparison of the baseline correction effects, as fixing all spectra to the same range could obscure the relative differences introduced by each correction method. By maintaining the natural variation in corrected spectra, it becomes easier to identify which techniques best preserve spectral

features while minimizing baseline distortions. In this chapter, the assessment of these effects was conducted indirectly through the subsequent modelling accuracy obtained via PLS-DA, using consistent training and test conditions across all pre-processing variations. This ensures that any observed differences in classification performance are attributable to the pre-processing technique itself.

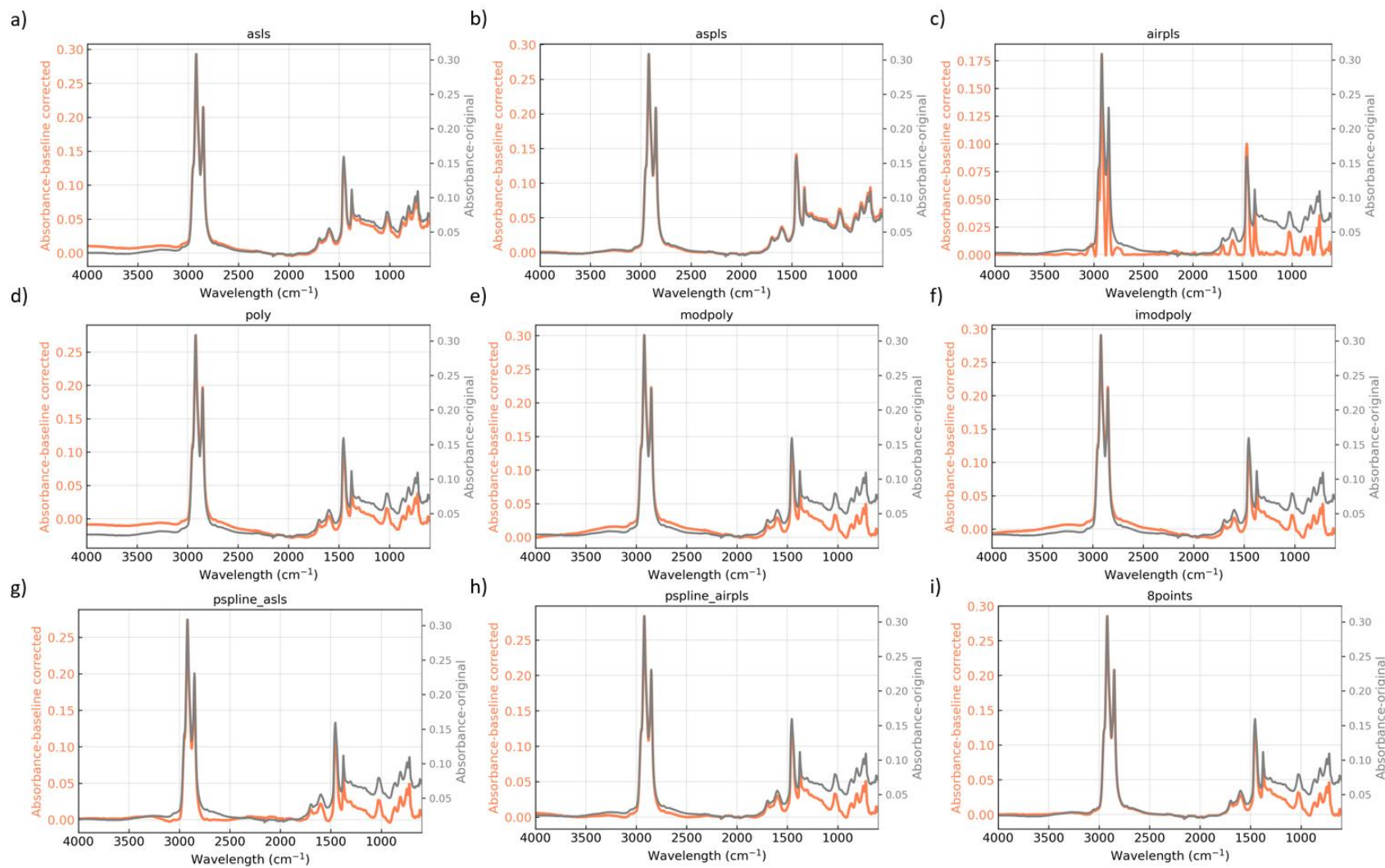


Figure 3.8 FTIR spectra before (Gray spectra, right vertical axis) and after (coral spectra, left vertical axis) the implementation of BDPs: a) asls, b) aspls, c) airpls, d) poly, e) modpoly, f) imodpoly, g) pspline_asls, h) pspline_airpls, i) 8points.

To evaluate the impact of different baseline correction methods on aging classification accuracy, PLSDA and HCA were applied to various FTIR-related peak areas and indices. Classification accuracies and clustering of different peak areas and indices were presented in Figure 3.9.

After applying BDP methods, the classification accuracies calculated from FTIR-related peak areas and indices showed both improvements and declines compared to those obtained from the raw spectra. HCA showed that the method used to compute peak areas and indices influenced the grouping of classification accuracies after baseline correction. A_{ALI} -based methods are more closely grouped compared to A_{TOTAL} -based indices. A_B and A_T varied in accuracy after baseline corrections, ranging from 0.70 to 0.83 for A_B and from 0.71 to 0.82 for A_T . Indices were less affected due to internal normalization by A_{ALI} or A_{TOTAL} .

Among baseline correction methods, *asls* and *aspls* significantly impacted classification accuracies, with *asls* showing the lowest and *aspls* the highest performance. *Asls* may not adapt well to local variations in classification tasks due to its emphasis on handling asymmetric errors in regression [57], while *aspls*'s penalty term for smoothing coefficients effectively reduces noise, enhancing classification accuracy by improving the signal-to-noise ratio in the data [58, 59]. This aligns well with previous findings that the importance of noise reduction in spectroscopic data analysis were emphasized [60, 61].

Polynomial fitting and *8points* methods also negatively affected classification accuracies. *Modpoly* [62] and *imodpoly* [63], despite being advanced methods, sometimes reduced accuracy due to overfitting [64, 65]. In this scenario, where data was collected from different studies with varying baseline characteristics, simpler methods outperform the modified versions. This suggests that complex baseline correction methods require a larger and more consistent dataset to fine-tune their hyperparameters effectively, whereas simpler methods perform more reliably under diverse conditions [65]. The *pspline_airpls* method performed worse than *airpls*, which adapts better to diverse baseline patterns [66]. The *8points* method notably reduced accuracies, particularly for indices, probably due to linear shifts in spectra causing information loss. While indices calculation stabilizes datasets, it can reduce valuable information for specific baseline-correction methods before classification.

In conclusion, only *aspls* consistently improved classification accuracy for all peak area or index calculations, mainly by effectively eliminating noise from the spectra. The ability of *aspls* to enhance signal quality suggests its potential application in other spectroscopic studies requiring high classification accuracy.

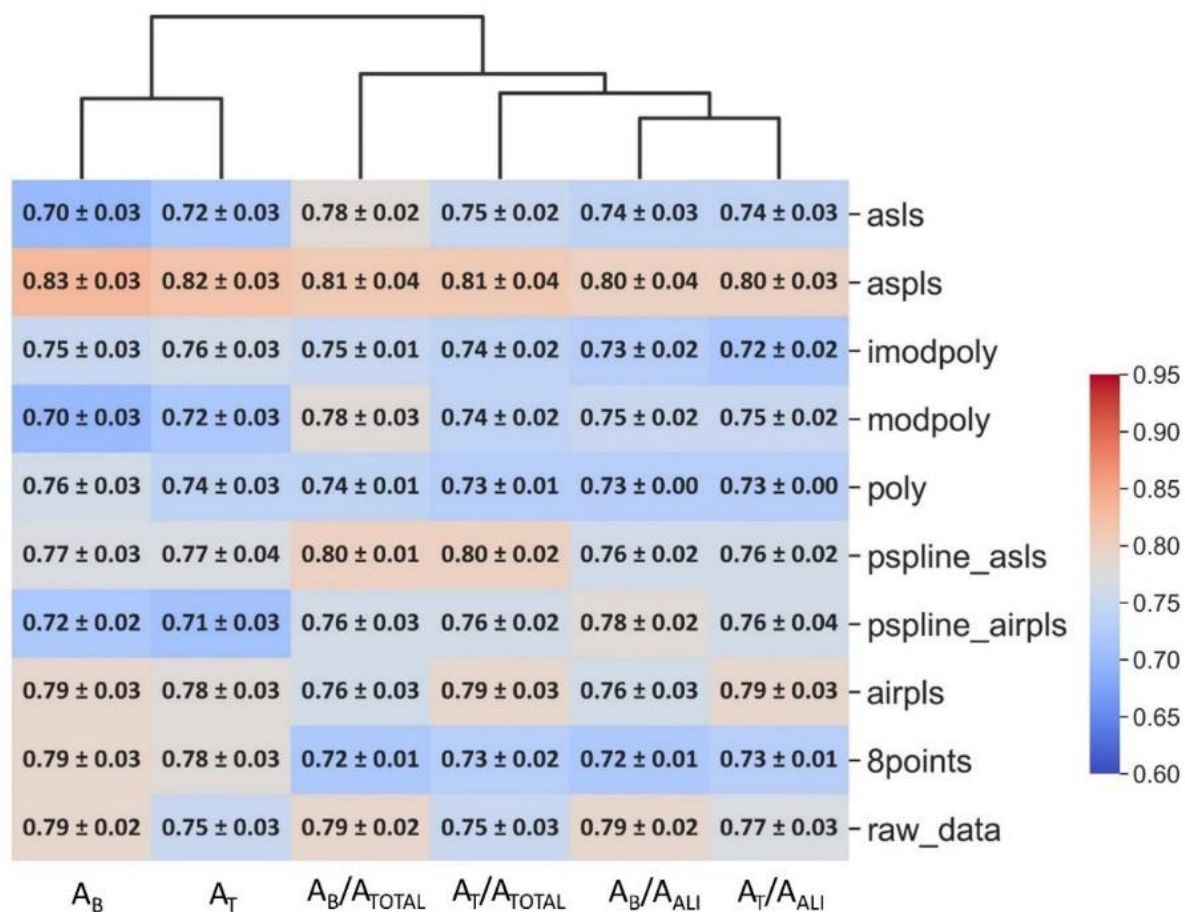


Figure 3.9 Cluster map illustrating aging classification accuracies associated with BDPs and the HCA dendrogram. Each column displays accuracies for various BDPs concerning a specific peak area or index calculation method, while each row represents the classification accuracies for a distinct BDP method but with different approaches to peak area and index calculations.

Effect of different normalization data pre-processing methods on aging classification of peak areas/indices

Figure 3.10 illustrates the impact of 9 normalization pre-processing methods on a group of 20 spectra. Each normalization method uniquely alters the raw spectra, as indicated by the formula outlined in Table 3.3. The application of the nine normalization methods to the FTIR spectra in Figure 3.10 results in spectra that retain the same overall shape but exhibit differences in absorbance values and relative positions. Although the peaks and their positions within each spectrum remain consistent, different normalization methods alter the relative positioning and spacing of the spectra in relation to each other. Consequently, each normalization technique modifies the variation within the dataset.

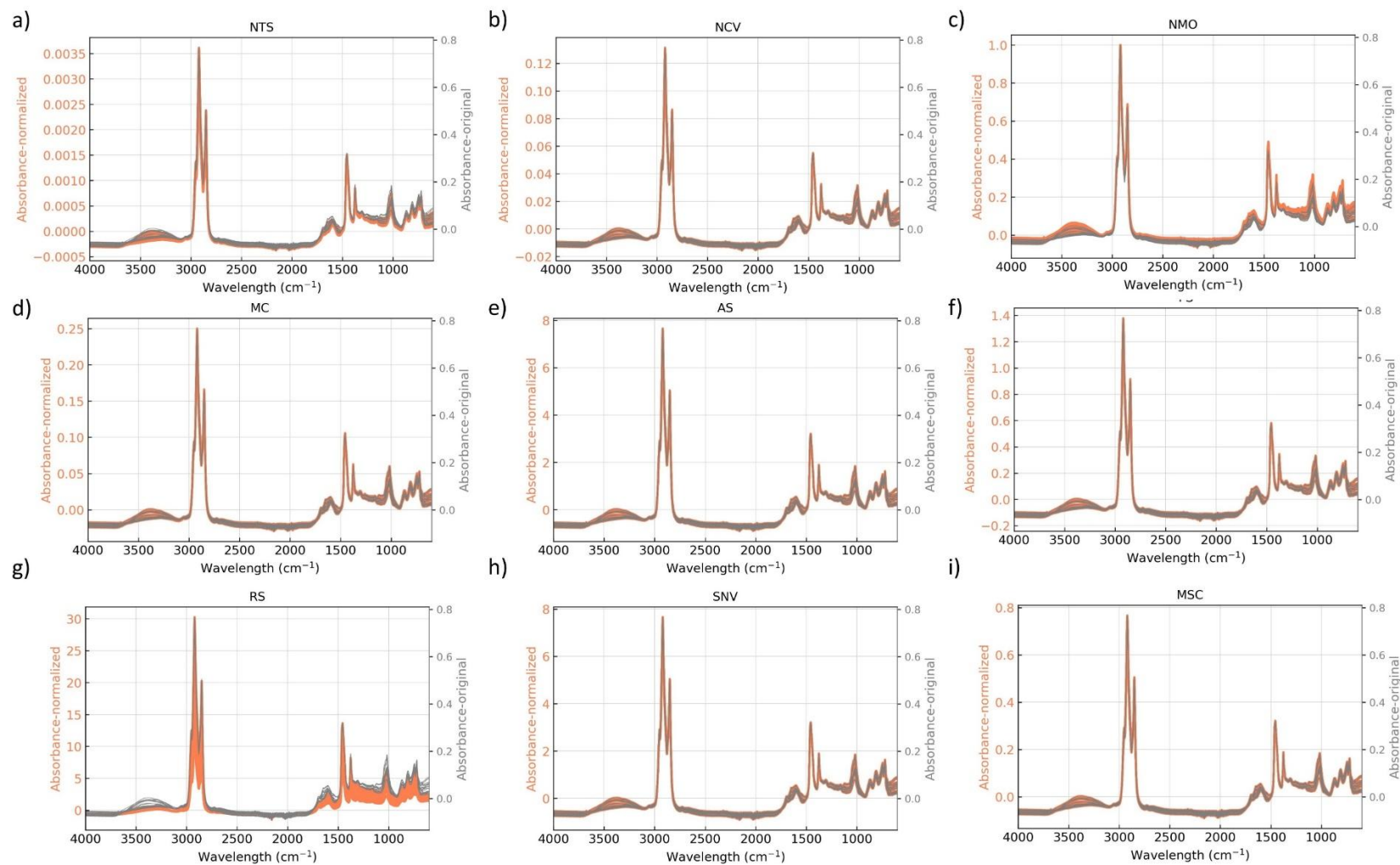


Figure 3.10 FTIR spectra of 20 samples before (Gray spectra, right vertical axis) and after (coral spectra, left vertical axis) the implementation of NDPs: a) NTS, b) NCV, c) NMO, d) MC, e) AS, f) PS, g) RS, h) SNV, and i) MSC.

Figure 3.11 presents a cluster map and HCA dendrogram showing the classification accuracies of aging states using index and peak area parameters. The HCA analysis reveals two distinct clusters for A_T -based and A_B -based methods. Indices using A_{ALI} as the reference are more distant than those with A_{TOTAL} or peak areas. Classification accuracy for raw data ranges from 0.75 to 0.79, with A_B and A_B -based indices consistently yielding higher accuracies than A_T and A_T -related indices. This indicates the robustness of A_B -based methods in capturing relevant features for classification aligns well with previous findings [2].

Among normalization methods, NDP is ineffective for A_T/A_{ALI} , likely due to its inability to appropriately scale spectral variations within these peak area definitions. In contrast, NCV is most effective for A_T and A_T/A_{TOTAL} , increasing classification accuracy from 0.75 to 0.82. This effectiveness is attributed to NCV's normalization of vector length, which reduces variability in spectral magnitudes while preserving the relative differences between peak areas, ensuring that the tangential area-based features remain distinguishable [23]. For A_B and A_B -based indices, NMO and RS show the highest improvement in classification accuracy. NMO preserves proportionality between features, and RS standardizes data, reducing sensitivity to outliers that could otherwise distort classification performance [67]. Outlier detection was not performed as all data points were integral and previous analyses showed no unusual findings [17, 29, 30], highlighting that extreme points impact full peak area classifications more significantly.

Integrating MC with A_T -based calculations (A_T , A_T/A_{TOTAL} , and A_T/A_{ALI}) shows no improvement in classification accuracy. This aligns with previous findings [37], as MC eliminates the mean effect, which does not contribute meaningfully to distinguishing spectral features when tangential area-based calculations are involved. Applying NTS to A_B -based calculations also proves ineffective. This suggests that eliminating the mean effect (MC) or focusing on relative contributions (NTS) is less effective than preserving absolute values (NMO) or standardizing data (RS).

In summary, the superior performance of NMO and RS for A_B and A_B/A_{TOTAL} indices, and NCV for A_T and A_T/A_{TOTAL} indices, suggests that normalization techniques that either preserve proportionality (NMO) or standardize data (RS) are particularly beneficial for full peak area-based features, while vector-length normalization (NCV) enhances classification performance for tangential area-based calculations. By matching normalization strategies to the indices, preprocessing can enhance the signal-to-noise ratio for relevant features, thereby improving the reliability of classification. These findings provide a foundation for optimizing data preprocessing techniques in spectroscopic analyses, particularly for aging studies where reliable classification is essential.

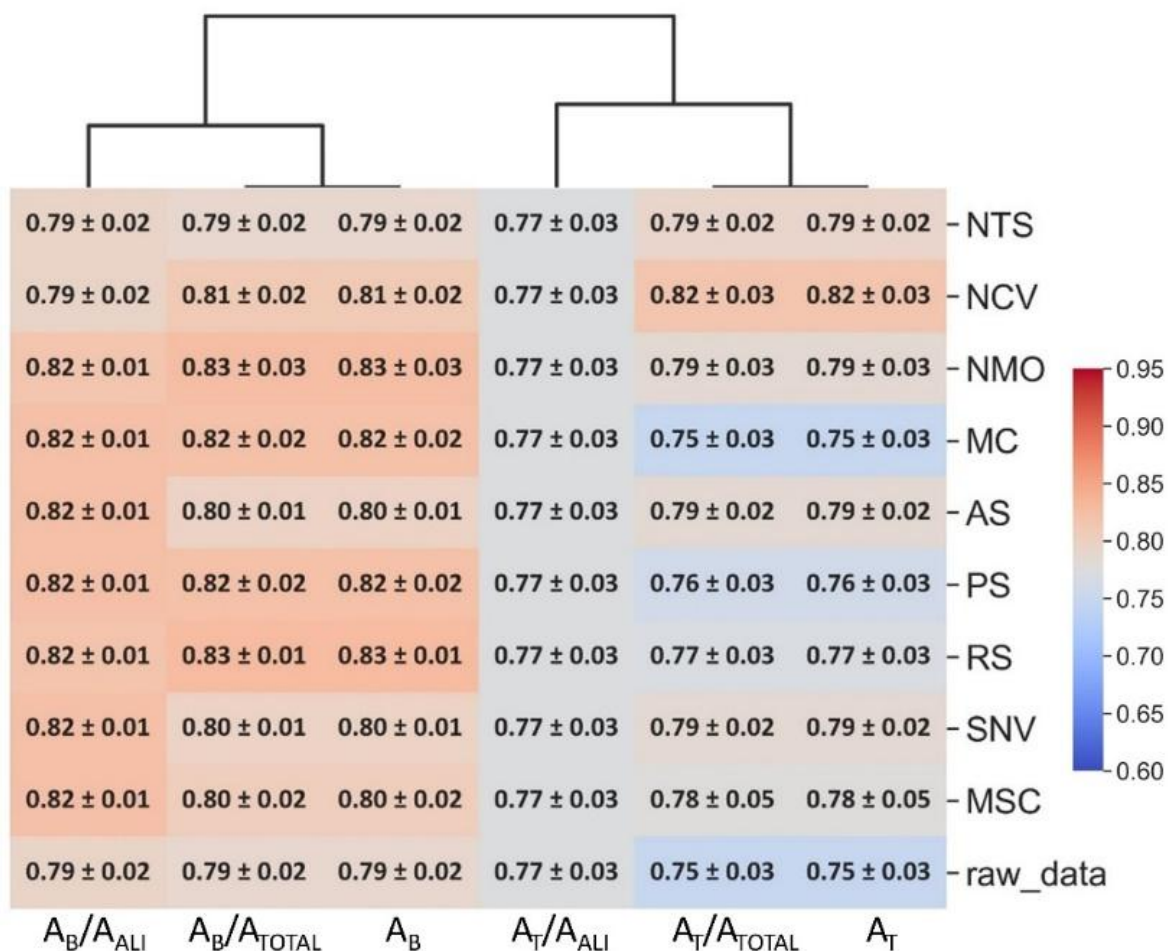


Figure 3.11 Cluster map illustrating aging classification accuracies associated with NDPs and HCA dendrogram. Each column displays accuracies for various NDPs concerning a specific peak area or index calculation method, while each row represents the classification accuracies for a distinct NDP method but with different approaches to peak area and index calculations.

Effect of combined BDP and NDP methods on aging classification of peak areas/indices

To evaluate the combined impact of baseline correction and normalization, the original data frame was transformed into 81 modified data frames using combinations of NDP and BDP methods. Peak areas and indices were computed for each modified data frame, resulting in 486 accuracy values from PLSDA analysis, with their standard deviations from a 10-fold CV. These values are provided in the supporting information, Table 1S in Appendix of chapter 3. This chapter focuses on the highest, lowest, and raw data accuracy values for each FTIR parameter calculation method, as shown in Table 1S in Appendix of chapter 3. Additionally, an HCA dendrogram of all 486 values is presented in Table 3.6, revealing three primary groups: one for peak area variables (A_B and A_T), another for aliphatic-based indices ($A_{B, T}/A_{ALI}$), and the last for summation of all peak area-based indices ($A_{B, T}/A_{TOTAL}$). This reveals the unique impact of peak area or index calculation methods on the effectiveness of different DP methods. One possible explanation is that aliphatic peaks, such as those related to CH_2 and CH_3 stretching, tend to be sharper and less prone to overlap than other functional group bands in fingerprint region. As a result, indices calculated with these regions (e.g., A_{ALI}) may be more robust to baseline distortions and normalization differences. In contrast, calculations involving broader spectral ranges (e.g., A_{TOTAL}) integrate across less well-defined regions, making them more sensitive to preprocessing choices.

This grouping suggests that the mathematical formulation of each feature (area-based, ratio-based, or summation) interacts with the spectral characteristics of the region involved, such as peak definition, intensity, and baseline stability. Further investigation is needed to assess whether such groupings consistently emerge across datasets or materials. Ideally, a theoretical rationale for such separability should be proposed, based on known chemical or spectral behaviours. However, at this stage, the empirical grouping provides a useful hypothesis for future studies.

The accuracy values indicate that the application of DP methods does not consistently enhance post-processing quality. The belief that randomly selecting DP methods or using multiple ones can be beneficial is disproved, as some DP methods result in lower accuracy than raw data. However, certain combinations might positively impact PLSDA classification. For example, in this case, combining aspls with NMO for A_B and A_T enhances accuracies to levels exceeding 0.80, although similar high accuracies are achieved by using either NMO or aspls alone, indicating no additional benefit from the combination.

Conversely, the lowest accuracies in each HCA cluster are from different combined methods. For datasets based on peak areas (A_B or A_T), the modpoly_MSC combination shows the lowest accuracy. MSC normalizes variations across the entire spectrum, which, while eliminating scatter effects, may diminish variations crucial for class discrimination in aging classification. Modpoly and imodpoly, designed to eliminate baseline variations, might lose discriminatory information when followed by MSC. Additionally, combining DP methods can result in an overly complex model, leading to overfitting and loss of important classification information.

For indices based on A_{ALI} , the asls_MC combination results in the lowest accuracy. Individually, asls decreased accuracy, and MC was either ineffective or slightly improved accuracy, but their combination significantly reduced accuracies. For indices based on A_{TOTAL} , the 8points_NMO method exhibited the lowest accuracy. While the 8points method individually performed poorly, its combination with NMO further reduced the final classification performance. Although baseline correction is crucial for compensating known physical artifacts, an improperly selected correction method, such as one with limited adaptability to local variations (e.g., 8points), may inadvertently distort relevant spectral information. These findings suggest that not all baseline correction methods are equally effective, and in some cases, the artifacts introduced by the correction process can outweigh the benefits of normalization. This emphasizes the importance of selecting baseline correction techniques appropriate to the spectral characteristics and analytical objectives.

To sum up, the impact of combining BDPs and NDPs on classification depends on the specific techniques used and can either enhance or weaken post-processing quality. It is advisable to use appropriate NDPs, which resulted in higher classification accuracies, such as NMO and RS for A_B and A_B/A_{TOTAL} , and NCV for A_T and A_T/A_{TOTAL} , or BDPs like aspls, rather than combined methods, to minimize unnecessary computational expenses. While reproducing the full evaluation may not always be practical, the findings suggest that assessing preprocessing techniques relative to the classification task and dataset remains important for ensuring reliable analysis.

Table 3.6 Upper and lower aging classification accuracy limits for the combination of NDPs and BDPs are provided, alongside raw data accuracies. The HCA dendrogram for the entire accuracy dataset (Table 1S, Appendix of chapter 3) is included for the clustering analysis of peak areas and indices.

Accuracy rank	A_B/A_{ALI}	A_T/A_{ALI}	A_T/A_{TOTAL}	A_B/A_{TOTAL}	A_B	A_T
Max	aspls_NMO 0.81 ± 0.02	aspls_NMO 0.80 ± 0.03	aspls_NMO 0.81 ± 0.02	aspls_NMO 0.81 ± 0.02	aspls_NMO 0.83 ± 0.03	aspls_NMO 0.83 ± 0.03
Raw data	0.79 ± 0.02	0.77 ± 0.03	0.75 ± 0.03	0.79 ± 0.02	0.79 ± 0.02	0.75 ± 0.03
Min	asls_MC 0.71 ± 0.01	asls_MC 0.72 ± 0.01	8points_NMO 0.72 ± 0.02	8points_NMO 0.72 ± 0.01	modpoly_MSC 0.73 ± 0.04	modpoly_MSC 0.70 ± 0.06

3.8.3 Influential spectral regions for aging classification of peak areas/indices

To determine the influential regions in bituminous binder spectra affecting PLSDA classification of aging, VIP scores for each peak region were calculated. VIP scores, which indicate the contribution of various features to the PLSDA modelling, were categorized into high, moderate, and low importance groups using thresholds of 1 and 0.7 [54]. This comparative analysis identified key regions for aging classification. Figure 3.12 shows VIP scores derived from classification using all peak areas and indices calculated from raw spectral data, revealing significant variability in scores based on the calculation method and region selection. Notably, the carbonyl region consistently attained the highest VIP score for aging classification when analysed using A_B , A_T , and the A_{ALI} -based indices. High VIP scores were also observed in the hydroxyl and fingerprint regions for indices-based classification, whereas the sulfoxide region demonstrated lower discriminatory power, particularly for A_B/A_{ALI} and A_T/A_{ALI} indices.

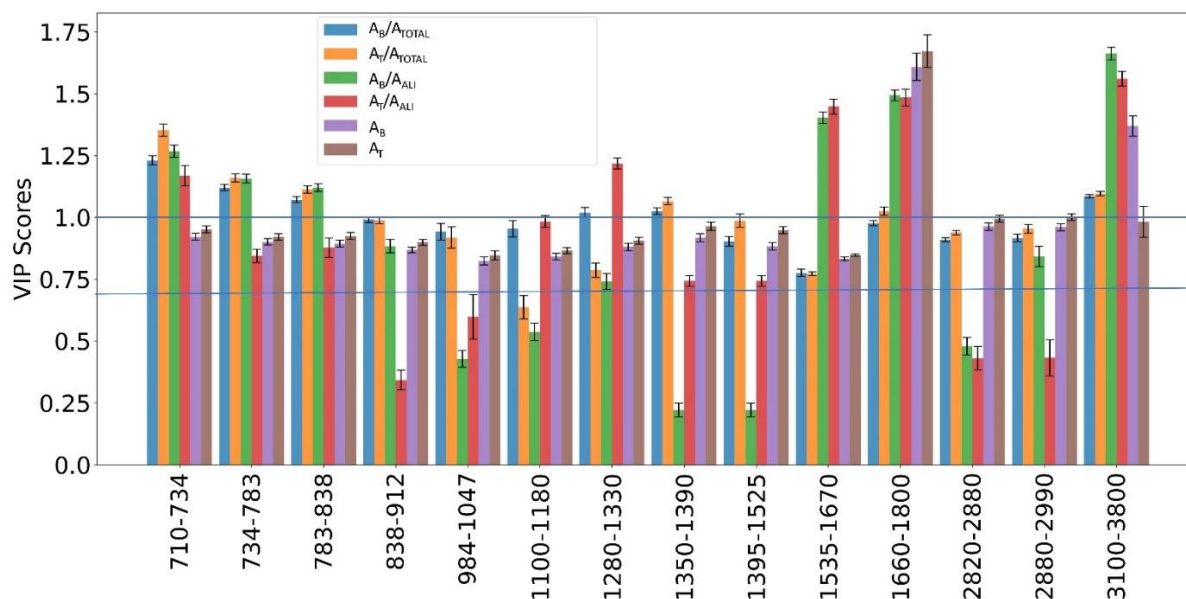


Figure 3.12 VIP scores of different regions in the PLSDA classification of aging on peak areas and indices of raw spectral. This study employs threshold values of 1 and 0.7 to categorize features into highly, moderately, and lowly important groups.

Figure 3.13 illustrates VIP scores for each peak region after applying DP methods, using classification scenarios with the highest accuracy: NMO and RS for A_B and A_B/A_{TOTAL} , NCV for A_T and A_T/A_{TOTAL} , and aspls for both A_B and A_T . To improve clarity and facilitate interpretation of the VIP score results, a summary table (Table 3.7) has been included below the figure. This table outlines the data preprocessing methods and area or index calculation strategies that yielded the highest classification performance and were therefore used in the VIP score analysis (Figure 3.13). Each row corresponds

to a specific combination of area/index type and the associated normalization or baseline correction method. The final column links these combinations to the corresponding panel in Figure 3.13. This structured overview is intended to reduce ambiguity and eliminate the need for repeated cross-referencing between the text and previous sections. It also helps the reader understand the rationale behind the selection of preprocessing conditions for the VIP analysis.

Table 3.7 Summary of data preprocessing methods and corresponding area/index calculation methods with highest classification performance used in VIP score analysis (Figure 3.13).

Area/index calculation	Normalization Method	Baseline-Correction Method	Figure Panel
$A_B, A_B/A_{TOTAL}$	NMO, RS	None	Fig. 3.13a & 3.13b
$A_T, A_T/A_{TOTAL}$	NCV	None	Fig. 3.13c
A_B, A_T	None	aspls	Fig. 3.13d
$A_B/A_{TOTAL}, A_T/A_{TOTAL}$	As above (NMO, RS, NCV)	None	Included in a–c

The VIP scores for each peak region is based on classification between fresh and aged bitumen samples. This classification framework, which has been applied throughout this chapter, is based on a binary grouping of samples: unaged and laboratory aged materials. The VIP scores identify which spectral regions contribute most significantly to this classification, and thus indicate which chemical changes are most informative for distinguishing aged from fresh binders for each pre-processing method. The results in Figure 3.13 are based on data pre-processed using the methods that gave the highest classification accuracy (as summarised in Table 3.7).

For NMO-based A_B (Figure 3.13 a), the regions 1280-1330 cm^{-1} , 1350-1395 cm^{-1} , and 1535-1670 cm^{-1} exhibit the highest VIP scores, indicating their significant contribution to aging classification. These regions correspond to various functional groups (Table 3.4), including branched aliphatic structures (CH_3) and aromatic structures ($\text{C}=\text{C}$ bonds), which play crucial roles in bituminous binder's aging behaviour [3]. This is expected, as oxidation during aging leads to the formation of oxygen-containing functional groups and the rearrangement of aromatic structures, altering the chemical and physical properties of the binder. Additionally, the regions 710-912 cm^{-1} , 1100-1180 cm^{-1} , and 2820-2880 cm^{-1} also show high importance. The 710-912 cm^{-1} region corresponds to bending vibrations of aromatic C-H bonds, which increase in intensity due to oxidation-induced aromatization. The 1100-1180 cm^{-1} region includes vibrations from sulfoxide groups ($\text{S}=\text{O}$), known markers of oxidative aging in bitumen. Interestingly, the 2820-2880 cm^{-1} region, associated with aliphatic C-H stretching, likely reflects the degradation of saturates, which decrease during oxidative aging. Interestingly, the 2880-2990 cm^{-1} region has the lowest impact, suggesting that CH_2 asymmetric stretching is less sensitive to aging, likely because these bonds remain relatively unchanged compared to more reactive functional groups. Other regions, such as sulfoxide, carbonyl, and hydroxyl, have moderate influence.

For NMO-based A_B/A_{TOTAL} indices, the highest VIP scores are in the 2820-2880 cm^{-1} and 2880-2990 cm^{-1} regions, associated with aliphatic C-H stretching. The prominence of these regions suggests that changes in aliphatic structures play a crucial role in the classification of aged binders when using A_B/A_{TOTAL} indices. The fingerprint region (710-912 cm^{-1}) and aromatic and carbonyl regio also exhibits high scores, emphasizing the role of structural rearrangements and compound oxidation in aging classification. Conversely, the regions 1350-1390 and 1395-1525 cm^{-1} (aliphatic C-H structure bending) exhibit the lowest contribution. This difference highlights the sensitivity of stretching vibrations to molecular alterations due to aging processes like oxidation. Stretching vibrations involve changes in bond length and are more responsive to these modifications, whereas bending vibrations,

which entail changes in bond angles, are generally less influenced by chemical alterations compared to stretching vibrations [68]. Other regions, such as sulfoxide, sulfones, and hydroxyl regions, hold a moderate impact on aging classification.

In RS-based A_B (Figure 3.13b), the 2820-2880 cm^{-1} and 2880-2990 cm^{-1} regions remain dominant, reinforcing the significance of aliphatic C-H stretching in aging classification. Additionally, the aromatic (C=C) and carbonyl (C=O) regions show high VIP scores, consistent with aging-induced aromatization and carbonyl formation due to oxidative degradation of binder components. The hydroxyl region shows the least contribution, likely because hydroxyl (-OH) formation is less extensive compared to carbonyl and sulfoxide formation in oxidative aging. Other regions have moderate impact. Similar to NMO patterns are observed for RS-based A_B/A_{TOTAL} indices.

For A_T/A_{TOTAL} based on NCV-modified spectra (Figure 3.13c), the fingerprint region exhibits the highest VIP score. This suggests that NCV normalization enhances the contribution of structural changes in the fingerprint region to classification accuracy. The 1350-1390 cm^{-1} region, which includes aliphatic CH bending, also has a relatively high contribution, possibly due to its role in distinguishing different oxidation levels. The hydroxyl and carbonyl regions contribute significantly, reinforcing the role of oxidation products in aging classification. In contrast, the sulfone region shows the lowest contribution. This aligns with expectations, as sulfones ($\text{S}=\text{O}_2$) form in relatively small amounts compared to sulfoxides ($\text{S}=\text{O}$), making them less impactful in classification. Other regions such as sulfoxide, aromatic, 2820-2990, and 1280-1330 cm^{-1} have moderate impact. Similar results were obtained for NCV-modified A_T .

For aspls-modified A_B and A_T (Figure 3.13d), only the carbonyl and aromatic regions have VIP scores above 1, demonstrating their significant contribution in aging classification. The low contribution of the hydroxyl region suggests that hydroxyl-containing aging products do not significantly impact classification when using aspls-modified data. Other regions, including sulfoxide, sulfone, fingerprint, and 2820-2990 and 1280-1525 cm^{-1} , have moderate VIP scores, indicating that while they contribute to classification, they are not as dominant as carbonyl and aromatic groups. This finding aligns with the VIP scores observed for raw data. Thus, it can be inferred that implementing the aspls modification has the potential to enhance the accuracy of peak area-based classification while maintaining the region's importance similar to the original data. The VIP scores for A_B and A_B/A_{TOTAL} indices indicate that calculating indices diminishes the significance of the aliphatic region (1350-1525 cm^{-1}) compared to A_B calculation. This is reasonable since indices normalize peak areas relative to total spectral features, minimizing the individual contribution of aliphatic CH bending. For A_T and A_T/A_{TOTAL} indices, there is no observable difference in scores for all spectral regions. Normalization methods and index calculations can alter the significance of various regions, highlighting the importance of methodological choices in aging classification.

In summary, the key regions for aging classification depend on the chosen normalization or baseline correction method, the approach to peak area or index calculation, and the underlying chemistry of aging. The results align with established knowledge of oxidative aging, where carbonyl and aromatic regions are the most significant markers, while sulfoxides and aliphatics also contribute to varying extents. Stretching vibrations (C-H, C=O, C=C) are more responsive to molecular changes than bending vibrations, making them more useful for classification. This highlights the importance of selecting appropriate data processing methods to enhance classification accuracy while preserving meaningful chemical information.

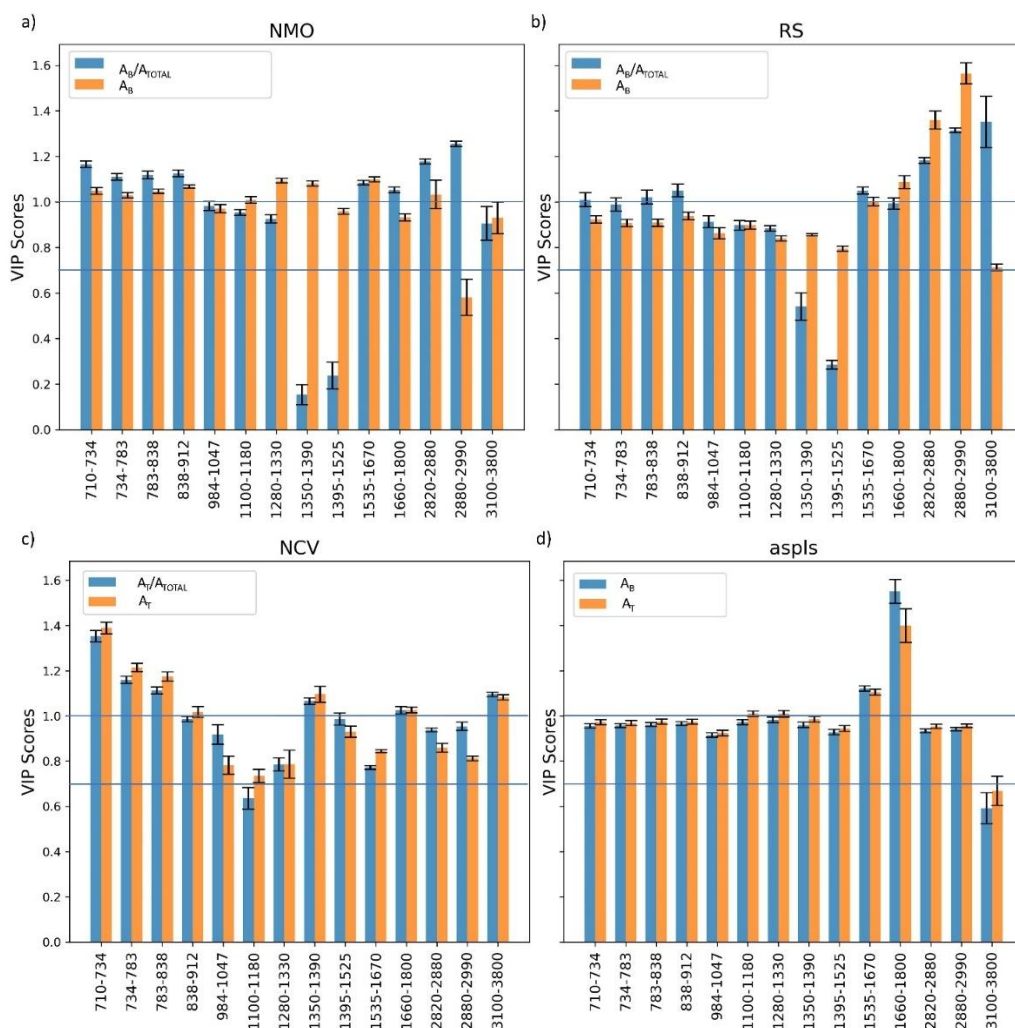


Figure 3.13 VIP scores of different regions in the PLSDA classification of aging on, a) NMO-modified A_B and A_B/A_{TOTAL} indices, b) RS-modified A_B and A_B/A_{TOTAL} indices, C) NCV-modified A_T and A_T/A_{TOTAL} , d) aspls-modified A_B and A_T . This study employs threshold values of 1 and 0.7 to categorize features into highly, moderately, and lowly important groups.

3.8.4 Effect of DPs on entire and first derivative spectra for aging classification

As previously mentioned in the introduction, research of bituminous binders using chemometrics often concentrates on entire spectra or their first derivatives. Working with derivative spectra can be particularly useful in addressing challenges such as overlapping peaks in FTIR, as it enhances spectral resolution and helps distinguish closely positioned absorption bands [11]. Consequently, this work investigated the impact of DP methods on the classification utilizing both the entire spectra and its first derivative (Figure 3.14).

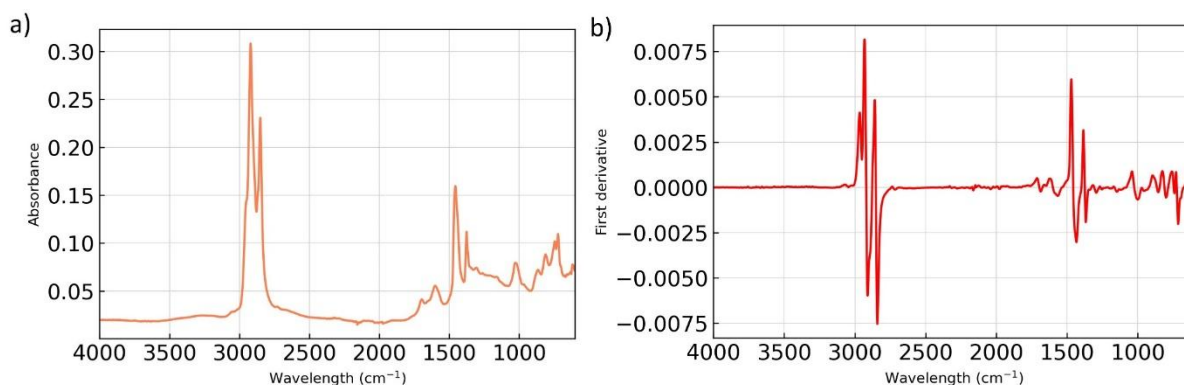


Figure 3.14 Representative spectrum before the implementation of DPs, a) raw FTIR spectrum, b) first derivative spectrum.

Table 3.8 lists the classification accuracies for the entire spectra with and without DPs. Results show that the accuracy of 80% for the entire raw spectra is nearly identical to the value of 79% when using peak area or index parameters calculated based on raw spectra. However, the influence of DP methods is more pronounced for the entire spectra compared to the classification based on peak area or index.

The baseline correction methods applied to the entire spectra did not significantly improve PLSDA performance, likely due to the minimal impact of baseline distortions on the overall spectral shape and pattern. Only the `pspline_asls` method showed a slight increase in accuracy for the entire spectra by correcting baseline distortions and improving peak measurement accuracy [69]. This method's improvement in spectra quality can enhance classification performance. However, when `pspline_asls` was used for peak area and index calculation, a lower accuracy was observed, as shown in Figure 3.9. This is because `pspline_asls` focuses on correcting distortions rather than the peak shapes crucial for classification.

For the entire spectra, the NDPs with the highest accuracies were autoscaling (AS), Pareto scaling (PS), and standard normal variate (SNV) methods, which effectively normalize data and reduce variations in absolute intensity levels [70]. Autoscaling and Pareto scaling [71] also minimize noise impact and highlight relevant spectral features by dividing by the standard deviation. However, these methods had less impact on peak area/indices-based classification, as shown in Figure 3.11, possibly due to their specific effectiveness in normalizing intensity levels rather than affecting peak regions significantly. When combined DP methods were applied to the entire spectra, the highest accuracy reached 0.87 ± 0.02 , comparable to normalization methods alone. However, the `poly_MC` method decreased PLSDA accuracy for the entire spectra, showing limited individual impact and poorer results when combined.

Table 3.8 also shows classification accuracies for the first derivatives of FTIR spectra affected by DP methods. Baseline correction applied to the entire spectra, or their first derivatives did not significantly enhance PLSDA performance. For first derivative spectra classification, autoscaling (AS), robust scaling (RS), and standard normal variate (SNV) methods again showed the highest accuracies. The `poly_MC` and `asls_MC` methods reduced PLSDA accuracy when applied to the entire spectra and its first derivative, respectively, indicating limited individual influence and even poorer results when combined.

Table 3.8 PLSDA aging classification accuracies for the entire and first derivative spectra in their raw form, after normalization, baseline correction, and using the top three accuracies along with the lowest accuracy achieved through the combination of NDPs and BDPs.

Entire spectra					
Baseline-correction method	Accuracy	Normalization method	Accuracy	Combined BDP and NDP methods	Accuracy
				Max accuracy	
asls	0.81 ± 0.02	NTS	0.82 ± 0.02	poly_RS	0.87 ± 0.02
aspls	0.80 ± 0.02	NCV	0.83 ± 0.02		
imodpoly	0.82 ± 0.01	NMO	0.84 ± 0.02	pspline_asls_RS	0.87 ± 0.02
modpoly	0.82 ± 0.02	MC	0.82 ± 0.02		
poly	0.78 ± 0.02	AS	0.86 ± 0.01	8points_RS	0.87 ± 0.02
pspline_asls	0.84 ± 0.02	PS	0.85 ± 0.02		
pspline_airpls	0.81 ± 0.02	RS	0.84 ± 0.02	Min accuracy	Accuracy
airpls	0.81 ± 0.02	SNV	0.86 ± 0.01	poly_MC	0.77 ± 0.02
8points	0.82 ± 0.02	MSC	0.84 ± 0.02		
raw_data: 0.80 ± 0.02					
First derivative spectra					
Baseline-correction method	Accuracy	Normalization method	Accuracy	Combined BDP and NDP methods	Accuracy
				Max accuracy	
asls	0.82 ± 0.02	NTS	0.82 ± 0.02	asls_NTS	0.87 ± 0.02
aspls	0.82 ± 0.02	NCV	0.86 ± 0.02		
imodpoly	0.83 ± 0.02	NMO	0.86 ± 0.02	asls_NCV	0.87 ± 0.02
modpoly	0.83 ± 0.02	MC	0.82 ± 0.02		
poly	0.82 ± 0.02	AS	0.87 ± 0.02	modpoly_NTS	0.87 ± 0.02
pspline_asls	0.82 ± 0.02	PS	0.83 ± 0.02		
pspline_airpls	0.82 ± 0.02	RS	0.87 ± 0.02	Min accuracy	Accuracy
airpls	0.82 ± 0.02	SNV	0.87 ± 0.02	asls_MC	0.82 ± 0.02
8points	0.82 ± 0.02	MSC	0.86 ± 0.02		
First derivative data: 0.82 ± 0.02					

In light of these findings, it is advisable to exclusively employ appropriate normalization methods (SNV, AS, PS, and RS) for both entire spectra and their first derivative datasets.

3.9 Conclusions

In conclusion, the impact of BDPs on classification accuracy varies, leading to both improvements and reductions. The selection of BDPs should be guided by the dataset's specific characteristics and the objectives of the classification task. However, to ensure methodological consistency and comparability across studies, it is advisable to base the selection on generalizable findings, such as those demonstrated here for aging classification, rather than performing a full optimization for each dataset. A detailed analysis may be justified in studies with unique sample characteristics or classification goals, but for broader applications, adopting processing strategies that have shown consistent high classification accuracies may offer a practical compromise between performance and comparability (RSQ1, RSQ2).

Moreover, the impact of normalization methods proves to be dependent on the specific objectives of the study and the calculation method for input data (whether it involves peak areas, indices, entire spectra, or their first derivative). Furthermore, the combination of normalization and baseline correction methods can yield diverse outcomes, dependent on the specific DP methods and input datasets employed (RSQ2).

Analysing the significance of different spectral regions for classification, the variable importance in projection (VIP) scores indicated that regions like carbonyl and sulfoxide are crucial, although their importance can change with different pre-treatment methods. Normalization methods and index calculations can alter the significance of various regions, highlighting the importance of methodological choices in aging classification. Relying solely on common practices of focusing on carbonyl and sulfoxide may not provide sufficient discrimination for multivariate analysis (RSQ4).

Based on the findings of this study, the comparison between the performance of entire spectra/first derivative and indices/peak areas showed that using entire/first derivative spectra yields higher classification accuracy, indicating greater informativeness. This finding supports the use of these approaches for future aging-related chemometric analyses (RSQ5).

Regarding the most suitable method for calculating peak areas or aging indices, the findings indicate that indices based on A_{TOTAL} outperform A_{ALL} -based indices and peak areas (either A_T or A_B) when subjected to different DP methods. The choice between A_T/A_{TOTAL} and A_B/A_{TOTAL} depends on the study's goal. For investigations aiming to use diverse data sources and recognize gradual changes across all sources (like aging), A_B/A_{TOTAL} indices are recommended. Thus, this calculation method will be used in the following chapters of this thesis (RSQ3).

Furthermore, the investigation into whether a single pre-processing method could be universally effective showed that the effectiveness of pre-processing methods is dependent on various factors. These factors include the specific classification goal (e.g., aging studies), the characteristics of the dataset, and the methods employed (peak areas, indices, entire spectra, or their first derivative). It is crucial to align the choice of DP methods with specific characteristics of the input dataset and the objectives of the classification study. Additionally, to choose the best DP methods rapidly and efficiently for a given study, multivariate analysis tools like PLS-DA are necessary. Among the methods employed in this research, it is advisable to include NCV, NMO, RS, and NTS methods for peak area or indices-based classification. For entire spectra and first derivative, NTS, NCV, AS, PS, and SNV methods are recommended. On the other hand, MC and poly methods showed poor performance in both classification analyses, so they are recommended to be excluded from future analyses. Lastly, aspls is a suitable option for studies focusing on gradual material changes, such as multi-level aging studies (RSQ2).

In summary, this study provides a comprehensive evaluation of DP methods for spectral data classification, offering valuable insights into selecting appropriate pre-treatment strategies to enhance classification accuracy. By identifying the most effective methods for aging classification, researchers can design more accurate and efficient experiments, optimize resource allocation and reduce operational risks. This targeted approach ensures reliable and robust classification outcomes, contributing to more efficient research and development processes in the field of bituminous binder analysis.

3.10 References

1. Costanzi, M. and D. Cebon, *Generalized phenomenological model for the viscoelasticity of bitumen*. Journal of Engineering Mechanics, 2015. **141**(5): p. 04014160.
2. Hofko, B., et al., *Repeatability and sensitivity of FTIR ATR spectral analysis methods for bituminous binders*. Materials and Structures, 2017. **50**: p. 1-15.
3. Mirwald, J., et al., *Understanding bitumen ageing by investigation of its polarity fractions*. Construction and Building Materials, 2020. **250**: p. 118809.
4. Brereton, R.G., *Chemometrics for pattern recognition*. 2009: John Wiley & Sons.
5. Fringeli, U., *ATR and reflectance IR spectroscopy, applications*. Encyclopedia of spectroscopy and spectrometry, 2000: p. 115-129.
6. Hofko, B., et al. *Alternative approach toward aging of bitumen and asphalt mixes*. in *Proceedings of the Transport Research Board 94th Annual Meeting*. 2015.

7. Eberhardsteiner, L., et al., *Towards a microstructural model of bitumen ageing behaviour*. International Journal of Pavement Engineering, 2015. **16**(10): p. 939-949.
8. Lamontagne, J., et al., *Comparison by Fourier transform infrared (FTIR) spectroscopy of different ageing techniques: application to road bitumens*. Fuel, 2001. **80**(4): p. 483-488.
9. Gaffney, J.S., N.A. Marley, and D.E. Jones, *Fourier transform infrared (FTIR) spectroscopy*. Characterization of materials, 2002: p. 1-33.
10. Smith, B.C., *Fundamentals of Fourier transform infrared spectroscopy*. 2011: CRC press.
11. Lee, L.C., C.-Y. Liong, and A.A. Jemain, *A contemporary review on Data Preprocessing (DP) practice strategy in ATR-FTIR spectrum*. Chemometrics and Intelligent Laboratory Systems, 2017. **163**: p. 64-75.
12. Chalmers, J.M., H.G. Edwards, and M.D. Hargreaves, *Vibrational spectroscopy techniques: basics and instrumentation*. Infrared and Raman spectroscopy in forensic science, 2012: p. 9-44.
13. Sun, D.-W., *Infrared spectroscopy for food quality analysis and control*. 2009: Academic press.
14. Khalighi, S., et al., *Evaluating the impact of data pre-processing methods on classification of ATR-FTIR spectra of bituminous binders*. Fuel, 2024. **376**: p. 132701.
15. Nivitha, M., E. Prasad, and J. Krishnan, *Ageing in modified bitumen using FTIR spectroscopy*. International Journal of Pavement Engineering, 2016. **17**(7): p. 565-577.
16. Rinnan, Å., F. Van Den Berg, and S.B. Engelsen, *Review of the most common pre-processing techniques for near-infrared spectra*. TrAC Trends in Analytical Chemistry, 2009. **28**(10): p. 1201-1222.
17. Ma, L., et al., *Chemical characterisation of bitumen type and ageing state based on FTIR spectroscopy and discriminant analysis integrated with variable selection methods*. Road Materials and Pavement Design, 2023: p. 1-15.
18. Primerano, K., et al., *Characterization of long-term aged bitumen with FTIR spectroscopy and multivariate analysis methods*. Construction and Building Materials, 2023. **409**: p. 133956.
19. Garmarudi, A.B., et al., *Origin based classification of crude oils by infrared spectrometry and chemometrics*. Fuel, 2019. **236**: p. 1093-1099.
20. Weigel, S. and D. Stephan, *The prediction of bitumen properties based on FTIR and multivariate analysis methods*. Fuel, 2017. **208**: p. 655-661.
21. Weigel, S. and D. Stephan, *Bitumen characterization with Fourier transform infrared spectroscopy and multivariate evaluation: prediction of various physical and chemical parameters*. Energy & fuels, 2018. **32**(10): p. 10437-10442.
22. Kessler, W., *Multivariate datenanalyse: für die pharma, bio-und Prozessanalytik*. 2011: John Wiley & Sons.
23. Wieser, M., et al., *Assessment of aging state of bitumen based on peak-area evaluation in infrared spectroscopy: Influence of data processing and modeling*. Construction and Building Materials, 2022. **326**: p. 126798.
24. Engel, J., et al., *Breaking with trends in pre-processing?* TrAC Trends in Analytical Chemistry, 2013. **50**: p. 96-106.
25. Lee, L.C., C.-Y. Liong, and A.A. Jemain, *Partial least squares-discriminant analysis (PLS-DA) for classification of high-dimensional (HD) data: a review of contemporary practice strategies and knowledge gaps*. Analyst, 2018. **143**(15): p. 3526-3539.
26. Yang, J. and J.-y. Yang, *Why can LDA be performed in PCA transformed space?* Pattern recognition, 2003. **36**(2): p. 563-566.
27. Barker, M. and W. Rayens, *Partial least squares for discrimination*. Journal of Chemometrics: A Journal of the Chemometrics Society, 2003. **17**(3): p. 166-173.
28. Nocairi, H., et al., *Discrimination on latent components with respect to patterns. Application to multicollinear data*. Computational statistics & data analysis, 2005. **48**(1): p. 139-147.

29. Ren, S., et al., *Aging and rejuvenation effects on the rheological response and chemical parameters of bitumen*. *Journal of materials research and technology*, 2023. **25**: p. 1289-1313.
30. Tarsi, G., et al., *Effects of different aging methods on chemical and rheological properties of bitumen*. *Journal of Materials in Civil Engineering*, 2018. **30**(3): p. 04018009.
31. Mocetti, F., *Characterization of moisture susceptibility of asphaltic bitumen*, in *Context-Sensitive Design in Transportation Infrastructures*. 2015, University of Bologna and TUDelft.
32. EN 12607-1, C., *12607-1: Bitumen and Bituminous Binders—Determination of the Resistance to Hardening under Influence of Heat and Air—Part 1: RTFOT Method*. European Committee for Standardization: Brussels, Belgium, 2014.
33. EN 14769, C., *14769: Bitumen and Bituminous Binders—Accelerated Long-Term Ageing Conditioning by a Pressure Ageing Vessel (PAV)*. European Committee for Standardization: Brussels, Belgium, 2012.
34. Porot, L., et al., *Fourier-transform infrared analysis and interpretation for bituminous binders*. *Road Materials and Pavement Design*, 2023. **24**(2): p. 462-483.
35. Erb, D., *pybaselines: A Python library of algorithms for the baseline correction of experimental data*. 2024.
36. Erb, D. *pybaselines Documentation, Release 1.1.0*. 2024; Available from: <https://pybaselines.readthedocs.io/en/latest/introduction.html>.
37. Lee, L.C., C.-Y. Liong, and A.A. Jemain, *Effects of data pre-processing methods on classification of ATR-FTIR spectra of pen inks using partial least squares-discriminant analysis (PLS-DA)*. *Chemometrics and Intelligent Laboratory Systems*, 2018. **182**: p. 90-100.
38. Lasch, P., *Spectral pre-processing for biomedical vibrational spectroscopy and microspectroscopic imaging*. *Chemometrics and Intelligent Laboratory Systems*, 2012. **117**: p. 100-114.
39. Hastie, T., R. Tibshirani, and J. Friedman, *The wrong and right way to do cross-validation*. *The Elements of Statistical Learning: Data Mining, Inference, and Prediction*, 2009: p. 245-247.
40. Jing, R., et al., *Ageing effect on chemo-mechanics of bitumen*. *Road Materials and Pavement Design*, 2021. **22**(5): p. 1044-1059.
41. Kumar, N., et al., *Chemometrics tools used in analytical chemistry: An overview*. *Talanta*, 2014. **123**: p. 186-199.
42. Trevisan, J., et al., *Extracting biological information with computational analysis of Fourier-transform infrared (FTIR) biospectroscopy datasets: current practices to future perspectives*. *Analyst*, 2012. **137**(14): p. 3202-3215.
43. Serrano-Cinca, C. and B. Gutiérrez-Nieto, *Partial least square discriminant analysis for bankruptcy prediction*. *Decision support systems*, 2013. **54**(3): p. 1245-1255.
44. Barker, M., *Partial least squares for discrimination: statistical theory and implementation*. 2010: LAP Lambert Academic Publishing.
45. Wu, L., et al., *Recent advancements in detecting sugar-based adulterants in honey—A challenge*. *TrAC Trends in Analytical Chemistry*, 2017. **86**: p. 25-38.
46. Manheim, J., et al., *Forensic hair differentiation using attenuated total reflection Fourier transform infrared (ATR FT-IR) spectroscopy*. *Applied spectroscopy*, 2016. **70**(7): p. 1109-1117.
47. Custódio, M.F., et al., *Identification of synthetic drugs on seized blotter papers using ATR-FTIR and PLS-DA: Routine application in a forensic laboratory*. *Journal of the Brazilian Chemical Society*, 2021. **32**: p. 513-522.
48. Boulesteix, A.-L., *PLS dimension reduction for classification with microarray data*. *Statistical applications in genetics and molecular biology*, 2004. **3**(1).
49. Yates, L.A., et al., *Cross validation for model selection: a review with examples from ecology*. *Ecological Monographs*, 2023. **93**(1): p. e1557.

50. Stone, M., *Cross-validation: A review*. *Statistics: A Journal of Theoretical and Applied Statistics*, 1978. **9**(1): p. 127-139.
51. Refaeilzadeh, P., L. Tang, and H. Liu, *Cross-validation*, in *Encyclopedia of database systems*. 2009, Springer. p. 532-538.
52. He, H. and Y. Ma, *Imbalanced learning: foundations, algorithms, and applications*. 2013.
53. Kubinyi, H., *3D QSAR in drug design: volume 1: theory methods and applications*. Vol. 1. 1993: Springer Science & Business Media. 523-550 p.
54. Zheng, R., et al., *Variable importance for projection (VIP) scores for analyzing the contribution of risk factors in severe adverse events to Xiyanping injection*. *Chinese Medicine*, 2023. **18**(1): p. 15.
55. Siroma, R.S., et al., *Clustering aged bitumens through multivariate statistical analyses using phase angle master curve*. *Road Materials and Pavement Design*, 2021. **22**(sup1): p. S51-S68.
56. Saraf, R. and S. P Patil, *Study Paper on How to Read a Dendrogram*. *International Journal of Computer Applications*, 2014. **103**(6): p. 8-11.
57. Newey, W.K. and J.L. Powell, *Asymmetric least squares estimation and testing*. *Econometrica: Journal of the Econometric Society*, 1987: p. 819-847.
58. Zhang, F., et al., *Baseline correction for infrared spectra using adaptive smoothness parameter penalized least squares method*. *Spectroscopy Letters*, 2020. **53**(3): p. 222-233.
59. Zhang, F., et al., *An automatic baseline correction method based on the penalized least squares method*. *Sensors*, 2020. **20**(7): p. 2015.
60. Butler, H.J., et al., *Optimised spectral pre-processing for discrimination of biofluids via ATR-FTIR spectroscopy*. *Analyst*, 2018. **143**(24): p. 6121-6134.
61. Yu, H.-G., et al. *Noise reduction for improving the performance of gas detection algorithms in the FTIR spectrometer*. in *Algorithms and Technologies for Multispectral, Hyperspectral, and Ultraspectral Imagery XXIV*. 2018. SPIE.
62. Lieber, C.A. and A. Mahadevan-Jansen, *Automated method for subtraction of fluorescence from biological Raman spectra*. *Applied spectroscopy*, 2003. **57**(11): p. 1363-1367.
63. Zhao, J., et al., *Automated autofluorescence background subtraction algorithm for biomedical Raman spectroscopy*. *Applied spectroscopy*, 2007. **61**(11): p. 1225-1232.
64. Hu, H., et al., *Improved baseline correction method based on polynomial fitting for Raman spectroscopy*. *Photonic Sensors*, 2018. **8**: p. 332-340.
65. Ying, X. *An overview of overfitting and its solutions*. in *Journal of physics: Conference series*. 2019. IOP Publishing.
66. Zhang, Z.-M., S. Chen, and Y.-Z. Liang, *Baseline correction using adaptive iteratively reweighted penalized least squares*. *Analyst*, 2010. **135**(5): p. 1138-1146.
67. Iglewicz, B. and D.C. Hoaglin, *Volume 16: how to detect and handle outliers*. 1993: Quality Press.
68. Dutta, A., *Fourier transform infrared spectroscopy*. *Spectroscopic methods for nanomaterials characterization*, 2017: p. 73-93.
69. Eilers, P. and B. Marx, *Splines, knots, and penalties*. *Wiley Interdisciplinary Reviews: Computational Statistics*, 2010. **2**: p. 637-653.
70. Xu, Y., et al., *Raman spectroscopy coupled with chemometrics for food authentication: A review*. *TrAC Trends in Analytical Chemistry*, 2020. **131**: p. 116017.
71. van den Berg, R.A., et al., *Centering, scaling, and transformations: improving the biological information content of metabolomics data*. *BMC Genomics*, 2006. **7**: p. 142.

4

Effect of aging factors on chemical properties of paving binders

This chapter² presents a detailed chemical analysis of the aging effects induced by various environmental factors on paving binders. The aim is to evaluate how different environmental factors impact the chemical properties of paving binders, with a particular focus on understanding the mechanisms behind the aging process. The chapter utilizes Fourier Transform Infrared (FTIR) spectroscopy to assess the changes in chemical structure caused by environmental stressors such as temperature, pressure, humidity, and exposure to reactive oxygen species (ROS).

The chapter explores the effects of these factors in a step-wise manner to gain a comprehensive understanding of their influence on paving binders. The chemical analysis is conducted using FTIR spectroscopy, with spectra pre-processed according to the methods outlined in Chapter 3. In section 4.5.1, the effects of hygrothermal, thermo-oxidative, and aqueous-thermal aging on paving binders are investigated under atmospheric pressure conditions. Building upon these results, section 4.5.2 extends the investigation by evaluating the impacts of various factors, including temperature, pressure, time, humidity, and sample thickness. Section 4.5.3 introduces a novel accelerated aging protocol, designed to simulate the effects of reactive oxygen species (ROS) in both liquid and gaseous forms. Additionally, field data (section 4.5.4) are incorporated to provide a direct comparison between field and laboratory aging, using new chemical indices and aging rates (section 4.6). This comparison enables the identification of laboratory conditions that best replicate field aging while ensuring optimal efficiency. In section 4.7, the challenge of overlapping peaks in FTIR spectra is addressed using a combination of deconvolution and dynamic time warping techniques, providing a more accurate analysis of the chemical changes occurring during aging. Section 4.8 provides a detailed discussion of the chemical aging mechanisms associated with the novel aging method introduced in section 4.5.3. Finally, Section 4.9 summarizes the key results and conclusions derived from this chapter.

² Apart from minor updates, this chapter has been published as " Khalighi, S., Erkens, S. and Varveri, A., 2024. Exploring the impact of humidity and water on bituminous binder aging: a multivariate analysis approach (TI CAB). *Road Materials and Pavement Design*, pp.1-25.

Khalighi, S., Ma, L., Mosleh, Y., van Lent, D. and Varveri, A., *Multivariate chemo-rheological framework for optimizing laboratory aging protocols of paving binders*, *Materials & Design*, 2024.

Khalighi, S., L. Ma, and A. Varveri, *Accelerated laboratory simulation of field aging for paving binders using hydrogen peroxide and UV light*. *Construction and Building Materials*. 2025."

4.1 Background

A thorough evaluation of binder aging under controlled laboratory conditions is essential to accurately approximate the aging behaviour of asphalt pavements in the field [1]. In real-world settings, bituminous binders are exposed to a range of environmental stressors, such as moisture, temperature variations, UV light, and reactive oxygen species, which are not fully captured in standard laboratory aging protocols. Different aging factors and the existing literature on their influence in aging studies of paving binders are discussed in Chapter 2. An effective aging protocol should incorporate these environmental factors and accelerate their effects to better simulate field conditions. However, before integrating these variables into laboratory protocols, it is crucial to assess their individual effects on binder properties to ensure an accurate representation of in-field aging mechanisms.

This chapter addresses the chemical changes of bituminous binders due to aging effects induced by various environmental factors. Bituminous binders experience complex chemical changes due to prolonged exposure to environmental factors such as temperature, pressure, moisture, and reactive oxygen species (ROS), each affecting the binder's composition and properties differently. By analysing the contributions of individual and combined environmental factors, this chapter introduces a novel, accelerated aging protocol. This protocol aims to provide a fast method for replicating real-world aging behaviours in bituminous binders.

4.2 Objectives and research structure

In this chapter, the following research sub-questions (RSQ) are addressed:

1. How do water molecules in liquid and vapor forms influence the aging of bituminous binders under different temperature and time conditions? (RQ1)³
2. What are the combined effects of moisture, temperature, pressure, film thickness, and aging time on the oxidation and degradation of bituminous binders from different sources? (RQ1 & 2)
3. How does the introduction of reactive oxygen species (ROS), specifically hydroxyl radicals generated through UV and hydrogen peroxide (H₂O₂), impact the oxidative aging of bituminous binders? How do key parameters of the UPA method, including H₂O₂ concentration, aging temperature, and aging time, affect its aging mechanism? (RQ1 & 2)
4. How does the UV-Peroxide Aging (UPA) protocol compare with standard aging methods in the efficiency of aging mechanisms? (RQ2)
5. How well do laboratory-aged binders, particularly those subjected to UPA and other efficient protocols, correlate with field-aged samples based on FTIR analysis and quantitative similarity assessments? (RQ2, 3 & 4)

The primary objective of this chapter is to examine the impact of environmental aging factors on the chemical composition of bituminous binders, with the aim of developing a laboratory aging method that accurately and fast simulates field aging. To achieve this objective, several research steps have been designed, each addressing a specific research question. These questions collectively contribute to the overarching goals of this thesis. Figure 4.1 illustrates the research steps and methodology applied in this chapter.

³ The references in parentheses show the link to the main Research Questions (RQ) of this thesis, as outlined in Chapter 1.

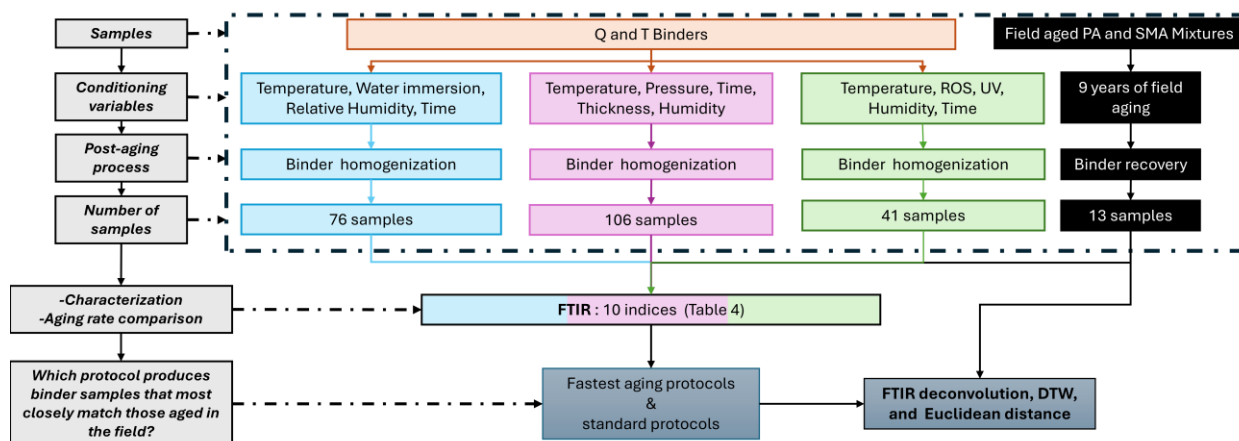


Figure 4.1 Schematic representation of the research methodology outlining the sequential steps undertaken to investigate the impact of environmental aging factors on the chemical composition of bituminous binders and the development of a laboratory aging method for accurate field aging simulation.

The first research question (RSQ 1) investigates the role of water molecules, both in liquid and vapor forms, in the aging of bituminous binders. This step aims to determine the extent to which moisture contributes to long-term binder aging under various temperature and time conditions. This is assessed relative to both unaged samples and samples aged under identical conditions but without the presence of humidity, which serve as reference points for isolating the effect of water. By analysing the influence of water, this chapter seeks to clarify its role in accelerating oxidative mechanisms. This investigation directly addresses RQ 1 by clarifying the role of moisture, an often-overlooked yet critical field variable, in accelerating oxidative mechanisms.

The second research question (RSQ 2) explores the combined effects of moisture, temperature, pressure, film thickness, and aging time on binder degradation. These factors are often interdependent in the field, yet are typically studied in isolation under laboratory conditions. This research step responds to RQ 1 by identifying the relative contributions and interactions of these environmental parameters, offering a more comprehensive view of aging under realistic scenarios. Furthermore, by understanding these interactions, the foundation is laid for designing more accurate and field-representative laboratory protocols, as explored in RQ 2.

The third research question (RSQ 3) focuses on the influence of reactive oxygen species (ROS), particularly hydroxyl radicals, on binder oxidation. The newly developed UV-Peroxide Aging (UPA) protocol combines UV light with hydrogen peroxide (H_2O_2) to generate hydroxyl radicals ($HO\bullet$ and $HO_2\bullet$), which are among the most reactive oxidative species. The combined use of UV and H_2O_2 has been widely implemented in environmental processes, such as wastewater treatment [2, 3], due to its ability to generate hydroxyl radicals, among the most powerful reactive species, with an oxidation potential of 2.8 V, surpassing that of ozone (2.1 V) [4]. Based on this, we anticipate that hydroxyl radicals generated from the photodecomposition of H_2O_2 under UV light may act as catalysts, accelerating the oxidation aging of bituminous binders. These radicals, which naturally occur in the field environment of asphalt pavements [5], offer a unique opportunity to simulate field-like aging mechanisms in the laboratory. To the best of our knowledge, the effect of hydroxyl radicals on bituminous binder aging has not been systematically investigated in the literature. This method introduces a liquid-phase oxidation mechanism, which may enhance the diffusion of oxidative agents into the binder matrix, leading to a more effective aging process. Additionally, the effects of key UPA parameters, including H_2O_2 concentration, aging temperature, and aging time, will be systematically evaluated to understand their influence on binder chemical property changes. This research step

supports RQ 1 by elucidating a potentially important chemical mechanism in binder oxidation and also contributes to RQ 2 by evaluating the UPA method as a novel protocol for simulating such mechanisms under controlled conditions.

The fourth research question (RSQ 4) focuses on comparing the efficiency of the UPA protocol with standard aging methods in replicating binder oxidation mechanisms. To assess the effectiveness, the oxidation behaviour of binders aged using UPA will be evaluated and compared to results obtained from conventional protocols such as the Pressure Aging Vessel (PAV) and Viennese Binder Aging (VBA). This comparison addresses RQ 2, which seeks to assess whether novel accelerated laboratory protocols can better replicate field aging than current methods. To establish the relevance of UPA, aging rates will be quantified using Fourier Transform Infrared Spectroscopy (FTIR) indices. These indices serve as chemical markers for oxidation and are used to compare the degree of aging across different protocols.

The final research question (RSQ 5) aims to validate the proposed protocol by evaluating the correlation between laboratory-aged binders and field-aged samples, with a particular focus on UPA and other efficient aging methods. The accuracy of different aging methods will be examined using Fourier Transform Infrared Spectroscopy (FTIR) spectra and quantitative similarity metrics. It supports RQ 2 by providing an evidence-based assessment of how well laboratory protocols reproduce field aging. Advanced analytical techniques, such as FTIR spectral deconvolution, Dynamic Time Warping (DTW), and Euclidean distance calculations, will be employed to quantify the degree of similarity between laboratory-aged and field-aged binders and contribute to RQ 3 and 4. This data-driven approach is intended to test whether laboratory protocols produce chemical alterations comparable to those observed in naturally aged binders, beyond individual functional group comparisons. This analysis aims to determine which laboratory protocol produces results most representative of real-world binder degradation.

Through these research steps, this chapter contributes to a detailed understanding of environmental aging factors and advances the development of more realistic and fast laboratory aging protocols. These findings not only inform the experimental design of subsequent chapters but also provide essential input to the multivariate analytical frameworks developed later in the thesis.

4.3 Materials and sample preparation

4.3.1 Materials

Binder PEN 70/100 is one of the most used bituminous binders for road construction in the Netherlands. In this research, two PEN 70/100 bituminous binders from two different suppliers (namely Q and Total) and thus from different crude oil sources were evaluated, named as Q and T, respectively. Table 4.1 shows the basic properties of the binders.

Table 4.1 Properties of Q 70/100 and T 70/100 in fresh (unaged) state.

Property		Q PEN 70/100	T PEN 70/100
Penetration at 25 °C (0.1mm)		70-100	70-100
Softening point (°C)		43-51	43-51
Complex shear modulus (G^* (kPa)) at 1.6 Hz & 60 °C		1.8	2.3
Phase angle (δ) at 1.6 Hz & 60 °C (°)		88	88
Elemental composition (%)	Nitrogen N	0.59	0.93
	Carbon C	79.19	87.23
	Hydrogen H	10.81	11.26
	Sulfur S	4.47	3.35

	Oxygen O	2.25	0.60
--	----------	------	------

4.3.2 Samples preparation

To prepare binder samples, 50 grams of fresh binder were poured onto pan with a diameter of 14.1 cm which yielded films of 3.2 mm in thickness. These pans were subjected to short-term aging using oven aging at a temperature of 163 °C for 5 hours, in line with the EN 12607-2 [6] standard. Short-term aged binder samples of 7.5, 15, and 22.5 grams were dispensed onto glass Petri dishes with a diameter of 9.6 cm to obtain target thicknesses of 1, 2, and 3.2 mm, respectively. Uniformity of the binder films was achieved by placing all petri-dishes in an oven at a temperature of 163 °C for 3 minutes. The entire process of sample preparation and aging is graphically depicted in Figure 4.2.

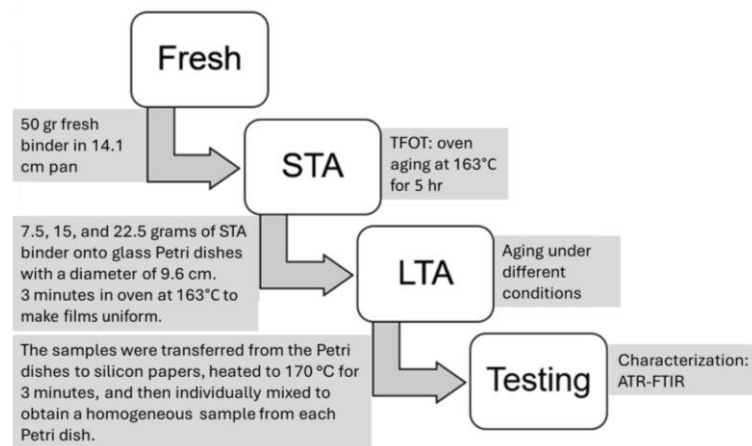


Figure 4.2 Workflow of sample preparation and experiments from fresh state to STA, then to LTA, and finally to characterization used for both Q and T binders.

4.3.3 Laboratory long-term aging method

To investigate the effects of different environmental aging factors on bituminous binders, a range of controlled laboratory aging protocols were employed. These protocols were designed to simulate various real-world aging conditions and systematically examine the impact of temperature, pressure, moisture, and oxidative agents. The aging methods can be categorized as follows:

Hygrothermal, thermo-oxidative, and aqueous-thermal aging

The experiment detailed in this section is conducted to investigate the first research question. Long-term aging was conducted using an oven and a climate chamber at three different temperatures: 60 °C, 70 °C, and 85 °C on 1mm binder films (Table 4.2). The thermo-oxidative aging was conducted in an oven with minimal humidity (<10% relative humidity (RH)) to simulate oxidative aging under dry conditions. hygrothermal aging was performed in a climate chamber at 95% relative humidity (RH) to assess the effect of moisture in vapor form. Figure 4.3b provides a graphical representation of the aging setup in the climate chamber. For aqueous-thermal aging samples were immersed in demineralized water within the climate chamber to examine the impact of liquid water exposure.

Each binder sample was prepared as a 1 mm thick film (Figure 4.3a) and aged for up to 21 days, with intermediate sampling at 1, 7, and 14 days. Unlike standard aging methods that accelerate oxidation using high pressure, this protocol relied on extended exposure durations under atmospheric pressure to mimic field conditions. After the aging process, samples were mixed and homogenized at 170 °C for 5 minutes to minimize potential aging gradients within the binder.

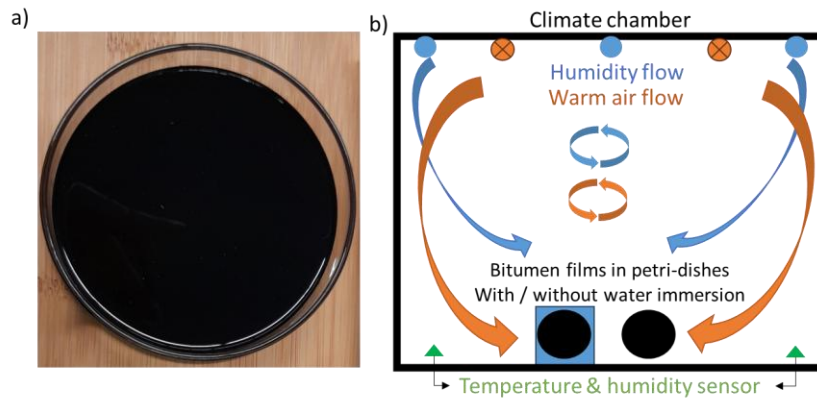


Figure 4.3 a) Bitumen film of 1 mm in a petri-dish, b) Climate chamber setup.

Table 4.2 Aging conditions for binder samples to evaluate effects of hygrothermal, thermo-oxidative, and aqueous-thermal aging.

Aging Protocol	Thickness (mm)	Temperature (°C)	Pressure (bar)	Time (days)	Humidity	# of samples
Thermo-Oxidative Aging	1	60, 70, 85	1	1, 7, 14, 21	RH<10%	24
Hygrothermal Aging	1	60, 70, 85	1	1, 7, 14, 21	RH>99%	24
Aqueous-Thermal Aging	1	60, 70, 85	1	1, 7, 14, 21	Liquid water	24

In this research, the naming convention for the samples is based on the type of binder and the specific aging conditions applied. Each sample undergoes different aging processes, denoted by labels such as STA (for short-term aged). The designation for long-term aged film samples follows a consistent format, comprising four parts: the first part indicates the binder type (Q or T), the second part represents the long-term aging temperature (60 °C, 70 °C, or 85 °C), the third part indicates the duration of aging (1, 7, 14, or 21 days), and the final part specifies the type of aging, including hygrothermal (RH), thermo-oxidative (O), and aqueous-thermal (W) aging (Figure 4.4). For instance, "Q-85C-14D-RH" signifies Q binder 1 mm films that underwent hygrothermal aging at 85 °C for 14 days.

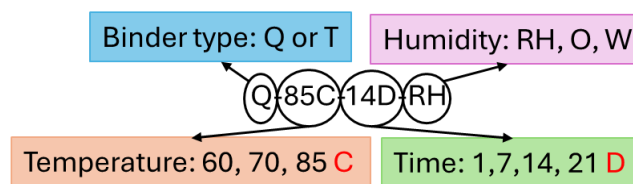


Figure 4.4 Annotation used for samples aged under hygrothermal, thermo-oxidative, and aqueous-thermal aging conditions.

Coupled aging of temperature, pressure, time, relative humidity, and thickness

For LTA, short-term aged binder underwent PAV treatment at varied conditions: temperatures (60, 70, 85°C), pressures (1, 5, 10, 20 bar), durations (5, 10, 20 hours), humidity levels (0 and 99% RH), and thicknesses (1, 2, 3.2 mm), across two binder types (Q and T) (Table 4.3). Additionally, the impact of extended hygrothermal aging was examined by subjecting 1mm binder films to prolonged exposure under hygrothermal conditions for 40 and 80 hours. To introduce humidity into the Pressure Aging Vessel (PAV), a quantity of 1000 grams of demineralized water at room temperature was utilized to create >99% relative humidity via evaporation (Appendix of chapter 4, Figure 1S). Further information regarding the humidity measurement in the PAV chamber can be found in the supporting information. To study the effect of extreme pressure, a custom-built oven was employed

to elevate the pressure within the aging environment to 150 bar. This chamber facilitated the investigation of the exceptionally high pressures effects on the aging characteristics of binders. Notably, due to limitations, moisture could not be introduced to this chamber, thereby restricting the experiment to thermo-oxidative conditions. Table 4.3 presents all testing conditions.

Table 4.3 Aging conditions for binder samples.

Aging Protocol	Thickness (mm)	Temperature (°C)	Pressure (bar)	Time (hour)	Humidity	# of samples
Modified PAV (PAV-MOD)	1, 2, 3.2	60, 70, 85	20	20	<10%, >99%	18
	1, 2, 3.2	85	1,5, 10,20	20	<10%, >99%	18+1
	1		150		<10%	
	1, 2, 3.2	85	20	5,10,20	<10%, >99%	18+2
	1			40,80	>99%	

The nomenclature of samples is based on their binder type and the specific aging conditions applied. The fresh and short-term aged binder samples are labelled as F and STA, respectively. The naming convention for long-term aged binder samples follows a structured framework consisting of four components (Figure 4.5). The first segment designates the binder type, either "Q" or "T." The second segment indicates the sample thickness, with "M" representing the millimeter unit of measurement. Thickness values may include 1, 2, or 3.2 mm; for simplicity, the value "3" is used in the naming scheme to represent 3.2 mm films. The third segment reflects the specific aging parameters, including temperature, pressure, and time, denoted by their respective units: "C" for Celsius, "B" for Bar, and "H" for Hours. The fourth segment specifies the aging environment, with "O" indicating a dry, thermo-oxidative condition and "RH" indicating a wet, hygro-thermal condition. In this experiment, one aging variable is varied at a time, while the others are held constant, as summarized in Table 4.3. For example, if "60C" appears in the sample name, temperature is the varying factor, with pressure and time held constant at 20 bar and 20 hours, respectively. Similarly, the inclusion of "10B" indicates that pressure is the variable, with temperature and time fixed at 85°C and 20 hours, respectively. Finally, "10H" denotes that time is the varying factor, while pressure and temperature remain fixed at 20 bar and 85°C, respectively. For instance, "Q-2M-5B-RH" signifies Q binder 2 mm films that underwent hygrothermal aging at 85 °C for 20 hours under 5 bar pressure.

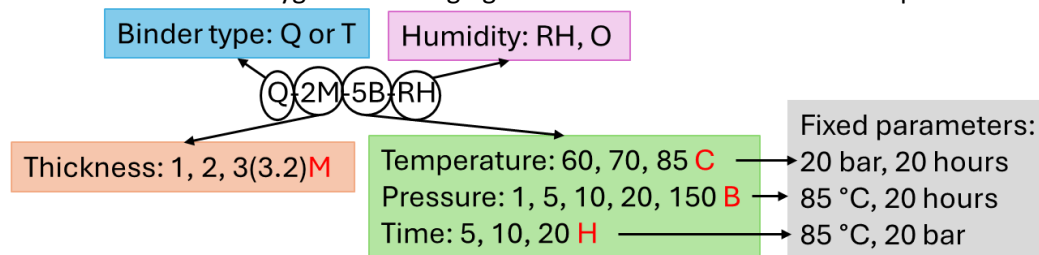


Figure 4.5 Annotation used for samples aged under modified PAV (PAV-MOD) aging conditions.

ROS aging

In this step, the prepared binder films were subjected to five different aging protocols, namely UPA(H₂O₂ +UV), VBA-DRY, VBA-WET, PAV-STD, PAV-MOD, as listed in Table 4.4.

For UPA (H₂O₂ + UV) aging, the Atlas XXL+ weatherometer was used to age 1 mm binder films at different H₂O₂ concentrations (12% and 33%) and temperatures (60, 70, 85 °C) for 3 hours. Additional tests at 60 °C for longer durations of 6 and 9 hours were also conducted. Furthermore, two control groups, namely UV and OVEN, were also prepared for comparison, each including samples aged both at 60 °C for 9 hours and 85 °C for 3 hours, the former conducted in the weatherometer with UV but without H₂O₂; and the latter in an oven without UV or H₂O₂. The H₂O₂ was directly applied on top of

the binder films, and the sample pan with binder and H₂O₂ was then sealed to prevent the evaporation of H₂O₂. The H₂O₂ concentrations of 12% and 33% were chosen for their commercial availability, relevance in oxidative stress research in wastewater treatment, their common use in research and industry, and for studying the effects of varying concentrations, while ensuring these concentrations remain within the safe operational range. The UV light source in the weatherometer was centered at 340 nm (range 300–400 nm) with an intensity of 40 W/m². The irradiance distribution across all sample surfaces was uniform, as ensured by the design of the commercial weatherometer. The UV source-to-sample distance was fixed at 37 cm and remained constant throughout the study. Different temperatures were achieved through the chamber's heating system. However, due to the black colour of binder films, they absorb more UV energy than the surrounding air, leading to slightly higher temperatures than the chamber setting. Therefore, to ensure binder film temperatures of 60, 70, and 85 °C, the chamber temperature was set to lower temperatures 40, 50, and 65 °C, respectively, which have been confirmed through monitoring sample surface temperatures during aging process. Humidity in the chamber was maintained at minimum level possible (<10% relative humidity) for all tests.

Furthermore, the Viennese Binder Aging (VBA) method was employed, using air enriched with 25 ppm NO₂ and 4 g/m³ ozone at 85 ± 1°C for three days (VBA-DRY). A variant (VBA-WET) was also conducted by introducing 75 g/m³ humidity via water spray, while keeping all other conditions the same [7].

Standard PAV (PAV-STD) aging was conducted at 90 °C, 20 bar, with a 3.2 mm film for 20 hours. A modified PAV (PAV-MOD) with >99 % relative humidity at 85 °C, 20 bar for 20 hours was also tested. Humidity was introduced using 1000 grams of demineralized water. Further details regarding setting humidity in PAV chamber can be found in [8].

Table 4.4 Aging conditions for binder samples including UPA, control conditions, PAV, and VBA.

Aging protocol	Thickness (mm)	Temperature (°C)	Pressure (bar)	Relative humidity (%)	Accelerator reactant	Time (Hours)	nomenclature	# of samples
UPA (H ₂ O ₂ +UV)	1	60, 70, 85	1	Binder covered by liquid	12% or 33% H ₂ O ₂ + UV	3	Q-12%-70C-3H	12
	1	60	1	Binder covered by liquid	12% or 33% H ₂ O ₂ + UV	6, 9	Q-33%-60C-9H	8
OVEN (Control groups for UPA)	1	60, 85	1	-	without UV or H ₂ O ₂	3, 9	Q/T-OVEN-60C-9H	4
UV (Control groups for UPA)	1	60, 85	1	-	UV, without H ₂ O ₂	3, 9	Q/T-UV-85C-3H	4
PAV-STD	3.2	90	20	-	Pressure, temperature	20	Q/T-PAV-STD	2
Q-1M-85C-RH (PAV-MOD)	1	85	20	>99% humidity	Pressure	20	Q/T-1M-85C-RH	2
VBA-DRY VBA-WET	1	85	1	<10% or ~21% humidity	NO ₂ and ozone	72	Q/T-VBA-DRY/WET	4

4.3.4 Field samples

Field-aged samples were collected and analysed as a reference to develop and validate laboratory aging protocols, ensuring that the simulated aging conditions accurately reflect real-world binder degradation. Pavement sections were constructed in October 2014, and have since been continuously exposed to the environmental conditions. The location, situated in the Netherlands, experiences a temperate maritime climate that bears the influence of the North Sea and the Atlantic Ocean, resulting in cool winters with daytime temperatures ranging from 2 °C to 7 °C and moderate summers with temperatures between 15 °C and 20 °C, as shown in Figure 4.6a. Precipitation is relatively evenly distributed throughout the year, with a minimum of 60 mm precipitation in April and maximum precipitation of almost 100 mm in August, Figure 4.6b. Moreover, the humidity level is generally high in The Netherlands with higher with a drier period spanning from April to September, Figure 4.6c.

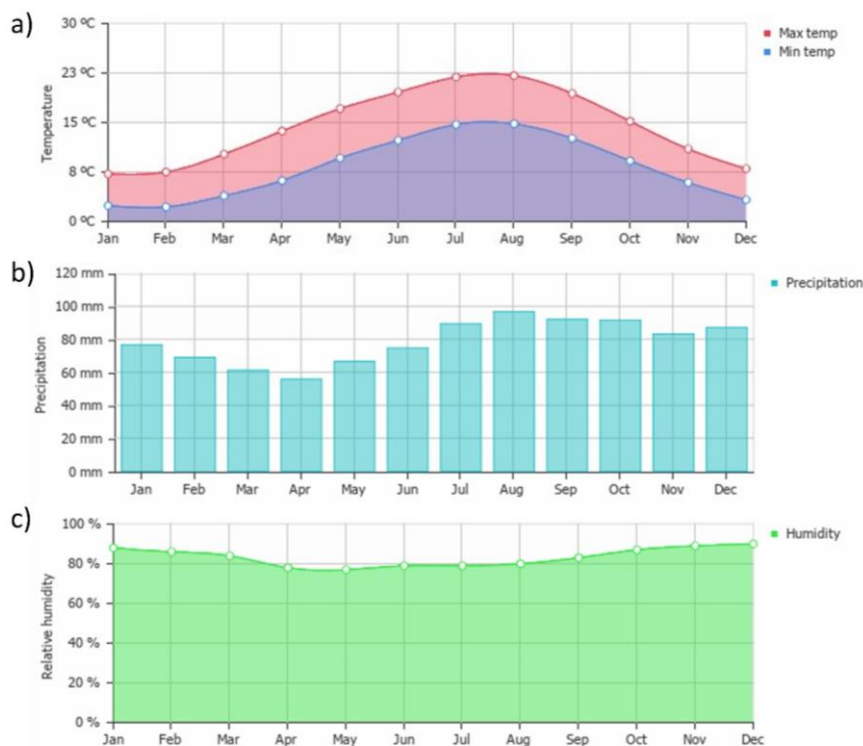


Figure 4.6 Average a) minimum and maximum temperature, b) precipitation (mm), c) relative humidity (%) in Amsterdam, Netherlands during Jan. 2021 to Dec. 2021, from weather-and-climate.com.

The complete structure of the pavement comprises a top layer of 50 mm thickness, consisting of Porous Asphalt (PA) and Stone Mastic Asphalt (SMA) placed on the left and right lanes separately, followed by a 230 mm dense asphalt layer and a 250 mm cement-bound asphalt granulate base (AGRAC) laid more than 10 years ago (Figure 4.7a). Constructed on October 9, 2014, with each layer compacted individually using a roller compactor. Annually, 100 mm diameter cores were extracted from the 50 mm thick PA and SMA layers, specifically focusing on the top 12–14 mm pertinent to this study. Analysis of the component distributions (Figure 4.7b) reveals that while the PA samples maintain a high air void content typically between 15% and 25%, the SMA samples exhibit a much denser structure with air voids remaining consistently below 10% (Figure 4.7c). Binder from these samples, which exclusively consisted of Q binder, was meticulously extracted and recovered from the target segments using dichloromethane as a solvent in accordance with European standard EN 12697-1 [9].

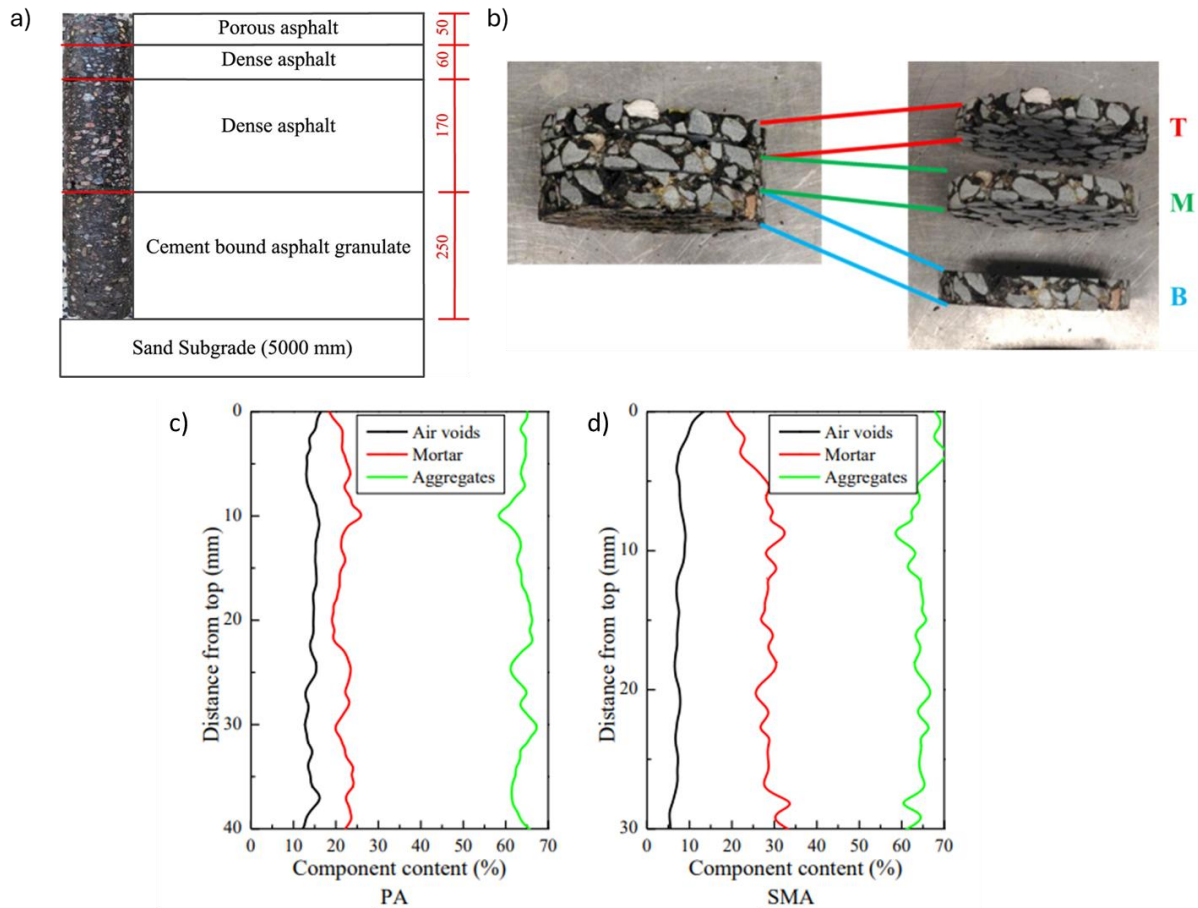


Figure 4.7 a) Structural composition of the field test section (dimensions in mm), b) Description of extracted slices (T = Top, M = Middle, B = Bottom), distributions of voids, mortar and aggregates (rock) over the height of c) PA and d) SMA.

4.4 Characterization and analysis methods

4.4.1 Attenuated Total Reflectance-Fourier Transform Infrared (ATR-FTIR) spectroscopy

ATR-FTIR spectroscopy serves as a valuable tool for acquiring insights into the chemical composition of binder samples, particularly those undergoing specific chemical changes during the aging process. To prepare FTIR samples, approximately 1 g of the material was heated in a metal spoon above a Hot plate until it reached a temperature of 110 °C. The sample was then stirred for 3 minutes using the tip of a thermometer. Small droplets of the material were transferred onto a silicon foil and covered with a lid to prevent contamination from dust or light-induced aging on the surface of the binder [10]. The measurements were conducted using a Nicolet iS5 Thermo Fisher Scientific instrument, equipped with an attenuated total reflection unit featuring a diamond crystal. Each spectrum was generated by collecting data from 24 scans, employing a resolution of 4 cm⁻¹. The binder samples were tested at three states: unaged (fresh), short-term aged (STA), and long-term aged (LTA). For each aging state, four samples were prepared and analysed in the solid state, resulting in four spectra per aging state in the range of 4000–400 cm⁻¹.

The spectral data underwent pre-processing steps. Initially, an Adaptive Smoothness Penalized Least Squares (aspls) correction was applied to address spectral shifts (chapter 3, Table 3.2) [11]. Subsequently, a normalization step known as normalization to a maximum of one (NMO) was conducted [11]. This step aims to standardize absorbance values across data collected from different devices by scaling them to a fixed range of 0 to 1. Specifically, the minimum point within the range of 2800–3200 is set to zero, and the maximum point is adjusted to 1 (chapter 3, Table 3.3). The

combination of these two pre-processing methods was selected because it achieved the highest performance in detecting aging-induced spectral changes, as demonstrated in Chapter 3. Consequently, they are chosen as the pre-processing approach for the subsequent chapters.

The wavenumber ranges of main functional groups identified by the FTIR spectra are listed in Table 3.4 in chapter 3. Equation 4.1 was used to calculate the indices for each functional group with the full area under the curve and the vertical limits mentioned in Table 3.4.

The computation of indices followed this equation:

$$index = \frac{A_x}{A_{Total}} \quad (4.1)$$

The symbol A_x denotes the peak area under the curve within specific ranges outlined in Table 3.4.

4.4.2 Cumulative chemical aging and aging rate

When assessing the efficacy of aging protocols and determining the optimal aging protocol, it is crucial to consider both the cumulative aging and the rate of aging. Cumulative aging (CA) represents the overall extent of aging. A cumulative aging closely aligning field aging indicates an accurate replication of real-world conditions. On the other hand, the aging rate (AR), defined as the change rate of aging extent over time, offers insights into the dynamics of the aging process, highlighting how rapidly aging occurs. A higher aging rate allows for a faster assessment of material aging behaviour, leading to significant savings of time and resources.

Chemical properties serve as a robust indicator of material aging performance. In this analysis, ten FTIR indices were utilized to quantify the cumulative aging and aging rate indices. Cumulative aging based on chemical properties, denoted as CA_{che} , was calculated as the summation of changes relative to the fresh condition using equation 4.2.

$$CA_{che} = \sum_{index=1}^{index=10} \frac{|PI_{fresh} - PI_{aged}|}{PI_{fresh}} \quad (4.2)$$

Where PI_{fresh} and PI_{aged} are the FTIR peak index (PI) values for the fresh and aged samples, respectively.

The aging rate, defined as AR_{che} was calculated using equation 4.3:

$$AR_{che} = \frac{CA_{che}}{t} \quad (4.3)$$

Where t is the duration of the aging process (in hours).

4.4.3 Deconvolution FTIR spectra

Fourier Transform Infrared (FTIR) spectroscopy provides information about the molecular structure of materials by measuring the absorption of infrared light at different wavenumbers, each corresponding to a vibrational mode of a chemical bond. However, the spectra obtained from complex materials, such as bituminous binders, often exhibit broad or overlapping absorption peaks. This overlap can obscure the contribution of individual functional groups, complicating the interpretation of spectral features. FTIR deconvolution is a mathematical technique used to resolve such overlapping peaks into distinct components, allowing for more precise identification and quantification of the chemical species present.

In the context of bituminous binders, which contain a complex mixture of hydrocarbons and oxygenated compounds, multiple functional groups may absorb infrared light at similar or overlapping wavenumbers. Deconvolution enables the separation of these overlapping signals, providing a clearer picture of the chemical changes occurring during aging.

The deconvolution process begins with spectral pre-processing. The raw FTIR data is first corrected for baseline drifts (to remove background signals) and normalized (to ensure comparable intensity scales across samples). Once pre-processed, peak identification is performed to locate the positions of individual peaks within the spectrum. This was done using the SciPy library in Python, which analyses the first and second derivatives of the spectrum. In general, a peak is identified where the first derivative changes sign (from positive to negative), indicating a local maximum. Additionally, second derivative information is used to confirm the presence of true peaks and distinguish them from noise or shoulder features.

Each identified peak is then mathematically represented by a Gaussian function. A Gaussian function is a symmetrical bell-shaped curve defined by three parameters: position (the central wavenumber), height (peak intensity), and width (related to the standard deviation, indicating how broad the peak is) [12]. The rationale for using Gaussian functions is that they approximate the natural shape of many IR absorption bands, especially in systems with some degree of inhomogeneous broadening.

To reconstruct the original spectrum, a sum of multiple Gaussian curves is fitted to each spectral region where peaks overlap. This fitting process was implemented using the *scipy.optimize.least_squares* function, which minimizes the difference between the measured spectrum and the sum of Gaussian components. To improve computational efficiency and reduce fitting errors, the FTIR spectrum was divided into smaller, chemically relevant segments, each deconvoluted independently based on previous literature [12]. This segmentation reduces the number of parameters optimized simultaneously and improves the accuracy of the fit, particularly in regions where peak crowding is severe.

Once the peaks are deconvoluted, their positions and shapes are compared against known reference spectra from previously published literature [12][13]. This comparison allows the assignment of specific peaks to functional groups such as carbonyls, sulfoxides, and hydroxyls. Tracking changes in the intensity and position of these deconvoluted peaks over aging time provides a sensitive measure of chemical oxidation and degradation processes in bituminous materials.

Figure 4.8 shows an example of deconvoluted spectra in the 1500–900 cm^{-1} region, a range typically associated with various oxygenated functional groups and aromatic structures that evolve significantly with aging [13].

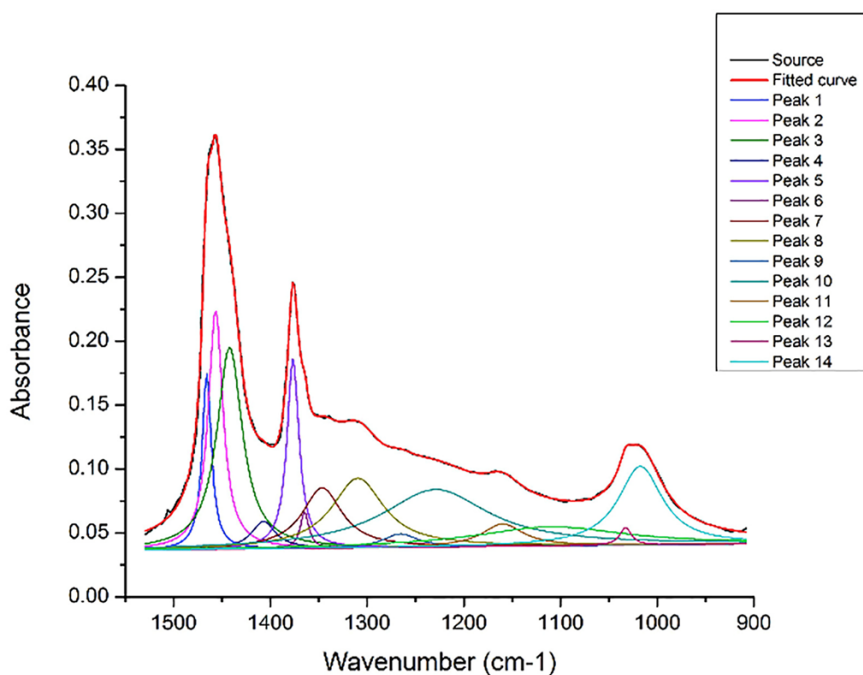


Figure 4.8 Deconvoluted spectra of the analyzed samples in the 1500–900 cm^{-1} region [13].

4.4.4 Dynamic time warping (DTW)

The similarity between laboratory-aged and field-aged samples was assessed using deconvoluted peaks from FTIR spectra. However, variations in aging conditions can lead to peak shifts and differences in peak numbers between samples, making conventional distance metrics like Euclidean distance unsuitable for direct comparison (Figure 4.9). To address this, the Dynamic Time Warping (DTW) algorithm was employed due to its ability to accommodate temporal shifts and non-linear variations in spectral data. DTW ensures that spectral peaks corresponding to the same chemical functional groups are properly aligned, enabling a meaningful comparison of oxidation-related changes between lab-aged and field-aged samples. Once the spectral features were aligned, the Euclidean distance was calculated based on the areas under the aligned peaks, providing a quantitative measure of oxidation similarity. This approach allowed us to evaluate how well the laboratory aging protocol replicates field aging by comparing the oxidation levels in lab-aged samples relative to field-aged ones.

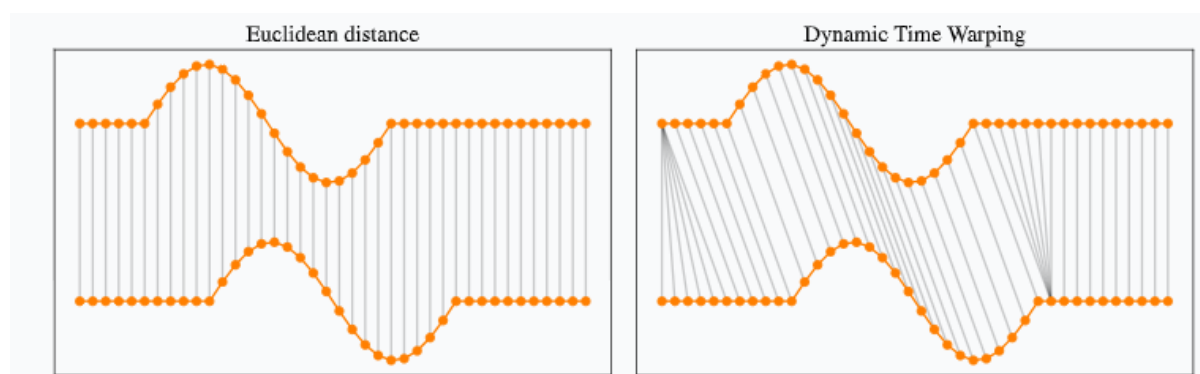


Figure 4.9 Comparison between Dynamic Time Warping (DTW) and Euclidean distance. For clarity, time series are vertically offset; however, their original feature value ranges (y-axis values) remain consistent [14].

To apply DTW, the deconvoluted peak positions were treated as time series data, with each peak position representing a distinct time point in the sequence.

The spectral data from the field-aged sample served as the reference data, denoted as T with a length of I , while the laboratory-aged sample data served as the training data, denoted as S with a length of J .

The DTW process begins by constructing a two-dimensional distance matrix, where each element $d(i,j)$ represents the Euclidean distance between the i -th peak position in the reference data T and the j -th peak position in the training data S [15-17]. The algorithm then searches for the optimal warping path D that minimizes the cumulative distance between two data, thus achieving the best alignment[15]. The optimal path is defined as:

$$D = \sum_{q=1}^Q d(i(q),j(q)) \quad \text{where } q \text{ is a step index along the path} \quad (4.4)$$

Where D is the total alignment cost along the optimal warping path. $d(i,j)$ is the Euclidean distance between the i -th peak position in the reference dataset T and the j -th peak position in the training dataset S . Q is the total number of steps in the optimal path. q is the step index along the path.

Here, the optimal path starts at the top-left corner and ends at the bottom-right corner of the matrix and maintains monotonicity and continuity. This ensures that the path progresses consistently through the sequence of peak positions without looping back or skipping any spectral features[17].

Given the computational intensity of the classic DTW algorithm, particularly its quadratic time and space complexity, we employed an optimized version known as Fast-DTW. This method reduces computational complexity by approximating the optimal path through a series of key operations [17]. First, the original time series data is coarsened by down-sampling to produce a simplified representation. Second, the minimum-distance warp path is identified within this coarser resolution. Third, this warp path is refined by making local adjustments at progressively finer resolutions, thereby improving the accuracy of the alignment. This approach allowed for a linear time and space complexity, making it feasible to handle the FTIR data efficiently without sacrificing alignment accuracy. The DTW distance, representing the total alignment cost, was calculated by summing the Euclidean distances along the identified optimal path. The `fastdtw` Python library, in combination with `scipy.spatial.distance` for Euclidean calculations, enabled this implementation.

4.5 Assessing changes in chemical properties of aged binders

The following sections present the results and discussion of this chapter, focusing on the evaluation of changes in the chemical properties of both laboratory-aged and field-aged binders.

4.5.1 Effect of hygrothermal, thermo-oxidative, and aqueous-thermal aging on chemical properties of laboratory-aged binders

The aim of this section is to analyse the chemical composition changes in binder samples due to aging under hygrothermal, thermo-oxidative, and aqueous-thermal conditions. ATR-FTIR spectroscopy was used to track these chemical changes. Figure 4.10a-c show representative spectra for Q binder subjected to hygrothermal aging at 60 °C for different durations in raw and pre-processed states. Key functional groups are identified in the spectra. Figure 4.10c focuses on the fingerprint region, where prolonged aging led to increased absorbance. Comparing indices enables a more detailed assessment of aging effects.

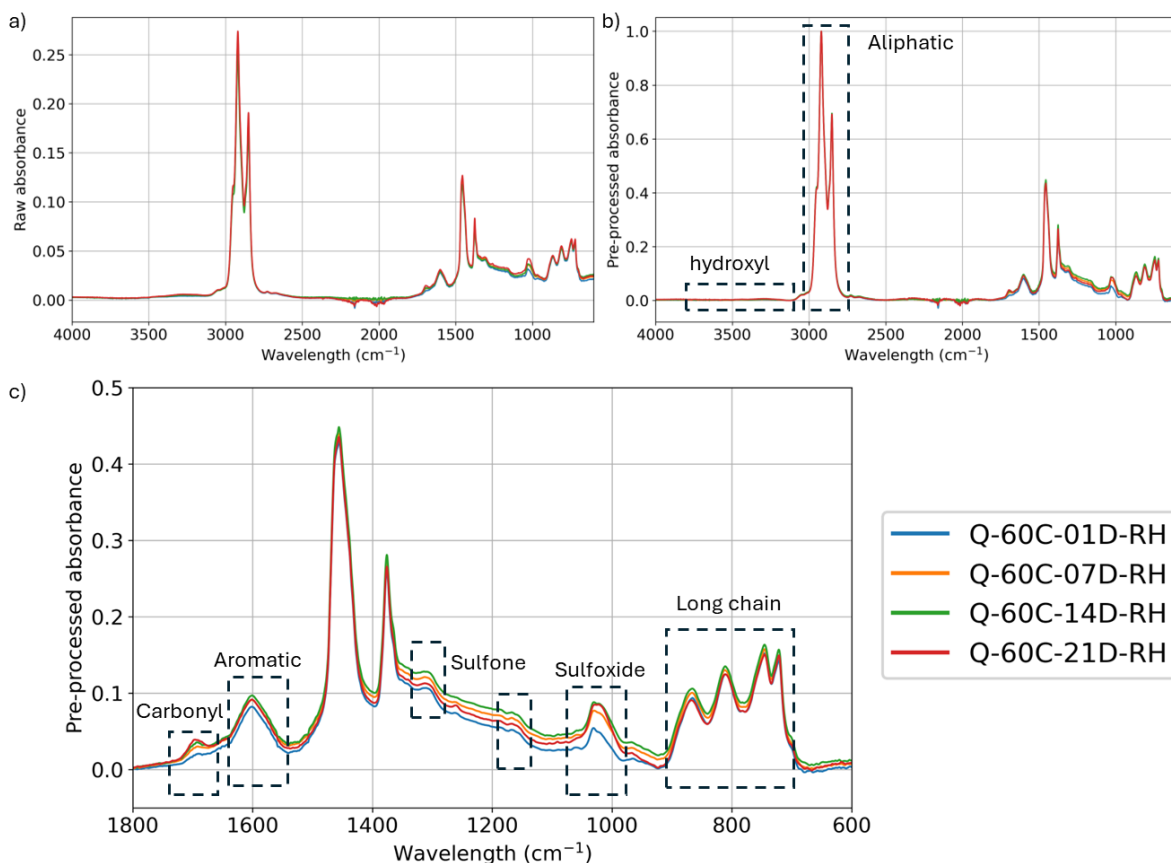
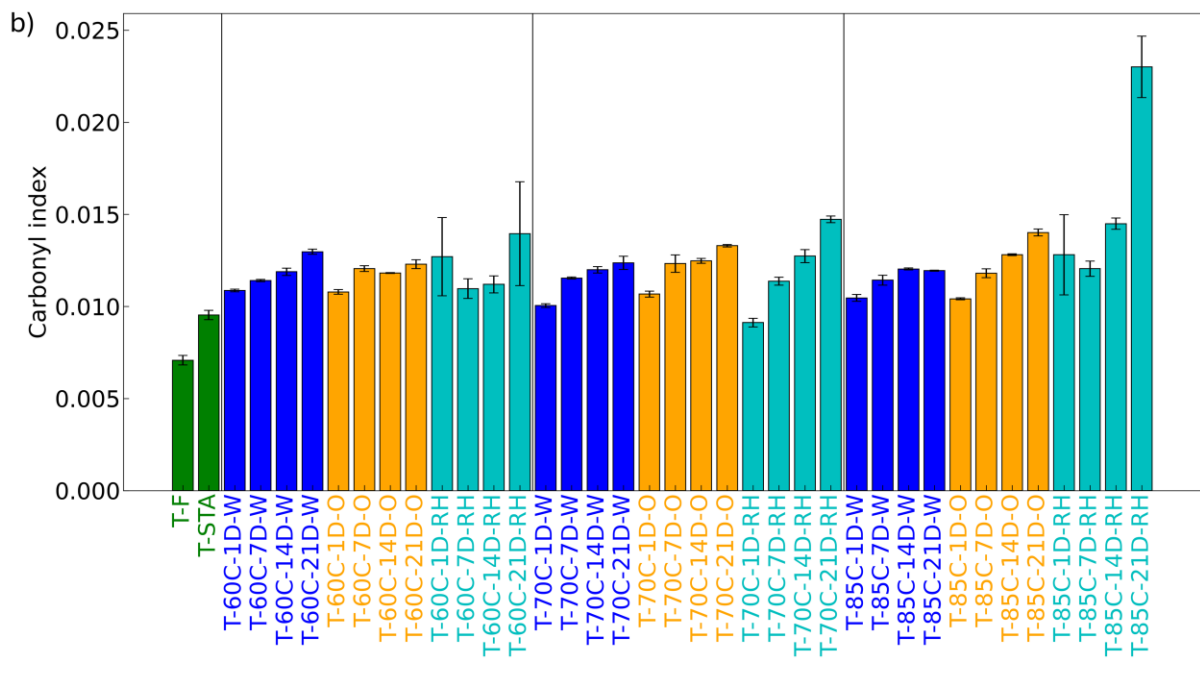
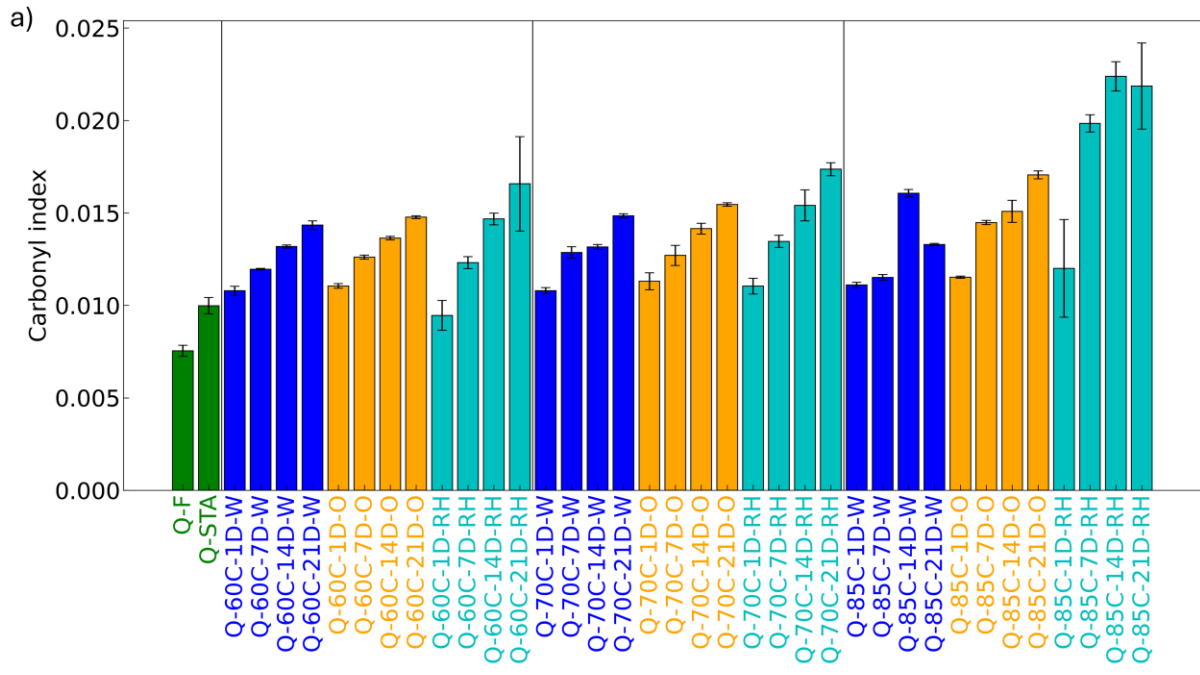


Figure 4.10 FTIR spectra illustrating Q binder aged at 60 °C with 95 % humidity during different aging times, i.e., 1, 7, 14, and 21 days, are presented in: a) raw spectral form, b) baseline-corrected and normalized spectra, and c) the 600-1800 cm^{-1} region to highlight variations in the fingerprint region.

To evaluate aging progression, functional group analysis was performed. The carbonyl and sulfoxide indices, commonly used in aging studies [18], are shown in Figure 4.11 a-d for Q and T binders. Over time, both indices increased. Q binder exhibited higher carbonyl index values (Figure 4.11 a-b), while T binder displayed higher sulfoxide index values (Figure 4.11 c-d). Given their similar initial conditions, this suggests different aging susceptibilities. Under identical aging conditions, distinct aging pathways are activated in each binder.



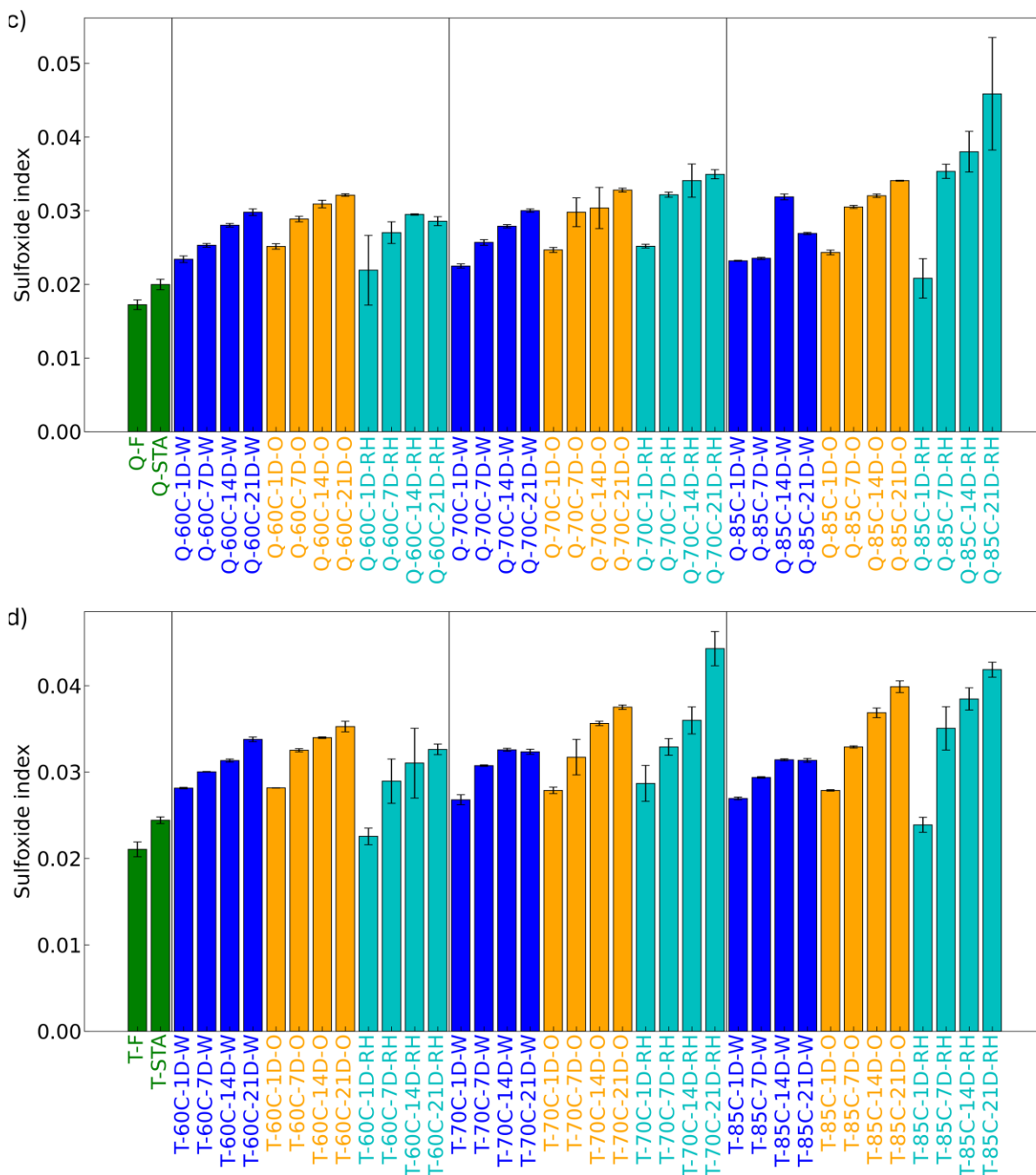


Figure 4.11 FTIR results for a) carbonyl index of Q samples, b) carbonyl index of T samples, c) sulfoxide index of Q samples, d) sulfoxide index of T samples aged at 60 °C, 70 °C, and 85 °C for 1, 7, 14, and 21 days in water-immersion (W), thermo-oxidative (O), and hydrothermal (RH) conditions.

The trends observed in other indices closely mirrored those of the carbonyl and sulfoxide changes for both binders. This discussion will focus on the results for both Q and T binders.

The trends observed for carbonyl and sulfoxide indices were also reflected in other functional group indices. Figure 4.12 show an increase in sulfone index following aging. Among the long-term aged samples, hydrothermal aging at the higher temperature of 85°C led to the most significant increase in this index, particularly when compared to thermos-oxidative and aqueous-thermal aging conditions or aging at lower temperatures. The sulfone region, associated with sulfur-containing oxidation products, generally shifts to higher absorbance values with aging, due to an increase in polarity.

However, the absorption bands between 1350 and 1100 cm^{-1} (Figure 4.10) may also arise from overlapping deformation vibrations of methylene and aromatic groups or from skeletal vibrations of branched aliphatic structures. To resolve these overlapping bands more accurately, deconvolution of the FTIR spectra would be necessary, which is discussed in greater detail in section 4.5.4.

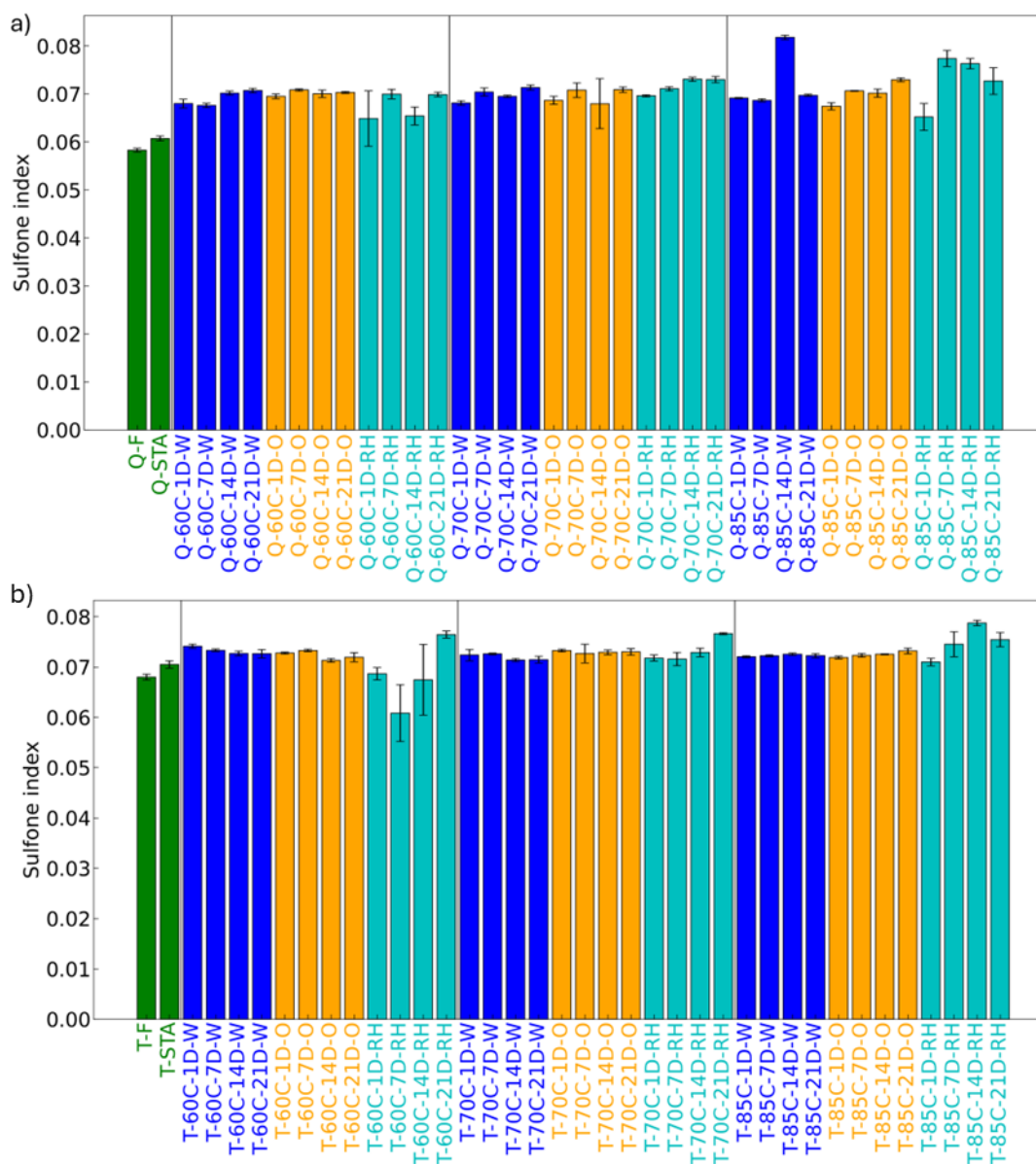


Figure 4.12 FTIR results of sulfone index for a) Q samples and b) T samples aged at 60 °C, 70 °C, and 85 °C for 1, 7, 14, and 21 days in water-immersion (W), thermo-oxidative (O), and hydrothermal (RH) conditions.

Similarly, the aromatic index (Figure 4.13) increased after aging. The Q-85C-21D-RH sample exhibited the highest aromatic index, indicating heightened sensitivity to water vapor at elevated temperatures. This suggests that aromatic compounds within the binder are particularly susceptible to oxidative reactions in humid environments, contributing to structural modifications in aged samples.

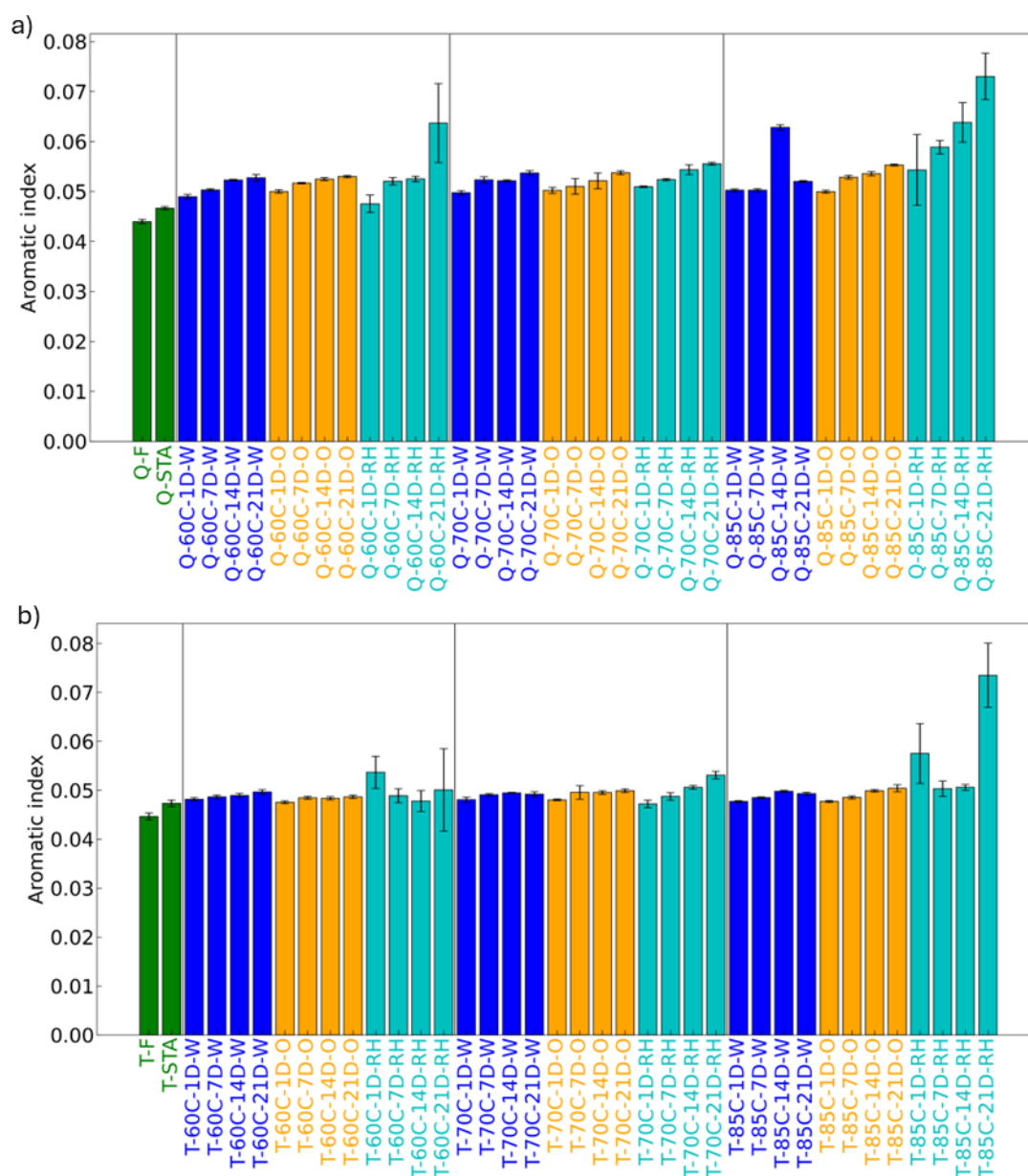


Figure 4.13 FTIR results of aromatic index for a) Q samples and b) T samples aged at 60 °C, 70 °C, and 85 °C for 1, 7, 14, and 21 days in water-immersion (W), thermo-oxidative (O), and hydrothermal (RH) conditions.

The aliphatic index (Figure 4.14) showed a slight decrease after aging. This minor change suggests that aliphatic structures in the binder are more resistant to oxidative aging compared to other functional groups. The stability of the aliphatic index could be attributed to the inherent robustness of C-H bonds in saturated hydrocarbons, which are less susceptible to oxidative cleavage under the studied aging conditions. However, the slight decline indicates some degree of structural modification, potentially due to gradual oxidation or chain scission.

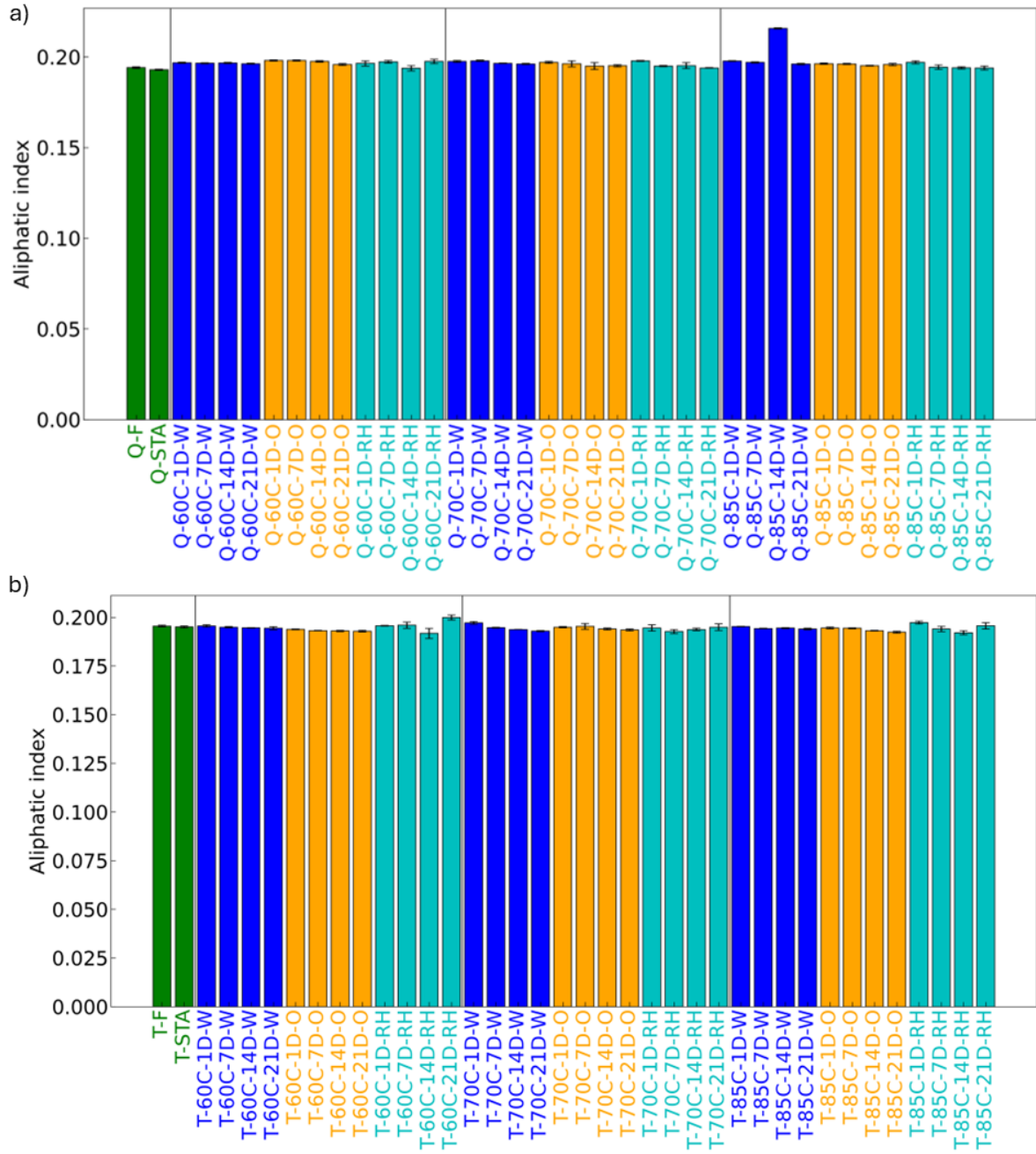


Figure 4.14 FTIR results of aliphatic index for a) Q samples and b) T samples aged at 60 °C, 70 °C, and 85 °C for 1, 7, 14, and 21 days in water-immersion (W), thermo-oxidative (O), and hydrothermal (RH) conditions.

The hydroxyl index (Figure 4.15) decreased after long-term aging. However, samples aged under hydrothermal conditions exhibited an increase in the hydroxyl index, with larger variations and greater standard errors. This suggests that humidity may promote the formation of alcohol groups in the binder, though further investigation is required to draw definitive conclusions.

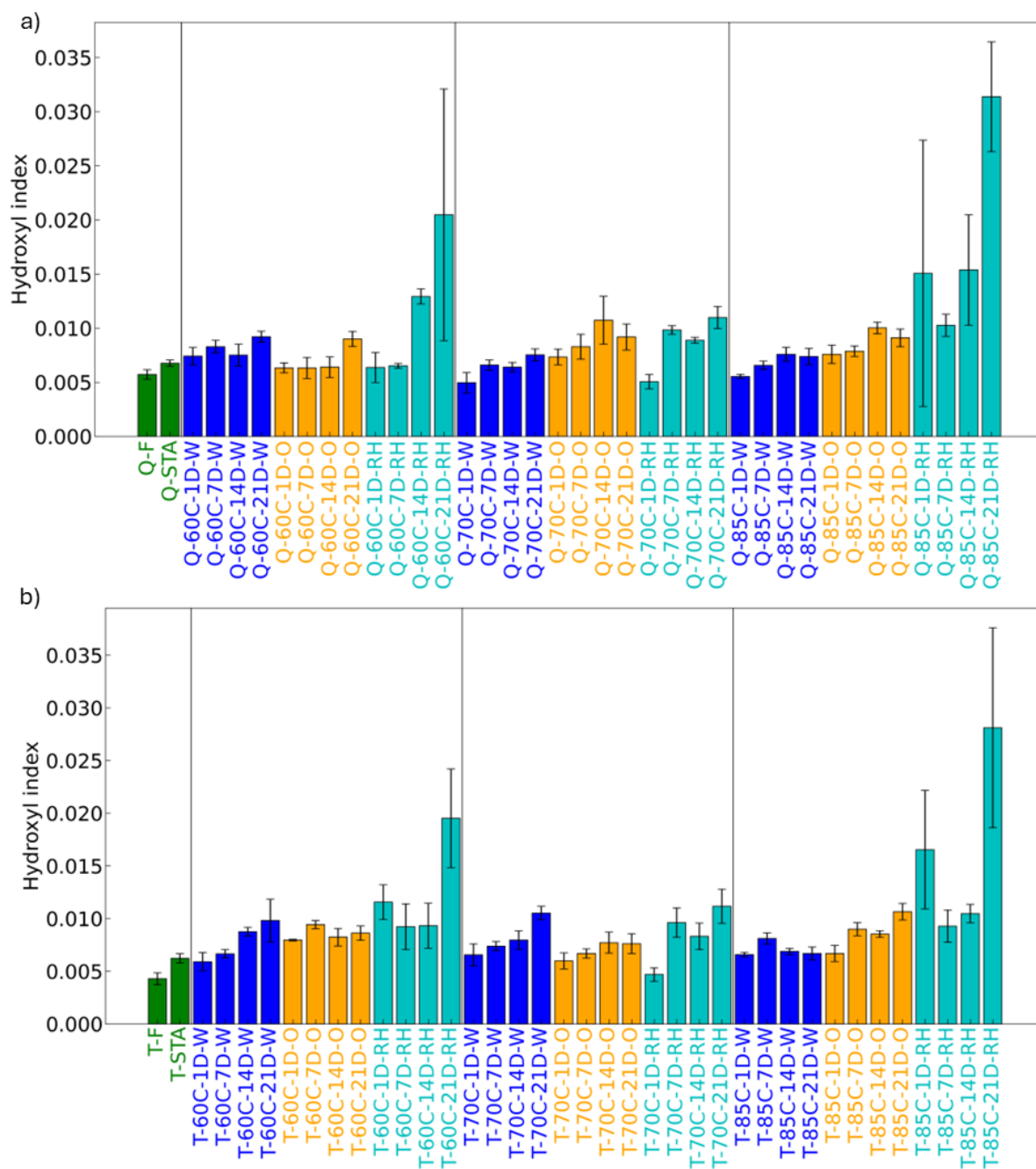


Figure 4.15 FTIR results of hydroxyl index for a) Q samples and b) T samples aged at 60 °C, 70 °C, and 85 °C for 1, 7, 14, and 21 days in water-immersion (W), thermo-oxidative (O), and hydrothermal (RH) conditions.

The spectral region between 710–912 cm^{-1} encompasses vibrations associated with aromatic ring bending, out-of-plane (o-p) C–H deformations in adjacent and isolated hydrogen aromatic rings, and rocking vibrations in alkyl side chains. The trends observed in aged samples indicate structural modifications due to oxidative degradation, molecular rearrangements, and potential loss of long-chain hydrocarbons.

By analysing the region between 710–734 cm^{-1} (Figure 4.16a and Figure 4.16b), which includes C–C aromatic ring bending ($\delta_{\text{C-C}}$) and out-of-plane N–H deformations ($\delta_{\text{o-p N-H}}$) in secondary amides at 710.25 cm^{-1} , as well as C–H out-of-plane deformations ($\delta_{\text{o-p C-H}}$) in four adjacent hydrogen aromatic rings and C–CH₂ rocking vibrations at 728.33 cm^{-1} , a general decline in intensity is evident

across all aging conditions. The most pronounced reductions occur under hygrothermal aging at 85°C, indicating significant structural degradation of aromatic rings and alkyl chains. Thermo-oxidative aging leads to moderate reductions, suggesting progressive loss of specific aromatic functionalities, while aqueous-thermal aging induces the least significant changes, supporting the hypothesis that limited oxygen diffusion in water slows oxidative transformations. Notably, the Q-85C-14D-W sample does not follow the general trend, necessitating further investigation.

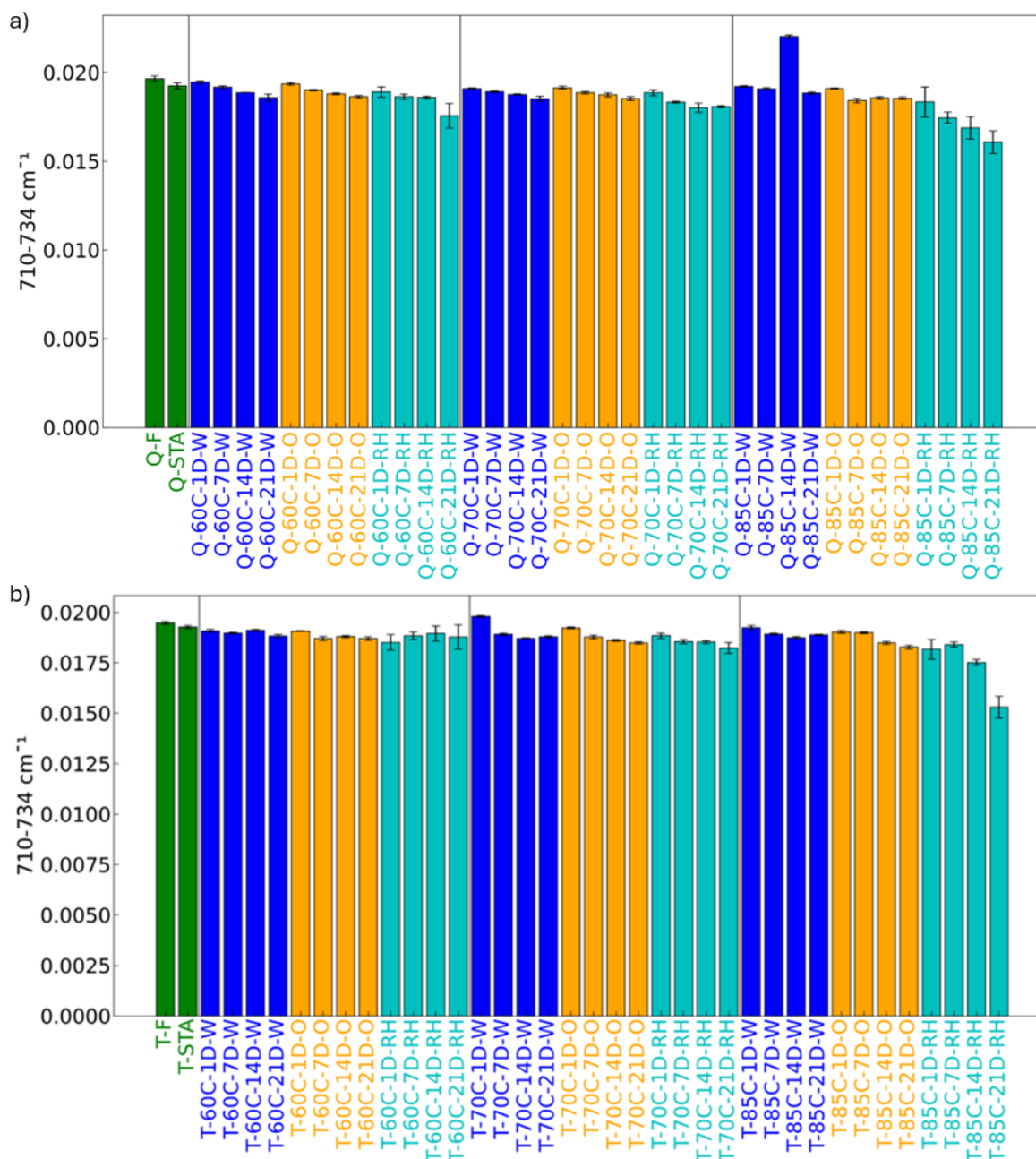


Figure 4.16 FTIR results for the region between 710–734 cm⁻¹ for a) Q samples and b) T samples aged at 60 °C, 70 °C, and 85 °C for 1, 7, 14, and 21 days in water-immersion (W), thermo-oxidative (O), and hygrothermal (RH) conditions.

In the region between 734–783 cm⁻¹ (Figure 4.17a and Figure 4.17b), where C–H out-of-plane deformations in four adjacent hydrogen aromatic rings appear at 754.02 cm⁻¹, the long-chain index values consistently decline with aging, reflecting structural alterations in polycyclic aromatic

compounds. Hygrothermal aging at 85°C induces the most substantial reduction, reinforcing the role of high humidity and temperature in accelerating oxidation. Thermo-oxidative aging also leads to a measurable decrease, though less pronounced compared to hygrothermal conditions, while aqueous-thermal aging shows minimal impact, further highlighting the reduced effectiveness of oxidation in water-submerged conditions.

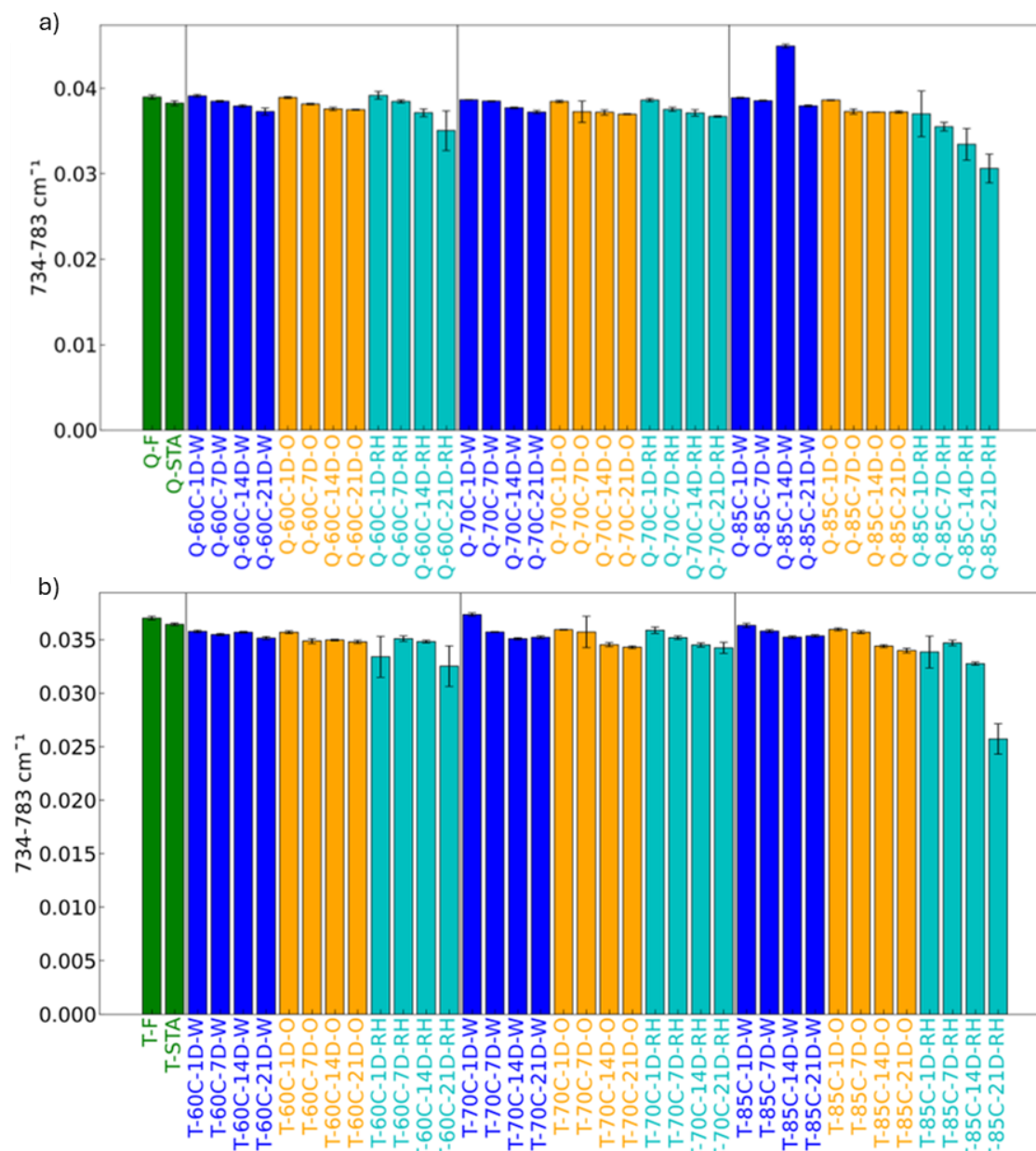


Figure 4.17 FTIR results for the region between 734–783 cm⁻¹ for a) Q samples and b) T samples aged at 60 °C, 70 °C, and 85 °C for 1, 7, 14, and 21 days in water-immersion (W), thermo-oxidative (O), and hygrothermal (RH) conditions.

The region between 783–833 cm⁻¹ (Figure 4.18a and Figure 4.18b) is associated with C–H out-of-plane deformations in two adjacent hydrogen aromatic rings at 818.36 cm⁻¹. The aging trend follows a similar pattern, with hygrothermal aging at 85°C producing the most significant reduction in spectral intensity. Thermo-oxidative aging results in moderate degradation, indicating oxidative cleavage of these specific aromatic ring structures. Aqueous-thermal aging has a limited effect, once again suggesting that oxygen availability plays a crucial role in dictating aging severity.

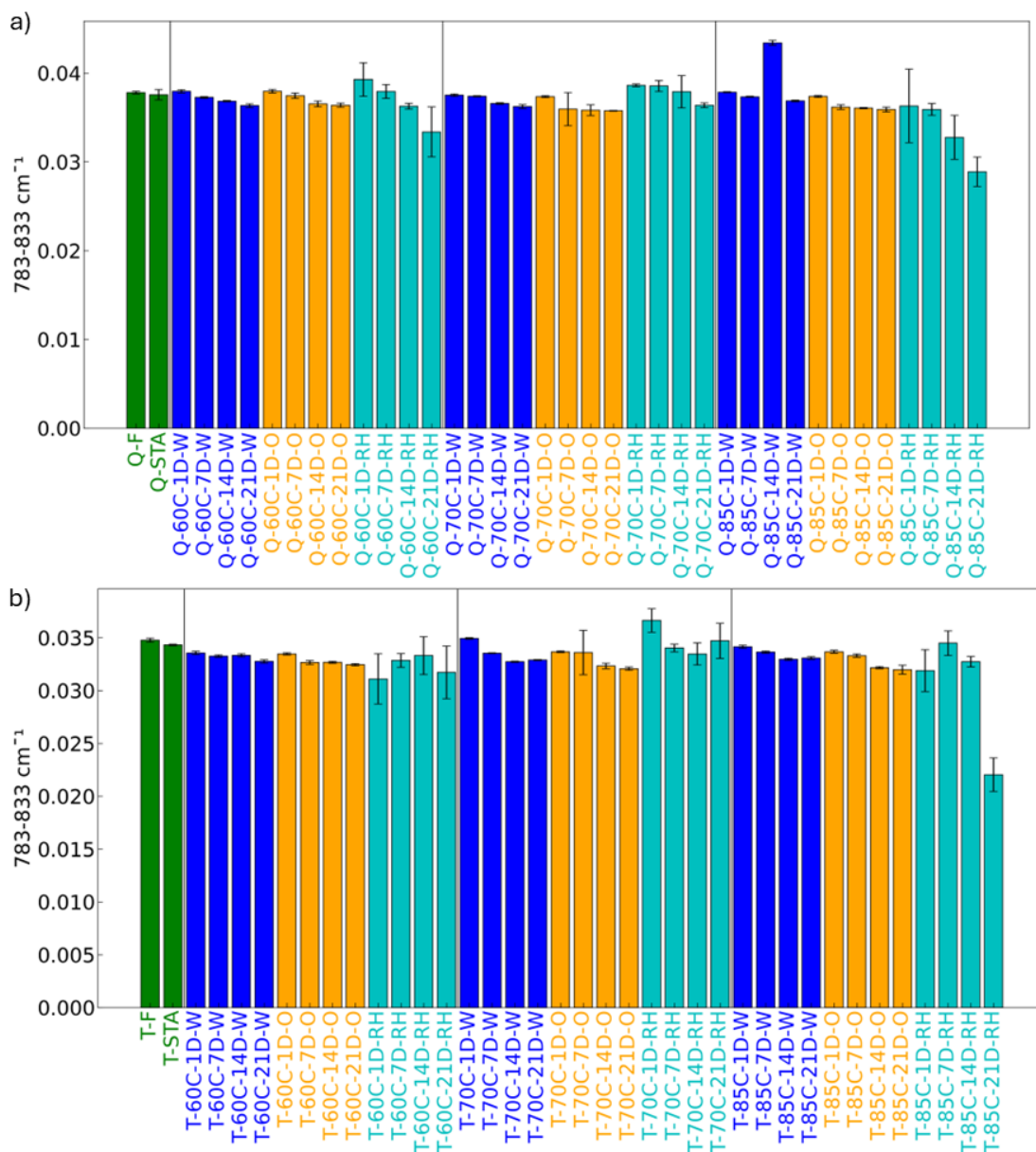


Figure 4.18 FTIR results for the region between 783–833 cm⁻¹ for a) Q samples and b) T samples aged at 60 °C, 70 °C, and 85 °C for 1, 7, 14, and 21 days in water-immersion (W), thermo-oxidative (O), and hydrothermal (RH) conditions.

In the last region between 833–912 cm⁻¹ (Figure 4.19a and Figure 4.19b), which primarily reflects C–H out-of-plane deformations in isolated adjacent hydrogen aromatic rings at 863.06 cm⁻¹ and 881.72 cm⁻¹, the greatest decline in intensity is observed under hydrothermal aging at 85°C. This confirms the susceptibility of isolated aromatic hydrogen structures to oxidation under high-temperature and humidity conditions. Thermo-oxidative aging leads to a moderate decrease, consistent with oxidative modification of aromatic components, while aqueous-thermal aging induces minimal changes, further reinforcing the hypothesis that oxidation is constrained in water-immersed conditions.

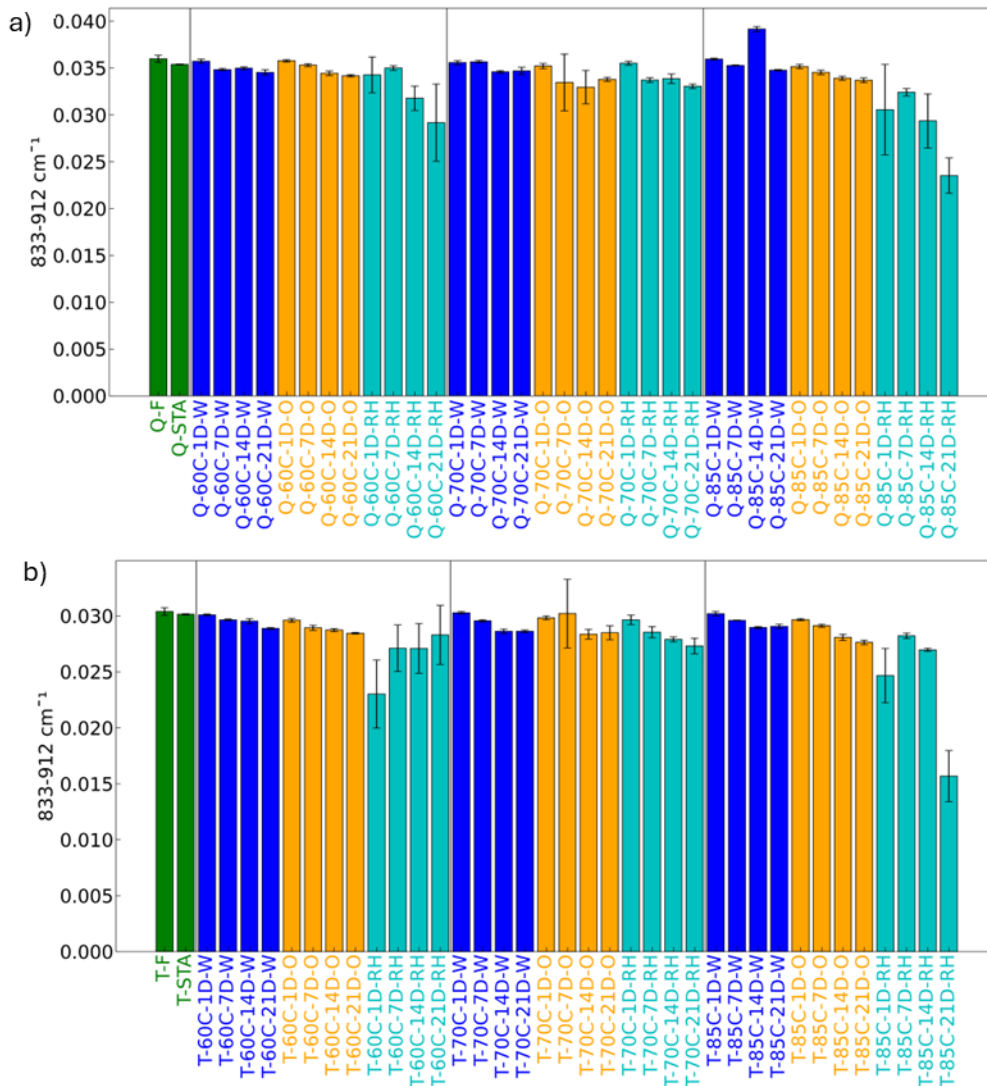


Figure 4.19 FTIR results for the region between 833–912 cm⁻¹ for a) Q samples and b) T samples aged at 60 °C, 70 °C, and 85 °C for 1, 7, 14, and 21 days in water-immersion (W), thermo-oxidative (O), and hygrothermal (RH) conditions.

Overall, the observed trends suggest that aging mechanisms in the 710–912 cm⁻¹ region are primarily driven by temperature and humidity, with hygrothermal conditions at 85°C inducing the most significant degradation. Thermo-oxidative aging contributes to structural modifications at a slower rate, while aqueous-thermal aging exhibits the least impact due to limited oxygen availability. These findings highlight the role of oxidation pathways in bitumen aging and the varying susceptibility of different structural components to environmental conditions.

Effect of temperature on aging progression

The observed trend, as revealed through the comparison of hygrothermal aged samples at different temperatures, wherein heightened temperature and humidity over 14 or 21 days induced more significant aging compared to lower temperatures with humidity, despite identical aging durations, can be attributed to several factors. Firstly, higher temperatures reduce the binder's viscosity, facilitating the diffusion of oxygen and oxidative species into the sample. Secondly, higher temperatures provide the necessary activation energy for oxidation reactions, expediting their initiation and progression. Moreover, increasing the temperature increases the average kinetic

energy of molecules, leading to more collisions with enough energy to form reactive species that may be more effective for aging.

Unlike hygrothermal and thermo-oxidative aging, increasing the temperature in aqueous-thermal conditions to 85 °C did not enhance oxidative aging. It is crucial to emphasize that the physical dissolution of oxygen in water is temperature dependent. While chemical reactions involving oxygen in water and binder may also be affected by temperature, the primary factor influencing oxygen solubility is the physical dissolution process described by Henry's Law. This law states that the solubility of a gas in a liquid is directly proportional to the partial pressure of that gas above the liquid and inversely proportional to the temperature. With an increase in water temperature, the kinetic energy of water molecules rises. This heightened thermal motion reduces the ability of water molecules to retain dissolved gases, including oxygen. Consequently, at higher temperatures, the solubility of oxygen in water decreases, leading to a reduction in the aging reaction of bitumen.

Effect of time on aging progression

Under various hygrothermal, thermo-oxidative, and aqueous-thermal conditions, extended durations generally lead to elevated values for both carbonyl and sulfoxide indices. Notably, only Q-85C-14D-W exhibits significantly higher indices compared to Q-85C-21D-W. This discrepancy may stem from the sample's inhomogeneity before FTIR measurements. Rheological characterization of these samples will explain whether the observed trend is attributed to binder heterogeneity or varying levels of aging.

Analysing aging rates by studying carbonyl and sulfoxide indices over time

The carbonyl and sulfoxide indices are among the most commonly used FTIR markers for aging analysis, and, as noted in the previous section, other indices exhibited similar trends. Therefore, in the following analysis, the focus will primarily be on these two indices. Additionally, Figure 4.20 illustrates the summation of the carbonyl and sulfoxide indices for the Q binder as a function of aging time across different temperatures. Results for the T binder can be found in the Appendix of chapter 4, Figure 2S.

As shown in Figure 4.20, aging under different conditions and at various temperatures demonstrated a generally linear relationship with aging time, with R-squared values exceeding 0.85 for nearly all conditions, except for the aqueous-thermal aging at 85°C. This deviation was expected, as the data for day 14 of this condition did not align with the typical aging trend, suggesting that further investigation is needed for this condition.

All aging conditions commenced with short-term aged samples, providing a consistent starting point. Among these, aqueous-thermal aging exhibited the lowest slope across all temperatures, indicating the slowest aging rate among the three aging conditions. In contrast, thermo-oxidative aging showed a steeper slope, indicating a faster aging reaction, while hygrothermal aging exhibited the highest slope, reflecting the most rapid aging process.

Interestingly, while increasing the temperature accelerated the aging reaction for both thermo-oxidative and hygrothermal conditions, no such effect was observed for aqueous-thermal aging. This suggests that temperature plays a more significant role in aging speed when sufficient oxygen is present to support oxidation reactions. In contrast, for conditions where a water layer acts as a barrier (such as in aqueous-thermal aging), the temperature does not seem to have a substantial impact on the aging rate.

Hygrothermal aging, in particular, showed the most significant increase in slope and reaction rate with increasing temperature. This can be explained by the fact that higher temperatures provide the necessary activation energy to facilitate oxidation reactions, thereby accelerating their initiation and progression. Moreover, in the presence of humidity, the increased temperature raises the average

kinetic energy of molecules, leading to more frequent molecular collisions. These collisions have a higher likelihood of providing the energy needed to form reactive species, which may enhance the aging process.

In summary, while temperature clearly influences aging rates under thermo-oxidative and hydrothermal conditions, its effect is less pronounced under aqueous-thermal conditions, where other factors, such as the presence of a water layer, may limit the impact of temperature on the aging speed.

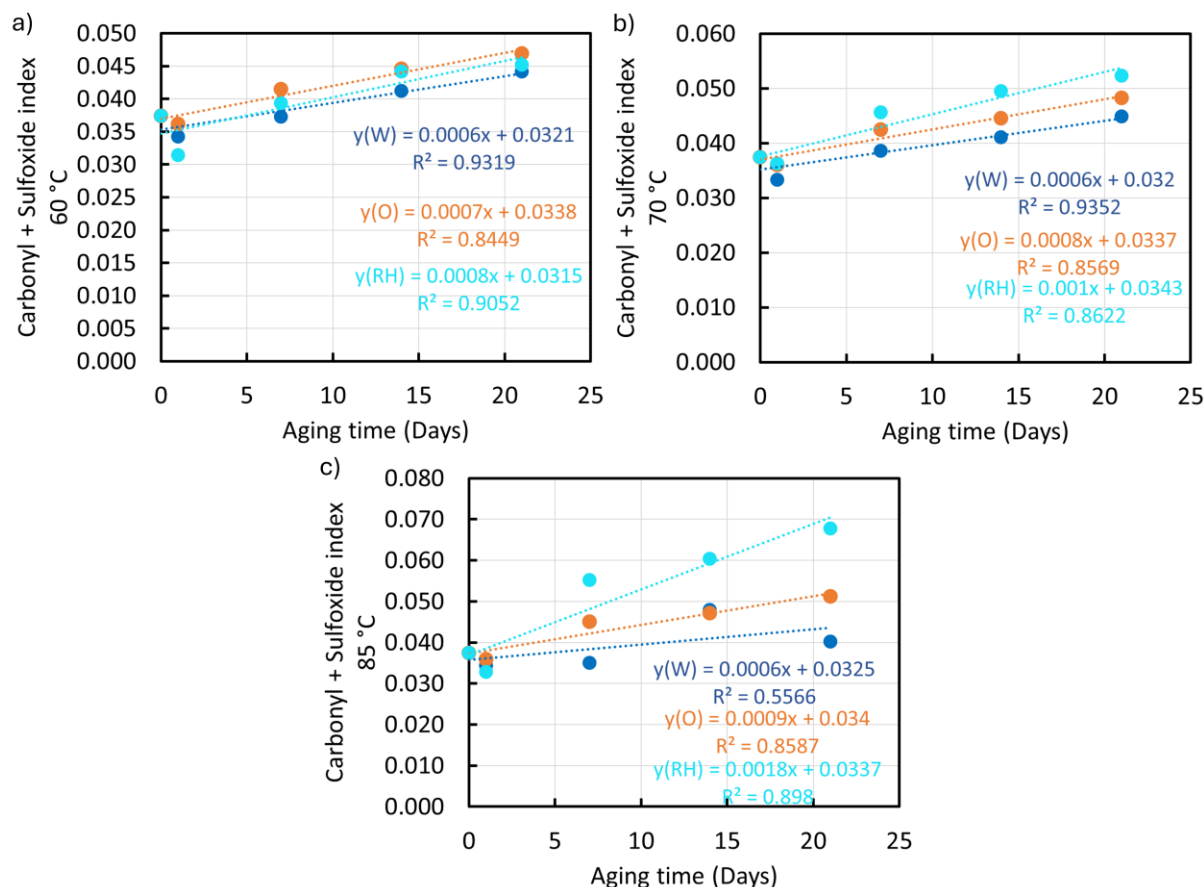


Figure 4.20 Summation of carbonyl and sulfoxide indices of Q binder versus aging time at a) 60 °C, b) 70 °C, c) 85 °C. Blue color represents the aqueous-thermally aged samples, orange color represents the thermo-oxidatively aged samples, and turquoise color represents the hydrothermal aged samples.

In summary, the carbonyl and sulfoxide indices serve as valuable markers for monitoring binder aging, reflecting the degree of chemical changes over time. Other FTIR indices exhibited similar trends, indicating that the formation of functional groups varies between binders depending on their susceptibility to aging. The presence of relative humidity has a more significant impact on binder aging than either thermo-oxidative or aqueous-thermal aging alone, with hydrothermal aging consistently yielding the highest index values at each temperature, followed by thermo-oxidative aging, while aqueous-thermal aging results in the lowest values. This suggests that hydrothermal aging accelerates oxidation, while aqueous-thermal aging slows it down. The reduced oxidation rate in aqueous-thermal conditions may be attributed to the water layer atop the binder films, which acts as a barrier to oxygen diffusion, whereas humidity in gas form, combined with atmospheric oxygen, promotes the formation of reactive species, enhancing oxidation. Additionally, increasing the aging temperature accelerates chemical degradation, particularly under hydrothermal conditions, where the combined effects of heat and humidity significantly enhance oxidation rates. Figure 4.21

illustrates the schematic of acceleration of oxidative aging for binder films under different conditions and the aging factor for each condition, with all samples aged at the same temperature.

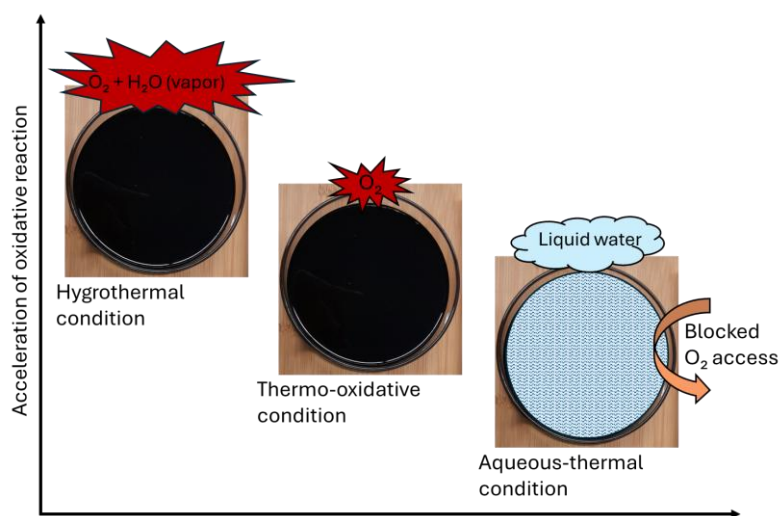


Figure 4.21 Schematic of acceleration of oxidative aging for binder films under different conditions and the aging factor for each condition. The aging temperature of all samples was kept the same.

4.5.2 Effect of temperature, pressure, time, humidity, and thickness on chemical properties of laboratory-aged binders

FTIR spectra of some of the lab-aged samples, before and after preprocessing, are plotted in Figure 4.22. As observed, the main changes in the spectra of samples with varying aging conditions occurs in the range of carbonyl and sulfoxide region, consistent with the finding from literature that sulfoxide and carbonyl indices are the most informative indices for oxidative aging effects [18]. Moreover, as concluded in the previous section, other FTIR indices exhibited similar trends to the carbonyl and sulfoxide indices, reinforcing their role as reliable indicators for aging analysis. Therefore, for the evaluation of the effects of various factors including pressure, time, and thickness on aging, sulfoxide and carbonyl indices will be utilized.

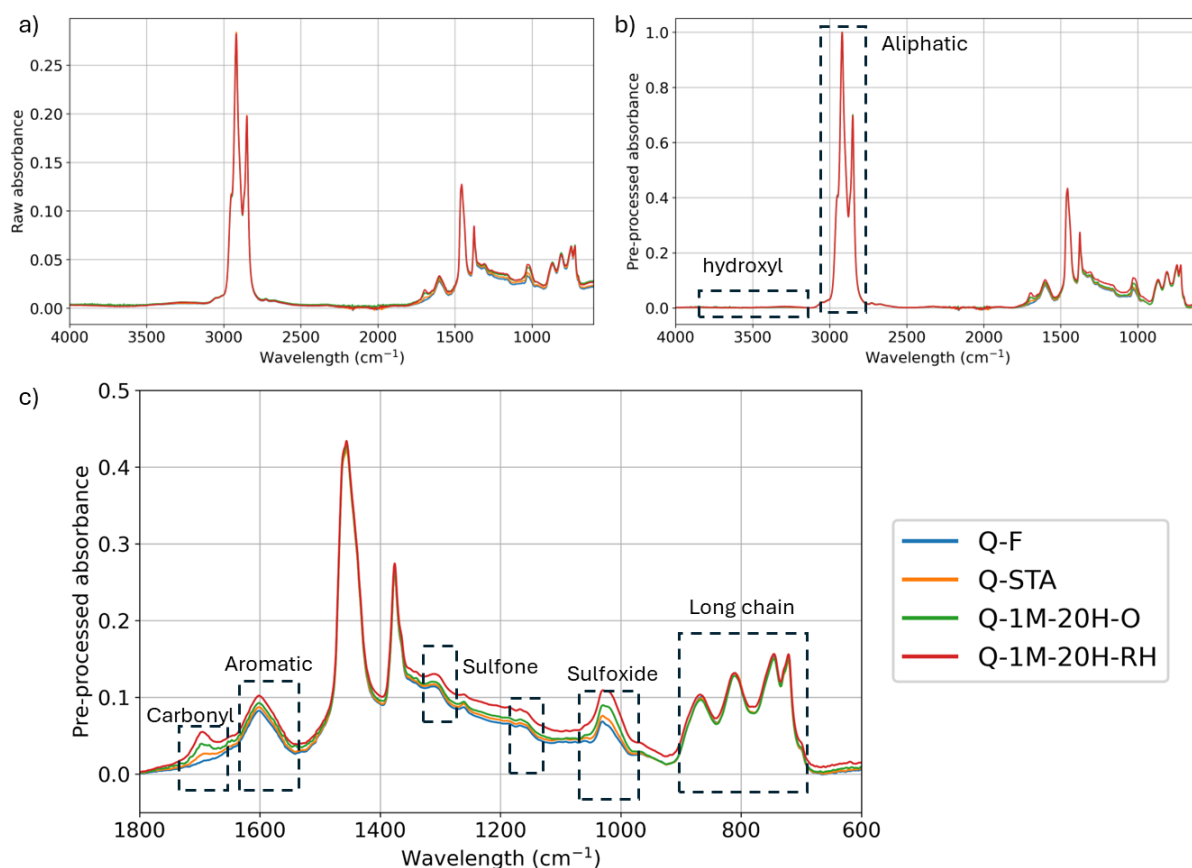


Figure 4.22 FTIR spectra illustrating fresh, short-term aged, long-term aged (with and without humidity) are presented in a) raw spectral form, b) baseline-corrected and normalized spectra, and c) the 900-1800 cm^{-1} region to highlight variations in carbonyl and sulfoxide peaks.

Effect of temperature on aging progression

Figure 4.23 shows sulfoxide and carbonyl indices of binder samples at different aging temperatures. Higher temperature led to higher sulfoxide and carbonyl indices in the binder. Hygrothermal aging resulted in higher indices than thermo-oxidative aging, especially at higher temperatures and thinner films. The indices increased with decreasing binder film thickness for both Q and T binders, especially at 85 °C. Notably, hygrothermal aged samples at 85 °C exhibited a sharp rise in the carbonyl index, particularly in 1 mm thick samples, indicating that high temperature and hygrothermal aging of thin films represent the most severe aging condition.

Compared to Q binders, T binders exhibited a higher sulfoxide index but a lower carbonyl index when aged under high pressure and high temperature. These differences may be attributed to the unique chemical compositions of each binder. The T binder contains lower oxygen and sulfur contents, higher nitrogen content, and a higher carbon-to-hydrogen ratio (indicating greater aromaticity and unsaturation) compared to Q, as shown in Table 4.1. The higher carbonyl index in the Q binder suggests that its chemical structure is more susceptible to oxidation pathways leading to carbonyl formation. This can be explained by the higher initial oxygen content in Q binder, which may indicate a greater presence of oxygen-containing functional groups or more oxidation-prone sites.

In contrast, T binder exhibits a higher sulfoxide index after aging, despite having lower initial sulfur content. This could be due to differences in oxidation pathways influenced by the chemical structure. The higher aromaticity and unsaturation in T binder may alter its oxidation behaviour, leading to a preference for sulfoxide formation rather than carbonyl accumulation. Additionally, the lower oxygen content in T binder may slow down early carbonyl formation, allowing oxidation to proceed

predominantly through pathways that favour sulfoxide accumulation over extended aging periods. These compositional differences suggest that under high pressure and temperature, Q binders are more prone to carbonyl-based oxidation, whereas T binders favour sulfoxide accumulation due to differences in molecular structure and oxidation susceptibility.

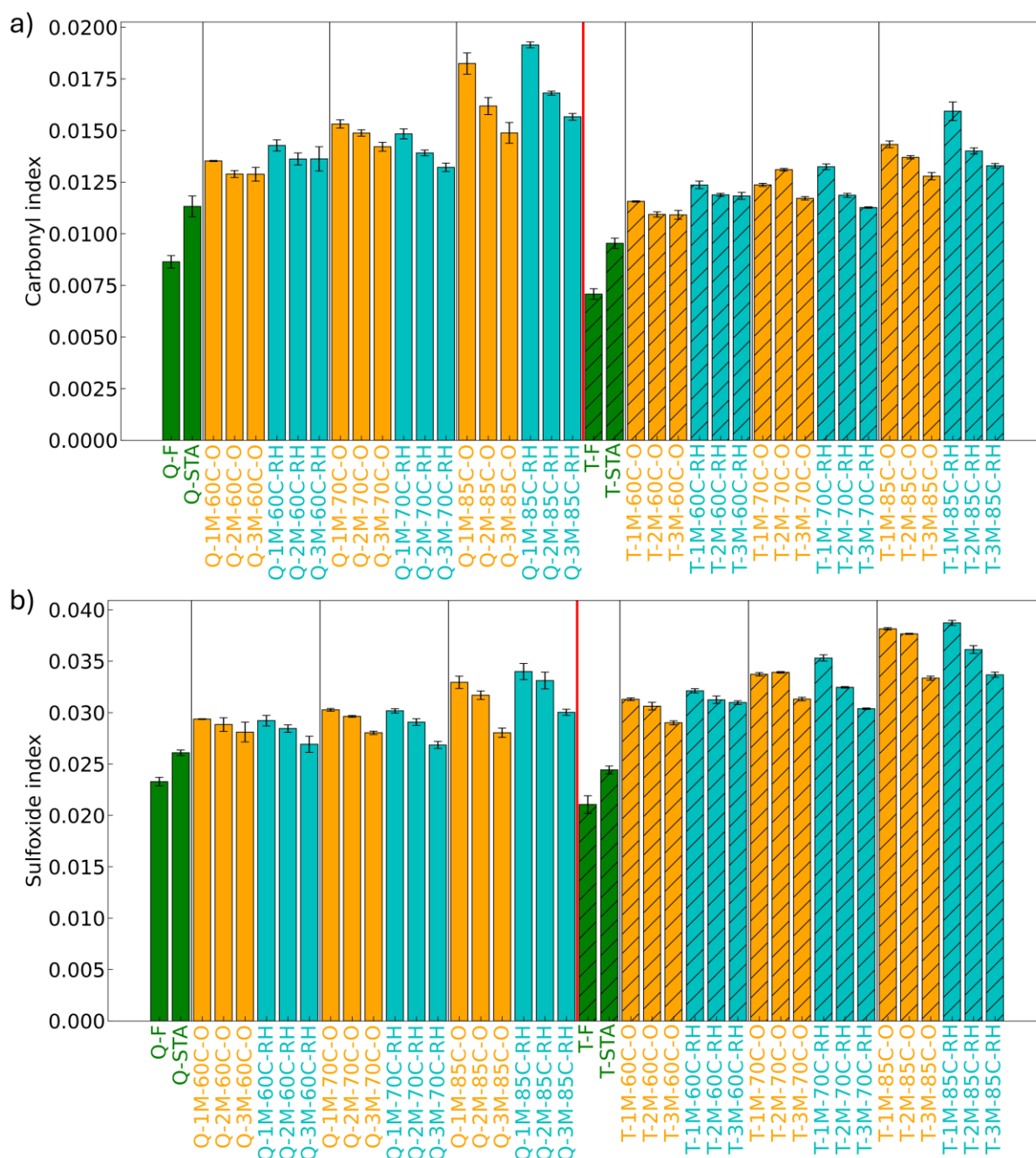


Figure 4.23 FTIR results, a) carbonyl index, b) sulfoxide index for the effect of different temperatures of 60, 70, and 85°C under 20 bar for 20 hours for both Q and T binder. The results are presented for all studied samples, after hydrothermal (RH) and thermo-oxidative(O) aging.

Figure 4.24 presents the combined FTIR index as a function of aging temperature. The FTIR index changes exponentially with temperature under both hydrothermal and thermo-oxidative aging conditions, consistent with previous studies [19]. This exponential relationship resembles the Arrhenius equation, which describes the temperature dependence of reaction rates. Furthermore, compared to thermal-oxidative aging, the Q binder exhibits a higher power under hydrothermal

aging, indicating an accelerating effect of humidity on aging at higher temperatures. In contrast, the T binder did not display an accelerating effect of humidity on aging at higher temperatures.

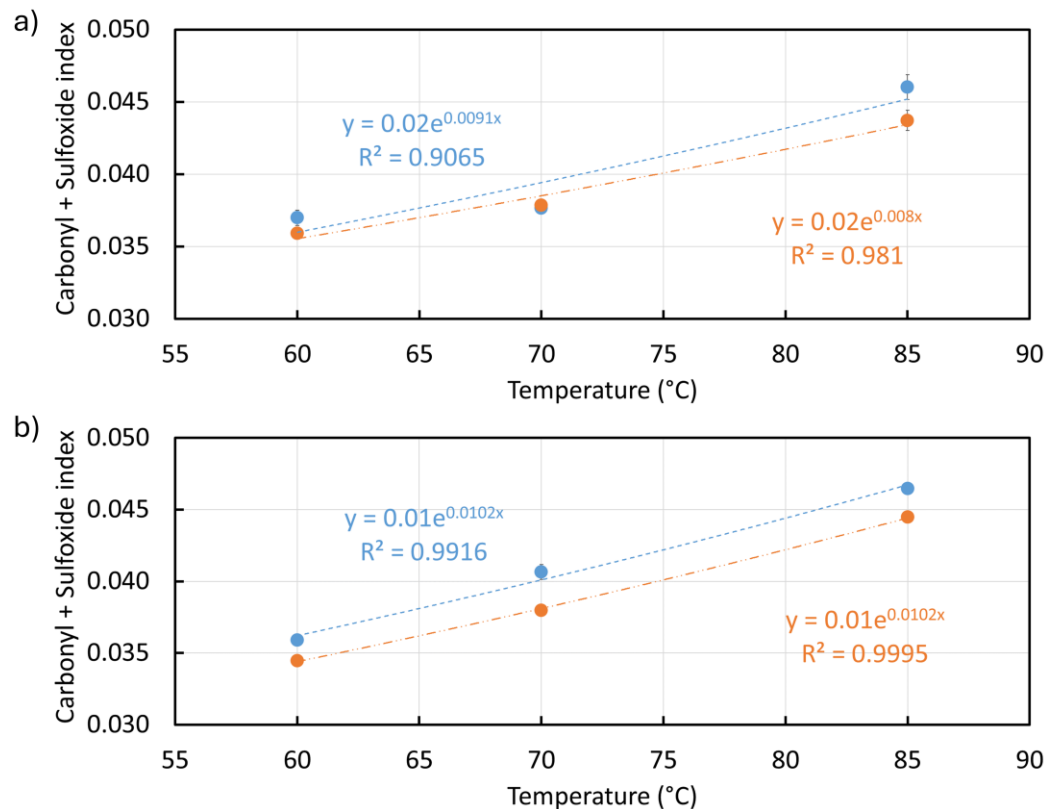


Figure 4.24 Summation of carbonyl and sulfoxide indices versus aging temperature for a) Q and b) T binders with a thickness of 1 mm. Blue color represents the hydrothermally aged samples and orange color represents the thermo-oxidatively aged samples.

Effect of pressure on aging progression

Figure 4.25 shows the carbonyl and sulfoxide indices of Q and T samples at different pressures (1, 5, 10, 20, and 150 bar). The carbonyl and sulfoxide indices increased with rising pressure, indicating more severe aging for higher pressure. Higher indices are observed for hydrothermally aged samples compared to thermo-oxidative aged samples at higher pressure, with a more noticeable increase in both indices is shown for samples with 1 mm thickness. This suggests that the presence of water vapor, combined with harsh aging conditions such as higher pressure or thinner films, accelerates binder oxidation more effectively than thermo-oxidative aging alone. The difference between hydrothermal and thermo-oxidative aging was more pronounced in Q samples than in T samples.

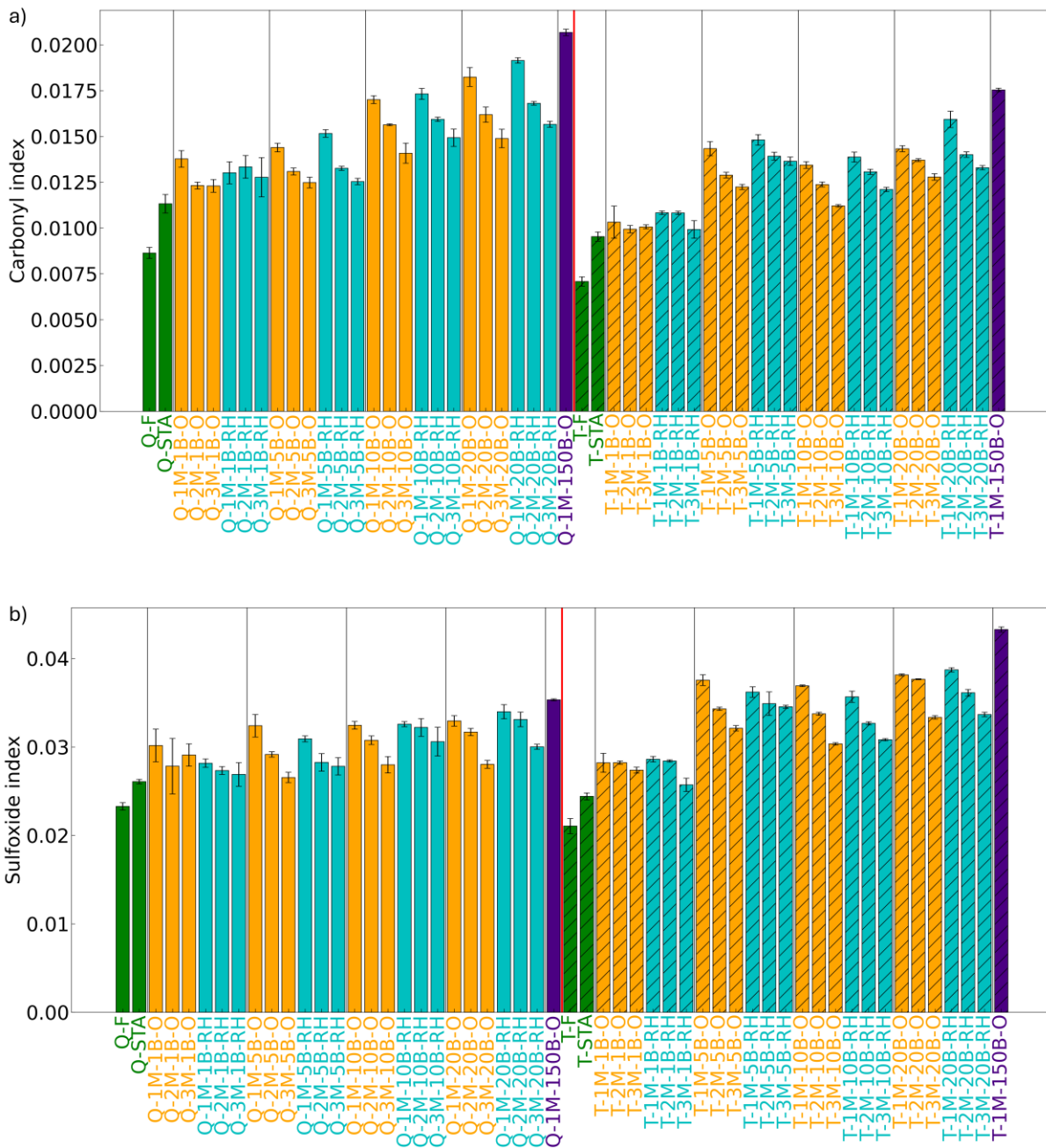


Figure 4.25 FTIR results, a) carbonyl index, b) sulfoxide index for the effect of different pressures of 1, 5, 10, 20, and 150 bar at 85 °C for 20 hours for both Q and T binder. The results are presented for all studied samples, after hydrothermal (RH) and thermo-oxidative(O) aging.

Figure 4.26 depicts the combined index at various pressures for samples with 1 mm thickness. A logarithmic correlation between the index and pressure was revealed, indicating that aging increases with pressure, but at a decreasing rate. This suggests a threshold beyond which higher pressure has limited impact on binder oxidation. Additionally, different sensitivities of Q and T binders to pressure with and without humidity were observed. The higher coefficient for hydrothermal aging compared to thermal-oxidative aging in the Q binder indicates that pressure has a more substantial effect on aging in the presence of humidity, while for T binder, humidity caused limited changes.

While the results qualitatively resemble Henry's Law in terms of pressure influencing oxygen uptake, the logarithmic trend indicates a diffusion-controlled oxidation process rather than a simple gas dissolution phenomenon. This suggests that the equation choice follows diffusion-oxidation models rather than strict Henry's Law.

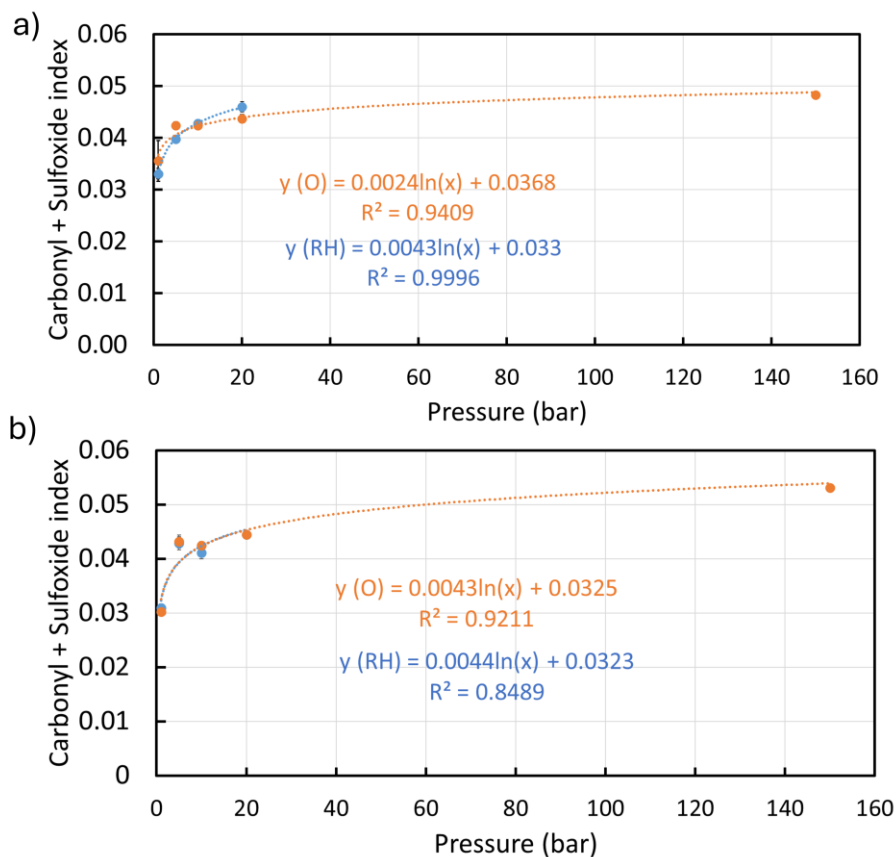


Figure 4.26 Summation of carbonyl and sulfoxide indices versus pressure for a) Q binder and b) T binder. The data for hydrothermal aging and thermo-oxidative aging is shown in blue and orange, respectively.

Effect of time on aging progression

Figure 4.27 a-d shows the changes in carbonyl and sulfoxide indices of Q and T binder at different aging time (5, 10, and 20 hours). Sulfoxide and carbonyl indices increased with aging time for all Q and T samples. Hydrothermal aging resulted in a higher carbonyl index after 20 hours compared to thermo-oxidative aging, indicating its greater effectiveness within this time frame. Thin films exhibited higher indices than thick films, suggesting that thicker films require more time to reach similar index values. For durations of 40 and 80 hours, the indices continued to rise, indicating the formation of more aging products with longer exposure times.

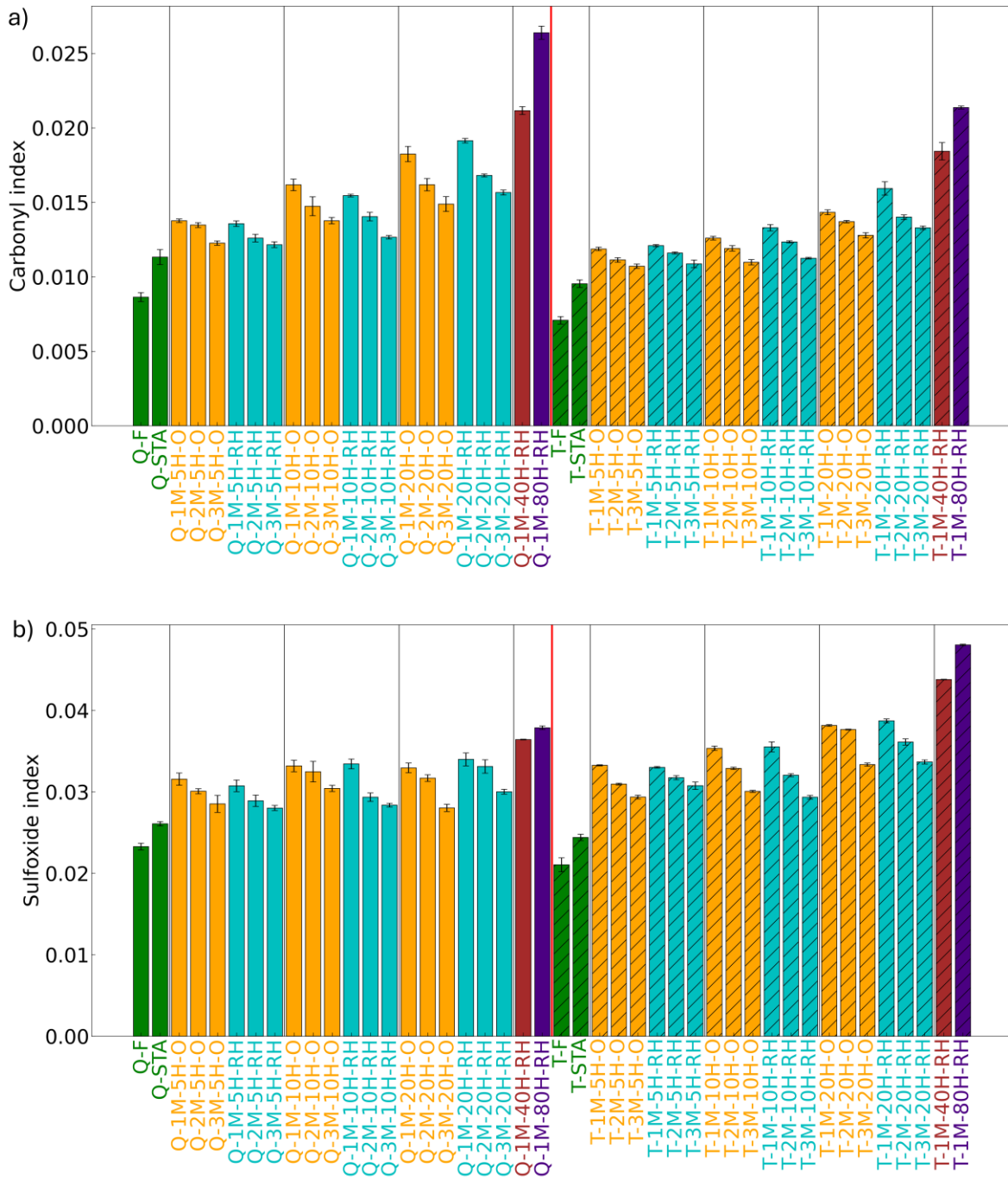


Figure 4.27 FTIR results, a) carbonyl index, b) sulfoxide index for the effect of different aging times of 5, 10, and 20 hours at 85 °C for 20 bar for both Q and T binder. The results are presented for all studied samples, after hydrothermal (RH) and thermo-oxidative(O) aging.

As show in Figure 4.28, the combination of carbonyl and sulfoxide indices showed faster hydrothermal aging during the initial 20 hours at 85 °C compared to thermo-oxidative aging.

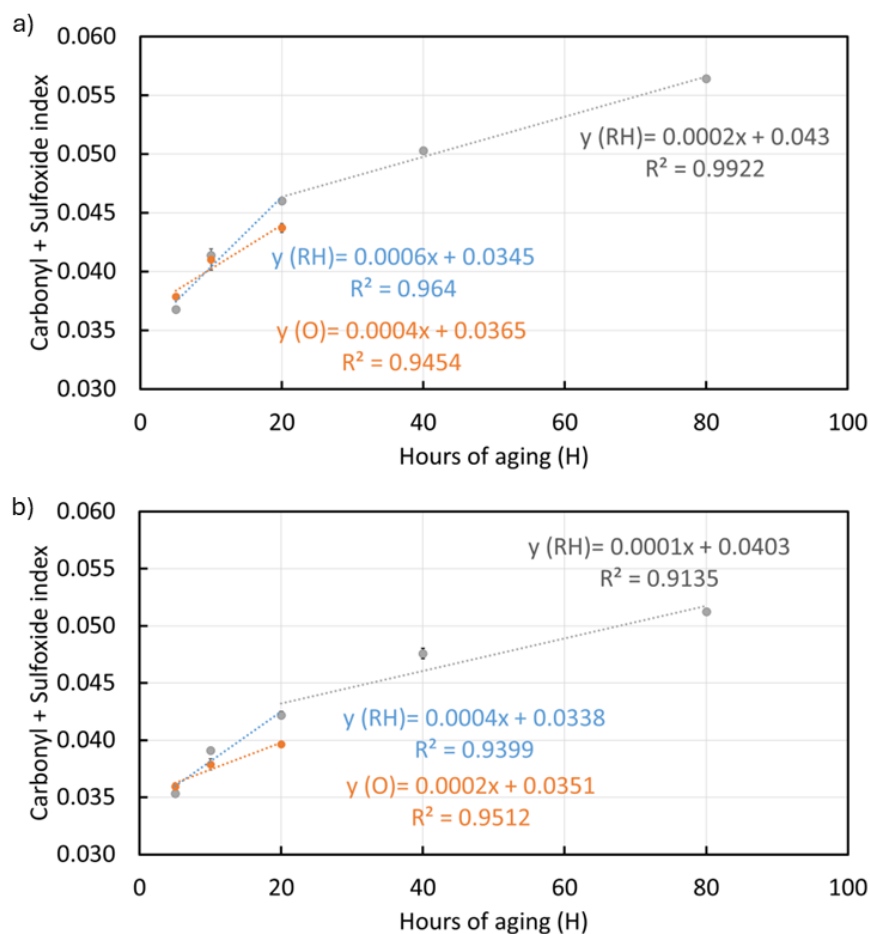


Figure 4.28 Summation of carbonyl and sulfoxide indices versus aging time (Hours) for a) Q binder, b) T binder. Blue and orange colors represent the hygrothermal aged and the thermo-oxidative aged samples, respectively.

This suggests that humidity accelerates the reaction, possibly due to hydrogen peroxide formation:



The potential formation and infiltration of H_2O_2 molecules into the binder binders can accelerate the oxidation of polycyclic perhydroaromatics [19]. At 85 °C, H_2O_2 can act as an oxidizing agent, reacting with electron-rich functional groups such as sulfur-containing species and unsaturated hydrocarbons. This could enhance the formation of sulfoxide (S=O) and carbonyl (C=O) functional groups via direct oxidation pathways.



Before 20 hours, a linear relationship between FTIR indices and time is observed. For durations beyond 20 hours, a linear relationship with a smaller slope was observed (Figure 4.28), consistent with prior studies [20, 21]. The two different slopes suggest two phases in long-term hygrothermal aging: an initial fast phase followed by a slower phase. Aging time less than 20 hours reveals faster reaction due to higher availability of oxidizable molecules at the onset of the reaction.

4.5.3 Effect of ROS on chemical properties of laboratory-aged binders

Figure 4.29 presents the FTIR spectra of the Q binder subjected to various aging conditions, including short-term aging via the TFOT method, UV aging, exposure to different concentrations and durations of H₂O₂, and VBA aging. The spectra indicate that different aging conditions affect the FTIR peaks to varying degrees especially in fingerprint region. Importantly, the aging protocol introduced in this chapter, which combines H₂O₂ and UV light, does not result in the appearance of new peaks in the spectra. This observation supports the hypothesis that radicals generated from the decomposition of H₂O₂ serve as catalysts, accelerating the oxidation process. The validity of this hypothesis will be further explored in this chapter through the calculation of indices for all peaks in the fingerprint region. Additionally, the deconvolution method, discussed in Chapter 6, will be employed to provide a more detailed analysis of the functional groups and their evolution over time.

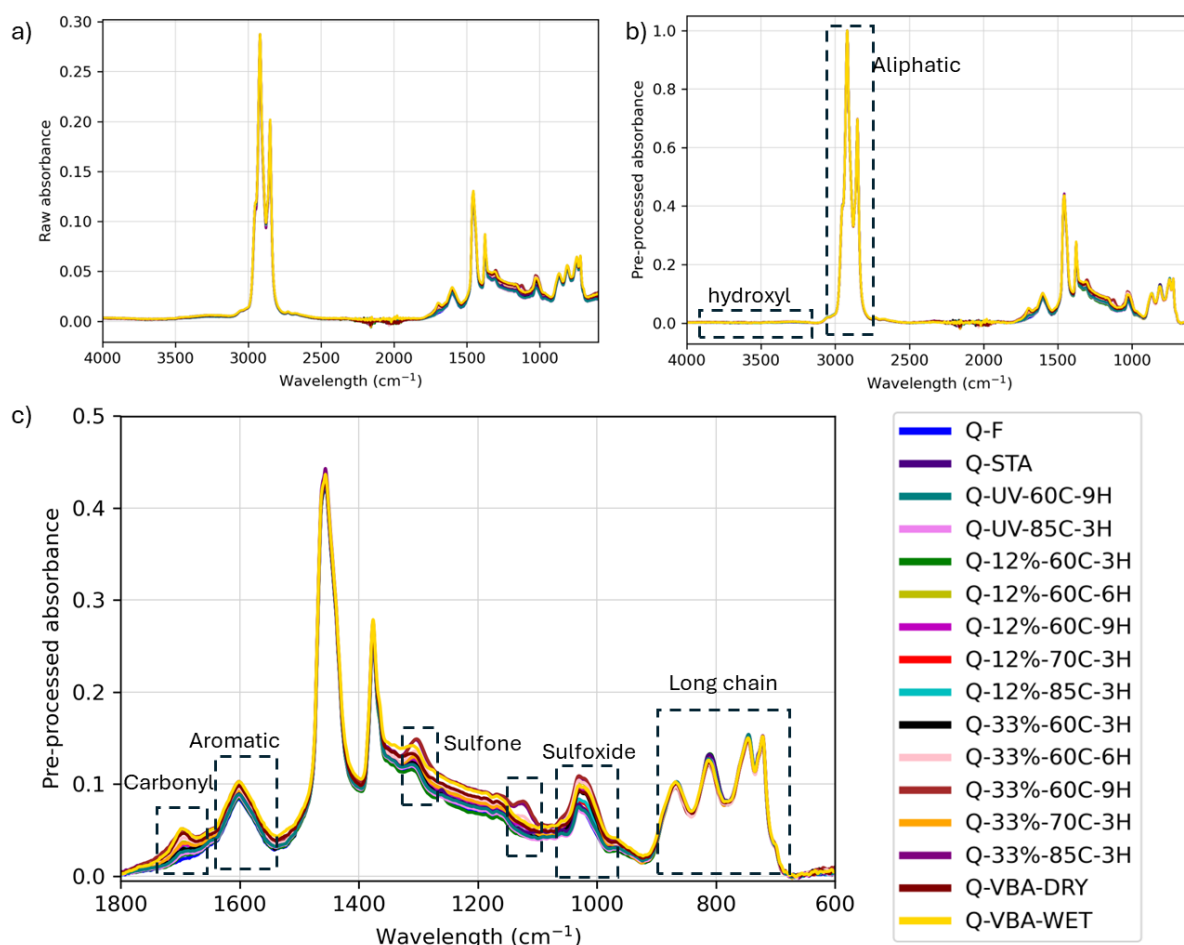


Figure 4.29 FTIR spectra illustrating fresh, short-term aged, long-term aged including all conditions of UPA, VBA, and PAV are presented in: a) raw spectral form, b) baseline-corrected and normalized spectra, and c) the 900-1800 cm⁻¹ region to highlight variations in carbonyl and sulfoxide peaks.

Figure 4.30 to Figure 4.34 display the ten FTIR indices as averages of four repetitions with standard deviations for Q and T binders, respectively.

The carbonyl and sulfoxide indices, identified as two most relevant FTIR indicators of aging levels, are specifically shown in Figure 4.30a-b. For both Q and T, UPA treatment increased carbonyl and sulfoxide indices for both 12% and 33% H₂O₂ concentrations, with a higher radical concentration led to more aggressive oxidation reactions especially at higher temperatures and longer durations. At

60°C, longer durations led to higher indices, indicating more aging. For a duration of 3 hours, the highest temperatures of 85°C caused the largest increase in both indices. Time and temperature exerted varying aging impact at two concentrations: time had a stronger effect at 12% H₂O₂, whereas temperature was more influential at 33 % H₂O₂.

The carbonyl and sulfoxide indices of other aging protocols are also presented in Figure 4.30a-b, including OVEN, UV, PAV-STD, 1M-85C-RH, VBA-DRY, and VBA-WET aging. For both Q and T, OVEN aging at 60°C for 9 hours resulted in a similar carbonyl index and a slightly lower sulfoxide index compared to the aging at 85°C for 3 hours. UV aging at 60°C for 9 hours increased both indices slightly more than UV aging at 85°C for 3 hours. As expected, adding humidity to PAV-STD and VBA-DRY increased carbonyl and sulfoxide indices, indicating that the combination of moisture and ROS accelerates the oxidative aging process. Compared to VBA-DRY, the T sampled aged by VBA-WET shows a much larger carbonyl index while for Q, the difference between VBA-DRY and VBA-WET is much smaller, indicating that the effect of moisture on aging process varies with binder type.

A comparison between UPA and other aging protocols revealed that, for both binders, exposure to a high concentration (33%) of H₂O₂ at 60°C for 9 hours and at 85°C for 3 hours resulted in carbonyl indices similar to those of 1M-85C-RH and VBA-WET (except for the T binder aged under VBA-WET conditions). This suggests that the UPA with high H₂O₂ for 3-9 hours are comparable to 20 hours of PAV and 3 days of VBA methods.

Compared to Q binders, most T binders revealed a higher sulfoxide index. These differences between Q and T may be attributed to the binders' unique chemical composition. Compared to Q, T binder contains lower oxygen and sulfur contents, higher nitrogen content, and a higher carbon-to-hydrogen ratio (indicating a higher degree of aromaticity and unsaturation), as shown in Table 1, which may undergo faster oxidation in the simultaneous presence of ROS and moisture. This suggests that the intrinsic chemical composition of the binder is an important factor affecting sensitivity of various binders to different aging factor combinations.

Furthermore, most T samples aged by UPA show higher carbonyl and sulfoxide indices than those of PAV and VBA methods, while for Q, the difference in both indices between UPA, PAV and VBA is smaller, suggesting that hydroxyl and perhydroxyl radicals contribute to more intense oxidation of sulfur- and carbon-containing species compared to conventional methods for T binders. This indicates that T binder is highly sensitive to ROS generated by H₂O₂ +UV, leading to rapid changes in its chemical composition and aging.

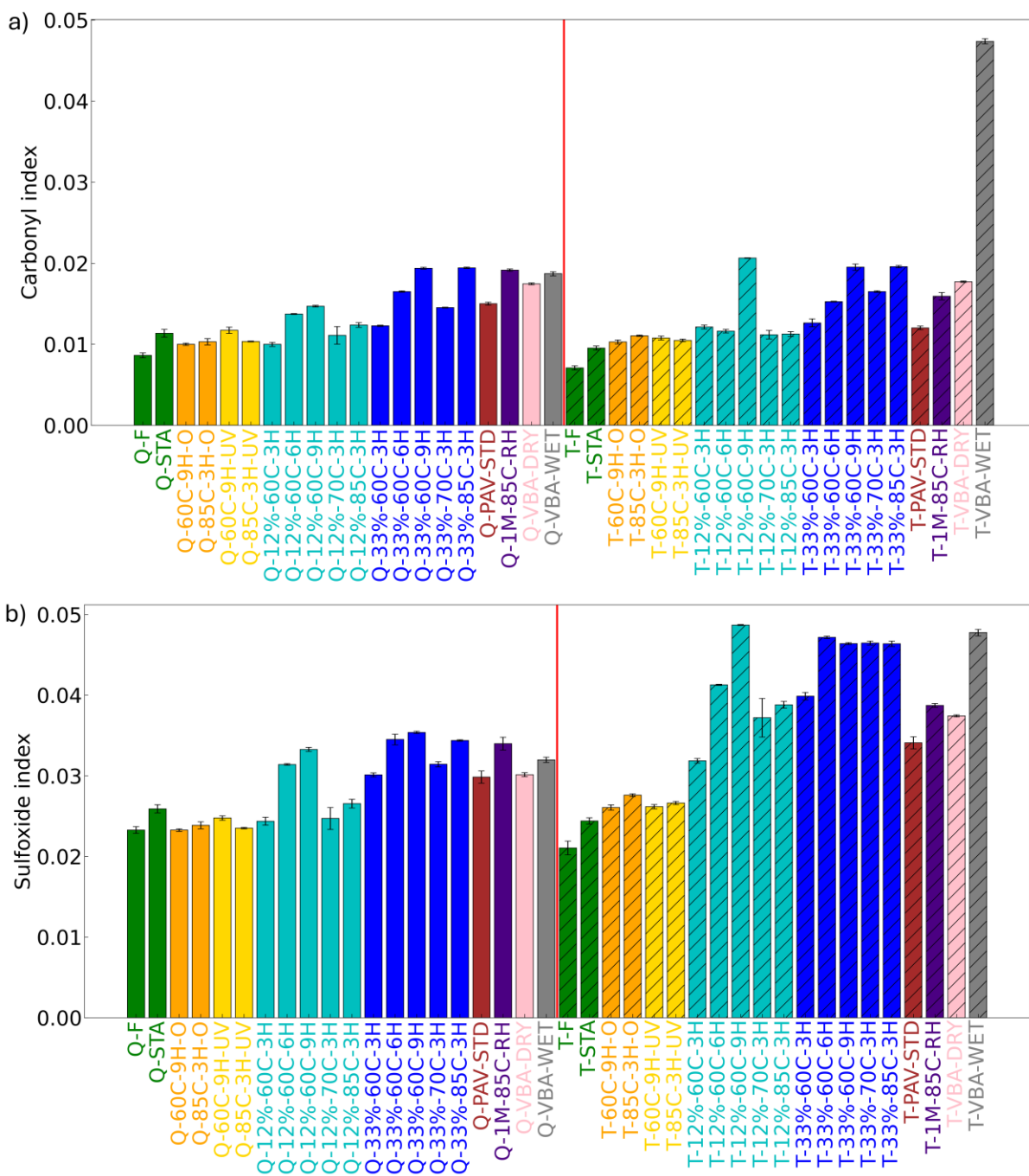


Figure 4.30 FTIR indices of Q and T binder at different aging conditions based on Table 4.4, a) carbonyl index, b) sulfoxide index.

Other indices showed trends similar to carbonyl and sulfoxide changes. Sulfones index (Figure 4.31) increased after both short-term and long-term aging. The sulfone region, representing sulfur-containing oxidation products, usually shifts to higher absorption with further aging. However, the absorption bands between 1350 and 1100 cm^{-1} may also arise from deformation vibrations of methylene and aromatic groups, or from skeletal vibrations of branched aliphatic motifs. To achieve a precise assignment of these overlapping bands, deconvolution of the FTIR spectra is necessary. This process will be discussed in detail later in this chapter.

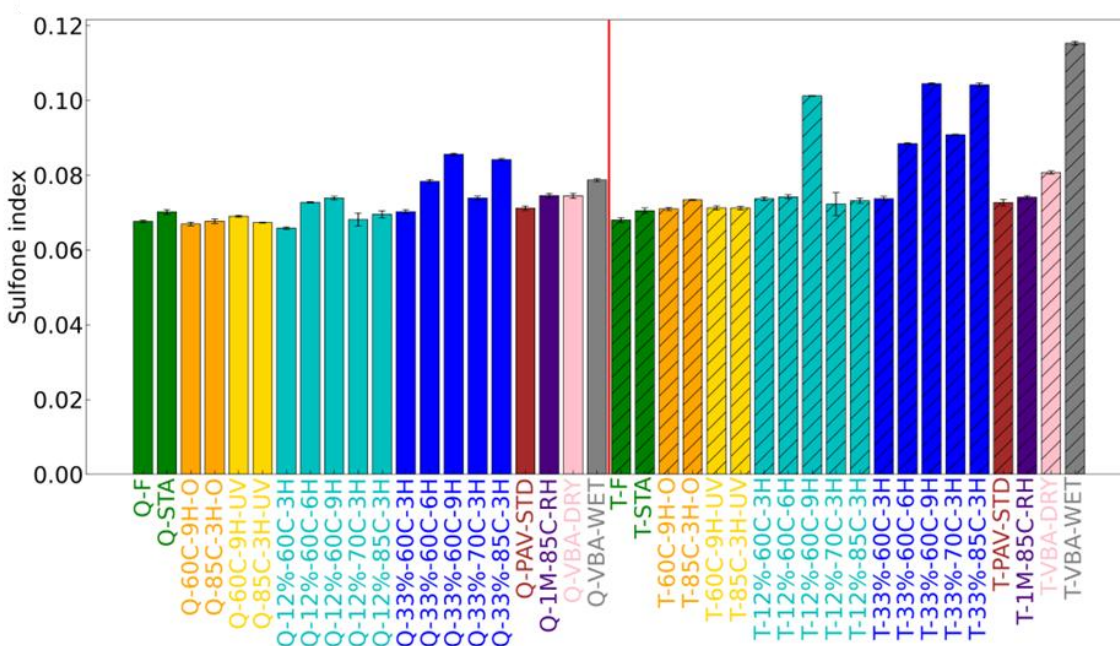


Figure 4.31 FTIR sulfone index of Q and T binder at different aging conditions based on Table 4.4.

Aging increases aromaticity, as reflected in the higher aromatics index after aging (Figure 4.32) [22]. The highest values were observed in 1M-85C-RH, VBA-WET, and high-concentration (33%) UPA samples aged at 60°C for 9 hours and 85°C for 3 hours, indicating greater sensitivity to ROS and water vapor. This suggests that higher H₂O₂ concentrations enhance oxidative polymerization, increasing aromatic content. As oxidation progresses, aliphatic components degrade, and smaller aromatic species polymerize into larger, more complex structures, contributing to bitumen stiffening and reduced ductility. The effect is particularly pronounced in 1M-85C-RH and VBA-WET samples, where moisture and high temperatures accelerate oxidation and polymerization.

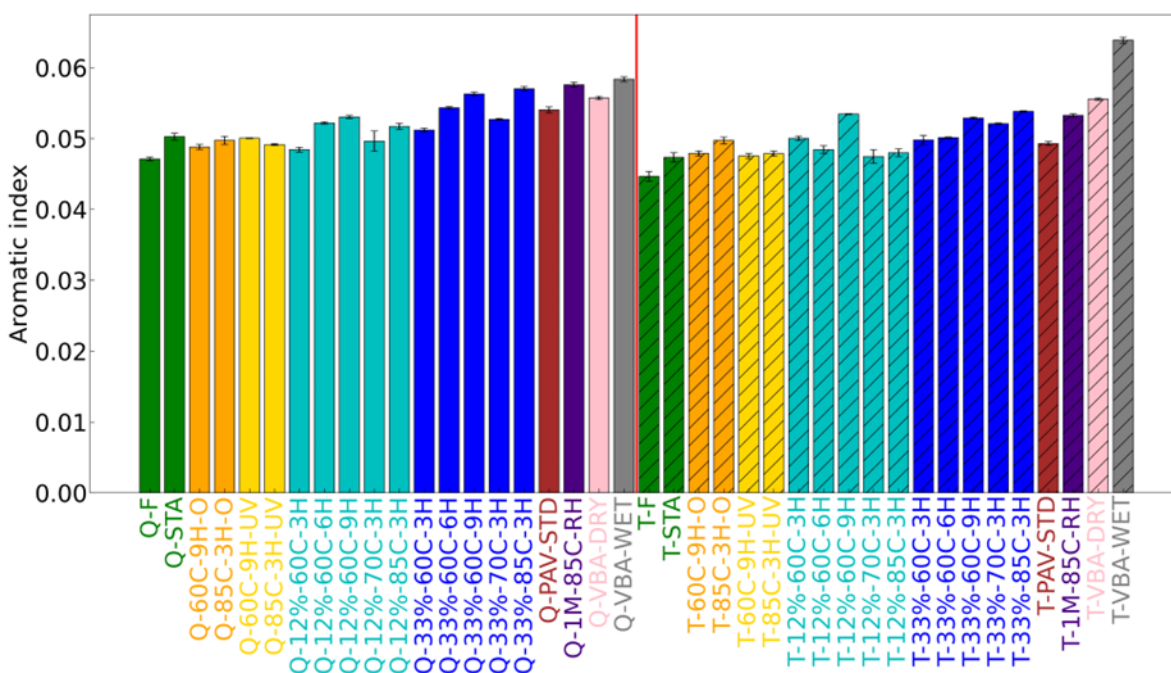


Figure 4.32 FTIR aromatic index of Q and T binder at different aging conditions based on Table 4.4.

The aliphatic index (Figure 4.33) decreased after aging, with 1M-85C-RH, VBA-WET, and high concentration (33%) UPA samples showing the strongest decreases. This suggests that increased ROS levels at higher H₂O₂ concentrations accelerate the breakdown of aliphatic structures. The observed decrease in aliphatic indices suggests that oxidation preferentially targets long-chain hydrocarbons, leading to chain scission and fragmentation. This breakdown reduces the proportion of flexible aliphatic structures in bitumen, contributing to increased stiffness and brittleness. The enhanced degradation observed in VBA and UPA samples can be attributed to the combined effects of moisture and ROS, which increase oxidative cleavage of alkyl side chains. Such degradation mechanisms agree with the chemical transformations reported in field-aged binders, further supporting the validity of UPA as a laboratory aging method.

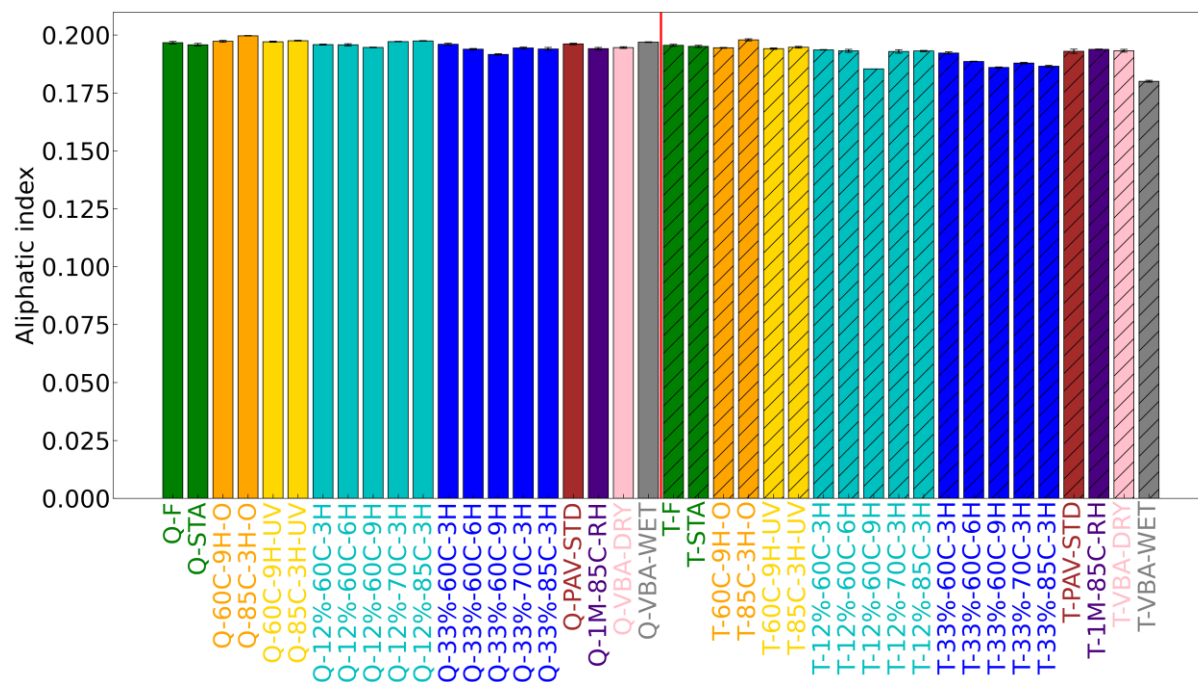
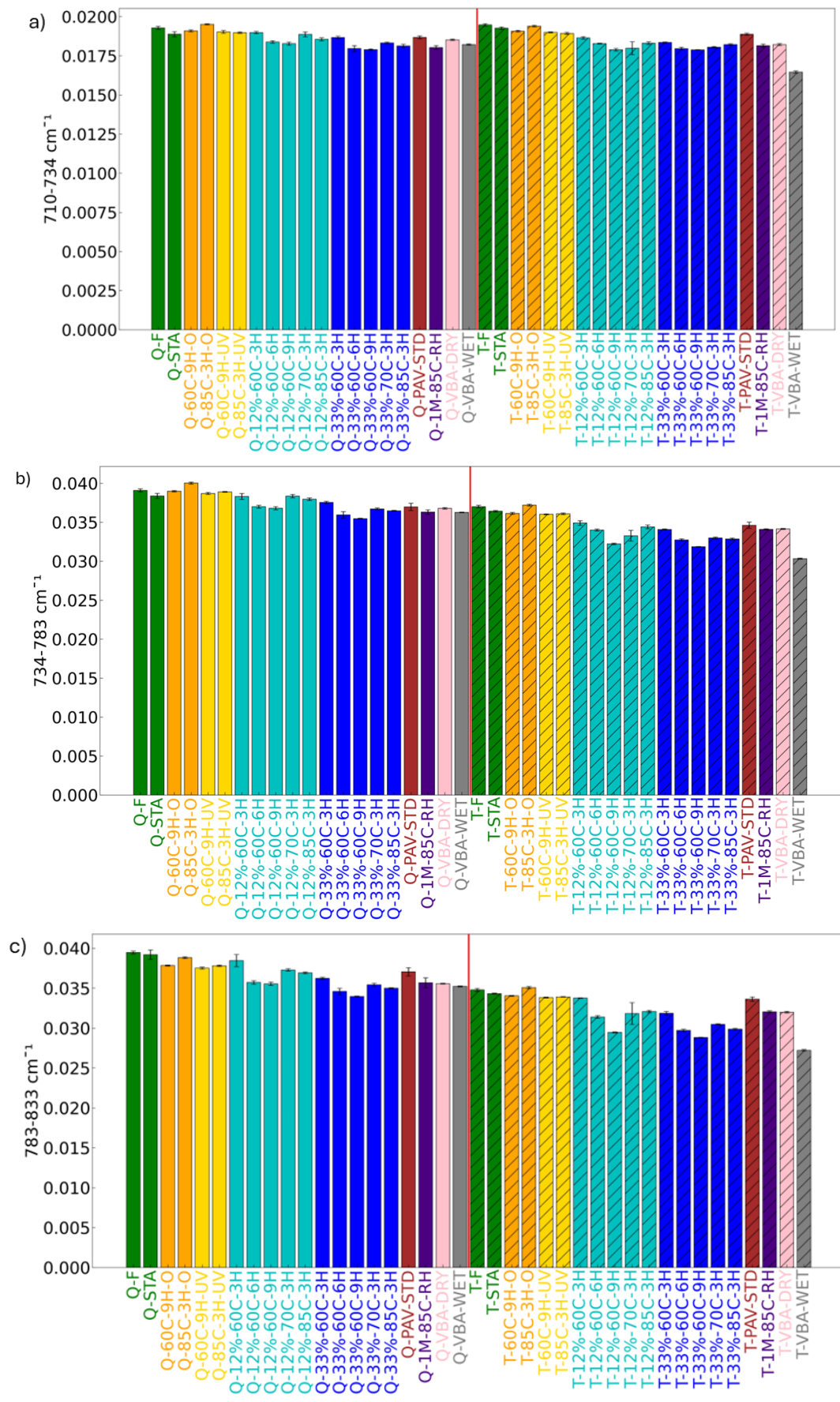


Figure 4.33 FTIR aliphatic index of Q and T binder at different aging conditions based on Table 4.4.

The long-chain indices (Figure 4.34a - d) also declined in aged samples compared to fresh conditions, with VBA-DRY and VBA-WET showing further decreases below field aging levels for the 710-734 cm⁻¹ range, indicating breakdown of long alkyl side chains. These four indices represent hydrocarbon chain, (CH₂)_n, C-H in isolated/two/four adjacent hydrogen aromatic rings or C-CH₂ rocking in alkyl side chains with more than four carbons.



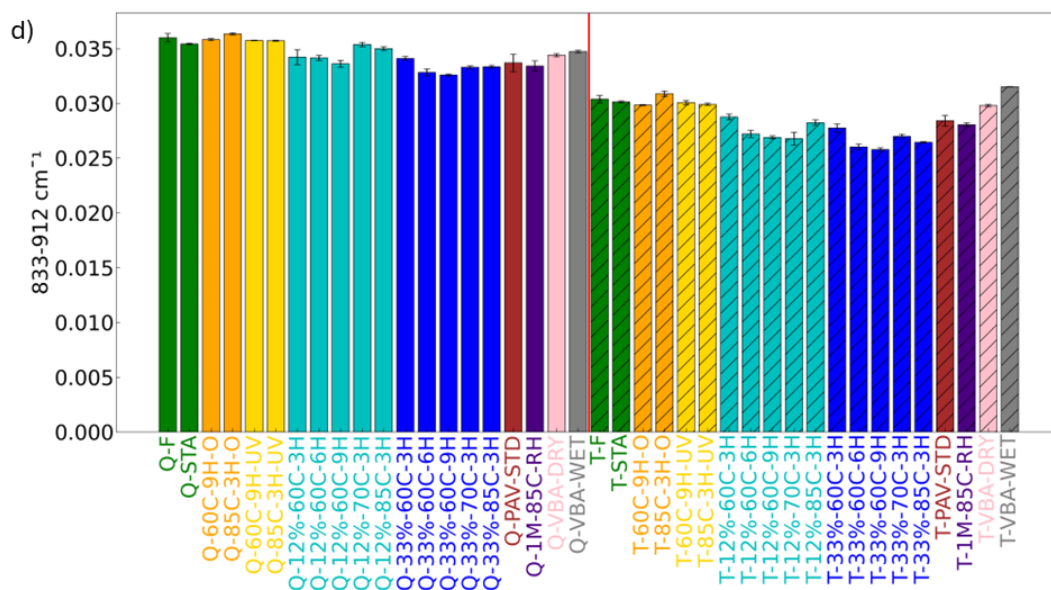


Figure 4.34 FTIR indices of Q and T binder at different aging conditions based on Table 4.4, long chain indices in the range of a) 710-734 cm^{-1} , b) 734-783 cm^{-1} , c) 783-833 cm^{-1} , d) 833-912 cm^{-1} .

To investigate the rate of oxidation with respect to temperature for different binders, the summation of the carbonyl and sulfoxide indices is plotted against temperature for both binders in Figure 4.35. Interestingly, the slope of the line for the higher concentration (33%) is 0.0005, which is steeper than the slope for the lower concentration (12%), which is 0.0002. The steeper slope (0.0005) observed at the 33% concentration suggests that the binder undergoes oxidation at a faster rate compared to when the concentration is 12%, as indicated by the smaller slope (0.0002). This could imply that a higher concentration of H_2O_2 makes the binder more susceptible to aging, reacting more intensively under the applied thermal conditions. Notably, these trends are consistent for both binders, which may suggest that their oxidation rates exhibit similar temperature sensitivity.

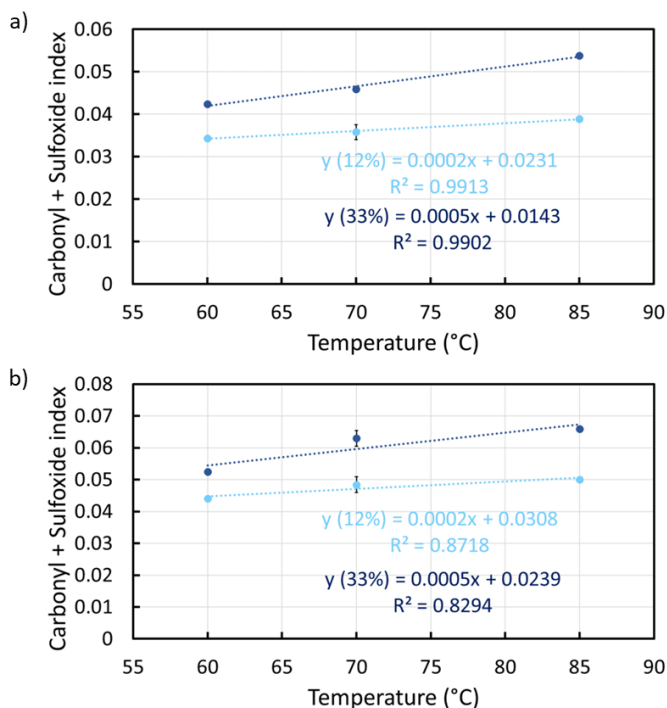


Figure 4.35 Summation of carbonyl and sulfoxide indices versus aging temperature for a) Q and b) T binders with a thickness of 1 mm. Blue color represents the UPA with 33% hydrogen peroxide and turquoise color represents the UPA with 12% hydrogen peroxide.

4.5.4 Assessing changes in chemical properties of field-aged recovered binders

The chemical composition of PA and SMA samples during 9 years of field aging were investigated using FTIR and the results are shown in Figure 4.36. For PA samples, both carbonyl and sulfoxide indices increased with time (Figure 4.36). Notably, the carbonyl index after 4 years of aging is unexpectedly higher than that of 5 to 9 years, likely due to the complexity of field aging. For SMA, samples from years 5 to 9 show minimal differences in indices. The sum of both indices exhibits a linear relationship with time for both PA and SMA (Figure 4.37). This field data will be compared with lab-aged samples in subsequent sections.

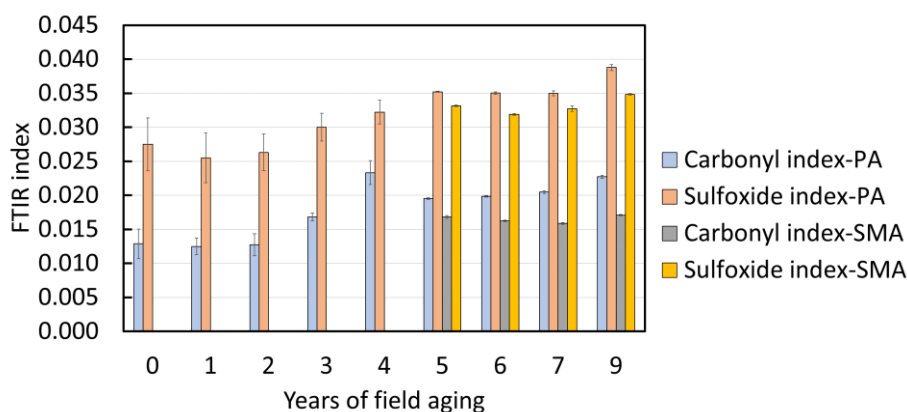


Figure 4.36 FTIR results, effect of field aging on PA and SMA mixture samples. In 2022 (year 8) no sampling was performed and for SMA samples, those from 2019 (year 5) to 2023 (year 9) were available.

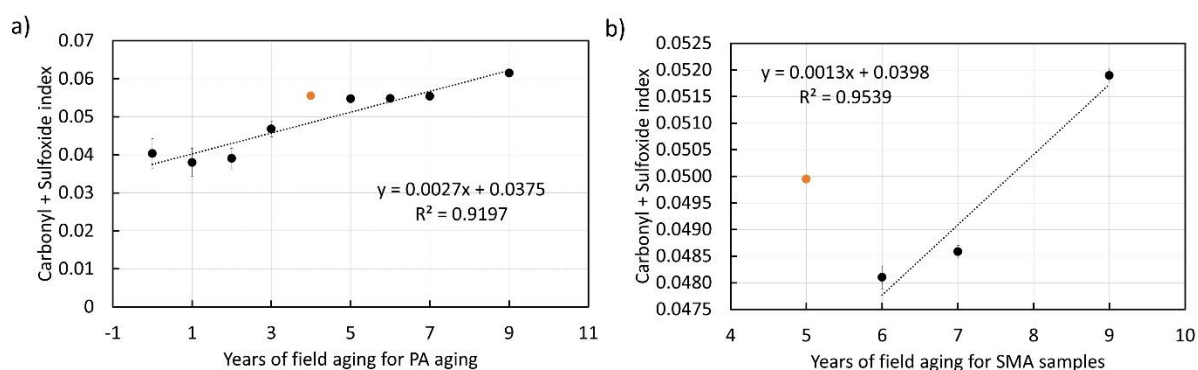


Figure 4.37 Combined FTIR index vs. years of aging, a) for PA samples, b) for SMA samples. For SMA samples, those from years 5 to 9 were available.

4.6 Comparison of aging rate for lab-aged samples based on chemical properties

In this chapter, new aging protocols have been developed to accelerate the oxidation rate of paving binders. This section focuses on identifying the protocol that achieves the highest oxidation rate by comparing the most aged samples from the previous sections. Since the primary objective is to evaluate the speed of aging, the extreme aging conditions discussed in Section 4.5.1 are not considered here, as these protocols involve durations of two to three weeks, which do not align with the goals of this section.

The aging protocols selected for comparison with the ROS aging method include hygrothermal aging in PAV for 20, 40, and 80 hours, thermo-oxidative aging at 150 bar for 20 hours, and standard PAV aging. To provide a comprehensive analysis, the aging changes and their rates for these different conditions were calculated based on all FTIR indices. This allows for a clearer understanding of how the different aging protocols impact the oxidation process.

Figure 4.38 shows the chemical aging rates for both Q and T binder samples, with UPA samples showing the highest aging rate. UPA of 12% and 33% for T binder showed higher rates compared to those of Q binder, indicating T binder's sensitivity to reactive species. UPA for 33%-85C-3H was the fastest aging process, followed by UPA for 33%-70C-3H for both binders. Other protocols had significantly lower acceleration rates due to weaker aging factors, requiring longer aging times to achieve a high aging level.

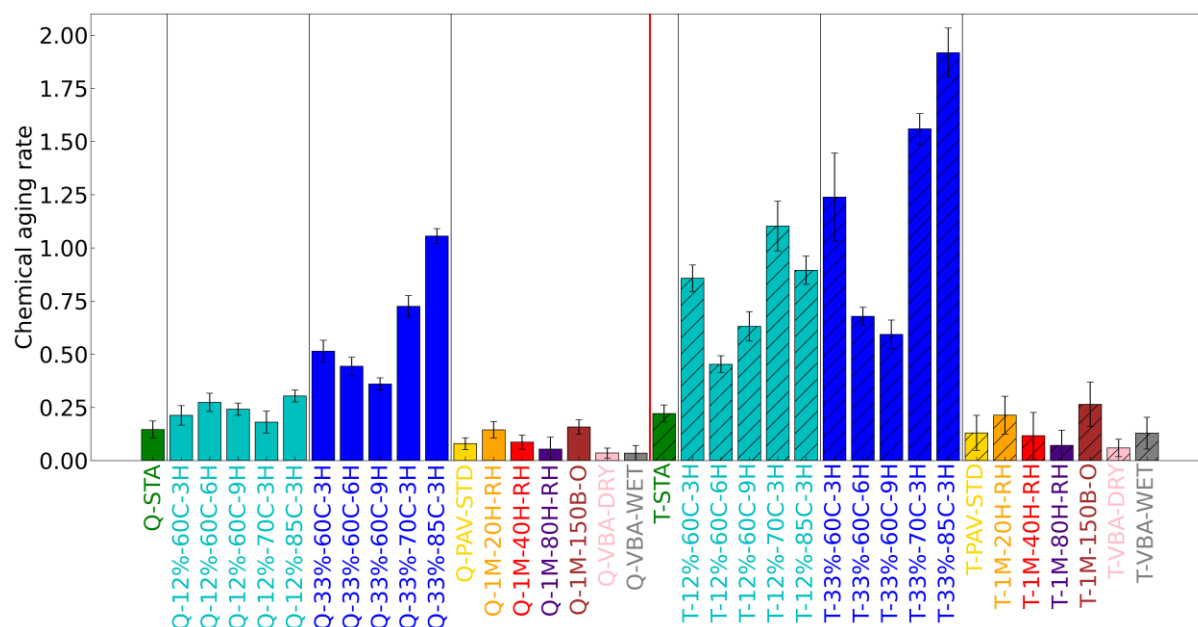


Figure 4.38 Chemical aging rate of aged samples of a) Q binder, and b) T binder.

4.7 Detailed chemical comparison of field- and lab-aged samples using FTIR deconvolution

To further explore the similarities and dissimilarities between field aged and lab-aged samples, a detailed deconvolution of the FTIR spectra was performed, focusing on the fingerprint region and 2600–3100 cm^{-1} region which are identified as significant by previous studies [8]. Deconvolution was necessary due to the substantial peak overlapping in these regions, where multiple functional groups contribute to absorption signals. In the fingerprint region (600–1800 cm^{-1}), peaks corresponding to carbonyl (C=O), sulfoxide (S=O), aromatic C=C stretching, and aliphatic bending modes often overlap, making it difficult to resolve individual contributions. Similarly, the 2600–3100 cm^{-1} region includes stretching vibrations from hydroxyl (O-H), aliphatic (C-H), and aromatic (C-H) groups, which can interfere with one another. The hypothesis is that deconvolution will enable a more precise identification of the chemical changes associated with different aging conditions by distinguishing overlapping contributions from these functional groups.

This section focuses on specific samples due to the computational expense of the deconvolution process. These samples include 9 years of field aging for porous asphalt as a reference, UPA with a 33% concentration of H₂O₂ at various temperatures and durations (since this concentration has been shown to result in a higher aging rate for both binders), standard PAV, modified PAV with humidity at 85°C for 20, 40, and 80 hours, thermos-oxidative aging under 150 bar, and VBA with and without humidity. This approach allowed for a more precise analysis of the functional groups involved in aging. The deconvoluted spectra of Field-9y are shown in Figure 4.39 a-d, covering the regions of 680–900 cm^{-1} (6 peaks), 900–1550 cm^{-1} (16 peaks), 1550–1750 cm^{-1} (5 peaks), and 2600–3100 cm^{-1} (5 peaks). Detailed information on the number of deconvoluted peaks, their positions, heights, and areas for all samples, along with visual representations of the deconvoluted spectra, are provided in Table 4.5 to Table 4.8.

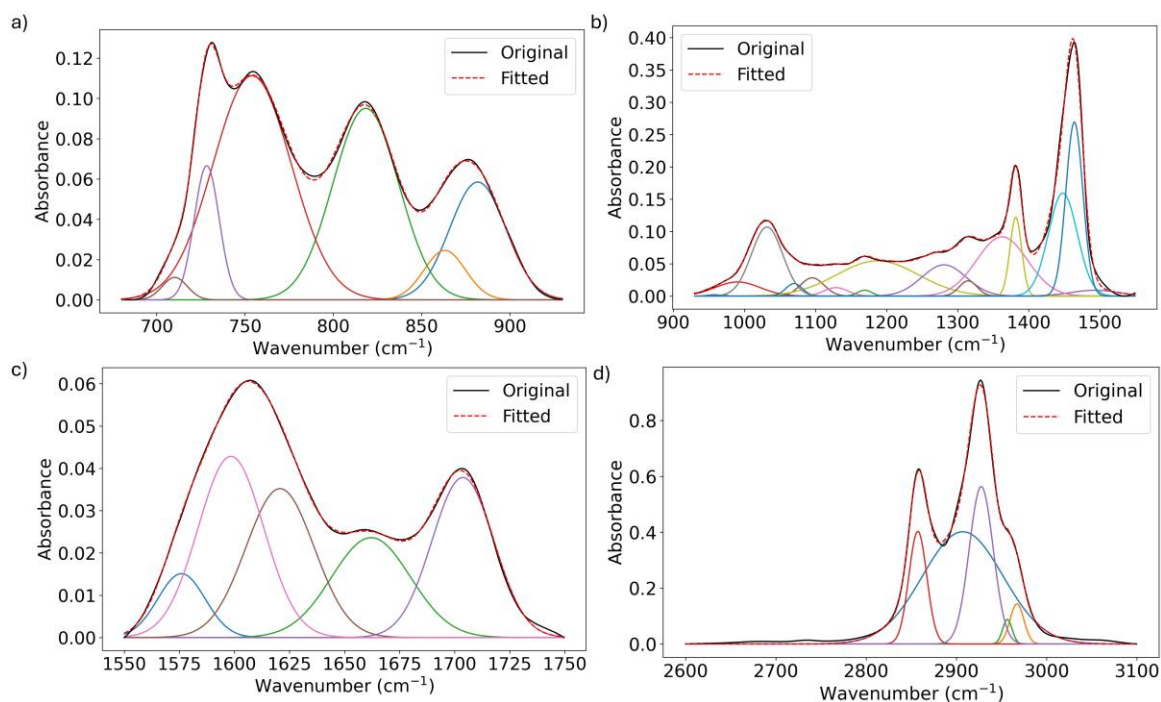


Figure 4.39 FTIR spectrum of the 9-year field-aged sample deconvoluted separately in different regions: a) 680-900 cm^{-1} , b) 900-1550 cm^{-1} , 1550-1750 cm^{-1} , and c) 2600-3100 cm^{-1} .

The exact deconvoluted peak positions and their corresponding functional groups can be found in Table 4.5 to Table 4.8. By resolving the overlapping peaks through deconvolution, it ensures that functional group changes contributing to binder oxidation are not masked by overlapping absorptions, allowing for a more accurate assessment of aging mechanisms. It enables a deeper comparison of field and lab aging effects on binder samples. This analysis helps determine which laboratory aging conditions produce chemical changes most similar to those observed in field-aged binders, providing insight into the representativeness of different aging protocols.

The region of 680-900 cm^{-1} primarily contains bands associated with out-of-plane ($\delta_{\text{o-p}}$) C–H bending in aromatic rings and the bending vibrations of secondary amides and alkyl side chains. The key peaks in this region (Table 4.5) include 710.25 cm^{-1} (aromatic ring bending and N–H bending in secondary amides), 728.33 cm^{-1} (C–H out-of-plane bending in four adjacent hydrogen aromatic rings and C–CH₂ rocking in alkyl side chains), and 754.02 cm^{-1} (out-of-plane C–H bending in aromatic rings). These peaks are relevant to binder aging as they indicate structural changes in aromatics and aliphatic side chains due to oxidation. The decrease in the long chain index and peak areas for this region suggests a reduction in the corresponding functional groups. The reduction in this region can be attributed to the oxidative degradation of aromatic hydrocarbons and the breakdown of secondary amides and alkyl side chains. During oxidative aging, the C–H groups adjacent to the aromatic ring in bitumen may be substituted by polar oxidized groups, leading to a reduction in the intensity of aromatic C–H bending vibrations. Additionally, secondary amides might be cleaved, leading to a reduction in the N–H bending intensity. Alkyl side chains, particularly those with four or more carbons, can undergo oxidation, resulting in shorter chains or the formation of oxidized products, thereby decreasing the C–CH₂ rocking vibrations.

Table 4.5 The assignment of bands in FTIR deconvoluted spectrum of 9-years filed aged sample in the region of 680-900 cm^{-1} .

Peak position	Representative functional groups
710.25 cm^{-1}	$\delta_{\text{C-C}}$ of the aromatic ring (ring-bending) and $\delta_{\text{o-p}}$ N–H in secondary amides.
728.33 cm^{-1}	$\delta_{\text{o-p}}$ C–H in four adjacent hydrogen aromatic rings and δ C–CH ₂ rocking in alkyl side chains with more than four carbons.

754.02 cm ⁻¹	δo-p C–H in four adjacent hydrogen aromatic rings.
818.36 cm ⁻¹	δo-p C–H in two adjacent hydrogen aromatic rings.
863.06 cm ⁻¹	δo-p C–H in isolated adjacent hydrogen aromatic rings near 875.67 cm ⁻¹
881.72 cm ⁻¹	δo-p C–H in isolated adjacent hydrogen aromatic rings similar to the peak at 875.67 cm ⁻¹

The 900-1550 cm⁻¹ region is rich in functional groups associated with C-H bending, C-O stretching in ethers, esters, and phenols, as well as sulfoxide and aromatic C=C stretching vibrations. Notable peaks in this region (Table 4.6) include 1031.75 cm⁻¹ (S=O stretching in sulfoxides), 1069.83–1187.23 cm⁻¹ (C–O stretching in alcohols, ethers, esters, and phenols), and 1492.66 cm⁻¹ (aromatic C=C stretching). These peaks are crucial in assessing oxidation, as sulfoxide formation and increases in C–O stretching indicate oxidative aging, while changes in aromatic C=C suggest molecular restructuring. The increase in the index for this region suggests an increase in these functional groups, which can be explained by the formation of oxidation products. Aromatic rings in bitumen can be functionalized through oxidation, leading to the formation of oxygen-containing functional groups such as ethers, esters, phenols, and sulfoxides. These groups contribute to the increase in C-O stretching (1069 to 1187 cm⁻¹) and S=O stretching (1031 cm⁻¹). Additionally, the formation of aromatic sulfoxides and the introduction of hydroxyl or alkoxy groups into the aromatic rings result in increased bending and stretching vibrations characteristic of these groups. The C-H bending modes associated with the aromatic ring structures also increase as new substituted aromatics are formed.

Table 4.6 The assignment of bands in FTIR deconvoluted spectrum of 9-years filed aged sample in the region of 900-1550 cm⁻¹.

Peak position	Representative functional groups
957.74 cm ⁻¹	C-H out-of-plane bending in aromatic rings or stretching in certain vinyl groups
971.72 cm ⁻¹	δi-p C–H bending in aromatics and Uas C–O–C in mixed ethers.
990.28 cm ⁻¹	C-H in-plane bending of aromatics or C-O stretching
1031.75 cm ⁻¹	U S=O in alkane-substituted sulfoxides.
1069.83 cm ⁻¹	U C-O bonds in alcohols, ethers, and esters.
1095.39 cm ⁻¹	U C-O bonds in alcohols, ethers, and esters.
1128.65 cm ⁻¹	C-O stretching in ethers and esters or C-C-O stretching in phenols
1169.15 cm ⁻¹	C-O stretching possibly in esters or phenols
1187.23 cm ⁻¹	C-O stretching possibly in esters or phenols
1280.76 cm ⁻¹	C-H bending in aromatic compounds.
1314.75 cm ⁻¹	C-H bending in aromatic compounds.
1362.48 cm ⁻¹	C-H bending in aromatic compounds.
1381.77 cm ⁻¹	C-H bending in aromatic compounds.
1448.06 cm ⁻¹	CH ₃ asymmetric bending, CH ₂ scissors, or both.
1464.21 cm ⁻¹	CH ₃ asymmetric bending, CH ₂ scissors, or both.
1492.66 cm ⁻¹	C=C aromatic stretching.

The 1550-1750 cm⁻¹ region is primarily characterized by the stretching vibrations of carbonyl groups (C=O) and aromatic C=C bonds. This region (Table 4.7) includes peaks at 1620.11 cm⁻¹ (C=O stretching in diaryl ketones), 1664.61 cm⁻¹ (C=O stretching vibration of secondary amides), and 1702.98 cm⁻¹ (C=O stretching in aromatic carboxylic acids). These peaks are essential in tracking aging since the growth of oxygenated functional groups, such as esters, ketones, and carboxylic acids, signifies oxidative degradation of the binder. The

increase in the index for this region suggests a growth in oxygenated functional groups, such as esters, carboxylic acids, and amides, which are products of oxidative aging. The presence of the carbonyl stretching vibrations is linked to the formation of conjugated systems, including ketones and carboxyl compounds, as well as the evolution of aromatic groups in the material. These carbonyl-related bands indicate the ongoing oxidation and breakdown of aliphatic chains, leading to the incorporation of oxygenated species. Additionally, the increase in aromatic C=C stretching and the reduction of aliphatic components further emphasize the aging process, where aromatic condensation and oxidation contribute to the changes in the chemical composition of the material.

Table 4.7 The assignment of bands in FTIR deconvoluted spectrum of 9-years filed aged sample in the region of 1550-1750 cm^{-1} .

Peak position	Representative functional groups
1575.03 cm^{-1}	C=C aromatic stretching and in-plane bending of N-H in secondary amides.
1597.93 cm^{-1}	Aromatic C=C stretching.
1620.11 cm^{-1}	C=O stretching in diaryl ketones.
1664.61 cm^{-1}	C=O stretching vibration of secondary amides.
1702.98 cm^{-1}	C=O stretching in aromatic carboxylic acids.

The 2600-3100 cm^{-1} region is dominated by C-H stretching vibrations of methyl and methylene groups. Significant peaks include 2857.35 cm^{-1} (symmetric C-H stretching of methyl), 2905.53–2927.46 cm^{-1} (asymmetric C-H stretching of methylene), and 2967.08 cm^{-1} (asymmetric C-H stretching of methyl)(Table 4.8). These peaks are vital in detecting binder oxidation, as a decrease in their intensity corresponds to a reduction in aliphatic hydrocarbons due to oxidative degradation. The decrease in this region index indicates a reduction in aliphatic hydrocarbons, particularly methyl and methylene groups. This reduction is likely due to oxidative degradation processes such as the breaking of C-H bonds in aliphatic chains, leading to the formation of carbonyl-containing compounds (e.g., aldehydes, ketones, and carboxylic acids) or the complete cleavage of these chains, leading to the loss of methyl and methylene groups. This process is consistent with the general understanding of bitumen aging, where the material becomes more oxygenated, leading to a decrease in the intensity of aliphatic C-H stretches.

Table 4.8 The assignment of bands in FTIR deconvoluted spectrum of 9-years filed aged sample in the region of 2600-3100 cm^{-1} .

Peak position	Representative functional groups
2857.35 cm^{-1}	Symmetric C-H stretching of methyl.
2905.53 cm^{-1}	Asymmetric C-H stretching of methylene.
2927.46 cm^{-1}	Asymmetric C-H stretching of methylene.
2956.43 cm^{-1}	Asymmetric C-H stretching of methyl.
2967.08 cm^{-1}	Asymmetric C-H stretching of methyl.

The peak positions within these regions are specific to each sample and reflect their aging level. To compare these peak positions effectively, the dynamic time warping (DTW) method was employed. DTW is particularly valuable for aging analysis as it accounts for non-linear shifts in peak positions, which often occur due to different oxidation rates and structural modifications in binders. This method enables a direct comparison between samples by aligning deconvoluted peak positions, ensuring that variations in chemical changes due to different aging protocols can be systematically assessed.

Table 4.9 presents the alignment cost and Euclidean distance of peak areas corresponding to the aligned peak positions of the selected samples closest to Field-9y. The alignment cost quantifies the extent to which peak positions need to be adjusted to match the reference spectrum (the field sample), with lower alignment costs suggesting that the peaks are more closely aligned, indicating minimal shifts in chemical structures due to different aging conditions and thus greater chemical similarity to field aging. Similarly, lower Euclidean distance of peak areas evaluates how closely the intensity of corresponding peaks matches the field sample, providing additional insight into chemical transformations beyond just peak shifts.

The analysis identified the samples Q-1M-150B-O, Q-33%-60C-6H, and Q-1M-20H/40H-RH as the closest to the field-aged sample based on peak position shifts, while Q-PAV-STD was the most distant. However, when the peak areas were considered, 33%-60C-6H and Q-1M-40H-RH remained the closest samples, though the ranking of other samples changed. This difference between peak shifts and peak area similarity underscores the importance of using both metrics for a comprehensive evaluation of aging effects.

Other samples examined in this section, except for 33%-70°C-3H, exhibit similar Euclidean distance values for peak areas corresponding to aligned peak positions, indicating comparable chemical performance. Given their chemical similarity, the aging duration becomes a decisive factor in selecting the optimal condition. Among these, the UPA samples have the shortest aging times. Consequently, after 33%-60°C-6H and Q-1M-40H-RH, the Q-33%-60°C-9H condition emerges as the closest to field-aged samples while also being the most time-efficient.

This result underscores the value of DTW analysis in distinguishing between aging conditions based on both peak shifts and intensity changes, ensuring a more accurate representation of field aging. Interestingly, considering both peak positions and peak areas suggests that incorporating ROS molecules into aging conditions at 60 °C for 6 hours enhances the resemblance to field aging more effectively than high-pressure aging. Additionally, ROS molecules in liquid form were found to induce faster oxidation compared to gaseous ROS, making them a more effective means of simulating field aging.

Table 4.9 Alignment cost and Euclidean distance of peak areas corresponding to the aligned peak positions of the samples closest to Field-9y based on PCA analysis.

Samples	Peak position shifts/DTW Alignment cost (cm⁻¹)	Samples	Euclidean distance of peak areas corresponds to aligned peak positions
Field-9y	0.00	Field-9y	0.00
Q-1M-150B-O	246.66	Q-33%-60C-6H	12.68
Q-33%-60C-6H	288.03	Q-1M-40H-RH	13.68
Q-1M-20H-RH	291.85	Q-1M-20H-RH	32.58
Q-1M-40H-RH	304.12	Q-PAV-STD	32.59
Q-33%-60C-3H	312.95	Q-VBA-DRY	32.77
Q-1M-80H-RH	322.92	Q-33%-60C-9H	32.79
Q-VBA-WET	333.83	Q-VBA-WET	32.95
Q-33%-70C-3H	341.88	Q-1M-150B-O	33.20
Q-VBA-DRY	345.71	Q-33%-60C-3H	33.33
Q-33%-85C-3H	369.72	Q-1M-80H-RH	33.37
Q-33%-60C-9H	381.35	Q-33%-85C-3H	33.49
Q-PAV-STD	396.06	Q-33%-70C-3H	36.36

The discrepancy in aging order (field sample as the reference) between the two methods, direct index calculation and deconvolution, likely results from their differing analytical approaches. Direct index calculation focuses on the overall spectral region, capturing the cumulative effect of multiple overlapping bands and providing a broader measure of chemical changes. In contrast, deconvolution isolates individual peaks, allowing for a more specific assessment of distinct functional group changes. The differences in how these methods handle spectral overlap, sensitivity to minor chemical changes, and the contributions of various functional groups, as well as potential artifacts from the deconvolution process, can lead to variations in the observed aging order.

4.8 UPA aging mechanisms

The mechanism of accelerated oxidation of UPA can be explained by the combined effects of UV radiation, elevated temperature, and the oxidative power of hydrogen peroxide.

The possible aging mechanism under this protocol can be summarized as follows:

In initiation phase, the exposure of hydrogen peroxide to UV light leads to its photolysis, producing hydroxyl radicals (HO•) (Figure 4.40) as described in reaction (4.8). This reaction is the rate-limiting reaction, since the other reactions' rates (reactions 4.9-4.19) are way higher than Equation 4.8.

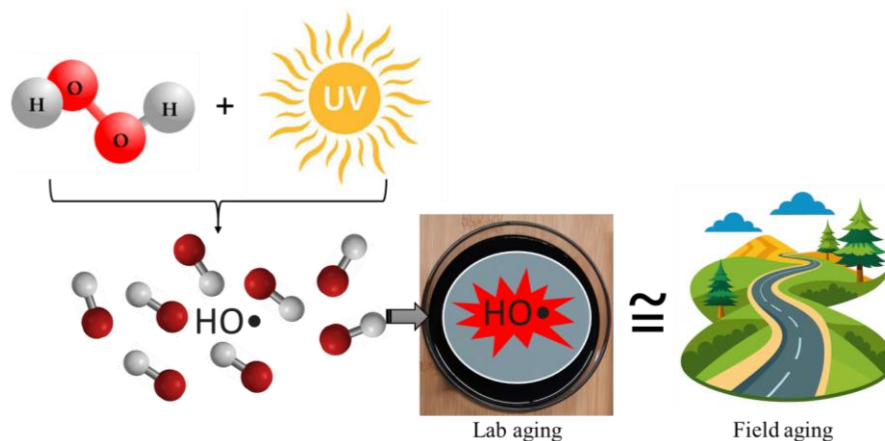


Figure 4.40 Schematic representation of binder aging under environmental conditions: UV radiation and hydrogen peroxide (H₂O₂) contribute to the formation of hydroxyl radicals (HO•), accelerating oxidation and degradation processes in asphalt pavements.

Given the similarity to field aging where oxidative degradation is a key process, the formation of HO• can be seen as analogous to the initiation of oxidation in the field, where atmospheric oxygen and environmental factors contribute to the formation of reactive oxygen species (ROS) such as HO•.

In propagation phase, hydroxyl radicals react with H₂O₂ to form perhydroxy radicals (HO₂•) and water (Equation 4.9). HO₂• further reacts with H₂O₂ to regenerate HO•, producing water and oxygen (Equation 4.10).



Binder aging happens at this stage when hydroxyl radicals abstract hydrogen from binder (RH), forming alkyl radicals (R•) (Equation 4.11). Then, alkyl radicals react with oxygen to form peroxy

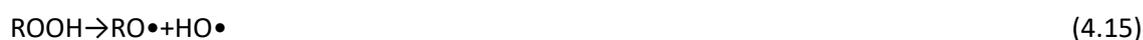
radicals ($\text{RO}_2\bullet$), and peroxy radicals react with more binder, forming hydroperoxides (ROOH) and regenerating alkyl radicals (Equation 4.12 and 4.13).



Moreover, hydroperoxides (ROOH) react with sulfides in the binder to form sulfoxides (Equation 4.14).



Furthermore, hydroperoxides decompose, especially at higher temperatures, to form free radicals which then react with benzylic carbons and lead to ketone formation (Equation 4.15 and 4.16).



The elevated temperature (85°C) enhances the reactivity of these radicals and the overall rate of chemical reactions. The formation of these oxidation products is consistent with the increase in C-O stretching and sulfoxide vibrations observed in the field-aged sample. The formation of ketones corresponds to the carbonyl-containing compounds observed in the field-aged sample, such as aldehydes, ketones, and carboxylic acids. The reduction in aliphatic C-H stretches in the $2600\text{--}3100\text{ cm}^{-1}$ region in field-aged samples suggests similar oxidative cleavage of C-H bonds leading to carbonyl formation.

While termination reactions by radical recombination (Equation 4.17-4.19) leads to the formation of less reactive species eventually reduce the concentration of radicals.



The field aging process involves the oxidative degradation of aromatic hydrocarbons, breakdown of secondary amides, and shortening of alkyl side chains, which are paralleled by the reactions in the UPA protocol. The observed decrease in long-chain index and the formation of oxidized products in both cases reflect similar chemical pathways. By focusing on these detailed oxidative mechanisms, the UPA protocol can be better understood as an accelerated aging process that replicates the primary chemical transformations occurring in field-aged bitumen. The correlation between the increase in sulfoxide content, carbonyl formation, and the oxidative breakdown of aliphatic structures reinforces the validity of UPA as a laboratory aging protocol that mimic field conditions.

This method's ability to reproduce a highly oxidative environment that mirrors the natural aging processes, and the complex interplay of photochemical, thermal, and oxidative processes makes it more representative of field aging compared to other laboratory methods that may lack one or more of these critical factors. The hydroxyl and perhydroxy radicals generated through the photolysis and subsequent reactions of H_2O_2 rapidly attack the binder, leading to the formation of hydroperoxides,

sulfoxides, and ketones, thereby increasing the rate of oxidation compared to typical lab and field aging conditions.

4.9 Conclusions

This chapter investigated the oxidative aging of bituminous binders under various conditions to understand the role of environmental factors and to develop effective laboratory aging protocols, focusing specifically on the chemical changes associated with oxidation as assessed through FTIR spectroscopy. As such, the analysis is limited to chemical aging indicators, without direct assessment of rheological property changes (chapter 5).

By investigating the influence of water molecules on aging (RSQ 1), the findings demonstrate that the presence and form of water critically influence the oxidative aging of bituminous binders. Hygrothermal conditions, particularly at elevated temperatures, substantially accelerate aging due to enhanced oxygen diffusion, highlighting the need to account for humidity effects in laboratory aging protocols. Conversely, aqueous-thermal conditions slow oxidation, underlining the protective role of water immersion by limiting oxygen availability. These insights underscore the importance of differentiating between vapor and liquid moisture effects when simulating field aging in laboratory environments.

By examining the combined effects of moisture, temperature, pressure, film thickness, and aging time on oxidation and degradation (RSQ 2), the results showed that aging severity is governed by the interaction of these factors. Higher temperatures increased oxidation through enhanced molecular kinetic energy, while elevated pressures, particularly in thinner films, promoted aging by facilitating oxygen diffusion. A two-phase aging pattern was observed, consisting of an initial rapid oxidation followed by a slower phase, likely due to the consumption of readily oxidizable components. Binder composition also influenced aging susceptibility, with different sources exhibiting varying oxidation levels under identical conditions.

By evaluating the role of reactive oxygen species (ROS), specifically hydroxyl radicals generated through UV and hydrogen peroxide (H_2O_2) exposure in the liquid phase (RSQ 3), it was shown that ROS significantly accelerated oxidation without altering the fundamental chemical structure of the binders. The UV-Peroxide Aging (UPA) protocol, combining ROS generation and UV exposure, promoted oxidation while maintaining chemical similarity to field-aged binders. Oxidation efficiency depended on parameters such as H_2O_2 concentration, temperature, and exposure time, with 33% H_2O_2 at 85°C producing the highest oxidation. Binder composition influenced oxidation sensitivity, with T binders showing greater response to ROS-induced aging than Q binders, highlighting the need for binder-specific evaluation.

By comparing the UPA protocol with conventional aging methods (RSQ 4), it was found that UPA promotes oxidation more effectively by integrating temperature, reactive oxygen species, and UV radiation. In contrast to standard thermo-oxidative protocols that depend on prolonged heating, UPA induces rapid oxidation over shorter durations. The presence of hydroxyl and perhydroxyl radicals in the UPA method likely enhances oxidative reactions, further distinguishing it from standard aging techniques.

By evaluating the chemical similarity between laboratory-aged and field-aged binders (RSQ 5), the UPA protocol was shown to reproduce the chemical changes observed in binders aged nine years in the field. Using spectral deconvolution, Dynamic Time Warping (DTW), and Euclidean distance analyses, aging conditions involving 33% H_2O_2 at 60°C for 6 hours, as well as Q-1M-40H-RH, were identified as closely resembling field-aged profiles. Among these, 33% H_2O_2 at 60°C for 9 hours

offered the most accurate and efficient simulation of long-term oxidation. However, confirmation through rheological assessment is necessary to evaluate long-term performance, as addressed in Chapter 5.

These results confirm the significant influence of environmental variables, moisture, temperature, pressure, and ROS, on oxidative aging of bituminous binders. Hygrothermal aging at elevated temperatures accelerated oxidation, likely due to enhanced formation or mobility of reactive species, while aqueous-thermal conditions limited oxidation by restricting oxygen access. The demonstrated effectiveness of UPA in replicating field aging supports its use as a reliable accelerated aging method. The differing sensitivities of Q and T binders across aging scenarios underscore the importance of binder-specific assessments. Further investigation incorporating intermediate aging durations and SARA fractionation is recommended to improve understanding of progressive chemical changes and inform predictive models for binder durability.

4.10 References

1. Hofer, K., et al., *Chemical and mechanical analysis of field and laboratory aged bitumen*. Road Materials and Pavement Design, 2023. **24**(sup1): p. 160-175.
2. Mierzwa, J.C., R. Rodrigues, and A.C. Teixeira, *UV-hydrogen peroxide processes*, in *Advanced oxidation processes for waste water treatment*. 2018, Elsevier. p. 13-48.
3. Boczkaj, G., A. Fernandes, and P. Makoś, *Study of different advanced oxidation processes for wastewater treatment from petroleum bitumen production at basic pH*. Industrial & Engineering Chemistry Research, 2017. **56**(31): p. 8806-8814.
4. Rodríguez-Peña, M., et al., *New insights about the electrochemical production of ozone*. Current Opinion in Electrochemistry, 2021. **27**: p. 100697.
5. Gligorovski, S., et al., *Environmental implications of hydroxyl radicals (\bullet OH)*. Chemical reviews, 2015. **115**(24): p. 13051-13092.
6. EN 12607-2, C., *12607-1: Bitumen and Bituminous Binders—Determination of the Resistance to Hardening under Influence of Heat and Air—Part 1: RTFOT Method*. European Committee for Standardization: Brussels, Belgium, 2014.
7. Khalighi, S., et al., *The Impact of Reactive Oxygen Species Coupled with Moisture on Bitumen Long-Term Aging*. 2024.
8. Khalighi, S., et al., *Multivariate chemo-rheological framework for optimizing laboratory aging protocols of paving binders*. Materials & Design, 2024: p. 113520.
9. Jing, R., et al., *Ageing effect on chemo-mechanics of bitumen*. Road Materials and Pavement Design, 2021. **22**(5): p. 1044-1059.
10. Mirwald, J., et al., *Impact of reactive oxygen species on bitumen aging—The Viennese binder aging method*. Construction and Building Materials, 2020. **257**: p. 119495.
11. Khalighi, S., et al., *Evaluating the Impact of Data Pre-Processing Methods on Classification of Atr-Ftir Spectra of Bituminous Binders*. Available at SSRN 4852406.
12. Porot, L., et al., *Fourier-transform infrared analysis and interpretation for bituminous binders*. Road Materials and Pavement Design, 2023. **24**(2): p. 462-483.
13. Asemani, M. and A.R. Rabbani, *Detailed FTIR spectroscopy characterization of crude oil extracted asphaltenes: Curve resolve of overlapping bands*. Journal of Petroleum Science and Engineering, 2020. **185**: p. 106618.
14. Tavenard, R. *An introduction to Dynamic Time Warping*. 2021 3/17/2025]; Available from: <https://rtavenar.github.io/blog/dtw.html>.
15. Müller, M., *Dynamic time warping*. Information retrieval for music and motion, 2007: p. 69-84.
16. Zhang, J., et al., *Defect identification of layered adhesive structures based on dynamic time warping and simulation analysis*. Infrared Physics & Technology, 2022. **120**: p. 103943.

17. Li, K., et al., *Using dynamic time warping self-organizing maps to characterize diurnal patterns in environmental exposures*. Scientific reports, 2021. **11**(1): p. 24052.
18. Hofko, B., et al., *Repeatability and sensitivity of FTIR ATR spectral analysis methods for bituminous binders*. Materials and Structures, 2017. **50**: p. 1-15.
19. Petersen, J.C., *A review of the fundamentals of asphalt oxidation: chemical, physicochemical, physical property, and durability relationships*. Transportation research circular, 2009(E-C140).
20. Ren, S., et al., *Toward the long-term aging influence and novel reaction kinetics models of bitumen*. International Journal of Pavement Engineering, 2022: p. 1-16.
21. Liu, F., et al., *On the linking of the rheological properties of asphalt binders exposed to oven aging and PAV aging*. International Journal of Pavement Engineering, 2021. **22**(3): p. 331-340.
22. Mirwald, J., et al., *Understanding bitumen ageing by investigation of its polarity fractions*. Construction and Building Materials, 2020. **250**: p. 118809.

5

Effect of aging factors on rheological properties of paving binders

This chapter⁴ presents a comprehensive rheological analysis of aging effects in paving binders. The primary objective is to evaluate the impact of various environmental factors, such as temperature, pressure, humidity, time, UV light, and exposure to reactive oxygen species (ROS), on the rheological properties of paving binders. The chapter employs dynamic shear rheometer (DSR) to assess the changes in the rheological properties of binders under different aging conditions. Key rheological parameters, such as complex shear modulus (G^), phase angle (δ) and crossover values, are used to track variations in binder behaviour throughout the aging process. The chapter adopts a stepwise approach to investigate the influence of these factors on binder rheology, providing a systematic analysis of the combined effects of multiple aging variables.*

The systematic evaluation of the rheological effects of various aging conditions on paving binders begins with an analysis of hygrothermal, thermo-oxidative, and aqueous-thermal aging under atmospheric pressure in Section 5.5.1. Building on these findings, Section 5.5.2 examines the influence of additional factors, including temperature, pressure, time, humidity, and sample thickness, to explore how these variables interact and contribute to binder aging mechanisms. Section 5.5.3 introduces an accelerated aging protocol designed to simulate the effects of UV light and reactive oxygen species (ROS) in both liquid and gaseous forms, assessing the impact of ROS exposure on the rheological properties of binders.

In Section 5.5.4, field data are integrated into the analysis, facilitating a direct comparison between laboratory-aged and field-aged samples. Section 5.6 focuses on the application of master curves to characterize the severity and mechanisms of aging while comparing cumulative aging effects and aging rates across different laboratory aging protocols. Section 5.7 identifies the laboratory aging conditions that most accurately replicate the rheological properties of field-aged binders, providing insights into both the efficiency and field relevance of these protocols. Finally, Section 5.8 summarizes the key findings and conclusions from the rheological analysis, highlighting the most effective laboratory aging protocols for simulating long-term rheological changes in binders.

⁴ Apart from minor updates, this chapter has been published as " Khalighi, S., Erkens, S. and Varveri, A., 2024. Exploring the impact of humidity and water on bituminous binder aging: a multivariate analysis approach (TI CAB). *Road Materials and Pavement Design*, pp.1-25.

Khalighi, S., Ma, L., Mosleh, Y., van Lent, D. and Varveri, A., Multivariate chemo-rheological framework for optimizing laboratory aging protocols of paving binders, *Materials & Design*, 2024.

Khalighi, S., L. Ma, and A. Varveri, Accelerated laboratory simulation of field aging for paving binders using hydrogen peroxide and UV light. *Construction and Building Materials*. 2025."

5.1 Background

Asphalt binder aging is a complex process driven by physicochemical transformations that significantly impact pavement performance. Aging occurs due to oxidative and evaporative phenomena, leading to the progressive stiffening and embrittlement of the binder. These changes reduce the binder's ability to accommodate mechanical stresses, making the pavement more prone to cracking and degradation over time [1-3]. The primary factors influencing asphalt aging include oxidative reactions with atmospheric oxygen, volatilization of lighter fractions, UV radiation exposure, and environmental conditions such as temperature, pressure, humidity, and sample thickness. The interaction of these factors alters the binder's chemical composition, leading to the formation of highly polar oxygenated species that increase viscosity and decrease ductility [4].

Understanding the impact of aging on asphalt binder properties is essential for predicting pavement lifetime and optimizing material selection. Aging changes the molecular structure of the binder, increasing the proportion of asphaltenes while reducing the maltenes, which negatively affects flow behaviour and adhesion properties. These chemical changes result in altered rheological properties, including increased stiffness and reduced elasticity. Rheological characterization provides a direct means of linking these molecular changes to macroscopic performance indicators, making it a critical tool for evaluating the extent and consequences of asphalt aging.

The Strategic Highway Research Program (SHRP) has established standardized methods to assess the rheological changes in aged binders, enabling direct correlations with field performance [5]. The Dynamic Shear Rheometer (DSR) is particularly useful for evaluating the binder's viscoelastic behaviour and resistance to permanent deformation and fatigue cracking [6]. By measuring the complex shear modulus (G^*) and phase angle (δ), the DSR quantifies the balance between elastic and viscous responses, providing insights into how aging affects load-bearing capacity and stress dissipation [5, 7].

This chapter examines the rheological consequences of aging by analysing key parameters such as complex modulus, phase angle, crossover frequency, and crossover modulus. These indices capture the evolution of binder properties under different aging conditions, linking chemical changes to mechanical performance. Through this approach, this chapter integrates chemistry and rheology to develop a comprehensive understanding of how aging influences asphalt pavement lifetime.

5.2 Objectives and research structure

In this chapter, the following research sub-questions (RSQ) are addressed:

1. How do water molecules in liquid and vapor forms influence the rheological aging of asphalt binders under different environmental conditions? (RQ 1)⁵
2. What are the combined effects of moisture, temperature, pressure, film thickness, and aging time on the viscoelastic properties of asphalt binders from different sources? (RQ 1)
3. How does the introduction of reactive oxygen species (ROS), specifically hydroxyl radicals generated through UV and hydrogen peroxide (H_2O_2), impact the rheological aging of asphalt binders? How do key parameters of the photodecomposition-induced aging method affect binder performance? (RQ 2)
4. How does the novel UV-Peroxide Aging (UPA) protocol compare with standard aging methods in altering rheological properties? (RQ 2)
5. How well do laboratory-aged binders, particularly those subjected to UPA and other efficient protocols, correlate with field-aged samples based on rheological similarity assessments? (RQ 2)

⁵ The references in parentheses show the link to the main Research Questions (RQ) of this thesis, as outlined in Chapter 1.

The primary objective of this chapter is to investigate the influence of environmental aging factors on the rheological properties of asphalt binders, complementing the chemical aging analysis presented in Chapter 5 (Figure 5. 1). This chapter extends the analysis from chemical changes to the mechanical consequences of aging, providing a direct link between molecular changes and pavement performance. By integrating rheological evaluations, this chapter offers a comprehensive approach to understanding asphalt binder aging.

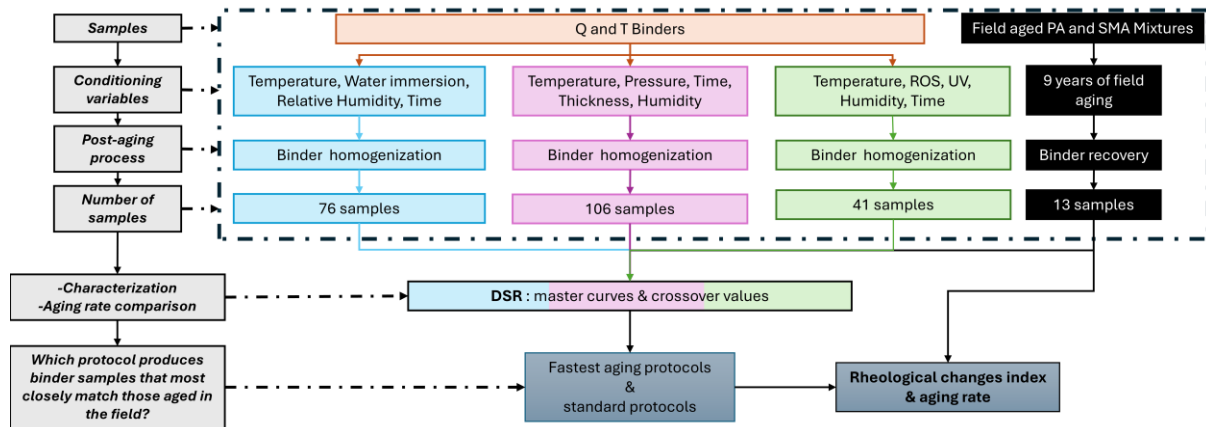


Figure 5. 1 Schematic representation of the research methodology outlining the sequential steps undertaken to investigate the impact of environmental aging factors on the rheological properties of paving binders and the development of a laboratory aging method for accurate field aging simulation.

These research sub-questions contribute primarily to addressing the first and second main research questions of the thesis. Specifically, they deepen our understanding of how diverse environmental factors, such as moisture, temperature, and oxidative agents, affect the rheological evolution of bituminous materials (related to RQ 1). In parallel, the chapter evaluates whether a newly proposed accelerated aging protocol (UPA) can simulate field aging more accurate and faster than conventional approaches (addressing RQ 2).

The first research sub-question (RSQ 1) examines the role of water molecules in binder aging, focusing on how moisture interacts with binders to alter their viscoelastic properties. This directly supports RQ 1 by isolating the effect of moisture as a key environmental factor influencing binder rheology.

The second research sub-question (RSQ 2) evaluates the combined effects of environmental factors such as temperature, pressure, humidity, film thickness, and aging time on the rheological performance of binders. This analysis establishes their relative influence on rheological properties, providing insights into the dominant mechanisms governing binder aging. This analysis further supports RQ 1 by simulating and reconstructing multi-factor environmental conditions typical of field exposure.

The third research sub-question (RSQ 3) focuses on the impact of reactive oxygen species (ROS) on binder aging. The chapter investigates how hydroxyl radicals, generated from UV-activated hydrogen peroxide, contribute to oxidative aging and influence rheological properties. This experimental development directly contributes to answering RQ 2 by investigating the chemical basis and practical implications of a novel laboratory aging mechanism.

The fourth research sub-question (RSQ 4) compares the efficiency and speed of the UPA protocol with standard aging methods in changing binder rheology. This section compares UPA with conventional methods (Pressure Aging Vessel (PAV) and Viennese Binder Aging (VBA)) based on changes in rheological parameters. This comparison is central to RQ 2, providing quantitative evidence for evaluating the performance of newly proposed versus established aging methods.

The final research sub-question (RSQ5) aims to validate the relevance of the laboratory aging protocols by comparing their rheological effects with those observed in field-aged samples. This step integrates the findings of sub-questions 1–4 and supports RQ 2 by evaluating the field

representativeness of accelerated aging protocols, including UPA. Together, these research sub-questions help to bridge the gap between laboratory protocols and field performance, ultimately contributing to the broader goal of developing robust and comprehensive aging evaluation methods as outlined in the main research question of the thesis in chapter 1.

Through these research steps, this chapter contributes a unique perspective by integrating rheology with chemical aging analysis. By systematically linking chemical changes to mechanical performance, this chapter provides valuable insights into binder behaviour under aging conditions, improving the predictive capabilities for pavement lifetime.

5.3 Materials and sample preparation

Details on the materials, sample preparation methods, and both short-term and long-term aging protocols are provided in Chapter 4, sections 4.3.1 to 4.3.4.

5.4 Characterization and analysis methods

5.4.1 Dynamic Shear Rheometer (DSR) - Frequency sweep

This approach aligns with the standard protocol (NEN-EN 14770 [8]), which supports strain adjustments according to the material's stiffness properties at various temperatures to maintain data integrity. Each sample was tested with two replicates to confirm repeatability and reliability of the results.

The Complex shear modulus (G^*) and phase angle (δ) were measured over a range of temperatures and frequencies using dynamic shear rheometer (DSR) with oscillatory loading. The DSR tests were completed with an 8-mm-diameter parallel plate and a 2-mm gap at temperatures range of 0 to 40 °C (with an increment of 10 °C). The tests were done in a frequency range from 15.9 to 0.0159 Hz (100 to 0.1 rad/s) and a strain load of 0.05% and 0.1% for 0-20 °C and 30-40 °C, respectively.

These strain levels were selected based on the need to maintain measurements within the linear viscoelastic region (LVER) of the binder, a requirement for obtaining valid and reproducible DSR results. Lower temperatures (0-20 °C) typically yield higher binder stiffness, requiring a smaller strain load (0.05%) to avoid exceeding the linear viscoelastic limit and risking non-linear responses that would compromise the accuracy of complex modulus (G^*) and phase angle (δ) measurements. At higher temperatures (30-40 °C), the binder becomes less stiff, allowing for a slight increase in strain (0.1%) without surpassing the linear viscoelastic threshold.

This approach aligns with the standard protocol (NEN-EN 14770 2012)[8]), which supports strain adjustments according to the material's stiffness properties at various temperatures to maintain data integrity. This testing procedure ensures that the rheological measurements, particularly G^* and δ , are not affected by plastic deformation or structural breakdown of the binder. The choice of test parameters (geometry, gap, temperature, frequency, and strain) follows standard recommendations for bituminous binders and is intended to enable direct comparison across samples aged under different protocols. Each sample was tested with two replicates to confirm repeatability and reliability of the results.

Based on the time-temperature superposition principle (TTSP), master curves of complex modulus and phase angle were constructed at a reference temperature of 20 °C [7]. Shift factors, typically denoted by " a_T ", are used in time-temperature superposition (TTS) to horizontally shift the binder response data obtained at various temperatures along the logarithmic frequency axis. The principle behind TTS is that the effects of temperature and frequency on the material's viscoelastic properties are equivalent. Therefore, multiple isothermal curves at different temperatures can be shifted into a single master curve at different frequencies, characterizing the material's behaviour across various

conditions. The shift factors used for constructing the master curves were derived using a least-squares minimization approach to maintain smooth continuity across the isotherms. This ensures that the final curve represents the true thermo-rheological behaviour of the material. The magnitude of the shift factors indicates the sensitivity of the binder's viscoelastic properties to temperature changes, with larger shift factors reflecting a greater temperature dependence.

The Sigmoidal Model, commonly employed to describe the rate dependency of the modulus master curve, has been extensively utilized by researchers to characterize the complex modulus master curve of asphalt mixtures and bituminous binders [9]. The model is mathematically represented as follows (Equation 5.1):

$$\log|G^*| = \sigma + \frac{\alpha}{1+e^{\beta+\gamma(\log(\omega))}} \quad (5.1)$$

In this model, $\log(\omega)$ represents the log of the reduced frequency, σ (sigma) denotes the lower asymptote, and α (alpha) represents the difference between the upper and lower asymptotes. Parameters β (beta) and γ (gamma) define the shape of the curve between the asymptotes and the location of the inflection point, which is determined by $10^{(\beta/\gamma)}$ [10].

The fitting of the sigmoidal model was performed using non-linear regression in Python, with convergence criteria based on minimizing the residual sum of squares. Goodness-of-fit was evaluated using the coefficient of determination (R^2), and typical values exceeded 0.98, indicating a strong fit.

The α (alpha) parameter reflects the overall stiffness or viscoelastic properties of the binder. A higher alpha value suggests a stiffer binder, while a lower value indicates a more flexible binder. The beta parameter represents factors such as the temperature dependence of the binder's stiffness or the transition between different rheological regimes (e.g., from elastic to viscous behaviour). The gamma parameter denotes the sensitivity of the binder's stiffness to changes in frequency, with a higher gamma value indicating a more pronounced change in stiffness with frequency or strain rate. The sigma parameter represents the baseline stiffness of the binder or any inherent structural characteristics that influence its rheological behaviour.

Fitting the master curve to this model provides a continuous representation of the rheological behaviour over a wide frequency domain and facilitates direct comparison between binders aged under different protocols.

5.4.2 Cumulative rheological aging and aging rate

In evaluating the effectiveness of aging protocols, it is important to consider both the cumulative changes and the rate of change in the rheological properties of the material. Cumulative rheological aging (CA_{rhe}) provide an overall measure of the extent of aging over time, which is essential for understanding the long-term effects on material performance. The rheological aging rate (AR_{rhe}), on the other hand, offers insight into the speed at which aging occurs, which is valuable for predicting the material's behaviour under different environmental conditions and assessing its durability in practical applications.

The DSR values selected for this analysis serve as reliable indicators of these rheological changes, reflecting key alterations in the binder's properties. By examining these values, a more comprehensive understanding of the impact of aging on the rheological characteristics of the material can be obtained. These parameters provide both macroscopic performance indicators and indirect information about underlying chemical and morphological changes.

To compare the aging protocols, both the magnitude and the rate of rheological changes were considered. Cumulative changes in rheological properties were calculated by summing the absolute differences between the DSR values of the aged samples and those of the fresh binder, as outlined in

Equation 5.2. The aging rate, based on rheological measurements, was determined using Equation 5.3.

$$CA_{rhe} = \sum_{i=1}^{80} \frac{|G_{i,fresh}^* - G_{i,aged}^*|}{G_{i,fresh}^*} + \sum_{i=1}^{80} \frac{|\delta_{i,fresh} - \delta_{i,aged}|}{\delta_{i,fresh}} \quad (5.2)$$

Where $G_{i,fresh}^*$ and $G_{i,aged}^*$ represent the complex shear moduli, and $\delta_{i,fresh}$ and $\delta_{i,aged}$ denote the phase angles of the fresh and aged samples, respectively, at the i -th master curve data point.

$$AR_{rhe} = \frac{\text{Cumulative rheological aging } (CA_{rhe})}{t \text{ (aging time (H))}} \quad (5.3)$$

Where t is the duration of the aging process (in hours).

5.5 Assessing changes in rheological properties of aged binders

The following sections present the results and discussion of this chapter, focusing on the evaluation of changes in the rheological properties of both laboratory-aged and field-aged binders.

5.5.1 Effect of hygrothermal, thermo-oxidative, and aqueous-thermal aging on rheological properties of binders

Evaluation of aging effect using master curves

This section examines how hygrothermal, thermo-oxidative, and aqueous-thermal aging affect the rheological properties of Q and T binder films by analysing master curve plots and making direct comparisons.

Effect of humidity on aging progression

Figure 5. 2, Figure 5. 3, and Figure 5. 4 illustrate the evolution of complex modulus (G^*) and phase angle (δ) master curves for Q and T binders at 60 °C, 70 °C, and 85 °C under different aging conditions. At 60 °C, the initial differences among aging methods, including oven aging, aqueous-thermal aging, and hygrothermal aging, are minimal. However, for Q binders, distinctions become apparent in the phase angle master curves at low frequencies after 14 or 21 days (Figure 5. 2a), with hygrothermal aging leading to the most significant aging effects. For T binders, the phase angle of thermo-oxidatively aged samples decreases slightly after 1 and 14 days, but by 21 days, the master curves converge, suggesting a comparable level of aging across different conditions (Figure 5. 2b).

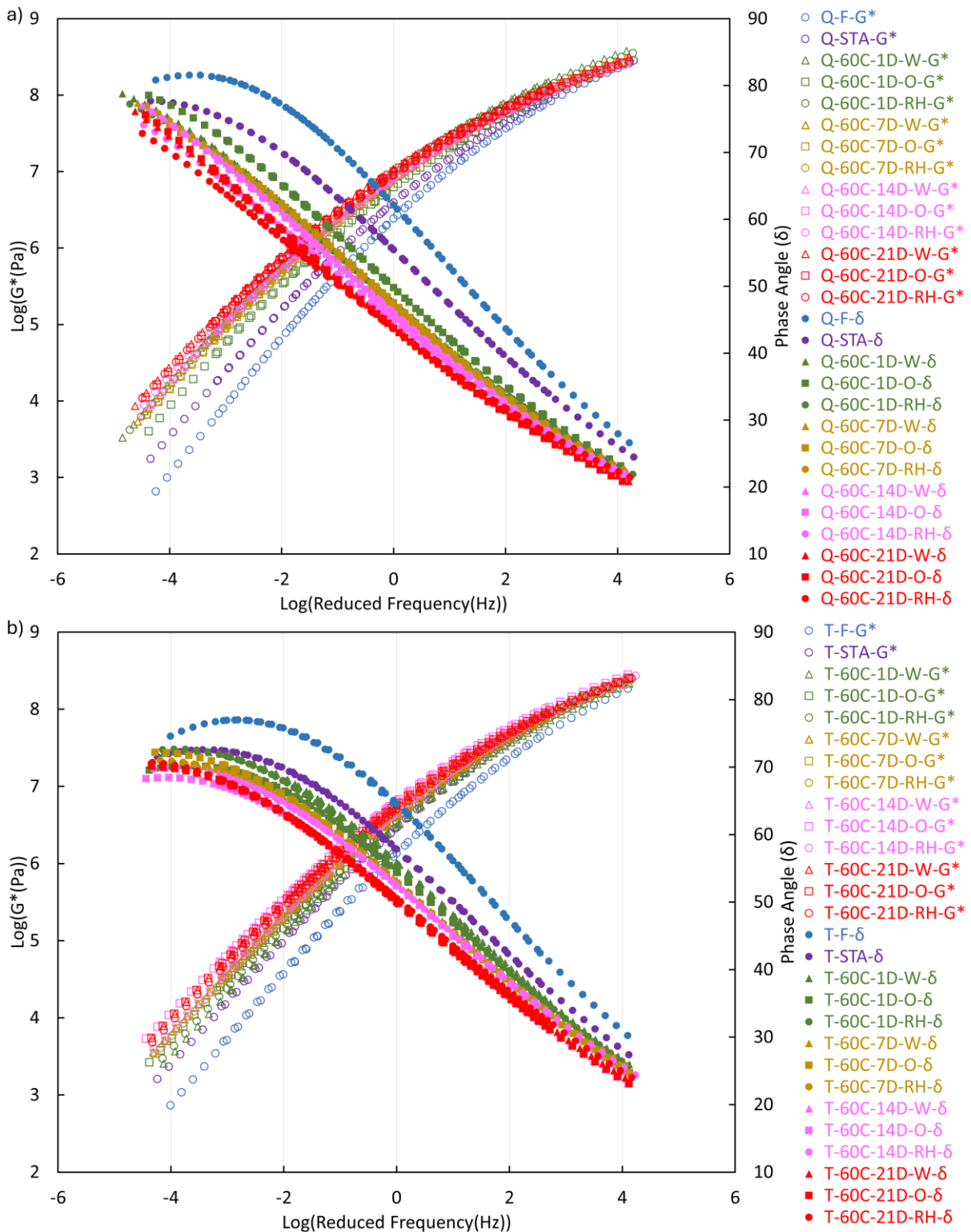


Figure 5. 2 Master curves of complex modulus and phase angle for (a) Q binder and (b) T binder, constructed using the time-temperature superposition (TTP) principle at a reference temperature of 20 °C. The curves represent different aging states, including fresh, TFOT short-term aged, and samples aged at 60 °C for 1, 7, 14, and 21 days under aqueous-thermal (W), thermo-oxidative (O), and hygrothermal (RH) conditioning.

At 70 °C, aging differences appear earlier in the process. For Q samples, the complex modulus and phase angle curves show clear distinctions at low frequencies, with aqueous-thermal and hygrothermal aging initially overlapping before diverging at longer durations. Hygrothermal aging consistently results in greater stiffness and lower phase angle values (Figure 5. 3a). T samples exhibit

similar initial trends across all conditions, but after 7 days, hydrothermal aging begins to induce more pronounced changes in phase angle at low frequencies (Figure 5. 3b). By 21 days, hydrothermal aging leads to the most significant aging effects, while thermo-oxidative and aqueous-thermal aging exhibit comparable trends.

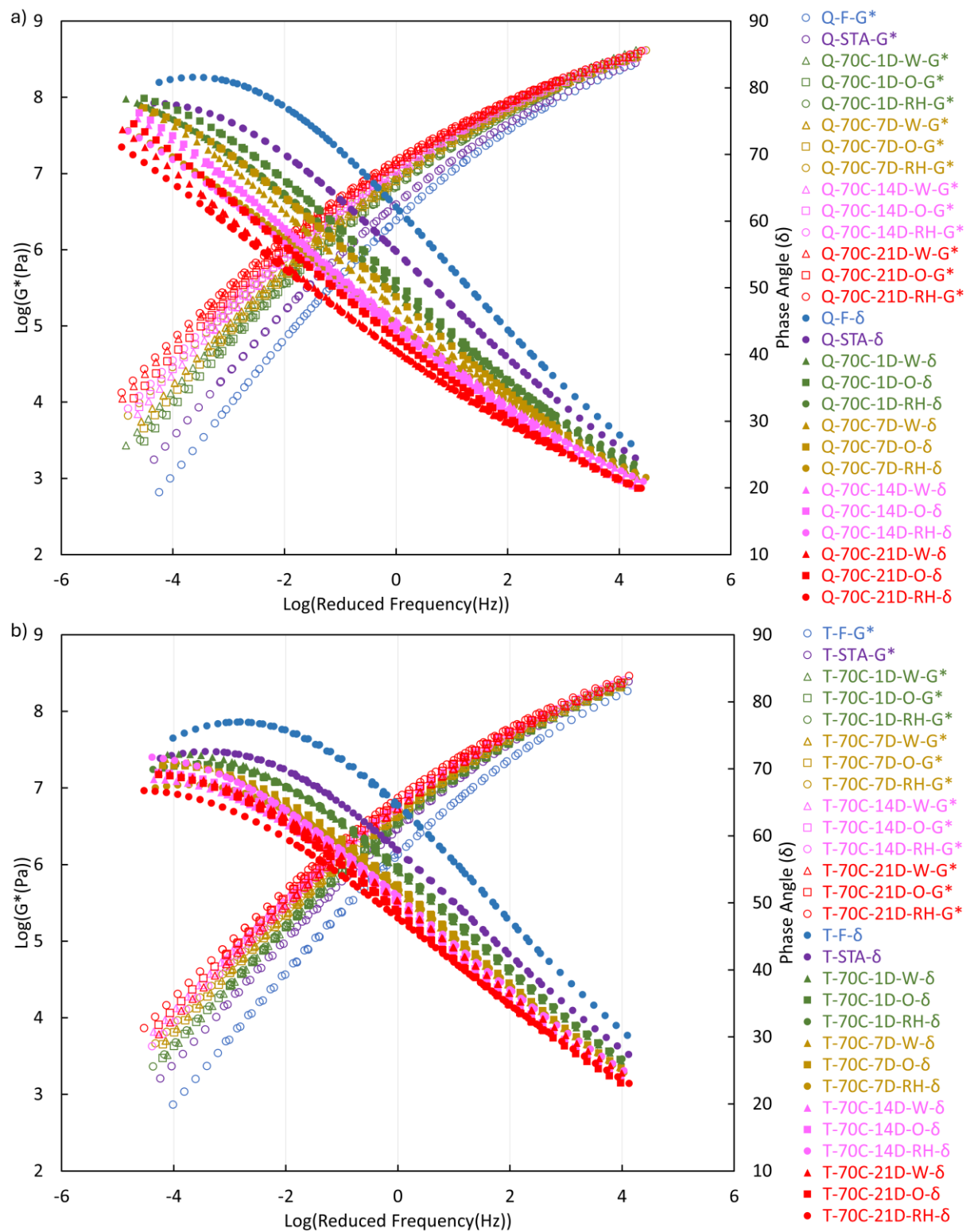
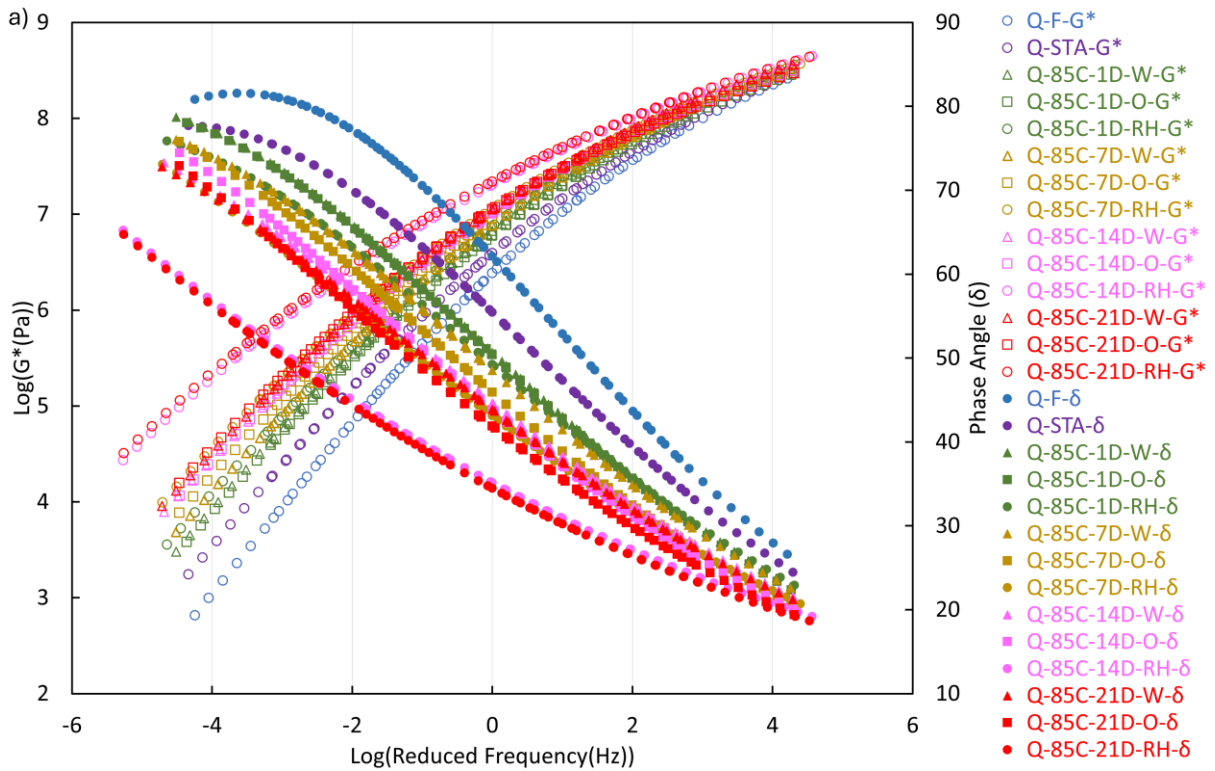


Figure 5. 3 Master curves of complex modulus and phase angle for (a) Q binder and (b) T binder, constructed using the TTP principle at a reference temperature of 20 °C. The curves represent different aging states,

including fresh, TFOT short-term aged, and samples aged at 70 °C for 1, 7, 14, and 21 days under aqueous-thermal (W), thermo-oxidative (O), and hygrothermal (RH) conditioning.

At 85 °C, humidity-induced differences in aging become even more pronounced for Q samples (Figure 5. 4a). Disparities extend beyond low frequencies and are evident at intermediate frequencies as well. After 14 and 21 days, hygrothermal aging shows the most severe impact, aligning with FTIR results. For T samples (Figure 5. 4b), thermo-oxidative aging initially results in lower phase angles at low frequencies, but hygrothermal aging effects become dominant after 7 days. By 14 and 21 days, hygrothermal aging leads to the most significant changes, whereas aqueous-thermal and thermo-oxidative aging display similar aging patterns.



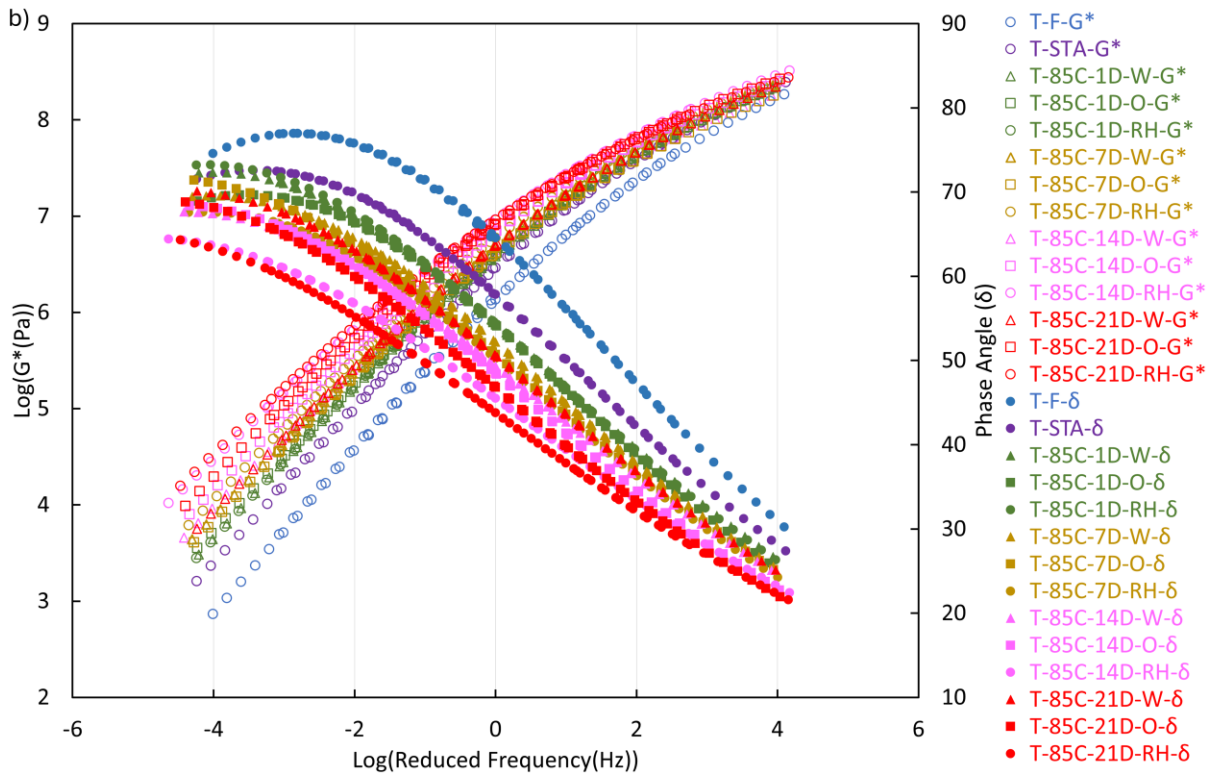


Figure 5. 4 Master curves of complex modulus and phase angle for (a) Q binder and (b) T binder, constructed using the TTP principle at a reference temperature of 20 °C. The curves represent different aging states, including fresh, TFOT short-term aged, and samples aged at 85 °C for 1, 7, 14, and 21 days under aqueous-thermal (W), thermo-oxidative (O), and hydrothermal (RH) conditioning.

Effect of temperature on aging progression

Temperature significantly influences the progression of binder aging, particularly under prolonged exposure. For Q binders aged at 60 °C (Figure 5. 2a), aging effects remain limited in the early stages, with notable differences emerging only at longer durations. However, at 70 °C (Figure 5. 3a), disparities among aging conditions become apparent earlier, with the phase angle master curve exhibiting a stronger divergence between hydrothermal and other conditions. At 85 °C (Figure 5. 4a), aging effects intensify further, with hydrothermal aging inducing significant changes even at intermediate frequencies.

A similar pattern is observed for T binders. At 60 °C (Figure 5. 2b), phase angle reductions occur gradually, with distinctions among aging conditions developing over time. At 70 °C (Figure 5. 3b), minor differences appear after 7 days, with hydrothermal aging leading to a greater reduction in phase angle. At 85 °C (Figure 5. 4b), the effect of temperature is evident, as hydrothermal aging results in the most pronounced stiffening of the binder, and aging progression is accelerated compared to lower temperatures.

Effect of time on aging progression

Aging duration strongly affects the rheological properties of Q and T binders, as reflected in both complex modulus and phase angle master curves. At 60 °C, Q binders exhibit minor differences among aging conditions initially, but hydrothermal aging results in a greater reduction in phase angle after 14 and 21 days (Figure 5. 2a). At 70 °C, distinctions among aging conditions develop earlier (Figure 5. 3a). After 14 and 21 days, hydrothermal aging leads to the highest complex modulus and lowest phase angle values. At 85 °C, the most pronounced aging effects occur after 14 days, beyond

which the difference between 14-day and 21-day aged samples is minimal (Figure 5. 4a), indicating a possible plateau in aging progression.

For T binders, aging trends follow a similar trajectory. At 60 °C, differences in phase angle among aging conditions become noticeable only after 21 days (Figure 5. 2b). At 70 °C, hygrothermal aging effects emerge after 7 days, with increased severity at 14 and 21 days (Figure 5. 3b). At 85 °C, aging differences are most significant after 7 days, and by 14 days, the aging rate appears to reach its maximum, as 21-day samples show little further change (Figure 5. 4b). The DSR analysis confirms that increasing aging duration results in higher complex modulus values and lower phase angles, highlighting the progressive stiffening of binders.

Notably, long-term aged Q samples exhibit a shift from a plateau region in the phase angle curve to a continuous increase at low frequencies, suggesting microstructural changes. The plateau region in the master curves of fresh and short-term aged Q samples is exclusively obvious in the phase angle curve due to its increased sensitivity to the chemical composition. Alterations in the phase angle master curves in response to fluctuations in frequency exhibit greater importance than changes in G^* at the same frequency range [11, 12].

In the context of binder aging, there are documented instances of modified binders displaying plateau regions within their phase angle curves. These regions signify the emergence of a polymer network or entanglements, resulting from the polymer's expansion into the maltene phase of the binder. The presence of an elastic plateau is more obvious on the curves when a stronger molecular interaction between the binder and polymer is present [13, 14]. While this chapter did not employ any polymer in conjunction with the binder, it remains plausible that binder aging induced such distinctions. The absence of aging effect in fresh and short-term aged samples displaying the plateau, ensures the preservation of the binder's microstructure and composition, allowing the material to naturally form chemical networks at lower frequencies. Conversely, long-term aged binders subjected to different conditioning may undergo microstructural changes, thereby impairing their capacity to form conventional chemical structures.

On the other hand, T samples at fresh and short-term aged conditions tend to reduce at $\text{Log}(\text{reduced frequency}) = -4$ after passing a plateau at $\text{Log}(\text{reduced frequency}) = -3$. Importantly, the presence of the plateau is more obvious for samples long-term aged at low temperatures like 60 °C and 70 °C than 85 °C aged samples. The reduction in phase angle values (increased elastic response) after the presence of a phase angle plateau, by moving towards lower frequencies, is an indication of the presence of 'elastic' networks in the fresh and short-term aged T binders [15]. This increased elastic response at low frequencies (equivalent to high temperatures) provides the fresh and short-term aged T binder with enhanced resistance to permanent deformation. However, this reduction tends to disappear for long-term aged samples and only the plateau present at low frequencies. The more obvious presence of plateau in low temperature long-term aged samples shows that aging and especially high temperature aging can change the binder's microstructure and composition, preventing the T binder to naturally form chemical networks at lower frequencies.

Overall, the results demonstrate that hygrothermal aging induces the most severe changes in binder rheology, particularly at higher temperatures and extended durations. Aging progression is more pronounced at 85 °C, while at lower temperatures, aging effects develop more gradually. The findings emphasize the importance of optimizing aging duration in laboratory protocols, as prolonged exposure beyond a critical threshold may not yield significant additional changes in binder stiffness.

Evaluation of aging effect using crossover values

In addition, the analysis calculated two key parameters: the crossover frequency (CR-Fr) and the crossover complex modulus (CR-CM).

Effect of humidity on aging progression

The crossover frequency (CR-Fr) and crossover complex modulus (CR-CM) were evaluated to assess the impact of hygrothermal, thermo-oxidative, and aqueous-thermal aging conditions on Q and T binders. Figures 6 and 7 present the logarithmic CR-CM values plotted against logarithmic CR-Fr values for all tested samples. Aging consistently resulted in a reduction in both CR-CM and CR-Fr values [16].

For Q samples aged at 60 °C and 85 °C, the 21- and 14-day hygrothermal aging conditions led to the most severe aging effects, confirming the observations from master curves and chemical analysis (Figure 5. 5a, c). At 70 °C, the 21-day hygrothermal and aqueous-thermal aged Q samples exhibited similar aging behaviours, further aligning with the master curve outcomes (Figure 5. 5b).

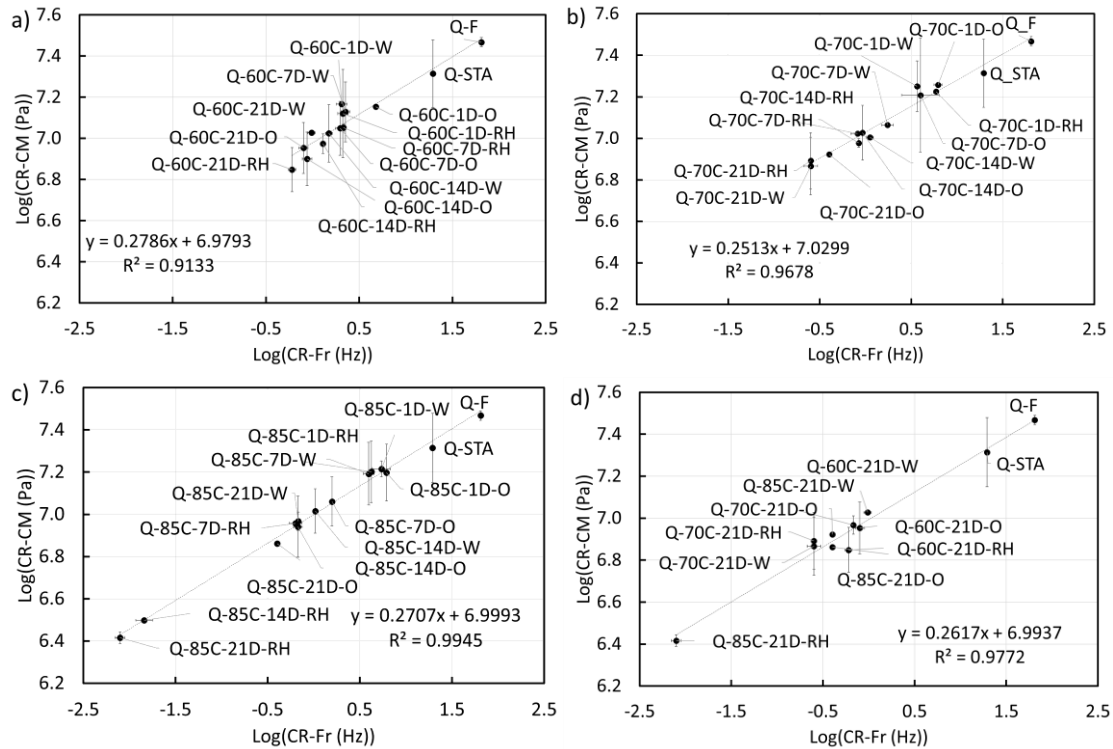


Figure 5. 5 Crossover complex modulus (CR-CM) versus crossover frequency (CR-Fr) for Q binder at different aging states: (a) 60°C, (b) 70°C, and (c) 85°C, including fresh, TFOT short-term aged, and 1, 7, 14, and 21 days (D) of aqueous-thermal (W), thermo-oxidative (O), and hygrothermal (RH) conditioning. (d) Comparison of all 21-day aged samples across all conditions.

For T samples (Figure 5. 6), aging also resulted in a shift towards lower CR-CM and CR-Fr values. At 85 °C, hygrothermal aging induced the most significant reduction in CR-Fr values, indicating extensive structural changes (Figure 5. 6c). Thermo-oxidatively aged samples exhibited lower CR-Fr values than aqueous-thermal aged counterparts, while CR-CM values remained within a similar range. The 21-day hygrothermal aging condition at 85 °C led to the most advanced aging, as reflected in both rheological and chemical analyses (Figure 5. 6d).

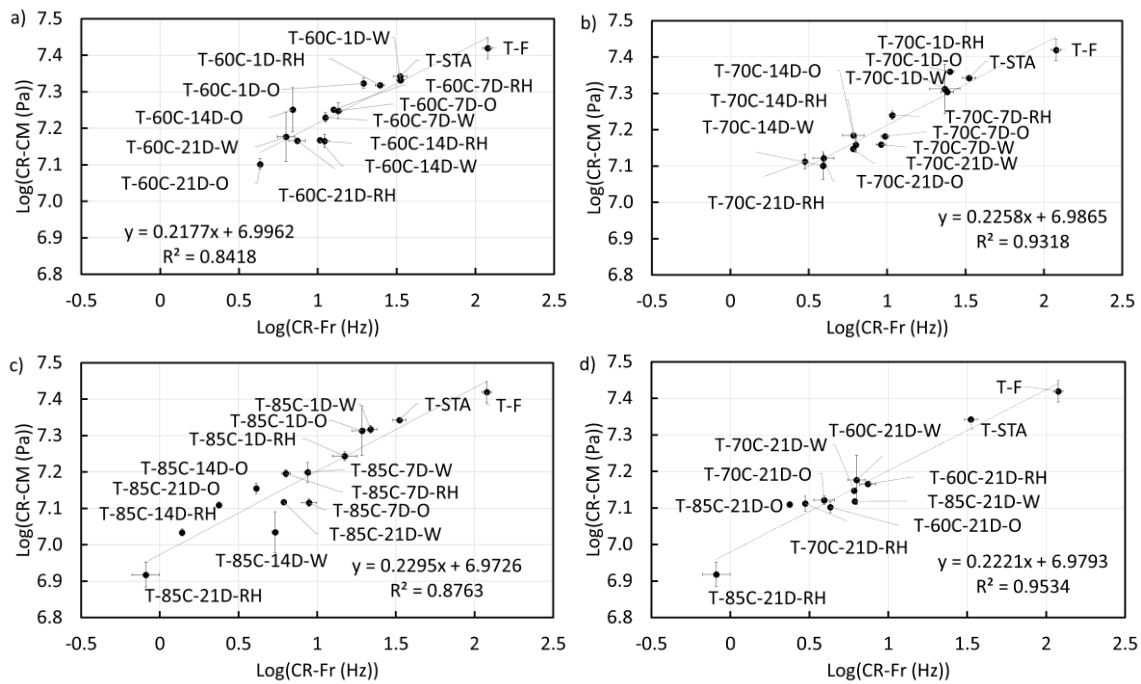


Figure 5. 6 Crossover complex modulus (CR-CM) versus crossover frequency (CR-Fr) for T binder at different aging states: (a) 60°C, (b) 70°C, and (c) 85°C, including fresh, TFOT short-term aged, and 1, 7, 14, and 21 days (D) of aqueous-thermal (W), thermo-oxidative (O), and hygrothermal (RH) conditioning. (d) Comparison of all 21-day aged samples across all conditions.

Effect of temperature on aging progression

Temperature influenced the extent of aging, with increasing temperature generally intensifying the aging process. The master curves and CR parameter trends consistently demonstrate that higher temperatures accelerate binder stiffening and structural changes.

For Q samples, hygrothermal aging at 85 °C led to the lowest CR-Fr and CR-CM values, confirming its severity (Figure 5. 5c). The thermo-oxidative aging effect became more prominent at 60 °C and 70 °C (Figure 5. 5a, b), while aqueous-thermal aging at 70 °C exhibited aging effects comparable to hygrothermal and thermo-oxidative conditions in terms of CR-Fr and CR-CM values. This similarity suggests that at 70 °C, aqueous-thermal aging influences the binder's microstructure and rheological properties to a similar extent as the other aging conditions, as confirmed by master curve analysis (Figure 5. 5b).

For T samples, aqueous-thermal aging at 1, 7, and 14 days resulted in more pronounced aging at 70 °C compared to thermo-oxidative and hygrothermal conditions (Figure 5. 6b). However, at 85 °C, hygrothermal aging had the most substantial impact, with a significant decrease in CR-Fr values (Figure 5. 6c). Thermo-oxidative aging resulted in more pronounced shifts in CR-Fr compared to aqueous-thermal aging, while CR-CM values remained relatively stable across conditions. These trends correlate well with the master curve phase angle results and chemical composition analysis, emphasizing the role of temperature in accelerating binder aging.

Effect of time on aging progression

Aging progression over time was evident in all tested samples, with prolonged exposure leading to further reductions in CR-CM and CR-Fr values. The master curves and chemical analysis confirm that longer aging durations increase stiffness and alter binder microstructure.

For Q samples aged at 60 °C, the 21-day thermo-oxidative aging condition resulted in the most severe aging effects, as shown by the significant reduction in CR-Fr and CR-CM values (Figure 5. 5a). At 70 °C, aqueous-thermal and hygrothermal aging at 21 days showed similar trends (Figure 5. 5b). For T samples aged at 60 °C, the aqueous-thermal sample exhibited the least aging after one day, but after 7 days, its CR values positioned it between hygrothermal and thermo-oxidative samples (Figure 5. 6). Over time, thermo-oxidative aging had a stronger impact on CR-Fr values, while aqueous-thermal aging primarily influenced CR-CM values.

At 85 °C, the 21-day hygrothermally aged T sample exhibited the highest degree of aging, as evidenced by the sharp decline in CR-Fr and CR-CM values (Figure 5. 6c). This effect was more pronounced in hygrothermal aged samples compared to thermo-oxidative and aqueous-thermal conditions.

When comparing all 21-day aged T samples across temperatures (Figure 5. 6d), the aging severity varied depending on the conditioning type. Aqueous-thermal aging showed negligible temperature dependence in long-term aging. In contrast, thermo-oxidative samples exhibited significant reductions in CR-Fr at 85 °C, and hygrothermal aged samples showed temperature-dependent reductions in both CR-CM and CR-Fr values. These findings underscore the necessity of incorporating both CR parameters to fully capture aging trends, as corroborated by master curve results and chemical analysis.

In conclusion, for both Q and T binders, the 21-day hygrothermally aged samples at 85 °C exhibited the most severe aging effects. Given the variations in aging patterns across different conditions, it is recommended to use both CR parameters in rheological evaluations to ensure a comprehensive assessment. These findings confirm that crossover values are effective in tracking and comparing the aging impact of different factors, supporting their further use in rheological assessments. Future analyses will focus on crossover values, while the master curve plots will be included in the appendix of Chapter 5.

5.5.2 Effect of temperature, pressure, time, humidity, and thickness on rheological properties of binders

Effect of temperature on aging progression

The frequency sweep test was conducted for all binder samples and their master curves are presented in Figure 1S in Appendix of chapter 5. An increase in temperature results in an elevated complex modulus (G^*) and a decreased phase angle, indicating a shift towards more elastic behaviour (Figure 1S). Hygrothermal and thermo-oxidative aging conditions further influence the rheological properties of Q and T binders, respectively, altering their mechanical response under loading. At 60 °C and 85 °C, Q samples aged with humidity exhibited higher G^* and lower phase angle for each thickness. As expected, the 1mm films showed more severe aging than the 2mm and 3.2mm films. Interestingly, Q samples aged at 70°C showed overlapping results for hygrothermal and thermo-oxidative aging across all thicknesses. The effect of hygrothermal aging on Q binder is predominantly visible at low frequencies, suggesting greater resistance to deformation under slow-loading conditions like heavy, slow-moving traffic, potentially improving performance against permanent deformation (rutting). Conversely, under fast-loading conditions like high-speed traffic and temperature fluctuations, the convergence at high frequencies implies comparable resistance to cracking for both hygrothermal and thermo-oxidative aged samples. The most severe aging condition for Q binder was observed in the 1mm film aged with humidity at 85°C and 20 bar. For T binder, the results showed slight differences. At 60°C, samples displayed more aging at low frequencies for thinner films with humidity. T samples aged at 70°C and 85°C demonstrated similar outcomes for hygrothermal and thermo-oxidative aging. The impact of different film thicknesses was

evident, with the 1mm films exhibiting the most aging. The most severe aging condition was observed in samples aged at 85°C. The DSR results are consistent with the FTIR findings for both Q and T binders in chapter 4.

Figure 5. 7 a-b presents the CR-CM versus CR-Fr for samples at different temperatures, revealing Q-LW85C-1 and T-LD85C-1 as having the lowest CR-Fr and CR-CM values, indicating their most severe aging. This underscores the varying sensitivity to hygrothermal aging for different binders. Elevated aging at 85°C was identified as a major factor in the aging of thin films, particularly those with a thickness of 1mm. Additionally, incorporating humidity during aging was shown to be beneficial for binders sensitive to hygrothermal conditions. A linear relationship was found between crossover values, regardless of binder type or aging conditions.

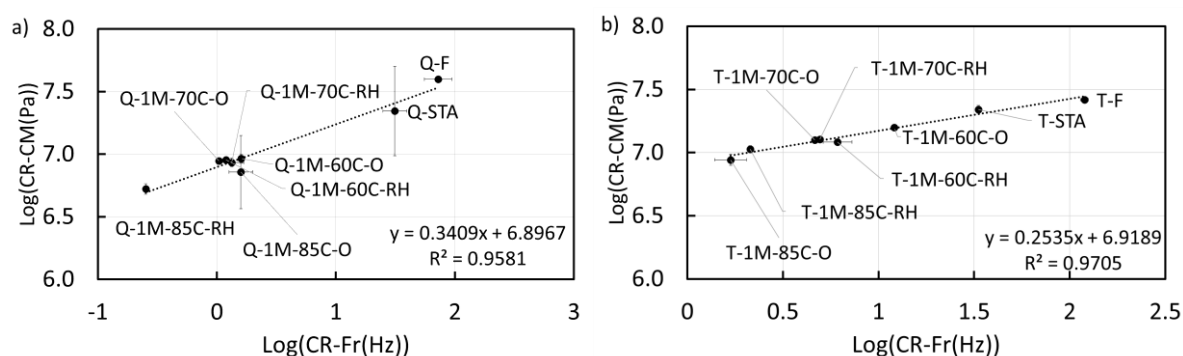


Figure 5. 7 Crossover complex modulus versus crossover frequency of 1mm samples aged at different temperatures, i.e., 60, 70, 85 °C after hygrothermal (RH) and thermo-oxidative (O) aging, a) for Q binder and b) for T binder.

Effect of pressure on aging progression

The effect of varying pressures (1, 5, 10, 20, and 150 bar) for both Q and T binder on different binder thicknesses is presented in Figure 2S in Appendix of chapter 5. As pressure increases, the gap between long-term and short-term aged samples widens, showing a marked increase in G^* and a decrease in phase angle, highlighting the severe impact of elevated pressure on binder aging. The effect of hygrothermal aging at higher pressures is observable in the phase angle master curves at lower frequencies for Q binder, aligning with previous observations on temperature effects showing lower sensitivity of T binder to hygrothermal aging. 1 mm films experience the most significant aging, with higher G^* values and lower phase angle values. Interestingly, samples aged at 150 bar do not show significant changes in G^* or δ values, suggesting that extremely high pressure does not necessarily cause harsher aging in binders. This rheological observation aligns with FTIR results, indicating that a limited number of reactive sites in the binder might render extremely high pressure unnecessary for accelerated aging protocols. For the Q binder, the distances between master curves are larger compared to the T binder, indicating higher pressure sensitivity.

Crossover values in Figure 5. 8 a–b illustrate the linear relationship between these values for both binders. The Q binder shows overlapping crossover values for aged samples, while the T binder exhibits clear differences between aged samples at different pressures. The Q binder displays similar results for samples aged at 20 and 10 bar under hygrothermal conditions, whereas the T binder shows more aging for samples aged at 20 bar. Notably, the Q binder film aged at 20 bar under thermo-oxidative conditions shows significant error bars, indicating substantial variation between repetitions. Future research should investigate the reasons for this variability.

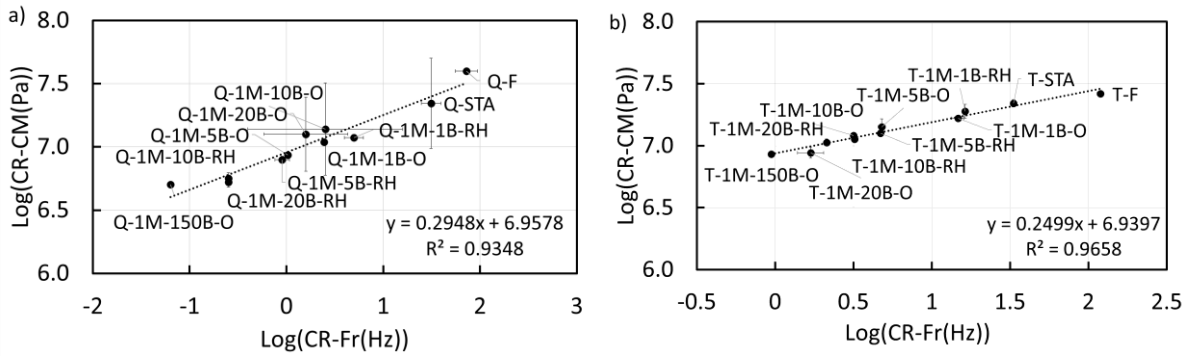


Figure 5. 8 Crossover complex modulus versus crossover frequency of 1mm samples aged at different pressures, i.e., 1, 5, 10, 20, 150 bar after hydrothermal (RH) and thermo-oxidative (O) aging, a) for Q binder and b) for T binder. Aging at 150 bar was performed only with thermo-oxidative aging.

Effect of time on aging progression

The influence of aging time on the rheological properties of both Q and T binders was presented (Figure 3S in Appendix of chapter 5). Aging durations of 5, 10, and 20 hours were chosen for both hydrothermal and thermo-oxidative conditions, with extended durations of 40 and 80 hours for hydrothermal aging. By increasing aging time, the G^* increases while the phase angle decreases, indicating a greater aging impact. For the Q binder, the differences between hydrothermal and thermo-oxidative aged samples became more pronounced with longer aging. In contrast, the T binder showed no significant effect from humidity, regardless of aging duration, indicating higher sensitivity of Q binder to hydrothermal aging. The results show that 1 mm films exhibit the most aging, with increased G^* values and decreased phase angle values. Aging effects were more pronounced at low frequencies.

Crossover values plotted in Figure 5. 9 a–b show that longer durations reduce both CR-CM and CR-Fr, indicating more aging in binder films, with a linear relationship between these values. Similar to the master curves, crossover values indicate that T binder is less sensitive to hydrothermal aging, while Q binder shows greater sensitivity to the presence of humidity during aging.

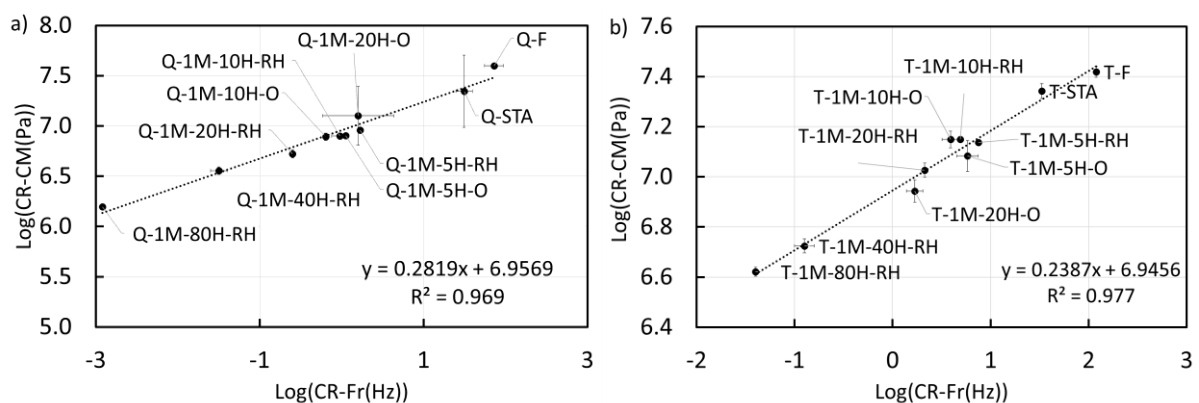


Figure 5. 9 Crossover complex modulus versus crossover frequency of 1mm samples aged at different aging durations, i.e., 5, 10, 20, 40, 80 hours after hydrothermal (RH) and thermo-oxidative (O) aging, a) for Q binder and b) for T binder. Aging for 40 and 80 hours was performed only under hydrothermal aging.

The DSR investigations indicate that the severity of hydrothermal aging depends on the binder's sensitivity to humidity during aging. Thinner films aged at high temperatures for longer durations show greater increases in G^* and more significant reductions in phase angle and crossover values.

The observed decrease in crossover values with increasing pressure demonstrates the impact of pressure on the aging of binder samples. Furthermore, crossover values and lower frequencies are more effective in distinguishing differences between aged samples than higher frequencies and the entire master curve. Thus, using lower frequencies and crossover values is recommended for comparing aging conditions in future studies.

5.5.3 Effect of reactive oxygen species (ROS) on rheological properties of binders

Evaluation of aging effect using master curves

Effect of ROS on aging progression

To compare the influence of different aging protocols, rheological properties were analysed to complement the chemical analysis results. Due to the large number of conditioned samples (22 for each binder), only those with the highest chemical aging rates (chapter 4) were included to maintain plot clarity. For both Q and T binders, the selected samples were fresh, STA, OVEN/UV-85C-3H, 12/33%-60C-9H, 12/33%-85C-3H, PAV-STD, Q-1M-85C-RH, VBA-DRY, and VBA-WET.

The master curves for Q and T binders are shown in Figure 5. 10a and b, respectively. The rheological response of the aged samples demonstrates that ROS play a key role in binder stiffening. The increase in complex modulus (G^*) with aging is primarily due to oxidative crosslinking and polymerization reactions, which elevate molecular weight and restrict molecular mobility. The formation of polar functional groups, such as carbonyl and sulfoxide, promotes intermolecular interactions, contributing to the development of a more rigid network. The phase angle (δ) master curves further support this, as aging results in a more pronounced slope change, indicating an evolving molecular structure.

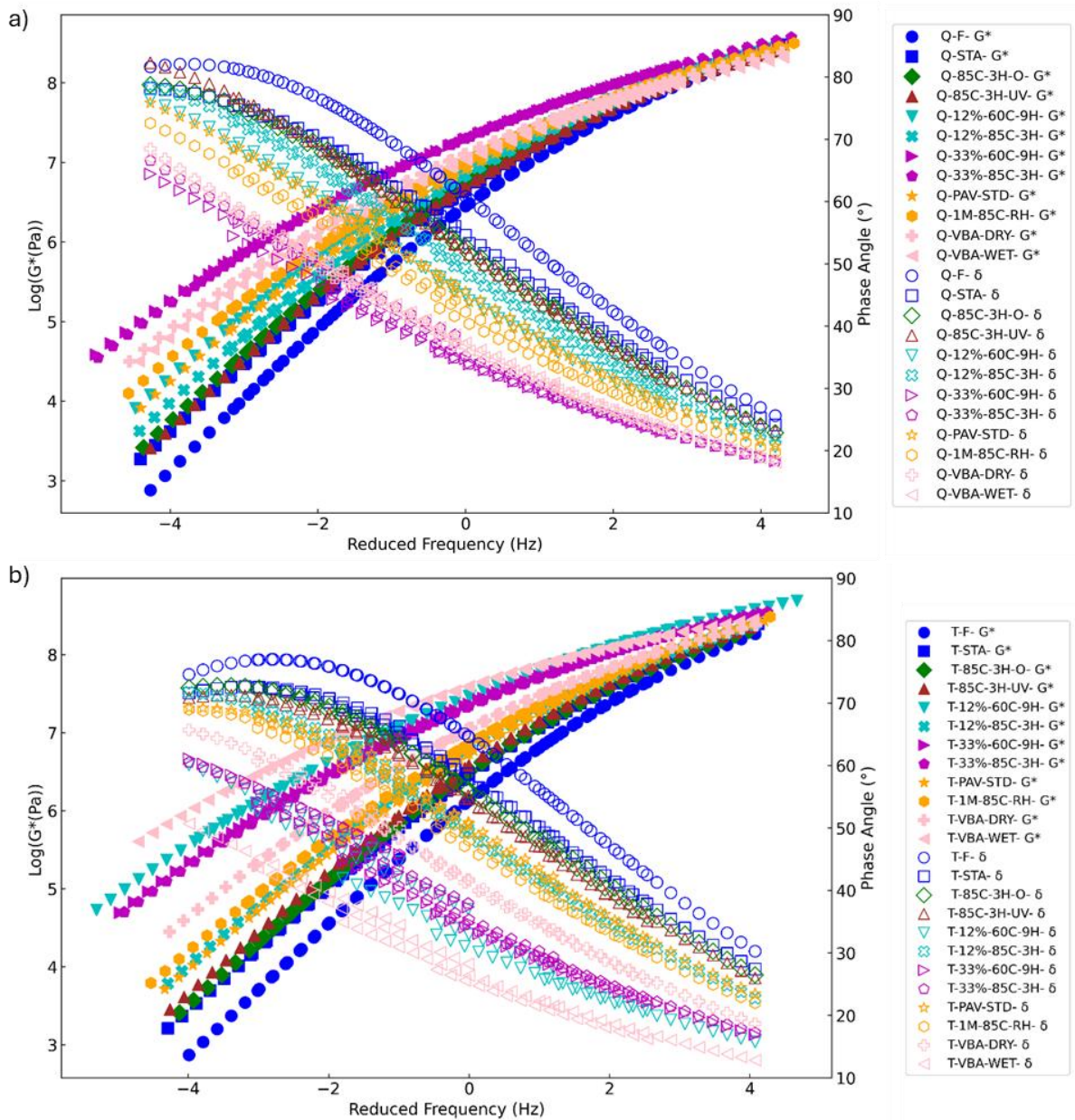


Figure 5. 10 Master curves of complex modulus and phase angle for (a) Q binder and (b) T binder, constructed using the TTP principle at a reference temperature of 20 °C. The curves represent different aging states, including fresh, TFOT short-term aged, and samples aged OVEN/UV-85C-3H, 12/33%-60C-9H, 12/33%-85C-3H, PAV-STD, Q-1M-85C-RH, VBA-DRY, and VBA-WET.

For the Q binder, the G^* and δ master curves of the OVEN/UV-85C-3H samples overlapped with the STA sample, indicating minimal aging. This suggests that short-term exposure to thermal and UV conditions at 85°C for 3 hours does not induce significant oxidative aging, as confirmed by chemical analysis. Similarly, the PAV-STD aged samples displayed slightly less aging than the Q-1M-85C-RH samples for both Q and T binders, indicating that more severe oxidation occurs under humidity modified PAV conditions. The VBA-WET and VBA-DRY samples behaved similarly for the Q binder, suggesting that water presence in VBA aging does not substantially alter ROS-driven oxidative aging.

For the T binder, the T-12%-60C-9H and T-VBA-WET samples exhibited extreme aging, consistent with FTIR results. This highlights that binder composition influences susceptibility to oxidative aging, as the T binder appears more reactive to ROS under mentioned conditions.

The concentration and phase of ROS significantly influence oxidative aging. For liquid-phase ROS, samples aged with 12% H₂O₂ showed more pronounced aging at 60°C for 9 hours than at 85°C for 3 hours. This indicates that at a lower ROS concentration, prolonged exposure at a moderate temperature leads to greater oxidation than a shorter duration at a higher temperature, likely due to the sustained nature of the reaction. In contrast, at a higher H₂O₂ concentration (33%), the master curves were similar regardless of temperature, suggesting that oxidation is primarily governed by ROS concentration rather than thermal effects. This saturation effect implies that, at high ROS concentrations, oxidation proceeds at a rapid rate, minimizing the relative impact of temperature.

Effect of temperature on aging progression

Temperature significantly affects the extent of oxidative aging. Elevated temperatures accelerate oxidation reactions, enhancing molecular crosslinking and reducing molecular mobility, as reflected in the master curve shifts.

For UPA-aged samples with 12% H₂O₂, those aged at 85°C for 3 hours exhibited less aging than those aged at 60°C for 9 hours. This suggests that, at a lower ROS concentration, prolonged exposure at a moderate temperature (60°C) leads to more oxidation than a shorter duration at a higher temperature (85°C), likely due to a more gradual but sustained reaction mechanism.

In contrast, at a higher H₂O₂ concentration (33%), the master curves for samples aged at 60°C and 85°C were similar. This indicates that, under high ROS concentrations, oxidation is predominantly driven by the presence of ROS rather than the temperature itself, suggesting a saturation effect where additional thermal energy does not significantly alter the oxidation kinetics.

Effect of time on aging progression

Prolonged aging durations lead to further reductions in δ and increases in G^* , indicating progressive oxidation and binder stiffening. Longer exposure times allow for more extensive oxidative crosslinking and polymerization, reinforcing the molecular network and restricting viscoelastic response. As mentioned in the discussion of ROS concentration effect, prolonged exposure to oxidation leads to increased molecular interactions, reinforcing the binder's structure. In this context, longer aging durations not only allow for sustained oxidative reactions but also provide more time for the gradual buildup of oxidative species, which further alters the binder's rheological properties. This extended oxidation process results in greater stiffening and reduction in phase angle, similar to the impact of higher temperature exposure.

For Q binder, the OVEN/UV-85C-3H condition showed minimal changes in rheological properties compared to STA, demonstrating that a short exposure time (3 hours) under these conditions is insufficient to induce significant oxidation.

These findings confirm that ROS concentration, temperature, and exposure time collectively influence oxidative aging, with their effects being interdependent. The rheological evolution captured in the master curves aligns with chemical analysis, underscoring the importance of evaluating both mechanical and chemical changes to fully characterize binder aging.

Evaluation of aging effect using crossover values

Furthermore, crossover frequency (CR-Fr) and crossover complex modulus (CR-CM) were calculated. For the Q binder, Figure 5. 11 illustrates the expected aging trend toward lower CR-Fr and CR-CM values. Considering the standard deviations of the measurements, oven-aged samples, UV-aged samples, and some of the 12% PIA-HP aged samples exhibited similar CR-Fr and CR-CM values.

ROS concentration strongly influences Q binder aging. Higher ROS concentrations in liquid-phase lead to lower CR-Fr and CR-CM values, reflecting increased oxidative crosslinking and stiffness, as seen in FTIR (carbonyl and sulfoxide indices in chapter 4) and master curves (higher G^* and lower δ). PAV-aged samples showed greater reductions in crossover values under humid conditions, perhaps due to the generation of more reactive species in the presence of humidity, as discussed in Chapter 4, while VBA-aged samples exhibited minimal humidity effects, indicating different ROS reactivity in gas-phase oxidation.

Elevated temperatures further decrease CR-Fr and CR-CM, indicating accelerated oxidation and polymerization for Q binder. Moreover, FTIR confirms increased oxidative species, while master curves show higher stiffness and lower δ values with temperature, linking thermal effects to molecular rigidity.

Longer exposure times continue reducing CR-Fr and CR-CM due to progressive oxidative aging. FTIR and master curves confirm sustained oxidation, increasing stiffness and restricting molecular mobility. Extended aging leads to a denser, less viscoelastic binder structure.

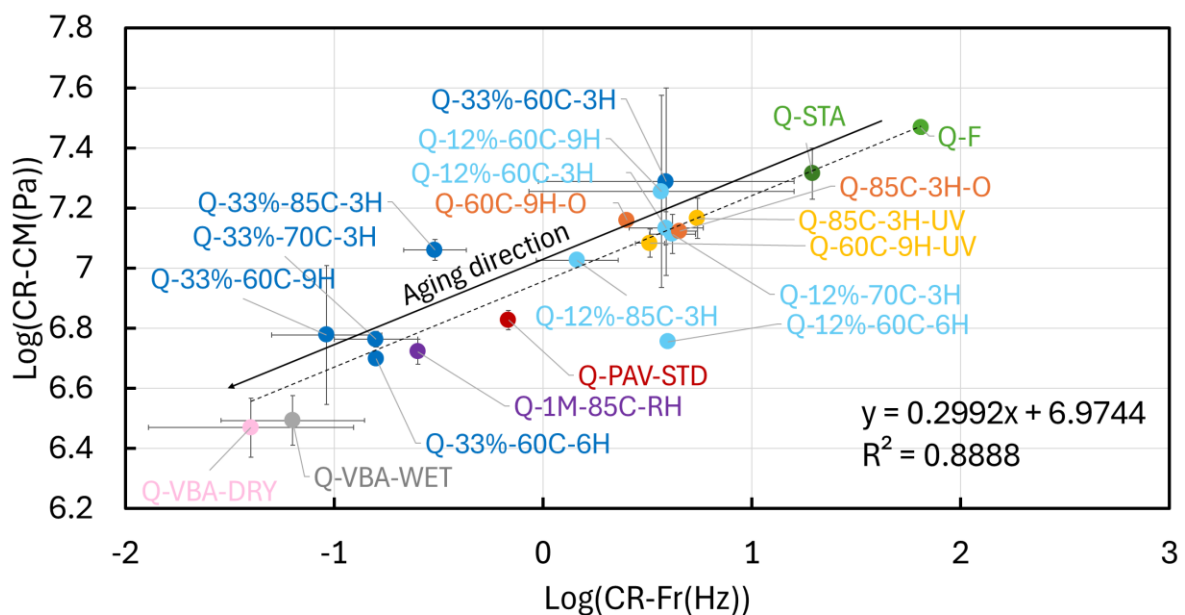


Figure 5. 11 Crossover complex modulus versus crossover frequency of Q binder samples, including fresh, short-term aged, long-term aged samples.

For the T binder, crossover values decrease significantly with increased ROS exposure (Figure 5. 12), indicating oxidative stiffening. Similar to Q binder, OVEN and UV-aged samples sharing similar crossover values. UPA-aged samples exhibit the lowest crossover values, confirming the strong impact of ROS-driven aging, as also observed in FTIR oxidation markers and master curve shifts. Compared to the Q binder, T binder appears more sensitive to ROS, with greater molecular modifications leading to more pronounced rheological changes. Moreover, PAV aged samples with or without humidity are located between oven and UV aged samples with high crossover values and UPA samples with lower crossover values showing that T binder is sensitive to the presence of ROS

during aging. Interestingly, considering standard deviations, all the 33% UPA aged samples are located in the same range of crossover values indicating stronger effect of high concentration H₂O₂ than temperature or time of aging for T binder. This suggests that for T binder, oxidative aging is primarily driven by H₂O₂ concentration rather than temperature or exposure duration.

Higher temperatures shift crossover values lower, reinforcing the role of thermal activation in accelerating oxidative aging. Master curves indicate a pronounced increase in stiffness, while FTIR confirms intensified oxidation at elevated temperatures. The sample T-12%-70C-3H is located higher than fresh sample showing fresh condition of binder. further repetitions and testing are needed to assure the location of this sample.

Extended exposure further reduces crossover values, indicating a cumulative effect of oxidative aging. Master curves show a progressive loss of viscoelasticity, while FTIR reflects continuous oxidative transformations. The T-VBA-WET and T-12%-60C-9H samples exhibit extreme aging, similar to the observation from master curves and FTIR data.

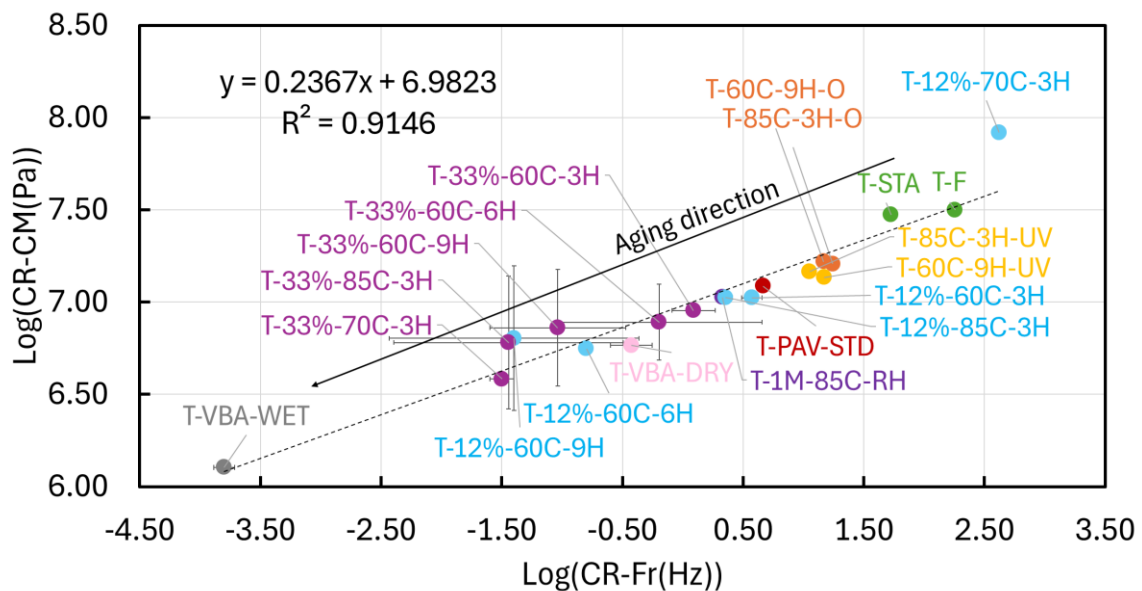


Figure 5. 12 Crossover complex modulus versus crossover frequency of T binder samples, including fresh, short-term aged, long-term aged samples.

5.5.4 Assessing changes in rheological properties of field-aged recovered binders

Evaluation of field aging effect using master curves

Investigating the master curves of field-aged porous asphalt over 0 to 8 years (Figure 5. 13) reveals that the phase angle decreases and G^* increases over time. Notably, the most significant changes occur during the initial four years, with more gradual changes in the final four years. This indicates that the initial stage of long-term field aging is more rapid.

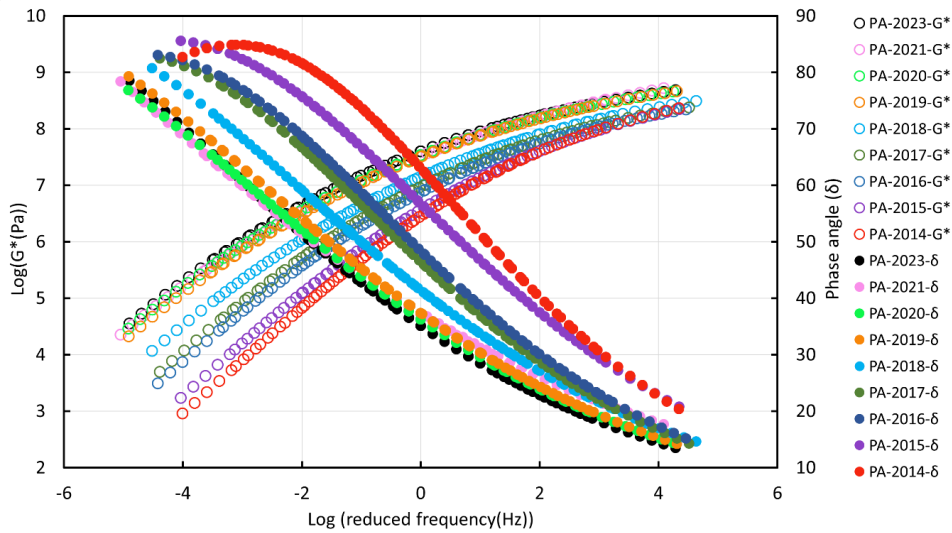


Figure 5. 13 Master curves of complex modulus and phase angle for recovered binders of field aged porous asphalt (PA) samples, constructed using the TTP principle at a reference temperature of 20 °C. The curves represent different aging durations (0-9 years of field aging).

For SMA samples, master curve values (Figure 5. 14) are similar from years 5 to 8, with only the 8-year sample showing a slight reduction in phase angle and an increase in G^* .

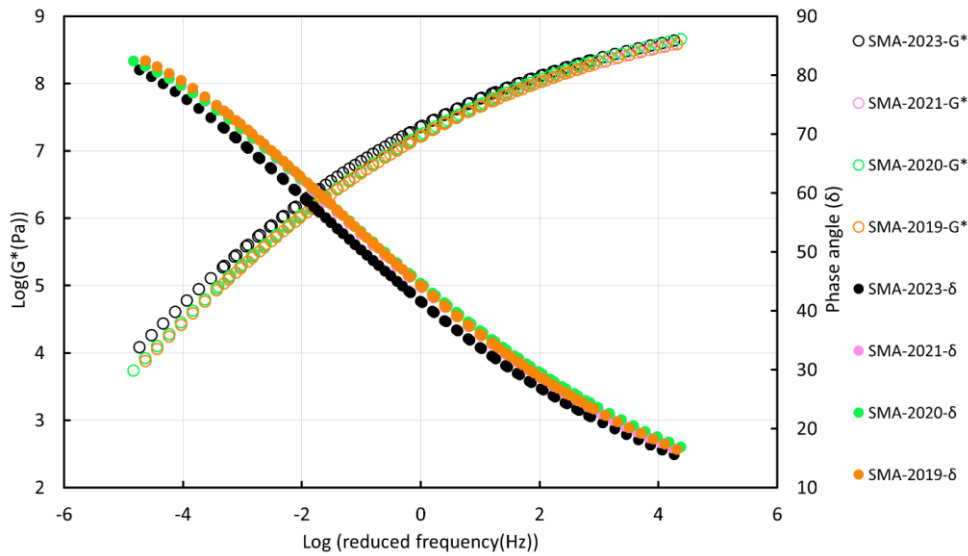


Figure 5. 14 Master curves of complex modulus and phase angle for recovered binders of field aged stone mastic asphalt (SMA) samples, constructed using the TTP principle at a reference temperature of 20 °C. The curves represent different aging durations. For SMA samples, those from years 5 to 9 were available.

Evaluation of field aging effect using crossover values

Similar conclusions can be drawn from the crossover values (Figure 5. 15), which align with the observation of hygrothermal aged samples, where a reduction in the slope of FTIR indices versus time was noted for longer aging durations.

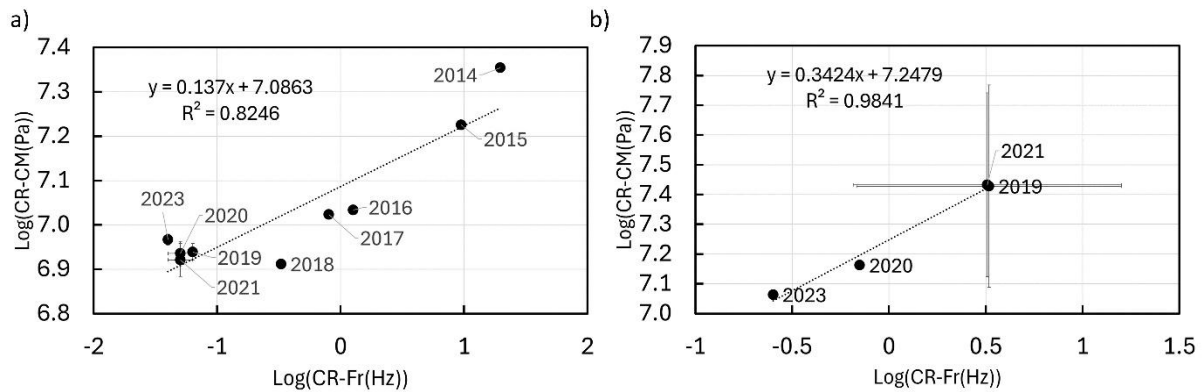


Figure 5. 15 Crossover complex modulus versus crossover frequency of field aged PA and SMA mixtures during 2014 to 2023, a) for PA mixture and b) for SMA mixture. In 2022 no sampling was performed and for SMA samples, those from 2019 to 2023 were available.

5.6 Comparison of aging rate for lab-aged samples based on rheological properties

This section identifies the aging protocol that results in the highest rheological aging rate by comparing the most aged samples from sections 5.4.1, 5.4.2, and 5.4.3. Protocols with extreme aging durations (two to three weeks) are excluded, as they do not align with the objective of evaluating aging rate within a practical timeframe. Similar to section 4.4.4, which examines the chemical oxidation rate, this section focuses on the speed of rheological changes.

Four aging conditions were compared to the ROS aging method:

- Hygrothermal aging in PAV for 20, 40, and 80 hours, assessing the impact of prolonged exposure to heat, pressure, and humidity.
- Thermo-oxidative aging at 150 bar for 20 hours, evaluating the effect of elevated pressure on oxidative aging.
- Standard PAV aging, serving as a reference condition for oxidative aging under controlled laboratory conditions.

These conditions provide a comprehensive comparison of different aging mechanisms, allowing assessment of how rapidly each protocol induces rheological changes. To provide a comprehensive analysis, the aging changes and their rates for these different conditions were calculated based on the complete master curve.

Figure 5. 16 shows the rheological aging rates for both Q and T binder samples, with UPA samples showing the highest aging rate. UPA of 12% and 33% for T binder showed higher rates compared to those of Q binder, indicating T binder's sensitivity to reactive species. UPA for 33%-85C-3H was the fastest aging process, followed by UPA for 33%-70C-3H for both binders. Other protocols had significantly lower acceleration rates due to weaker aging factors, requiring longer aging times to achieve a high aging level.

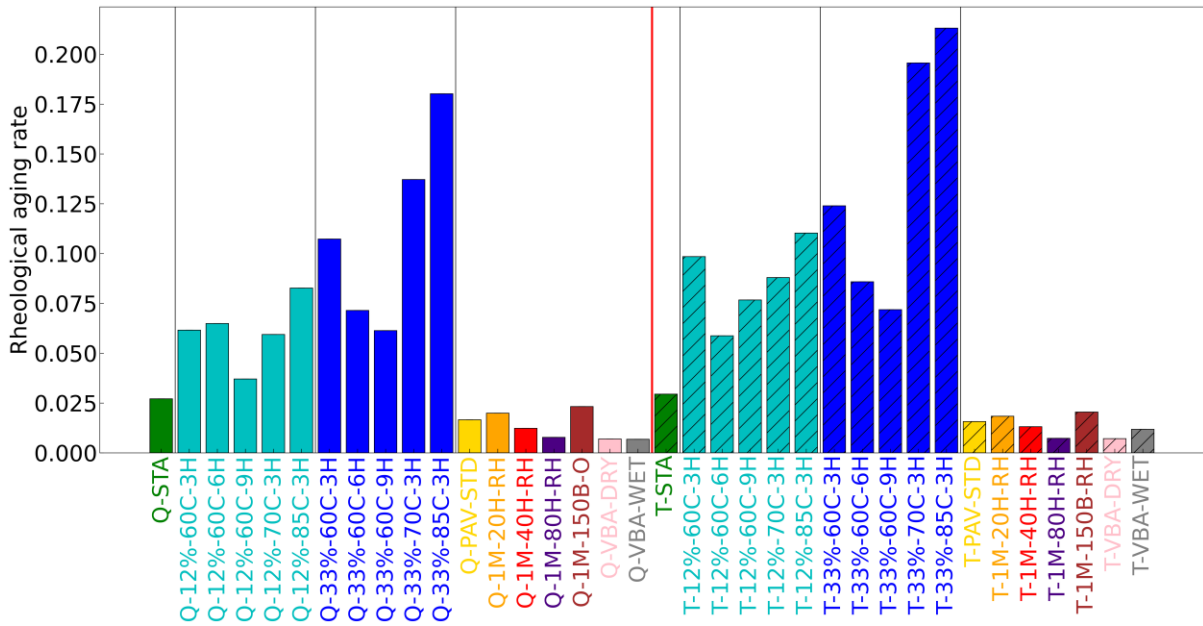


Figure 5. 16 Rheological aging rate of aged samples of Q binder and T binder.

5.7 Detailed rheological comparison of field- and lab-aged samples

To assess the rheological differences among the samples from sections 5.5.1, 5.5.2, and 5.5.3, master curves under extreme conditions were plotted, as shown in Figure 5. 17. Since the field-aged sample was derived from Q binder, only lab-aged Q binder samples were evaluated against it. As expected, aging led to an increase in G^* and a decrease in phase angle, particularly at lower frequency ranges. At high frequencies, the G^* values for most samples were similar, with only the VBA samples exhibiting slightly lower values compared to the other aged samples. In contrast, at lower frequencies, G^* increased for the lab-aged samples. Among these, the 33%-85C-3H, 33%-60C-9H, Q-85C-21D-RH, Q-1M-40H-RH, and Q-1M-150B-O conditions produced values closest to those of the field-aged sample, while the Q-1M-80H-RH and VBA-aged samples showed more deviation from the field-aged G^* values.

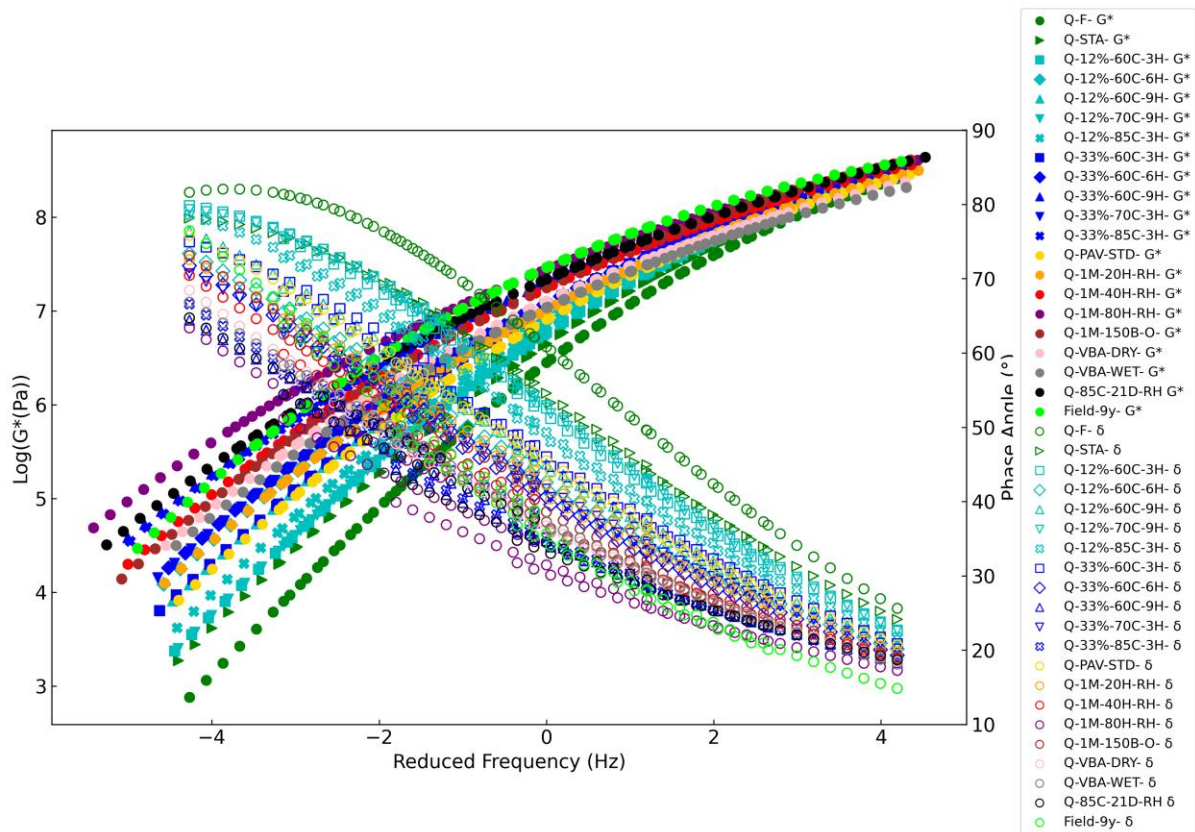


Figure 5. 17 Master curves (at 20 °C) for Q binder aged under various conditions, including 12% and 33% H₂O₂ at different temperatures and durations; hygrothermal aging in PAV and climate chamber; and VBA aging with and without humidity. Aging durations are indicated in hours (H) and days (D).

In terms of phase angle, high-frequency values for all samples overlapped, with the field-aged sample exhibiting slightly lower values, indicating more severe aging under field conditions compared to the laboratory simulations. At lower frequencies, the phase angle decreased significantly for the lab-aged samples, whereas the field-aged sample showed a less pronounced decrease. Notably, the phase angle of the field-aged sample was closest to the Q-1M-40H-RH and Q-1M-150B-O lab-aged samples.

At high frequencies, the field-aged bitumen exhibits a lower phase angle compared to the lab-aged sample, indicating that it behaves more elastically and is stiffer under rapid loading conditions. This can be attributed to long-term thermal aging in the field caused by daily and seasonal temperature cycles, which gradually lead to the formation of a more interconnected molecular structure. Conversely, at low frequencies, the field-aged bitumen shows a higher phase angle than the lab-aged sample, signifying a more viscous (fluid-like) response under slow loading. This difference arises because lab aging protocols accelerate aging through harsh conditions, causing faster oxidation and the loss of lighter fractions, which stiffen the material. In contrast, field aging occurs more gradually under natural conditions, allowing some residual viscous behaviour to persist. Overall, field aging results in a stiffer, more elastic material under rapid loading and retains more viscous properties at slow loading, whereas lab aging produces more uniformly stiffened bitumen with reduced viscous behaviour across frequencies.

To complement the analysis of master curves, a single parameter, termed the ‘cumulative rheological aging (CA_{rhe})’ index, was calculated for all samples using Equation 2 (Figure 5. 18). This index quantifies the cumulative rheological changes of aged samples relative to the fresh binder and offers

a concise measure of aging severity under various conditioning protocols. The index accounts for absolute differences in G^* and phase angle (δ) between fresh and aged samples, normalized by the fresh values, thus capturing the magnitude of rheological alterations.

As expected, the index increases with harsher aging conditions, such as higher temperatures, longer durations, or greater concentrations of H_2O_2 . For comparative analysis, rheological aging change index of the field sample serves as a reference, as it represents the cumulative effects of real-world aging.

Among the Q binder samples, Q-33%-60C-9H and Q-33%-85C-3H exhibited identical rheological aging index values to the field-aged sample; this suggests that these laboratory conditions can effectively replicate the stiffness and phase angle changes observed in the field within the linear viscoelastic region. A comparison of Q-33%-60C-6H and Q-33%-70C-3H reveals that their rheological aging indices are nearly identical. This suggests that increasing the aging duration at 60°C to 6 hours can induce a similar level of rheological aging as raising the temperature from 60°C to 70°C for a 3-hour duration. Furthermore, extending the aging time at 60°C to 9 hours produces nearly the same rheological changes as increasing the temperature to 85°C for 3 hours. These observations indicate that time and temperature interact in oxidative aging, where prolonged exposure at moderate temperatures can partially offset the effects of higher temperatures over shorter durations. However, further tests under intermediate conditions are required to precisely quantify these equivalencies and refine the understanding of their influence on binder aging.

Conversely, Q-1M-80H-RH displayed a higher index, indicating more severe aging than observed in the field. All other lab-aging conditions yielded lower indices compared to the field sample, reflecting less pronounced rheological changes under these conditions. This approach enables a more systematic comparison of aging protocols by providing a quantifiable metric to evaluate their effectiveness in replicating field aging.

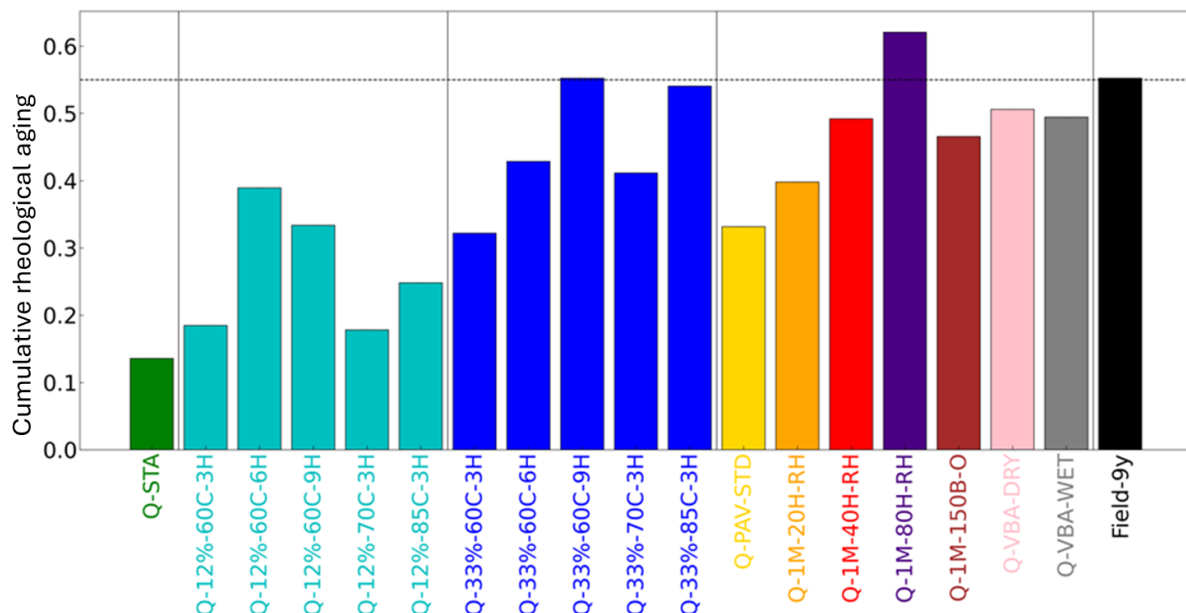


Figure 5. 18 Cumulative rheological aging of aged samples of Q binder and field-aged binder.

Based on the discussions in sections 5.4.6 and 5.4.5, it can be concluded that the 33%-60C-9H and 33%-85C-3H conditioning protocols are the most effective in replicating 9 years of field aging in porous asphalt in the shortest time, compared to PAV or VBA aging. One limitation of this chapter is

that the reference field sample used was not subjected to traffic, which may result in slight differences in aging compared to binders in actual pavement. Therefore, additional field data could be used to further refine and optimize the laboratory aging protocols.

5.8 Conclusions

This chapter investigated the rheological evolution of Q and T binders under various laboratory and field aging conditions, focusing on the effects of thermo-oxidative, aqueous-thermal, hygrothermal, and ROS-based protocols. Key parameters, including temperature, pressure, humidity, film thickness, and reactive oxygen species, were evaluated to identify their influence on viscoelastic behaviour and to determine suitable laboratory methods for simulating long-term field aging.

Rheological changes due to moisture exposure showed that aging increased stiffness (G^*) and reduced phase angle (δ), with phase angle master curves effectively capturing microstructural changes. Hygrothermal aging at elevated temperatures had a stronger impact on rheological properties than aqueous-thermal conditions (RSQ 1).

Among all parameters, ROS concentration had the strongest effect on rheology, followed by temperature, humidity, and exposure time. Aging effects were more pronounced in thinner films and under high pressure. Q binders were more sensitive to elevated temperatures, while T binders responded more to oxidative conditions, indicating source-specific differences (RSQ 2).

ROS-based aging protocols using 33% H_2O_2 induced rapid and severe rheological changes, especially at 85°C (3 h) and 60°C (9 h). Phase angle master curves and crossover parameters (CR-Fr, CR-CM) were sensitive to these changes and served as consistent indicators of aging progression (RSQ 3).

UPA with 33% H_2O_2 at 85°C for 3 hours was identified as the most time-efficient protocol, achieving comparable aging levels to conventional methods over significantly shorter durations. In contrast, thermo-oxidative and hygrothermal methods required longer exposure to reach similar rheological states (RSQ 4).

ROS-based aging at 33% H_2O_2 (85°C for 3 h or 60°C for 9 h) most closely matched the rheological characteristics of nine-year field-aged binders. In contrast, harsher conditions (e.g., the combination of high temperature at 85°C, high pressure at 150 bar, and long aging duration) resulted in over-aging, highlighting the need to balance acceleration with field relevance. The cumulative rheological aging index confirmed the similarity between optimized UPA protocols and field-aged materials (RSQ 5).

In conclusion, ROS concentration was the most influential factor in determining rheological aging, with temperature, humidity, and exposure time also contributing. ROS-based protocols at controlled conditions provided both accelerated aging and good field representativeness, making them suitable candidates for laboratory simulations of long-term performance. Rheological metrics derived from master curves and crossover points offered robust tools for evaluating binder aging. Future studies should refine these protocols using broader field data and account for additional variables such as traffic and environmental variability to enhance predictive accuracy.

5.9 References

1. Qin, Q., et al., *Field aging effect on chemistry and rheology of asphalt binders and rheological predictions for field aging*. Fuel, 2014. **121**: p. 86-94.
2. Zhang, H., et al., *Influence of surface modification on physical and ultraviolet aging resistance of bitumen containing inorganic nanoparticles*. Construction and Building Materials, 2015. **98**: p. 735-740.

3. Zhang, H., et al., *Evaluation of aging behaviors of asphalt binders through different rheological indices*. Fuel, 2018. **221**: p. 78-88.
4. Tauste, R., et al., *Understanding the bitumen ageing phenomenon: A review*. Construction and Building Materials, 2018. **192**: p. 593-609.
5. Hainin, M.R., et al., *Performance of modified asphalt binder with tire rubber powder*. Jurnal Teknologi, 2015. **73**(4).
6. Widyatmoko, I. and R. Elliott, *Characteristics of elastomeric and plastomeric binders in contact with natural asphalts*. Construction and Building Materials, 2008. **22**(3): p. 239-249.
7. Basu, A., M.O. Marasteanu, and S.A. Hesp, *Time-temperature superposition and physical hardening effects in low-temperature asphalt binder grading*. Transportation research record, 2003. **1829**(1): p. 1-7.
8. 14770, E., *Bitumen and bituminous binders—Determination of complex shear modulus and phase angle using a Dynamic Shear Rheometer (DSR)*. 2012, European Committee for Standardization Brussels.
9. Yusoff, N.I.M., et al., *Modelling the rheological properties of bituminous binders using mathematical equations*. Construction and Building Materials, 2013. **40**: p. 174-188.
10. Rowe, G., G. Baumgardner, and M. Sharrock, *Functional forms for master curve analysis of bituminous materials*, in *Advanced testing and characterization of bituminous materials, two volume set*. 2009, CRC Press. p. 97-108.
11. Airey, G.D. and B. Rahimzadeh, *Combined bituminous binder and mixture linear rheological properties*. Construction and Building Materials, 2004. **18**(7): p. 535-548.
12. Lu, X., U. Isacson, and J. Ekblad, *Rheological properties of SEBS, EVA and EBA polymer modified bitumens*. Materials and Structures, 1999. **32**: p. 131-139.
13. Wu, S.-p., et al., *Influence of aging on the evolution of structure, morphology and rheology of base and SBS modified bitumen*. Construction and building materials, 2009. **23**(2): p. 1005-1010.
14. Bulatović, V.O., V. Rek, and K.J. Marković, *Effect of polymer modifiers on the properties of bitumen*. Journal of elastomers & plastics, 2014. **46**(5): p. 448-469.
15. Airey, G., et al., *Time dependent viscoelastic rheological response of pure, modified and synthetic bituminous binders*. Mechanics of time-dependent materials, 2016. **20**: p. 455-480.
16. Jing, R., et al., *Ageing effect on chemo-mechanics of bitumen*. Road Materials and Pavement Design, 2021. **22**(5): p. 1044-1059.

6

Multivariate chemo-rheological framework for optimizing laboratory aging protocols of paving binders

This chapter⁶ presents a multivariate analysis framework designed to evaluate the chemo-rheological aging behaviour of paving binders. Building upon the chemical and rheological data generated in Chapters 4 and 5, the objective is to integrate these data streams using advanced statistical and machine learning techniques. The analysis focuses on identifying key indicators of aging, comparing laboratory protocols with field aging, and assessing the predictive capability of multivariate models. The chapter addresses the need for accurate laboratory aging simulations by combining chemical and rheological responses into a unified analytical approach.

The study begins by constructing a dataset from binders of two different origins, aged under various laboratory conditions and from binders extracted from field-aged pavements. Section 6.4.1 describes the construction of this dataset, integrating full FTIR spectra, FTIR indices, DSR master curves, and rheological parameters. Section 6.4.2 examines the suitability of FTIR indices and selected rheological parameters in capturing aging-related changes compared to their full-spectrum and full-curve counterparts. Principal Component Analysis (PCA) is used to assess information loss and to determine the most relevant variables for pattern recognition. Section 6.4.3 evaluates the similarity between laboratory-aged and field-aged binders through Euclidean distances in PCA space, identifying the laboratory protocols that most closely replicate field aging. In Section 6.4.4, the influence of aging factors (temperature, pressure, and time) on chemo-rheological properties was quantified using Multiple Linear Regression (MLR) and laboratory conditions equivalent to nine years of field aging was estimated. Section 6.4.5 investigates the interdependence between chemical and rheological variables, highlighting the key chemo-rheological interactions that characterize binder aging. Sections 6.4.6 and 6.4.7 focus on the predictive capabilities of multivariate models. Deep Artificial Neural Networks (ANNs) are used to predict rheological parameters and crossover values, using only FTIR indices, potentially reducing the need for extensive rheological testing. The equivalent number of field aging years for laboratory-aged samples based on field data was estimated using Support Vector Regression (SVR). Section 6.5 discusses the limitations of the modelling approaches used. Finally, Section 6.6 summarizes the findings and outlines the implications of multivariate methods for improving the accuracy and field relevance of laboratory aging protocols.

⁶ *Apart from minor updates, this chapter has been published as* Khalighi, Sadaf, Lili Ma, Yasmine Mosleh, Diederik van Lent, and Aikaterini Varveri. "Multivariate chemo-rheological framework for optimizing laboratory aging protocols of paving binders." *Materials & Design* 248 (2024): 113520."

6.1 Background

The aging of bituminous materials, a critical factor in their long-term performance, is influenced by a combination of chemical, physical, and environmental factors [1]. Laboratory aging protocols are designed to simulate and accelerate these processes under controlled conditions, allowing researchers to study the evolution of material properties over time [2]. However, a comprehensive understanding of the aging process requires simultaneous evaluation of chemical and rheological properties and their comparison with field-aged samples as a reference [3]. This comparison is vital to ensure that laboratory aging accurately mimics the complex and variable conditions experienced in real-world scenarios.

Each characterization method employed in studying aging generates a vast amount of data. For example, Fourier Transform Infrared Spectroscopy (FTIR) typically produces thousands of absorbance measurements, representing the molecular and chemical changes in the binder [4, 5]. Similarly, Dynamic Shear Rheometer (DSR) testing generates extensive rheological data, including parameters such as stiffness, phase angle, and frequency response [6]. The sheer volume of data from these methods makes it challenging to extract meaningful information, identify patterns, and draw reliable conclusions. Simple statistical methods often fall short in capturing the intricate relationships between variables, particularly in the presence of nonlinear interactions and overlapping effects.

Multivariate analysis offers a robust framework for handling such complex datasets, enabling the simultaneous consideration of multiple variables. These techniques can identify key chemical and rheological factors responsible for aging, establish relationships between aging conditions and material properties, and compare laboratory-aged samples with field-aged counterparts [3, 7, 8]. By integrating the vast pools of data from FTIR and DSR, multivariate methods not only uncover hidden patterns and trends but also provide a systematic approach for validating laboratory aging protocols against field aging. This ensures that laboratory procedures can better replicate real-world aging conditions and enhance the predictive accuracy of laboratory tests for the long-term performance of bituminous materials.

In this context, the application of advanced multivariate techniques is critical to bridging the gap between laboratory and field aging. Principal Component Analysis (PCA) [9], Multiple Linear Regression (MLR) [3], Support Vector Regression (SVR) [10], and Artificial neural networks (ANNs) [11] serve as powerful tools to evaluate aging trends, investigate the chemical-rheological interplay, compare laboratory protocols with field data, and predict the aged binder properties. This approach not only improves the interpretation of aging-related data but also aids in developing more reliable and field-representative laboratory aging procedures.

6.2 Objectives and research structure

In this chapter, the following research sub-questions (RSQ) are addressed:

- 1- Do FTIR indices and rheological parameters capture aging-related changes in bituminous binders as effectively as full FTIR spectra and complete rheological master curves? (RQ 3 & 4)⁷
- 2- Can multivariate techniques identify distinct chemical and rheological signatures of aging across different binder types and aging protocols? (RQ 1 & 3)
- 3- How do aging conditions, specifically temperature, pressure, and time, influence the chemical and rheological properties of bituminous binders, and can these relationships be used to estimate equivalent field aging durations? (RQ 1 & 2)

⁷ The references in parentheses show the link to the main Research Questions (RQ) of this thesis, as outlined in Chapter 1.

- 4- Which laboratory aging conditions produce chemical and rheological characteristics most similar to field-aged binders? (RQ 2 & 3)
- 5- Can models trained on field data predict the equivalent field aging years for binders aged under various laboratory protocols? (RQ 2 & 3)
- 6- Is it possible to estimate rheological parameters, such as those derived from the sigmoidal model and crossover values, based solely on FTIR indices using machine learning methods? (RQ 3 & 4)

The main objective of this chapter is to develop a comprehensive chemo-mechanical framework for analysing the aging of bituminous binders using multivariate analysis techniques. This analysis incorporates both chemical and rheological data obtained from previously aged binders, as presented in Chapters 4 and 5. The data set includes binders of different origins (Q and T), aged under various controlled conditions, hygrothermal, thermo-oxidative, aqueous-thermal, and others involving temperature, pressure, time, film thickness, and UV-H₂O₂ protocols, as well as binders retrieved from field-aged pavement. Figure 6.1 shows the methodology flowchart used in this work. The details of each section are extensively explained in the material and method section. This objective is aligned with main research questions 3 and 4, which aim to integrate chemical and rheological data using multivariate tools, and to optimize data processing for reliable characterization.

The first sub-question (RSQ1) investigates whether FTIR indices and selected rheological parameters sufficiently represent the aging trends observed in full FTIR spectra and complete master curves. Using Principal Component Analysis (PCA), the analysis quantifies information loss when simplified descriptors are used, forming the foundation for subsequent multivariate analyses. This supports data reduction strategies for spectral analysis (RQ4) and contributes to the integration of chemical and rheological datasets (RQ3).

The second sub-question (RSQ2) applies PCA to identify chemical and rheological variables most responsive to aging and to classify binders by type and condition. The aim is to extract patterns that improve interpretation of aging mechanisms and binder differentiation (RQ3, also supports RQ1 through enhanced understanding of condition-dependent responses).

The third sub-question (RSQ3) uses Multiple Linear Regression (MLR) to model the effects of temperature, pressure, and time on aging indicators. The model is also used to identify laboratory conditions equivalent to nine years of field aging. This enables predictive assessment of aging severity (RQ1) and informs the selection of representative laboratory protocols (RQ2).

The fourth sub-question (RSQ4) compares laboratory- and field-aged binders by calculating multivariate distances using PCA. This analysis evaluates which protocols best reproduce the chemical and rheological characteristics of field-aged materials (RQ2) and applies statistical similarity metrics (RQ3).

The fifth sub-question (RSQ5) involves training a Support Vector Regression (SVR) model to estimate field-equivalent aging durations for laboratory-aged samples. This enables direct translation between laboratory results and real-world binder aging (RQ2, RQ3).

The sixth and final sub-question (RSQ6) investigates whether Artificial Neural Networks (ANNs) can predict rheological parameters, such as sigmoidal model outputs and crossover points, directly from FTIR indices. This approach aims to reduce the need for direct rheological testing while preserving predictive performance (RQ4) and further strengthens the link between chemical and rheological data (RQ3).

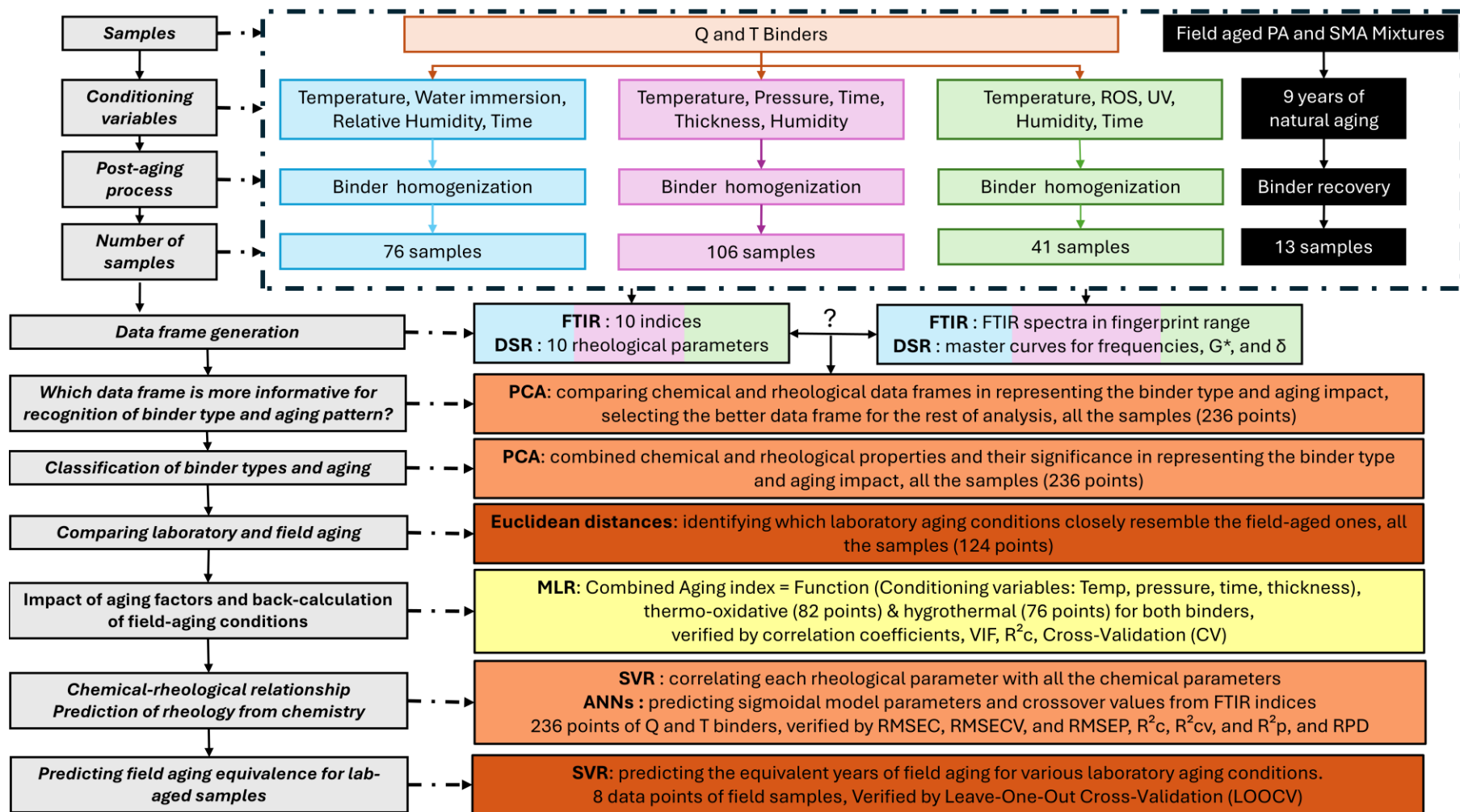


Figure 6.1 Schematic representation of the research methodology, detailing the sequence of steps including sample preparation, variation of aging condition parameters, post-aging procedures, number of generated samples, characterization using FTIR and DSR, and subsequent multivariate analysis for development of chemo-mechanical framework.

Collectively, these sub-questions contribute to the development of multivariate and machine learning tools that improve the accuracy, efficiency, and field relevance of laboratory aging protocols by linking chemical and rheological responses under varied aging conditions.

6.3 Multivariate analysis methods

The selection of analytical models in this chapter, PCA, MLR, SVR, and ANN, was guided by the nature of the data, the objectives of the analysis, and the specific predictive or interpretive tasks required for chemical–rheological characterization of bituminous binders. Each model was chosen for its suitability to address a distinct aspect of the dataset structure or its analytical goal, and each offers clear advantages when compared to more traditional statistical or empirical modelling techniques.

PCA is a statistical technique used to reduce the dimensionality of data by transforming it into a set of uncorrelated variables, called principal components, that capture the most variance in the data (Figure 6.2). PCA was selected primarily as a dimensionality reduction tool to simplify the dataset without significant loss of information. The original dataset contained a high number of interrelated chemical and rheological variables, many of which were collinear. PCA enabled the transformation of this high-dimensional space into a smaller set of orthogonal principal components that retained most of the variance. This allowed for efficient visualization and grouping of samples based on binder type and aging conditions. It also allowed the identification of clusters that correspond to distinct aging protocols or binder sources. Traditional univariate or bivariate methods (e.g., correlation analysis, scatter plots) are inadequate in such cases, as they cannot effectively handle multicollinearity or visualize data structures in high-dimensional space. PCA not only facilitated sample categorization but also highlighted the most informative variables contributing to variance, which is essential for subsequent regression or classification tasks. It is important to note that PCA is an unsupervised method and does not require prior knowledge of sample labels; thus, it is particularly suited for exploratory analysis and pattern discovery in complex datasets.

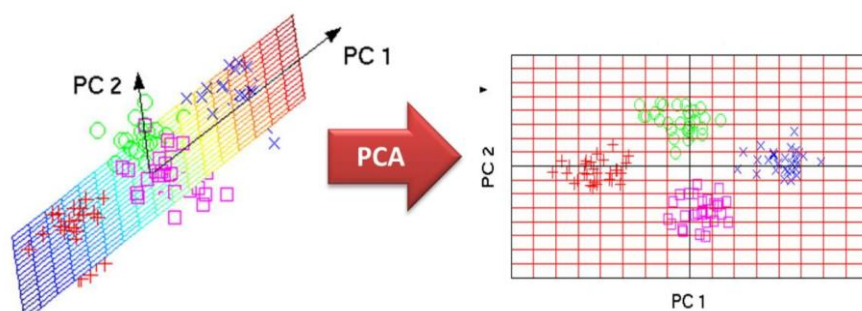


Figure 6.2 Illustration of PCA applied to a high-dimensional dataset. The left side shows the original data in a multidimensional space with overlapping and collinear variables. PCA projects the data onto a lower-dimensional space defined by orthogonal principal components (PC1 and PC2), shown on the right, where variance is preserved and sample groupings become more distinct [12].

Multiple linear regression is a statistical method that models the relationship between a dependent variable and two or more independent variables by fitting a linear equation to the observed data[3] (Figure 6.3). MLR was employed to quantify the influence of aging parameters (temperature, pressure, time, thickness) on binder degradation. The model was particularly suited for this task due to its interpretability and ability to isolate the individual and interactive effects of predictor variables. In contrast to black-box models, MLR provides direct insight into variable influence through coefficient estimation, which was necessary to evaluate the relative significance of aging conditions. Additionally, multicollinearity was addressed through prior correlation and VIF analyses. While traditional empirical models could potentially capture some aspects of aging behaviour, they

generally lack flexibility and fail to consider interactions among variables explicitly. MLR, especially with interaction terms, thus provided a more rigorous framework for analysing multifactorial effects on aging indices.

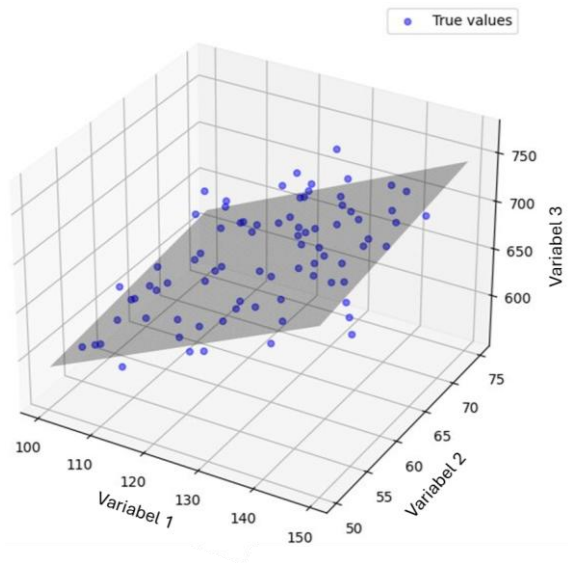


Figure 6.3 Visualization of a MLR model applied to a dataset with three variables. The grey plane represents the fitted linear surface capturing the relationship between the dependent variable (Variable 3) and two independent predictors (Variables 1 and 2). Blue dots indicate the observed values [13].

Support vector regression (SVR) is a machine learning method that aims to find a hyperplane in a high-dimensional space that best fits the target values within a specified margin width, ϵ , allowing deviations from actual values to be no larger than ϵ . Slack variables, ξ_i and ξ_i^* , are introduced to account for deviations beyond this margin [10] (Figure 6.4). SVR was adopted to model non-linear relationships between FTIR indices and rheological parameters, and to estimate equivalent field aging durations. Specifically, SVR was trained using binder samples aged under known field conditions (with recorded pavement exposure times) and tested on laboratory-aged samples. This allowed the translation of laboratory-induced aging into field-equivalent durations.

SVR is particularly effective for datasets with complex, non-linear associations and limited sample sizes, which are common in experimental materials research. Its use of kernel functions allows for the capture of intricate non-linear mappings that linear models such as MLR cannot accommodate. Moreover, SVR includes mechanisms to prevent overfitting, such as the introduction of a margin of tolerance (ϵ) and the regularization parameter (C), which is essential in noisy or sparse datasets. In comparison to classical regression models or even polynomial regression, SVR provides superior flexibility and generalization, especially when hyperparameters are appropriately optimized. The application of SHAP analysis further enabled the interpretability of SVR models, a key advantage over many other machine learning methods. Although SVR is a black-box method, model interpretability was enhanced through SHAP (SHapley Additive exPlanations) analysis, which identifies the contribution of each input variable to the model's predictions. This made it possible to determine which FTIR indices were most influential in predicting rheological properties.

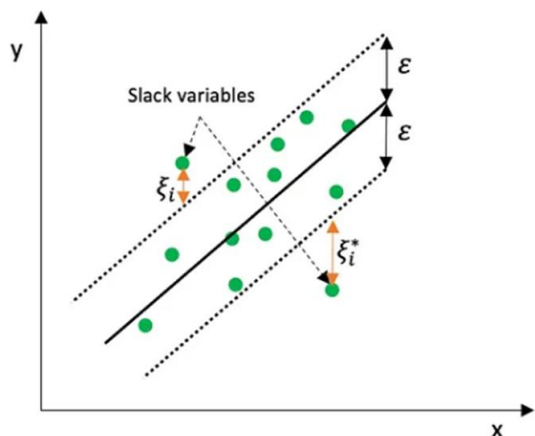


Figure 6.4 Conceptual illustration of Support Vector Regression (SVR). The solid line denotes the regression function, while the dashed lines represent the ϵ -insensitive margin. Green dots correspond to data points, and slack variables (ξ_i and ξ_i^*) account for points lying outside the ϵ -tube. These slack variables quantify the extent of deviation beyond the margin, enabling SVR to handle non-linear and noisy data while maintaining model robustness through controlled tolerance [14].

Artificial Neural Networks (ANNs) are machine learning models composed of interconnected layers (Figure 6.5) of nodes that approximate nonlinear relationships between input and output variables by adjusting connection weights through iterative optimization based on a loss function. ANNs were used to predict sigmoidal model parameters and rheological behaviour from FTIR indices.

The choice of ANN was justified by its capacity to approximate complex, non-linear functions and to learn hidden patterns from data through iterative training. In comparison to traditional regression models, which require explicit model formulation and often perform poorly when assumptions such as linearity or normality are violated, ANNs can learn arbitrary functional relationships with minimal a priori assumptions. This is particularly relevant when the underlying physical or chemical mechanisms linking FTIR spectra to rheological properties are not explicitly known or easily modelled. The model was trained on a curated dataset with known input-output relationships derived from laboratory tests. The data preprocessing steps, including transformation using the Yeo-Johnson method and standardization, ensured that the data conformed to the distributional requirements of the ANN, thus enhancing training stability and predictive accuracy. While ANN models offer high accuracy, they require sufficiently large datasets for training and careful tuning to avoid overfitting. Therefore, model generalizability should be interpreted with respect to the specific range of binder types and aging conditions represented in the training data.

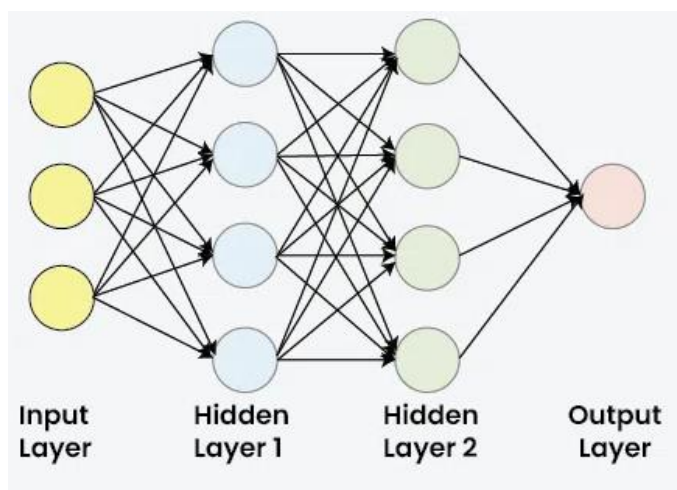


Figure 6.5 The structure of the artificial neural network, consisting of an input layer, two hidden layers, and an output layer. Each neuron in a given layer is connected to all neurons in the subsequent layer [15].

In summary, the selected models provided a balanced methodological framework capable of addressing the different analytical needs of the chapter. PCA served to reduce dimensionality and reveal latent structures; MLR offered interpretable quantification of aging effects; SVR enabled robust prediction in non-linear settings with limited data; and ANN facilitated the modelling of complex functional relationships. Each model was selected not only for its technical suitability but also based on the nature of the task, whether exploratory, inferential, or predictive. In doing so, the framework supports both mechanistic interpretation of aging effects and practical estimation of aging severity across different binder types and protocols. Compared to traditional statistical or empirical modelling approaches, these methods offered increased flexibility, predictive accuracy, and interpretability, thereby ensuring a more rigorous and comprehensive analysis of the chemical–rheological interactions in aged bituminous binders.

6.3.1 Principle component analysis (PCA)

The dataset utilized in this chapter comprises all experimental data (238 samples) from Chapters 4 and 5, including laboratory-aged samples under various conditions and field-aged samples. These samples were analysed for their chemical and rheological properties. The laboratory-aged samples included short- and long-term aging protocols applied to two base binders (Q and T), using temperature, pressure, duration, and film thickness as aging parameters. Field-aged samples were collected from pavements with known service times.

To assess whether FTIR indices and DSR parameters are as informative as FTIR spectra and DSR master curves, four initial datasets were constructed and compared: 1) FTIR spectra without the noisy region of $1900\text{--}2300\text{ cm}^{-1}$, which is typically excluded due to CO_2 and H_2O interference, 2) FTIR indices (including the indices listed in Table 3.4, which correspond to four peaks in the range of $710\text{--}912\text{ cm}^{-1}$), 3) DSR master curves containing reduced frequency, complex modulus, and phase angles, and 4) rheological parameters, which include four sigmoidal model parameters (α , β , γ , σ), four shift factors at 0, 10, 30, and 40 °C, as well as the CR-Fr and CR-CM. The four FTIR indices from the $710\text{--}912\text{ cm}^{-1}$ region correspond to bending and out-of-plane deformation modes of C–H bonds in substituted aromatic or aliphatic structures. The sigmoidal model parameters (α , β , γ , σ) describe the transition zone of the complex modulus master curve; shift factors indicate the temperature-dependent horizontal shift of rheological curves relative to the reference temperature.

CR-Fr and CR-CM denote the crossover frequency and crossover modulus, respectively, both used to characterize stiffness and elasticity changes during aging.

These datasets were compared to select the one that offered the best balance between reduced complexity and greater informativeness for the subsequent analysis. All the samples discussed in Chapters 4 and 5 were included in the dataset. To ensure comparability, all datasets were pre-processed using appropriate standardization. Standardization and PCA were implemented in Python using the StandardScaler and PCA classes from the sklearn.preprocessing and sklearn.decomposition modules, respectively.

For the chemical-rheological analysis, PCA was applied to categorize the samples based on binder type and aging effects. This was achieved by incorporating both chemical and rheological parameters, which facilitated an evaluation of their significance in distinguishing binder types and aging effects, key for classification and regression tasks. The dataset used for PCA was derived from the previous step's findings and consisted of both FTIR data (including all indices from Table 3.4, with the four peaks in the 710–912 cm^{-1} range treated as separate indices) and DSR data, which included the four sigmoidal model parameters (alpha, beta, gamma, sigma), four shift factors at 0, 10, 30, and 40 °C, and the CR-Fr and CR-CM. A total of 20 features were selected for PCA analysis, replacing the need for the entire FTIR spectra or master curves, as determined in the previous analysis. These 20 features were selected based on their statistical relevance (e.g., variance explained) and chemical interpretability, enabling a more compact and interpretable representation of the dataset.

All the samples discussed in Chapters 4 and 5 were also included in the PCA dataset.

To perform PCA, the scores of target samples are computed using the equation $\mathbf{Y}=\mathbf{X}\times\mathbf{W}$, where \mathbf{X} represents the dataset comprising m samples (grouped into l categories) and n variables. \mathbf{W} denotes an $n\times p$ loading matrix, with p indicating the number of selected principal components, while \mathbf{Y} forms an $m\times p$ score matrix describing the projection of \mathbf{X} into a p -dimensional feature space. To derive \mathbf{W} , the eigenvectors and eigenvalues of the covariance matrix of the variables within a spectral dataset are calculated. Subsequently, the eigenvalues are arranged in descending order, and p eigenvectors with the largest eigenvalues are chosen to construct \mathbf{W} . Additionally, PCA loadings are analysed to identify significant regions for cluster formation [16]. High loading values indicate variables with strong influence in distinguishing sample clusters, thus aiding in feature importance assessment and guiding future regression or classification model input selection.

6.3.2 Multiple linear regression (MLR)

To evaluate the relationship between the independent variables, temperature, pressure, and time, during the aging process of bituminous binders, a multiple linear regression (MLR) approach was utilized. Moreover, MLR model was used to determine the relative influence of each aging condition on the aging indices and to capture the combined effects of temperature, pressure, time, and thickness on aging. This analysis focuses on Q and T binder samples. A dataset comprising 158 lab-aged samples was employed for this purpose. The data points were divided into two subsets: thermo-oxidative (82 points) and hygrothermal (76 points). The analyses were performed separately for thermo-oxidative and hygrothermal data. Laboratory aging conditions were systematically varied as detailed in chapter 4: temperature ranged from 60 to 85 °C, pressure from 1 to 150 bar, duration from 3 to 80 hours, and film thickness from 1 to 3.2 mm.

The multiple linear regression (MLR) analysis was conducted using a combined index from FTIR and DSR as the dependent variable. This combined index was calculated for each sample by summing all standardized FTIR indices and DSR parameters, which included eight sigmoidal parameters and crossover values. The combined aging index considered whether the FTIR and DSR indices increased (+1) or decreased (-1) with aging during the summation process. The directionality (+1 or -1) was

defined based on known trends observed in the literature and in experimental data: parameters increasing with age (e.g., Carbonyl index) were assigned +1, while those decreasing (e.g., phase angle at low frequency) were assigned -1.

Once the combined aging index was calculated, it was plotted against the aging variables to check for a linear relationship (Figure 6.6). The purpose of the MLR was to quantify how aging conditions affected the combined index and to assess the relative influence of each condition on binder properties.

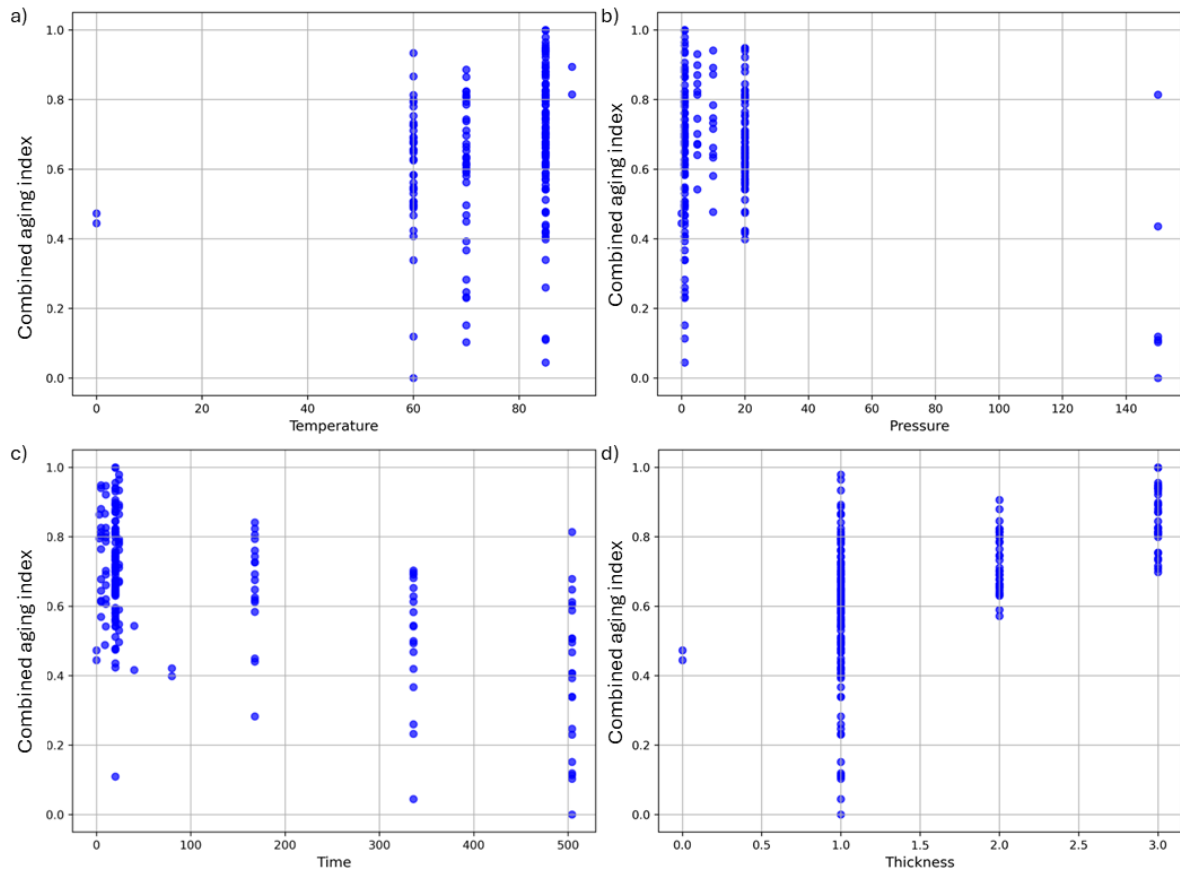


Figure 6.6 Combined index (FTIR and DSR) plotted against a) temperature (°C), b) pressure (bar), c) time (hours), and d) thickness (mm).

Interaction terms, accounting for the combined effects of temperature, pressure, time, and thickness, were included to evaluate the interaction of different parameters. Additionally, the model can be applied to back-calculate aging conditions that would produce similar aging levels as those observed in field samples. The regression models used in this analysis are shown in Equation 6.1 and 6.2.

$$\text{Combined Index} = \alpha_0 + \alpha_1(\text{Temperature}) + \alpha_2(\text{Pressure}) + \alpha_3(\text{Time}) + \alpha_4(\text{Thickness}) + \epsilon \quad (6.1)$$

$$\begin{aligned} \text{Combined Index} = & \alpha_0 + \alpha_1(\text{Temperature}) + \alpha_2(\text{Pressure}) + \alpha_3(\text{Time}) + \alpha_4(\text{Thickness}) + \alpha_5 \\ & (\text{Temperature} \cdot \text{Pressure}) + \alpha_6(\text{Temperature} \cdot \text{Time}) + \alpha_7(\text{Temperature} \cdot \text{Thickness}) + \alpha_8(\text{Pressure} \cdot \text{Time}) + \alpha_9 \\ & (\text{Pressure} \cdot \text{Thickness}) + \alpha_{10}(\text{Time} \cdot \text{Thickness}) + \epsilon \end{aligned} \quad (6.2)$$

Where α_i are coefficients to be determined, and ϵ is the error term.

Prior to performing the MLR analysis, the Pearson correlation coefficient (Equation 6.3) and Variance Inflation Factor (VIF) (Equation 6.4) were calculated to evaluate the multicollinearity among the independent variables.

$$\rho_{xy} = \frac{\text{Cov}(x,y)}{\sigma_x \sigma_y} \quad (6.3)$$

ρ_{xy} is Pearson product-moment correlation coefficient, $\text{Cov}(x,y)$ is covariance between variables x and y , σ_x and σ_y are standard deviation of x and y , respectively.

$$VIF_i = \frac{1}{1-R_i^2} \quad (6.4)$$

R_i^2 is unadjusted coefficient of determination for regressing the i th independent variable on the remaining ones.

The correlation coefficient, a statistical measure of the strength of a linear relationship between two variables, ranges from -1 to 1. A correlation coefficient of -1 signifies a perfect negative or inverse correlation, indicating that values in one series rise as those in the other decline, and vice versa. Variance inflation factors provide a rapid assessment of the extent to which a variable contributes to the standard error in regression analysis. A VIF exceeding 10 indicates the presence of substantial multicollinearity, necessitating alternative measures to address this issue. In cases of significant multicollinearity, the variance inflation factor will be notably high for the involved variables. This preliminary analysis was essential to verify the independence of the predictors. All statistical analyses, including correlation assessment, standardization, and regression modeling, were implemented in Python using the following libraries: pandas for data handling, scikit-learn for standardization and regression modeling, statsmodels for model diagnostics.

This MLR analysis not only provided quantitative insight into the influence of aging conditions but also allowed for predictive modeling of binder aging response under different laboratory scenarios. The use of standardized inputs ensured robustness against scale-induced biases, and the interaction terms enabled a more realistic capture of the multifactorial aging process.

6.3.3 Support vector regression (SVR)

SVR was utilized in two distinct applications: predicting rheological parameters based on FTIR indices and training a model to estimate the duration of field aging a laboratory sample simulates. The former included FTIR indices as input dataset (\mathbf{X}) and a selected rheological parameter as the output variable (\mathbf{Y}), while the latter used FTIR/DSR-derived indices of laboratory sample to estimate equivalent field aging duration.

SVR seeks to minimize both the coefficients of the hyperplane (to ensure flatness) and the sum of the slack variables (to reduce errors) simultaneously (Equations 6.5 and 6.6):

$$\text{minimize } \frac{1}{2} \|w\|^2 + C \sum_{i=1}^l (\xi_i + \xi_i^*) \quad (6.5)$$

$$\text{Subject to } \begin{cases} y_i - w^T x_i - b \leq \epsilon + \xi_i \\ w^T x_i + b - y_i \leq \epsilon + \xi_i^* \\ \xi_i, \xi_i^* \geq 0 \end{cases} \quad (6.6)$$

In this context, w represents the feature vector, b is a constant, and x_i and y_i are the independent and dependent variables in \mathbf{X} and \mathbf{Y} , respectively. The constant $C > 0$ balances the trade-off between the flatness of the hyperplane and the deviations from the marginal range [17]. A high value of C emphasizes correct prediction of all training examples, which is not recommended for datasets with many noisy observations. A low value of C promotes generalization by tolerating small prediction errors, while high values enforce stricter fitting, increasing risk of overfitting.

Non-linear relationships were addressed using kernel functions. Kernel functions, such as linear, polynomial, radial basis function (RBF), can be used to preprocess \mathbf{X} , facilitating the effective description of non-linear relationships between predictors and responses. When employing kernel functions, the kernel coefficient γ (gamma) must be determined, as it defines the influence of a

training sample on the regression process. A high γ value indicates better fitting of the training data but comes with the risk of overfitting.

The SVR model was initially optimized through hyperparameter tuning, a process of optimizing the set of hyperparameters (C , ϵ , kernel, gamma). This process was conducted using grid search in Python, which involves specifying a set of possible values for each hyperparameter and systematically evaluating the model's performance for every combination of these values. The optimized hyperparameters, which provide the best performance (based on mean squared error (MSE) and R^2) on a validation set (a subset of data used during model training to tune parameters and prevent overfitting), improve the model's generalizability to unseen data (new data that the model has not encountered during training or validation, typically referring to the test set or real-world data).

To evaluate the influence of FTIR indices on the prediction of the rheological parameter with highest predictivity using a Support Vector Regression (SVR) model, SHapley Additive exPlanations (SHAP) analysis was performed. SHAP is a model-agnostic interpretability framework that quantifies the contribution of each input feature to a machine learning model's prediction [18]. The goal of this analysis was to identify and rank the importance of FTIR indices in predicting the rheological parameter, thereby elucidating the underlying relationship between FTIR spectral features and the viscoelastic properties of asphalt binders.

The SVR model was trained to correlate the rheological parameter to FTIR indices using optimized hyperparameters derived from a grid search process. SHAP values were computed using the shap Python library, leveraging the kernel-based approximation for feature importance. The SHAP values were calculated for all features, and the mean absolute SHAP value for each feature was used as a measure of its importance in predicting the rheological parameter. Additionally, a summary plot was generated to visualize the distribution of SHAP values for each FTIR feature, highlighting both global importance and individual contributions. The feature values were color-coded to reflect their magnitude (low to high) and their corresponding impact on the predictions (positive or negative). This analysis provided a comprehensive understanding of how each FTIR index influenced the model's predictions of rheological parameter, supporting the interpretation of chemical-rheological interactions.

6.3.4 Deep artificial neural networks (DNNs)

Artificial Neural Networks (ANNs) were utilized to predict the parameters of the sigmoidal model, specifically, alpha (α), beta (β), sigma (σ), and gamma (γ), as well as the crossover frequency values, based on FTIR spectroscopy indices. These ten FTIR indices served as input features (\mathbf{X}), while the output variables (\mathbf{Y}) consisted of the four sigmoidal parameters and the crossover frequency. The predicted parameters were subsequently used to estimate the dynamic modulus ($|G^*|$) values across different frequencies, enabling the characterization of rheological properties without conducting the Dynamic Shear Rheometer (DSR) test. The dataset utilized in this section comprises all experimental data (238 samples) from Chapters 4 and 5, including laboratory-aged samples under various conditions and field-aged samples.

Prior to implementing the Artificial Neural Networks (ANNs), the input and output data were evaluated for normality. As shown in Figure 6.7, neither the input nor output variables followed a normal distribution. Additionally, negative values were present in the dataset, necessitating the application of a transformation technique to address skewness and variance.

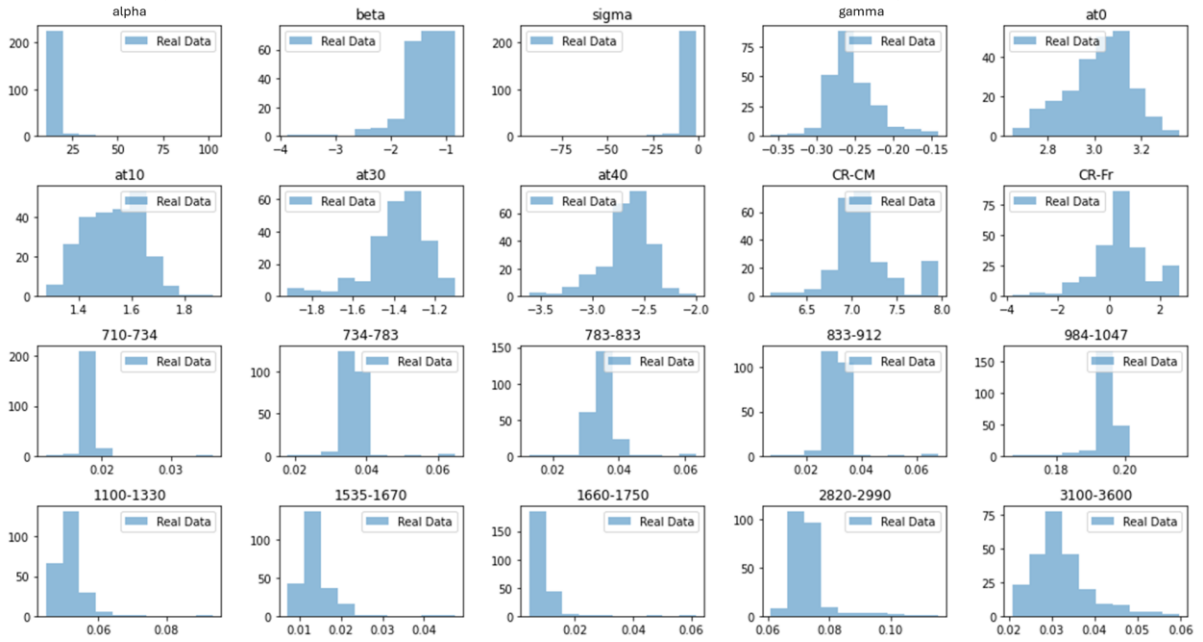


Figure 6.7 Rheological and chemical data for all 238 data points are shown before applying the normal distribution adjustment. In each subplot, the x-axis represents the variable values, and the y-axis indicates the number of samples.

To address this, the Yeo-Johnson transformation was applied. This transformation is a statistical method available in the `scipy.stats.yeojohnson` library in Python (Figure 6.8). This transformation is particularly effective in stabilizing variance, reducing skewness, and transforming data to approximate a normal distribution. The mathematical formulation of the Yeo-Johnson transformation [19] is provided in Equation (7):

$$T(y; \lambda) = \begin{cases} \frac{[(y+1)^\lambda - 1]}{\lambda} & \text{if } y \geq 0 \text{ and } \lambda \neq 0, \\ \log(y + 1) & \text{if } y \geq 0 \text{ and } \lambda = 0, \\ -\frac{[(-y+1)^{2-\lambda} - 1]}{2-\lambda} & \text{if } y < 0 \text{ and } \lambda \neq 2, \\ -\log(-y + 1) & \text{if } y < 0 \text{ and } \lambda = 2, \end{cases} \quad (6.7)$$

Where y is the original data value and λ is the transformation parameter that determines the shape of the transformation. It is typically estimated from the data to maximize the likelihood of a normal distribution of the transformed values[20, 21].

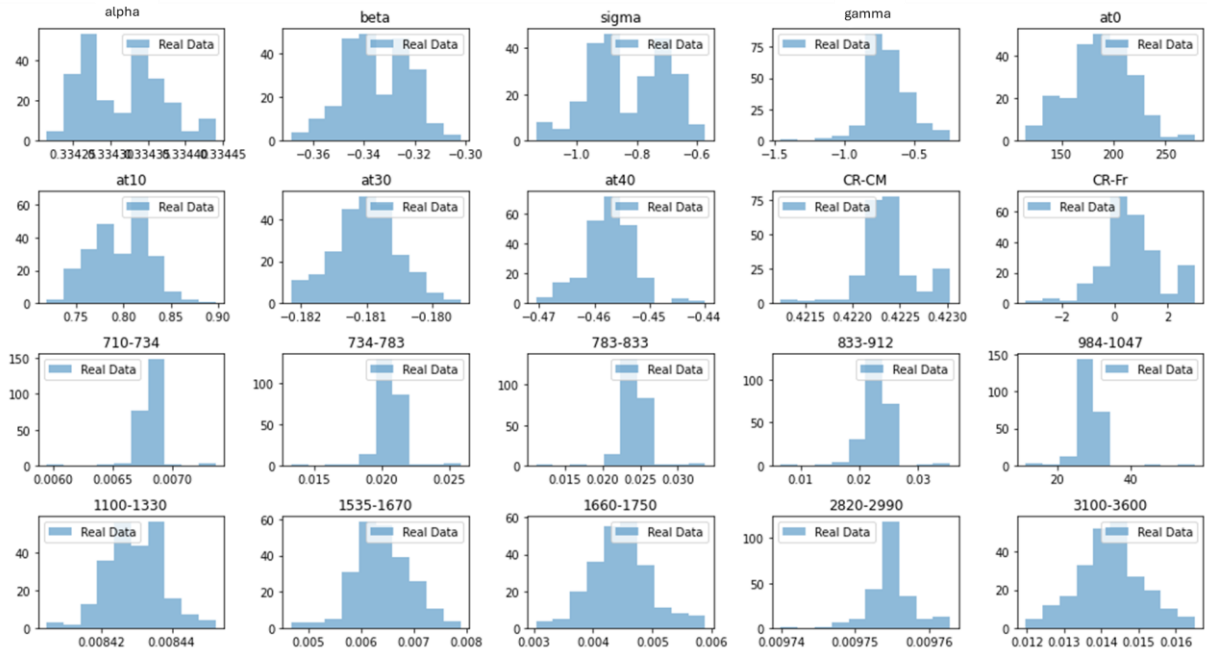


Figure 6.8 Rheological and chemical data for all 238 data points are shown after adjusting the normal distribution using the Yeo-Johnson transformation. In each subplot, the x-axis represents the normalized values of variables, and the y-axis indicates the number of samples.

Following the Yeo-Johnson transformation, standard scaling was applied to both input and output variables using the StandardScaler from sklearn.preprocessing, ensuring model compatibility and numerical stability.

The implemented model constituted a deep artificial neural network (DNN), as the number of hidden layers was determined through hyperparameter optimization to lie in the range of three to six layers (presented in Table 6.6 in section 6.4.6). The model was initially inspired by the classical perceptron model [22], a binary classifier based on a simplified representation of a biological neuron, which forms the foundation of modern artificial neural networks (ANNs) [11]. However, the architecture adopted in this chapter extends beyond the shallow configuration typically associated with ANNs. Owing to the inclusion of three or more hidden layers, the model qualifies as a DNN. For the remainder of this chapter, the term DNN will be used to refer to the implemented architecture. It computes a weighted sum of the input features $z = \sum_{i=1}^n w_i x_i$, where x_i are the input features w_i are the corresponding weights, and n is the number of input features. To improve the model's learning capability, DNNs extend the perceptron by incorporating multiple layers (e.g., input, hidden, and output layers) and employing advanced learning algorithms like backpropagation [23].

In the DNN used for this chapter, each neuron in the network computed a weighted sum of its inputs, expressed as equation 6.8:

$$z_j^{(l)} = \sum_{i=1}^n w_{j,i}^{(l)} x_i^{(l-1)} + b_j^{(l)} \quad (6.8)$$

Where $w_{j,i}^{(l)}$ represents the weights connecting the i -th neuron in layer $l-1$ to the j -th neuron in layer l , $x_i^{(l-1)}$ are the outputs from the previous layer, and $b_j^{(l)}$ is the bias term for neuron j in layer l . The weighted sum was passed through a non-linear activation function to produce the neuron's output (equation 6.9):

$$a_j^{(l)} = f(z_j^{(l)}) \quad (6.9)$$

where f is the activation function. The architecture of the DNN, including the number of layers, number of neurons per layer, type of activation functions, regularization techniques, and optimization algorithms, was determined through a parameter grid search in Python. For the activation functions, the parameter grid considered both the Rectified Linear Unit (ReLU) and hyperbolic tangent (tanh) functions for the hidden layers, depending on the problem's nonlinearity requirements.

The model was trained using the backpropagation algorithm, where the weights were iteratively adjusted to minimize the mean squared error (MSE) loss function in equation 6.10:

$$Loss = \frac{1}{m} \sum_{i=1}^m (y_i - \hat{y}_i)^2 \quad (6.10)$$

where y_i and \hat{y}_i are the actual and predicted values, respectively, and m is the number of training samples. Early stopping was applied based on validation loss to prevent overfitting.

6.3.5 Model validation

For the SVR analysis of predicting rheological parameters, the dataset of 60 data points was split into training (70%) and testing (30%) sets using the scikit-learn library in Python, with a fixed random state to ensure reproducibility. Despite the relatively small dataset, this size is common in research studies or specialized applications, though caution must be exercised regarding overfitting. A 10-fold cross-validation strategy was applied, wherein the dataset was divided into 10 equal segments. Nine segments were used for model training, and one segment was reserved for testing, iterating this process 10 times with a different testing segment each iteration. The accuracy outcomes were averaged to provide a robust evaluation of the model's effectiveness.

For the MLR analysis of aging factors, the 10-fold cross-validation strategy was also used. While the dataset size may limit the robustness of model performance, cross-validation mitigates this issue by using all data points efficiently across multiple training and testing iterations.

The regression model's performance was evaluated using several metrics to ensure a comprehensive assessment. These metrics include the root mean square errors of calibration ($RMSEC$), cross-validation ($RMSECV$), and prediction ($RMSEP$) (Equation 6.11), along with the determination coefficients of calibration (R^2_c), cross-validation (R^2_{cv}), and prediction (R^2_p) (Equation 6.12), and the relative percent difference (RPD) (Equation 6.13) [10]. These metrics were computed using `mean_squared_error` and `r2_score` functions from the `scikit-learn.metrics` module, and standard deviation calculations using `numpy` or `pandas`:

$$RMSE = \sqrt{\frac{1}{N} \sum_{i=1}^N (\hat{y}_i - y_i)^2} \quad (6.11)$$

$$R^2 = 1 - \frac{\sum_{i=1}^N (\hat{y}_i - y_i)^2}{\sum_{i=1}^N (y_i - \bar{y}_i)^2} \quad (6.12)$$

$$RPD = \frac{SD}{RMSE} \quad (6.13)$$

In these evaluations, y_i and \hat{y}_i represent the measured and predicted values for sample i , \bar{y}_i is the mean value of y_i , N denotes the number of samples for calibration, cross-validation, or prediction, SD is the standard deviation of measured values for N samples.

RPD indicates the model's predictive ability relative to data variability. Given the limited dataset, *RPD* values and other performance metrics should be interpreted carefully to avoid overstating the model's generalizability. An *RPD* value higher than 2 implies good model accuracy, while an *RPD* larger than 3 indicates excellent performance [24]. The Coefficient of Determination (R^2) quantifies the proportion of variance in the dependent variable predictable from the independent variables, *RMSE* measures the average magnitude of prediction errors, and *RPD* is the ratio of the standard deviation of the training data to the *RMSE*, indicating model predictability. These metrics were used in parallel to provide different perspectives on the model's performance, allowing for a thorough evaluation and comparison of all models to identify the most robust and accurate one for our specific objectives.

When applying SVR to the prediction of equivalent field ageing time of a laboratory sample, Leave-One-Out Cross-Validation (*LOOCV*) was employed due to the limited field data (8-10 points) using the `LeaveOneOut` module from `scikit-learn.model_selection`. Given the small number of data points, *LOOCV* is ideal as it maximizes the usage of each observation for both training and testing, although the performance might be sensitive to the inherent variability of such a small dataset. *LOOCV* uses one observation as the validation set and the remaining observations as the training set, repeating this process for each observation in the dataset. The *RMSE* was calculated and reported to evaluate the model performance.

During training of DNNs, 238 datapoints, the network was evaluated using the coefficient of determination (R^2) and the root mean squared error (*RMSE*) for both the training and testing datasets. These metrics were computed using the TensorFlow and Keras libraries, with additional evaluation metrics obtained via `scikit-learn.metrics`. Although the dataset size is larger in this case, ANN models typically require even larger datasets to capture complex relationships reliably. Nonetheless, the metrics provided a reasonable evaluation of the model's performance given the available data. These metrics quantified the model's ability to accurately predict the sigmoidal model parameters and crossover values based on the FTIR indices, demonstrating the feasibility of estimating rheological properties without performing physical DSR measurements.

6.4 Results and discussion

6.4.1 Dataset construction

Figure 6.9 presents the PCA plots for the chemical datasets derived from the full FTIR spectra and the FTIR indices. Both plots distinctly exhibit two separate clusters corresponding to the two binders. Additionally, the aging direction is clearly evident in both cases, indicating the influence of aging on the chemical characteristics. The explained variances for each principal component are higher in the analysis using the complete spectral dataset compared to those using the FTIR indices. This observation aligns with expectations, as datasets with greater detail generally yield higher explained variances for individual components. However, given that both datasets provide comparable levels of classification, using the FTIR indices offers practical advantages. By focusing on the indices, it is possible to mitigate issues such as the computational burden and the curse of dimensionality associated with the full spectral dataset. Therefore, for subsequent steps in the analysis, the FTIR indices will be used, balancing efficiency with the preservation of critical chemical information.

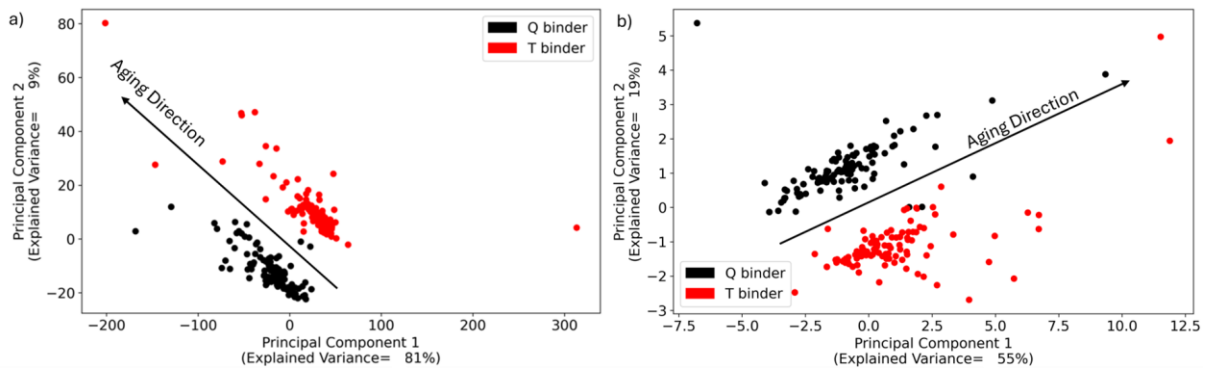


Figure 6.9 PCA score plot of both Q and T binder types based on a) entire FTIR spectra without noisy region of 1900-2300 cm^{-1} , and b) FTIR indices.

Figure 6.10 displays the PCA plots for the rheological datasets derived from the DSR master curves containing reduced frequency, complex modulus, and phase angles, and rheological parameters, which include four sigmoidal model parameters (α , β , γ , σ), four shift factors at 0, 10, 30, and 40 $^{\circ}\text{C}$, as well as the CR-Fr and CR-CM. Both plots reveal two distinct clusters corresponding to the two binders, with some degree of overlap. Additionally, the aging direction is evident in both cases, highlighting the impact of aging on the rheological properties. The explained variances for the principal components are higher when using the complete master curve dataset compared to the analysis based on the rheological parameters. This trend is consistent with the observations from the FTIR analysis. However, since both datasets provide comparable levels of classification accuracy, the use of rheological parameters is advantageous. This approach reduces computational demands and avoids issues related to the curse of dimensionality associated with the more detailed master curve dataset.

For subsequent analyses, the rheological parameters will be utilized to achieve a balance between computational efficiency and the retention of essential rheological information. This decision ensures that chemo-rheological relationships are investigated effectively while minimizing unnecessary complexity.

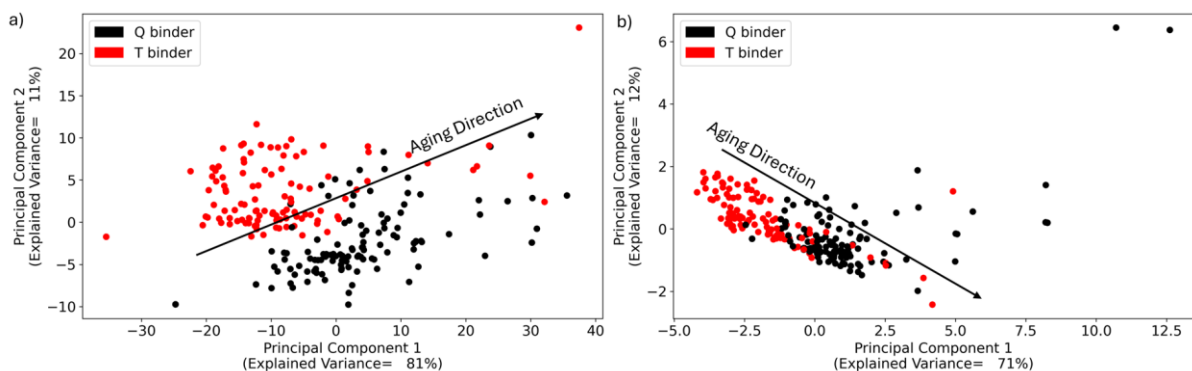


Figure 6.10 PCA score plot of both Q and T binder types based on a) complete master curve data containing reduced frequency, complex modulus, and phase angles, and b) rheological parameters include four sigmoidal model parameters (α , β , γ , σ), four shift factors at 0, 10, 30, and 40 $^{\circ}\text{C}$, as well as the CR-Fr and CR-CM.

6.4.2 Chemical and rheological features importance for aging pattern recognition by PCA

The PCA analysis was performed on binder samples using their combined chemical and rheological properties as input. Based on the explained variance, the first two principal components account for

70% of the variance in the data (Figure 6.11). A two-dimensional plot of PC1 versus PC2 (Figure 6.11) can effectively represent the input data. As shown in Figure 6.11, there is a clear distinction between Q and T binder samples. Moreover, the aging direction trends towards the top right quadrant, indicating an increase in aging with both PCs.

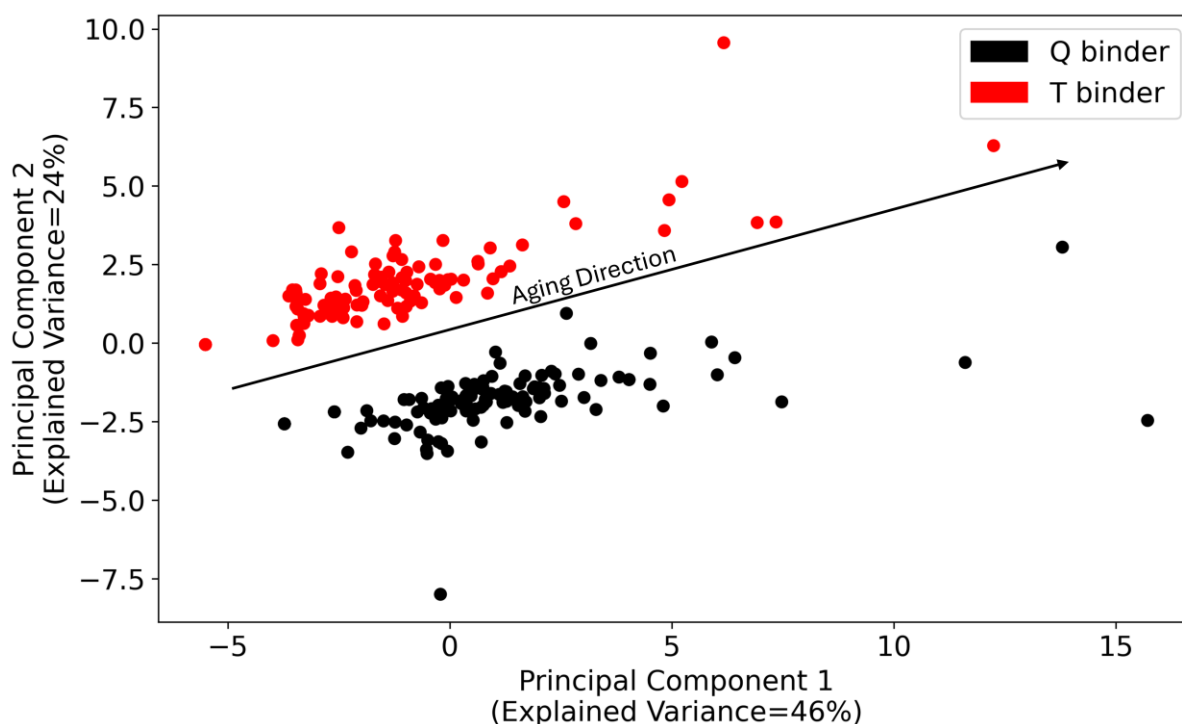


Figure 6.11 PCA score plot of both Q and T binder types based on FTIR+DSR input data. The interactive plot can be found in Figure 1S in appendix of chapter 6 with annotated samples.

PCA loadings are the coefficients that represent the contribution of the original variables to the principal components. A variable with a high absolute loading signifies its more significant influence on the principal component, and thus on the classification of binder type and aging state. In this chapter, loadings were normalized to a range of -1 to +1, and a threshold of ± 0.8 was set, with values beyond this threshold considered important. The sign of the loading—positive or negative—indicates whether the variable is positively or negatively correlated with the principal component.

Figure 6.12 presents the loadings of all features for the first and second principal component (PC1 and PC2). In this context, the principal components are not only statistical abstractions, but also represent underlying physical processes related to binder aging. The importance of the PC1 axis lies in aging direction of both Q and T binders. Key contributors to PC1 include beta (transition between viscous and elastic regimes), gamma (sensitivity of the binder's stiffness to changes in frequency), the shift factor at 10, 30, and 40 °C from rheological measurements. The beta and gamma parameters are sensitive to changes in binder elasticity and viscosity, which are influenced by both oxidative aging. The shift factor variation is an indicator of molecular rearrangement due to oxidation aging process where addition of oxygen species may alter binder stiffness.

The importance of the PC2 axis lies in both aging direction and differentiating between Q and T binders. Key contributors to PC2 include beta (transition between viscous and elastic regimes) and sigma from rheological measurements, along with FTIR indices in the ranges of 833-912 cm^{-1} (C-H in isolated adjacent hydrogen aromatic rings), 984-1047 cm^{-1} (S=O in oxygenated function-sulfoxide), and 1100-1330 cm^{-1} (Tertiary alcohol C-C-O, C-O in carboxylic acid, C-C-C in diaryl ketones, C-N secondary amides, O=S=O in sulfone). Changes in the FTIR spectra reflect oxidation mechanisms, as

evidenced by the appearance of new oxygenated functional groups (S=O in sulfoxides) due to oxidative degradation. The variations in the 1100-1330 cm^{-1} range suggest the formation of new chemical bonds linked to hydrothermal or thermo-oxidative aging, influencing the binder's molecular network. The beta parameter's contribution to PC2 indicates the interplay between the mechanical properties and chemical modifications, which help differentiate between the Q and T binders, likely due to distinct aging behaviours under different environmental conditions.

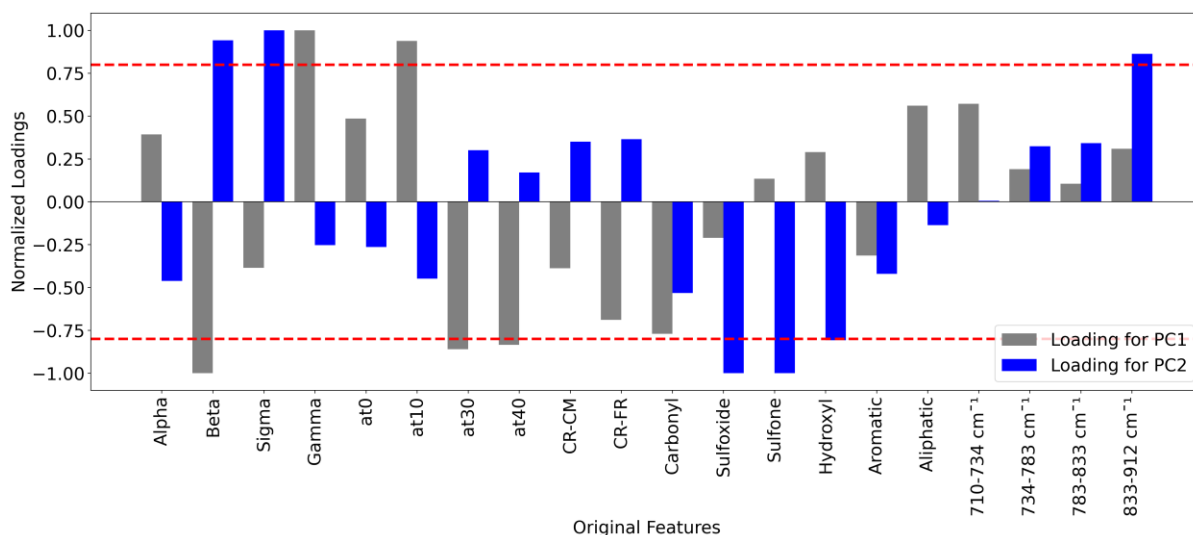


Figure 6.12 Loadings of all features (FTIR + DSR parameters) for PC1 and PC2. All the Q and T binder samples were used as input. A threshold of ± 0.80 was applied and marked by the red horizontal lines to determine the significance of these loadings.

Both components highlight how aging impacts the viscoelastic properties and molecular structure of the binders, enabling effective differentiation between the two types. Key contributors include rheological measurements and FTIR spectral data, suggesting that changes in chemical structure correlate with aging and binder performance. The changes in molecular structure, particularly due to oxidation (oxygen functional groups), explain the observed shifts in viscoelastic behaviour. The reduction in elasticity, for example, can be attributed to oxidative crosslinking of the binder matrix. This understanding could facilitate the development of predictive models that integrate these parameters, enhancing material selection and formulation strategies for specific applications.

To further understand the correlation between different aging conditions, Q binders and Q mixture samples (PA and SMA) aged in field were used for PCA. It is shown that over 80% of the variance in the input data can be explained by the first two principal components (Figure 6.13). Figure 6.13 depicts the PC1 versus PC2 plot for all Q-based samples, with detailed sample names omitted for clarity. An interactive plot with sample names is available in the supporting information (Figure 2S in appendix of chapter 6). In this plot, the aging direction is towards the upper left quadrant.

Three main groups can be identified in this plot. The first group (circle 1 in Figure 6.13) includes the field-aged PA sample from 2021 (after 7 years of field aging) and the 1 mm film of Q binder hydrothermally aged at 85 $^{\circ}\text{C}$ for 80 hours under 20 bar pressure (Q-LW80H-1) or for 14 and 21 days under 1 bar pressure (Q-85C-14/21D-RH). The samples are located in the upper left corner of the plot, indicating a high degree of aging. Notable by visual inspection, the lab-aged samples are positioned within the region of highly aged samples. Conversely, the placement of the sample that has undergone 7 years of field aging (PA 2021) is unexpected, raising questions about the reliability or consistency of the data for this specific sample. The second group comprises all binder films aged under different laboratory conditions (discussed in chapter 4 and 5), along with some PA and SMA samples aged in field (from 2019 to 2023). The third group contains field-aged samples from 2014 -

2017. In groups 1 and 2, both mixture and binder film samples are present, indicating that differentiation between binder films and extracted binder samples cannot be achieved solely by PCA analysis of specific FTIR indices and rheological properties.

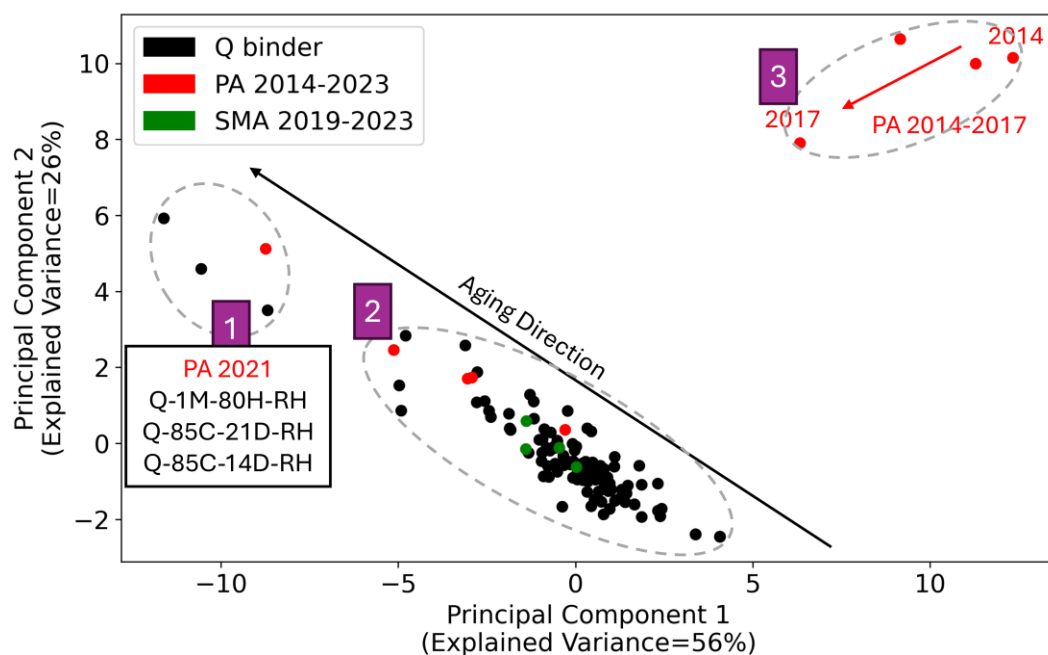


Figure 6.13 PCA plot based on FTIR and DSR data for Q samples including lab-aged binder films and field-aged mixtures. An interactive version of this plot, showing the exact sample names, is available in the supporting information (Figure 2S in appendix of chapter 6).

Figure 6.14 shows the loadings on PC1 and PC2 for all features. For PC1, high loadings are observed for rheological features such as alpha and beta. Aging, as indicated by PCA analysis, is associated not only with movement towards negative PC1 values but also towards positive PC2 values.

The loadings on PC2, presented in Figure 6.14, indicate that β and the crossover frequency values from the rheological properties, along with the carbonyl index, aromatic index, and FTIR indices in the ranges of $710\text{--}734\text{ cm}^{-1}$, $783\text{--}833\text{ cm}^{-1}$, and $833\text{--}912\text{ cm}^{-1}$ from the chemical properties, contribute more than 80% to PC2. The carbonyl index and FTIR bands in the $710\text{--}912\text{ cm}^{-1}$ region are indicative of oxidative aging, as carbonyl and aromatic groups are commonly formed in the oxidation and condensation of hydrocarbons. These features suggest that oxidation is a key aging mechanism influencing binder stiffness and molecular structure. The presence of these oxidation-related features in the FTIR spectra further underscores the correlation between chemical changes and rheological behaviour, with increased oxidation leading to changes in both mechanical properties (e.g., crossover frequency and β) and molecular structure (carbonyl and aromatic functional groups).

The differentiation among all groups can be effectively accomplished using either PC1 or PC2, with the PC1 loadings highlighting the high significance of rheological features and the PC2 loadings emphasizing the importance of both rheological and chemical properties. This dual contribution suggests that binder aging involves complex interactions between mechanical properties and molecular transformations. The rheological changes observed in PC1 are linked to physical modifications of the binder, while the chemical shifts in PC2 indicate structural degradation or modification, providing a more comprehensive view of the aging process. Consequently, there should be a discernible difference in the rheological features and FTIR values between these groups. Notably, group 3 samples were measured using a different sample preparation method and FTIR device compared to group 2 samples. Such differences may contribute to slight variations in FTIR

spectra, but the PCA analysis effectively captures the overall trends, ensuring that the chemical changes due to aging are not masked by the measurement method.

Although the carbonyl and sulfoxide values of these samples were within the normal range, PCA analysis of all FTIR indices collectively distinguished between measurements taken by different sample preparation and devices. This highlights the robustness of PCA in isolating key features related to binder aging, even when external factors such as measurement conditions are present. It also emphasizes the need for standardized sample preparation and measurement protocols to avoid confounding variables in future studies. It is important to note that normalization, baseline correction, and indices calculation did not mask the information. For future studies, it is recommended to analyse how different sample preparations and devices affect FTIR data. Understanding the impact of such variables would enhance the reliability of FTIR-based diagnostics for binder aging and contribute to more accurate predictions of binder behaviour in practical applications.

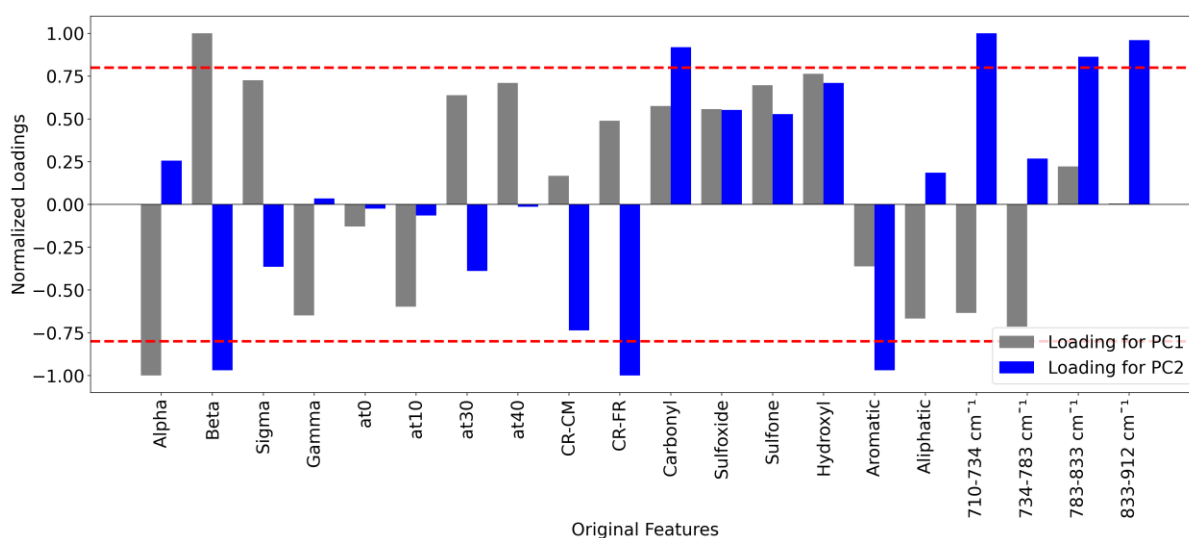


Figure 6.14 Loadings of all features (FTIR + DSR parameters for Q binder samples, including lab-aged binder films and field-aged mixture) for PC1 and PC2. All the Q binder samples were used as input. A threshold of ± 0.80 was applied and marked by the red horizontal lines to determine the significance of these loadings.

In summary, combining all the important features identified from both PCA analyses shows that both chemical and rheological properties are important for aging studies.

6.4.3 Evaluating lab-field aging similarity based on Euclidean distance

To study the similarity between field- and lab-aged samples, the Euclidean distance was calculated based on the PCA score plot (Figure 6.13). For this distance calculation, field samples of PA-2023 and SMA-2023 were considered as the reference groups. The reason PA-2023 and SMA-2023 were considered as references is that these samples are the most field-aged samples, each representative of 9 years of field aging for their respective mixture types. The distances between reference samples and all other samples are presented in Table 1S (in appendix of chapter 6) in an ascending order based on distance value. The illustrative distance results are presented in Figure 6.15, showing that the samples Q-33%-85C-3H, Q-1M-40H-RH, Q-1M-150B-O, and Q-33%-60C-9H are, in order, the closest to PA-2023. Similarly, for SMA-2023, the closest samples, in order, are Q-85C-21D-O, Q-70C-21D-O, Q-1M-85C-O, and Q-33%-70C-3H.

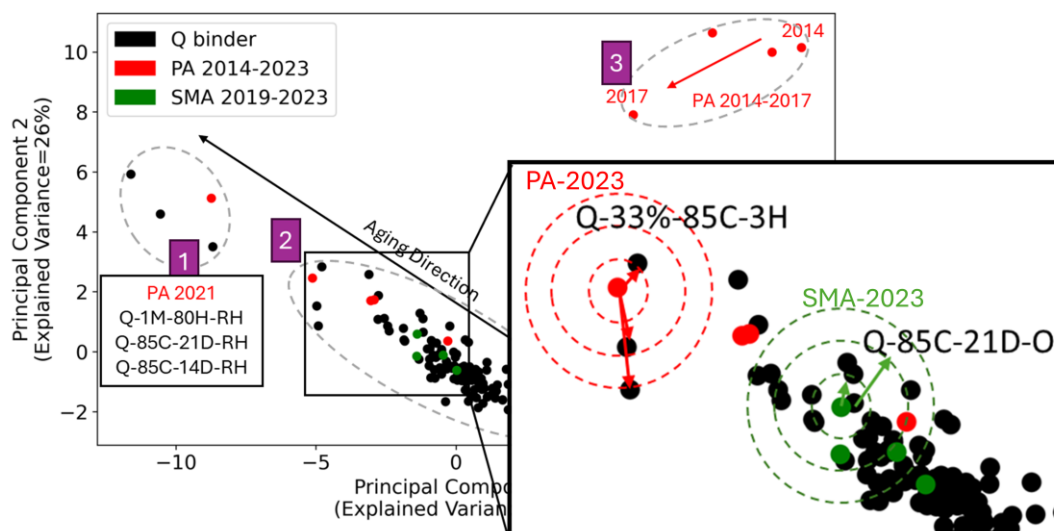


Figure 6.15 Euclidean pairwise distances identifying the samples closest to PA-2023 and SMA-2023. The inset on the right provides an enlarged view of the relevant section of the PCA plot. Circles indicate the distances around each field sample.

6.4.4 Quantifying the impact of aging factors and back-calculation of field-aging conditions by MLR

This MLR analysis aims to quantify how various aging factors (i.e., temperature, pressure, thickness, and time) contribute to resulting aging in a binder and to elucidate the relationships among these factors. The trained model is then used to back-calculate the aging conditions required to achieve the same level of aging observed in field samples. A combined aging index was utilized for the MLR analysis instead of relying solely on FTIR or DSR parameters since based on PCA analysis in section 6.4.2, both chemical and rheological properties are important for aging studies. The analysis separated lab-aged binders into hygrothermal and thermo-oxidative aging groups, expecting that the presence of humidity during aging could change the effect of other aging factors. This categorization aimed to account for the unique impacts of humidity on the aging process and binder properties. The low Pearson correlation coefficients (between ± 0.30) and VIF values of aging factors (~ 1) (Table 2S in appendix of chapter 6) indicated no significant multicollinearity among the input variables, justifying the appropriate use of MLR.

Thermo-Oxidative aging model

The thermo-oxidative aging dataset was analysed using Multiple Linear Regression (MLR) without considering humidity, incorporating predictors such as temperature, pressure, time, and thickness. Key outputs, including multicollinearity assessment, regression summaries, and cross-validation results, provide insights into the dataset's characteristics and model performance.

The Variance Inflation Factor (VIF) values for the predictors—temperature (1.156), pressure (1.083), time (1.384), and thickness (1.211)—are all below the threshold of 10, indicating negligible multicollinearity. This suggests that the predictors are relatively independent of each other, allowing for stable estimation of regression coefficients. The Pearson correlation matrix supports this conclusion, showing generally weak to moderate linear correlations between predictors, with the strongest negative correlation observed between time and thickness (-0.404).

The base regression model without interaction terms explains 75.5% of the variability in the normalized aging index ($R^2 = 0.755$). This explanatory power demonstrates the overall utility of the predictors in explaining the variability in the aging index. All predictors have statistically significant effects, as indicated by their coefficients and associated p-values. Table 6.1 shows the estimated coefficients for each factor of Equation 10 based on the MLR model: temperature (0.3036, $p < 0.001$),

pressure (-0.3700, $p < 0.001$), time (-0.2107, $p = 0.002$), and thickness (0.4420, $p < 0.001$). These coefficients reveal that the aging index increases with temperature and thickness but decreases with pressure and time, holding other factors constant.

A more complex model including interaction terms was also evaluated, yielding a higher R^2 (0.821). Key interaction terms, such as temperature \times pressure (0.4065, $p = 0.001$) and pressure \times time (0.3693, $p < 0.001$), were statistically significant, indicating that combined effects of these variables amplify the aging index (Table 6.1). The significance of the temperature \times pressure and pressure \times time interactions is likely due to their physical relevance in aging processes. Temperature and pressure are both known to influence chemical reaction rates, such as oxidation or thermal degradation, while time acts as a cumulative factor that affects these processes. The interaction between temperature and pressure, for example, may be critical in understanding how these variables together influence aging by accelerating or decelerating certain chemical pathways.

However, some interaction terms, such as temperature \times thickness (-0.0577, $p = 0.451$), were not significant, suggesting limited utility in this context. The lack of significance for the temperature \times thickness interaction might be due to the relative independence of these two variables in influencing aging. While temperature is a direct driver of chemical reactions and physical changes in the binder, thickness may primarily influence diffusion rates or the distribution of aging effects throughout the material. Since the mechanisms behind thickness-related changes might not strongly interact with temperature in the context of this model, the interaction term does not add substantial explanatory value.

Despite the improved explanatory power, the interaction model performed less effectively during cross-validation, with an R^2 of 0.625 compared to 0.672 for the base model. The higher cross-validation mean squared error (MSE) of 0.380 for the interaction model versus 0.331 for the base model further indicates that the simpler model generalizes better to new data. This reduction in cross-validation performance is likely due to overfitting. By including multiple interaction terms, the model becomes more complex and sensitive to the specificities of the training data, leading to a higher R^2 on the training set. However, this complexity reduces the model's ability to generalize to new data, as evidenced by the increase in MSE during cross-validation. The base model, with fewer parameters, avoids overfitting and maintains better predictive accuracy on unseen data. This suggests that while interactions may provide deeper insights into mechanisms, they may not always translate into better generalizability, particularly when the dataset is limited or contains noise.

Table 6.1 Estimated coefficient for each factor of Equation 10 based on MLR model. Temp stands for temperature.

Thermo-oxidative aging								
Simple model			Model with interaction terms					
Coefficient		P-value	Coefficient		P-value	Coefficient		P-value
Constant (α_0)	-4.732	0.000	Constant (α_0)	-4.523	0	Temp \times Pressure	0.002	0.21
Temp (α_1)	0.185	0.008	Temp (α_1)	0.024	0.013	Temp \times Time	-0.001	0.324
Pressure (α_2)	-0.293	<0.001	Pressure (α_2)	-0.317	0.001	Pressure \times Time	-0.004	0.056
Time (α_3)	-0.508	<0.001	Time (α_3)	-0.405	0.001	Pressure \times Thickness	0.007	0.098
Thickness (α_4)	0.598	<0.001	Thickness (α_4)	0.527	0	Time \times Thickness	-0.003	0.075

Hygrothermal aging model

The analysis of the hygrothermal dataset was conducted using a MLR model incorporating the effects of temperature, pressure, time, and thickness as predictors of the normalized aging index under humid conditions. Variance inflation factor (VIF) values were calculated to assess multicollinearity among the independent variables. All VIF values were below 10, indicating low levels of multicollinearity and suggesting that each predictor contributes distinct information to the regression model. This was further corroborated by the Pearson correlation coefficient matrix, which revealed only moderate interdependence between some variables, such as the negative correlation between pressure and time (-0.437) and time and thickness (-0.408). None of these correlations were sufficiently strong to raise concerns about collinearity influencing the model's stability.

The regression model explained 72.7% of the variance in the normalized aging index, as reflected by the R-squared value of 0.727. Examination of the regression coefficients revealed that temperature had a significant positive effect (coefficient = 0.176, $p = 0.008$), whereas pressure (coefficient = -0.317, $p < 0.001$) and time (coefficient = -0.505, $p < 0.001$) exhibited significant negative effects on the aging index (Table 6.2). Thickness, in contrast, showed a strong positive relationship (coefficient = 0.571, $p < 0.001$). These findings highlight the importance of thickness and time as dominant factors influencing the aging index, with the latter exerting a substantial negative effect.

A model incorporating interaction terms was also developed to explore potential interactions between the predictors. While the inclusion of these terms slightly increased the R-squared value to 0.760 indicated only a modest improvement in model fit compared to the simpler model. Most interaction terms were not statistically significant, with the exception of the marginal effects observed for time and thickness (coefficient = -3.109, $p = 0.089$) (Table 6.2). Cross-validation results further supported the selection of the simpler model. The mean squared error (MSE) for the simple model was 0.3078, compared to 0.3387 for the model with interaction terms, indicating a lower error and better generalizability for the simple model. Similarly, the cross-validated R-squared values were 0.6883 and 0.6532 for the simple model and the interaction model, respectively, underscoring the robustness of the simpler approach.

Table 6.2 Estimated coefficient for each factor of Equation 10 based on MLR model. Temp stands for temperature.

Hygrothermal aging								
Simple model			Model with interaction terms					
Coefficient		P-value	Coefficient		P-value	Coefficient		P-value
Constant (α_0)	-4.899	0	Constant (α_0)	-4.761	0	Temp × Pressure	0.003	0.185
Temp (α_1)	0.177	0.008	Temp (α_1)	0.022	0.014	Temp × Time	-0.002	0.289
Pressure (α_2)	-0.317	<0.001	Pressure (α_2)	-0.345	0.001	Pressure × Time	-0.005	0.039
Time (α_3)	-0.506	<0.001	Time (α_3)	-0.398	0.001	Pressure × Thickness	0.009	0.065
Thickness (α_4)	0.572	<0.001	Thickness (α_4)	0.491	0	Time × Thickness	-0.004	0.049

In conclusion, the analysis demonstrates that the predictors of temperature, pressure, time, and thickness significantly influence the normalized aging index under humid conditions, with thickness and time exhibiting the most pronounced effects. While the inclusion of interaction terms provided slight improvements in explanatory power, the associated increase in model complexity and

reduction in cross-validation performance suggest that the simpler model is more effective for predicting the aging index under the current experimental conditions.

Comparative analysis for thermo-oxidative vs. hygrothermal models

The comparison between the thermo-oxidative model (without humidity) and the hygrothermal model (with humidity) offers insights into the effects of including humidity as a predictor. Both models were evaluated using metrics such as variance inflation factor (VIF), Pearson correlation coefficients, model summary statistics, interaction terms, and cross-validation performance.

For multicollinearity, VIF values for both models were well below the threshold of 10, indicating no significant multicollinearity in either case. However, the VIF values were generally lower in the model with humidity, suggesting slightly improved independence among predictors. Correlation matrices revealed stronger pairwise relationships in the humidity model, particularly between pressure and time and between time and thickness, indicating that humidity introduces specific interactions among predictors. While VIF captures the overall linear dependency of a predictor on all others, the correlation matrix highlights pairwise relationships. Stronger pairwise correlations in the humidity model may reflect enhanced physical or chemical interactions among variables due to humidity, redistributing interdependencies rather than uniformly increasing multicollinearity. These stronger pairwise correlations in the hygrothermal model may suggest that humidity accelerates certain aging mechanisms, such as moisture-driven chemical reactions, which could modify the physical interactions between pressure, time, and thickness. This redistribution of interdependencies helps explain the more complex aging processes under hygrothermal conditions, where humidity may influence the binder's structural integrity, its resistance to oxidation, and its response to physical stress over time.

The full model summary highlighted a slightly better fit for the hygrothermal model, as indicated by higher R-squared (0.727 vs. 0.713) values. Coefficients remained consistent across models, with the exception of pressure, which exhibited a stronger effect in the presence of humidity. This indicates that humidity amplifies the influence of pressure on the aging index, while the effects of temperature, time, and thickness remained similar.

Incorporating interaction terms provided a slight increase in R-squared for both models, but the improvement was marginal (0.760 for the hygrothermal model vs. 0.749 for the thermo-oxidative model). Despite these differences, most interaction terms were not statistically significant in either model, and their inclusion did not substantially improve predictive performance.

Cross-validation results favoured the thermo-oxidative model in terms of generalizability, as it achieved a lower mean squared error (MSE) and higher cross-validated R-squared (0.6883 vs. 0.6532). These findings suggest that the model without humidity is better suited for prediction on unseen data, while the model with humidity may overfit slightly to the training dataset.

Sensitivity analysis and compensatory effects of aging factors

The sensitivity of the aging index to different factors can be assessed by examining the coefficients of the regression models, where larger coefficients indicate higher sensitivity. For both the hygrothermal and thermo-oxidative models, the aging index is most sensitive to the time factor, which exhibits the largest magnitude coefficient in both cases. Using the regression model coefficients, compensatory changes in one variable for a one-unit change in another can be determined. For a one-unit change in Time ($\Delta\text{Time}=1$), the relationships $\alpha_3 \times \Delta\text{Time} = \alpha_2 \times \Delta\text{Pressure}$, $\alpha_3 \times \Delta\text{Time} = \alpha_1 \times \Delta\text{Temperature}$, and $\alpha_3 \times \Delta\text{Time} = \alpha_4 \times \Delta\text{Thickness}$ were used to derive equivalent changes in other variables. These compensatory values are summarized in Table 6.3.

Table 6.3 Compensatory changes in pressure, temperature, and thickness for $\Delta\text{Time} = 1$ hours, based on model coefficients.

Aging Condition	$\Delta\text{Pressure}$ (bar)	$\Delta\text{Temperature}$ (°C)	$\Delta\text{Thickness}$ (mm)
Thermo-oxidative	1.734	2.746	0.849
Hygrothermal (with humidity)	1.596	2.859	0.885

These results highlight that both models exhibit similar sensitivity patterns, with slightly reduced compensation requirements for Pressure and Temperature in the presence of humidity, but an increased compensation requirement for Thickness. This shift may reflect altered diffusion kinetics or additional physicochemical effects introduced by moisture, which are not captured under dry (thermo-oxidative) conditions. These insights are crucial for designing experiments to better control aging factors in materials.

These findings indicate that while the inclusion of humidity in the hygrothermal model improves the statistical fit and enhances the significance of certain predictors—most notably pressure—it does not consistently translate into better predictive performance. In contrast, the thermo-oxidative model, despite its comparatively lower explanatory power, performs more reliably during cross-validation, indicating superior generalizability. Therefore, the choice between models should be guided by the intended application: if interpretability and detailed understanding of variable effects are prioritized, the hygrothermal model may be preferable; however, for predictive purposes and robustness across datasets, the thermo-oxidative model remains the more reliable option.

Back-calculation of laboratory conditions corresponding to nine years of field aging

The trained MLR coefficients were applied in Equation 6.10 to back-calculate the aging conditions corresponding to nine years of field aging for porous asphalt (PA) and stone mastic asphalt (SMA). The combined indices were derived from the measured properties of PA-2023 and SMA-2023. Boundary conditions were constrained within the experimental ranges: $60\text{ °C} < \text{Temperature} < 85\text{ °C}$, $1\text{ bar} < \text{Pressure} < 20\text{ bar}$, $5\text{ hours} < \text{Time} < 40\text{ hours}$, and $1\text{ mm} < \text{Thickness} < 3.2\text{ mm}$. The optimized laboratory aging conditions for each mixture are summarized in Table 6.4.

Table 6.4 Back-calculated laboratory aging conditions simulating nine years of field aging for PA-2023 and SMA-2023, based on MLR model inversion.

Mixture	Temperature (°C)	Pressure (bar)	Time (hours)	Thickness (mm)
PA-2023	75.5	18.3	33.2	1.0
SMA-2023	81.0	8.2	17.1	3.2

This finding suggests that the model can serve as a starting point for guiding the design of laboratory aging conditions that simulate a specific year of field aging. This is supported by the model's ability to back-calculate laboratory conditions that yield combined aging indices closely matching those observed in long-term field-aged samples (Table 6.4). While not definitive, this alignment indicates the model captures relevant trends in the aging mechanisms. Nevertheless, the models presented here are intended primarily for exploratory use in experimental design rather than as precise predictive tools. Their current level of accuracy, evaluated via cross-validation metrics and

comparison with field-derived indices, is sufficient for feasibility assessment but requires further refinement through expanded datasets and validation.

6.4.5 Chemo-rheological relationships in aging studies

In this section, the aim is to understand the relationship between chemical properties and rheological properties using all the lab-aged samples, and field samples. SVR regression was used to correlate each of the rheological parameters such as α , β , γ , σ , CR-CM, CR-Fr, and shift factors (aT at various temperatures) with all the chemical parameters, and R^2 and RMSE for calibration, prediction, cross-validation, and RPD are reported in Table 3S in appendix of chapter 6. The optimal combination of SVR parameters (C, epsilon, gamma, and kernel) is presented for each rheological parameter and varies across different properties due to the unique nature of the dataset and their distinct characteristics.

The performance of SVR in modelling these properties varied significantly. Among the tested features, the β parameter demonstrated the highest predictive accuracy, making it the best-modelled rheological parameter. For β , the optimal SVR configuration was an RBF kernel with $C=1$, $\epsilon=0.01$, and $\gamma=scale$. The results, summarized in Table 6.5, show that calibration yielded excellent agreement between predicted and observed values, while cross-validation and prediction retained reasonable accuracy.

Table 6.5 SVR modelling performance for the β rheological parameter using the optimal configuration (RBF kernel, $C = 1$, $\epsilon = 0.01$, $\gamma = scale$).

Phase	R^2	RMSE	RPD
Calibration	0.950	0.080	4.218
Cross-validation	0.700	0.180	1.874
Prediction	0.650	0.290	1.685

The β parameter characterizes the rate of change of binder stiffness with temperature. It is frequently associated with the slope of the log-log plot of modulus versus temperature or frequency, reflecting how sharply the material transitions between viscous and elastic regimes. A higher β implies a more sensitive response to temperature variation, which is crucial for evaluating performance in climates with wide temperature fluctuations. In practical terms, this means β serves as an indicator of how quickly a binder softens or stiffens with temperature, thus providing insight into the susceptibility of pavement to rutting at high temperatures or cracking at low temperatures. These results suggest that β , representing the temperature dependence of the binder's stiffness or the transition between rheological regimes, is well captured by SVR.

Other rheological parameters showed varying degrees of predictive success. The findings suggest that SVR can effectively capture complex nonlinear relationships for specific rheological parameters, with β being the most reliably modelled. This parameter's high predictability and importance in describing temperature-dependent rheological behaviour highlight its potential as a key feature for understanding binder performance. However, the variability in SVR performance across parameters emphasizes the need for careful optimization and parameter selection to improve model generalization and predictive accuracy.

The SHAP analysis aimed to investigate the contribution of FTIR indices to the prediction of the β rheological parameter (Figure 6.16). The results revealed that the FTIR index corresponding to the wavenumber range $1535\text{--}1670\text{ cm}^{-1}$ was the most influential feature, exhibiting the largest spread of

SHAP values and the highest average importance. High values of this index strongly increased the predicted β , while low values reduced it, suggesting a significant correlation with the stiffness or elasticity of the binder, possibly due to specific interactions of aromatic structures influencing the material's rheological properties. The indices $833\text{--}912\text{ cm}^{-1}$ and $3100\text{--}3600\text{ cm}^{-1}$ also contributed notably to the predictions, with their impacts varying depending on their values. The former, possibly linked to specific bond vibrations associated with binder degradation, exhibited a moderate effect, while the latter, related to O-H stretching vibrations, showed a less pronounced but still relevant influence. Lower-ranked indices, such as $710\text{--}734\text{ cm}^{-1}$ and $1660\text{--}1750\text{ cm}^{-1}$, had minimal contributions, indicating their limited role in predicting β . Overall, this analysis highlights the key FTIR features that govern the β parameter, providing a basis for further exploration of the chemical and rheological interactions in asphalt binders.

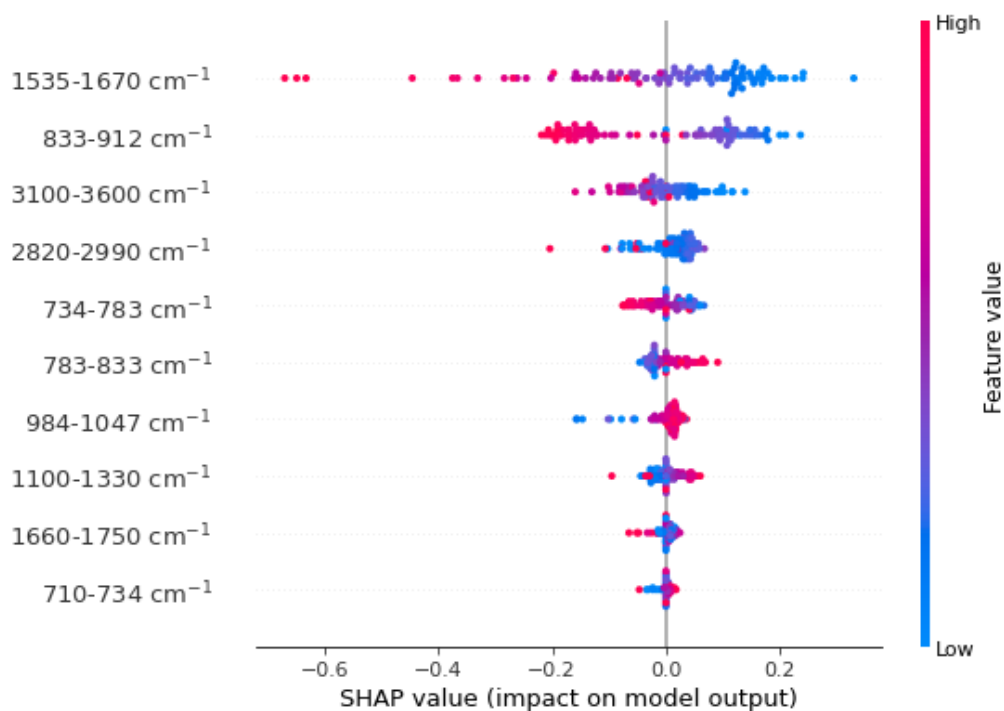


Figure 6.16 SHAP plot for importance of FTIR features for SVR prediction of beta from sigmoidal model. The SVR model used the following optimized parameters: (Kernel: rbf, Best Parameters: C: 1, epsilon: 0.01, gamma: scale).

The data used for the chemo-rheological relationship analysis comprises a diverse set of binders, including samples aged in the laboratory under various controlled conditions and those aged in the field. This diversity ensures that the model is general and not constrained by specific binder types or aging scenarios, making it broadly applicable to different conditions. However, this generality could also introduce challenges, such as increased variability in the data, which might obscure subtle relationships or reduce the model's ability to capture specific interactions unique to certain binders or aging processes. Furthermore, the use of heterogeneous data may lead to overgeneralization, potentially limiting the model's accuracy when applied to highly specialized conditions.

6.4.6 Prediction of G^* master curve with FTIR indices using DNNs

The objective of this section is to evaluate the ability of DNNs (Figure 6.17) to predict key rheological parameters, including the sigmoidal model parameters (α , β , σ , and γ) and crossover values, based on chemical indices obtained from Fourier Transform Infrared Spectroscopy (FTIR).

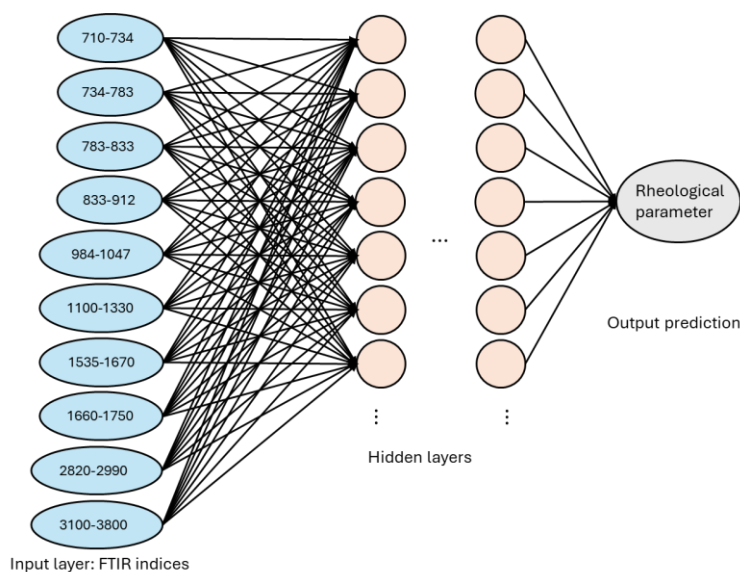


Figure 6.17 Schematic representation of the DNN used to predict rheological parameters from FTIR-derived chemical indices. The input layer consists of ten neurons corresponding to selected FTIR spectral ranges (expressed in cm^{-1}), which serve as chemical indices. The hidden layers and output layer represent a generalized network architecture. Specific network hyperparameters, including the number of hidden layers, neurons per layer, and activation functions, are optimized in subsequent steps.

These rheological parameters are essential for constructing the complex modulus master curve ($|G^*|$), a critical descriptor of the viscoelastic behaviour of paving binders. Accurate prediction of these parameters eliminates the need for time-consuming laboratory tests, such as the Dynamic Shear Rheometer (DSR) test, offering a more efficient and cost-effective approach. In the field of pavement engineering, where rheological properties significantly influence the performance and durability of asphalt binders, this approach enables better design and optimization of materials. By integrating DNNs into predictive modelling, this chapter provides a framework for using chemical data to estimate mechanical properties, which can be particularly useful in scenarios with limited resources or when rapid assessments are required.

In the previous section, SVR models demonstrated their utility in providing insights into the relationships between chemical indices obtained from FTIR data and the rheological properties of paving binders. SVR is known for its ability to handle small datasets effectively and capture linear and moderately nonlinear relationships. This makes it a valuable tool for exploring and gaining a general understanding of chemo-rheological interactions. However, when tasked with predicting the parameters of a rheological model, such as the sigmoidal model, SVR exhibited limitations in fully capturing the complex and highly nonlinear dependencies inherent in the data ($R^2 < 0.70$). Given the need for precise prediction of parameters for a well-established sigmoidal model, a more advanced method was required.

To address this limitation, DNNs were employed. DNNs offer a significant advantage over SVR due to their superior capability to model complex, nonlinear relationships within datasets. This characteristic makes DNNs particularly well-suited for the task of predicting the sigmoidal model parameters (α , β , σ , and γ) and crossover values from FTIR data. By leveraging their ability to learn from large datasets and capture intricate patterns, DNNs provide a more reliable and accurate means of establishing a chemo-rheological relationship, thereby overcoming the limitations observed with SVR.

The DNN model was built using a systematic approach that involved optimizing key hyperparameters through a grid search. The architecture of the DNN consists of several layers, with the number of hidden layers and neurons in each layer being selected based on the problem's complexity and the need for capturing nonlinear relationships. The grid search considered different activation functions, including the Rectified Linear Unit (ReLU) and the hyperbolic tangent (tanh), depending on the nonlinearity requirements of the task. Regularization techniques, such as dropout, were applied to prevent overfitting, with dropout rates optimized for each scenario. The learning rate, batch size, and the number of epochs were also fine-tuned to balance training speed and model performance. The final optimized hyperparameters for each case, such as the number of layers, neurons, activation function, dropout rate, and learning rate, are summarized in Table 6.6, which also includes performance metrics (R^2 and RMSE) for both training and testing data.

Table 6.7 presents the predictive performance of the DNNs used to estimate the sigmoidal model parameters, alpha, beta, gamma, sigma, and the crossover values (CR-CM and CR-Fr) from the input data. The results indicate that the model performs quite well across all parameters, with the metrics of R^2 and RMSE providing insight into the quality of the predictions for both the training and testing datasets.

For the alpha parameter, the DNN demonstrates strong predictive performance, with an R^2 value of 0.87 and RMSE of 0.34 for the training data, reflecting a good fit between the predicted and actual values. However, for the testing data, the R^2 drops slightly to 0.80, and the RMSE increases to 0.47, indicating a mild reduction in performance. This decrease suggests that while the model generalizes well, there is a small trade-off in accuracy when applied to new, unseen data.

Similarly, the beta parameter shows even more impressive performance, with the training data yielding an R^2 of 0.94 and an RMSE of 0.24, demonstrating excellent learning capability. The testing data also performs well, with an R^2 of 0.85 and an RMSE of 0.41. Although there is a slight drop in both metrics, the model remains reliable in predicting the beta parameter, and the results suggest a consistent generalization to new data.

For the gamma parameter, the results are particularly strong. The training and testing datasets both exhibit R^2 values of 0.91 and 0.85, with RMSE values close to 0.01 for both sets. This shows exceptional accuracy and minimal prediction error, indicating that the model effectively captures the relationship between the FTIR data and gamma values.

The sigma parameter also demonstrates strong performance, with an R^2 of 0.88 and an RMSE of 0.33 for the training set, and an R^2 of 0.82 and RMSE of 0.46 for the testing set. While there is a slight drop in R^2 for the testing data, the results remain robust, confirming that the model effectively predicts the sigma parameter despite the inherent complexity of the relationship.

In terms of crossover values, the model performs well for both CR-CM and CR-Fr. For CR-CM, the training data yields an R^2 of 0.85 and an RMSE of 0.13, indicating a solid prediction. The testing data shows slightly reduced performance with an R^2 of 0.75 and an RMSE of 0.22, but the results still demonstrate reasonable accuracy. CR-Fr shows a similar trend, with the training data yielding an R^2 of 0.94 and RMSE of 0.34. However, the testing data shows a slight drop in performance with an R^2 of 0.82 and an RMSE of 0.54, which is still within an acceptable range.

Table 6.6 Performance metrics (R^2 and RMSE) for the training and testing data, along with the optimized hyperparameters of DNNs.

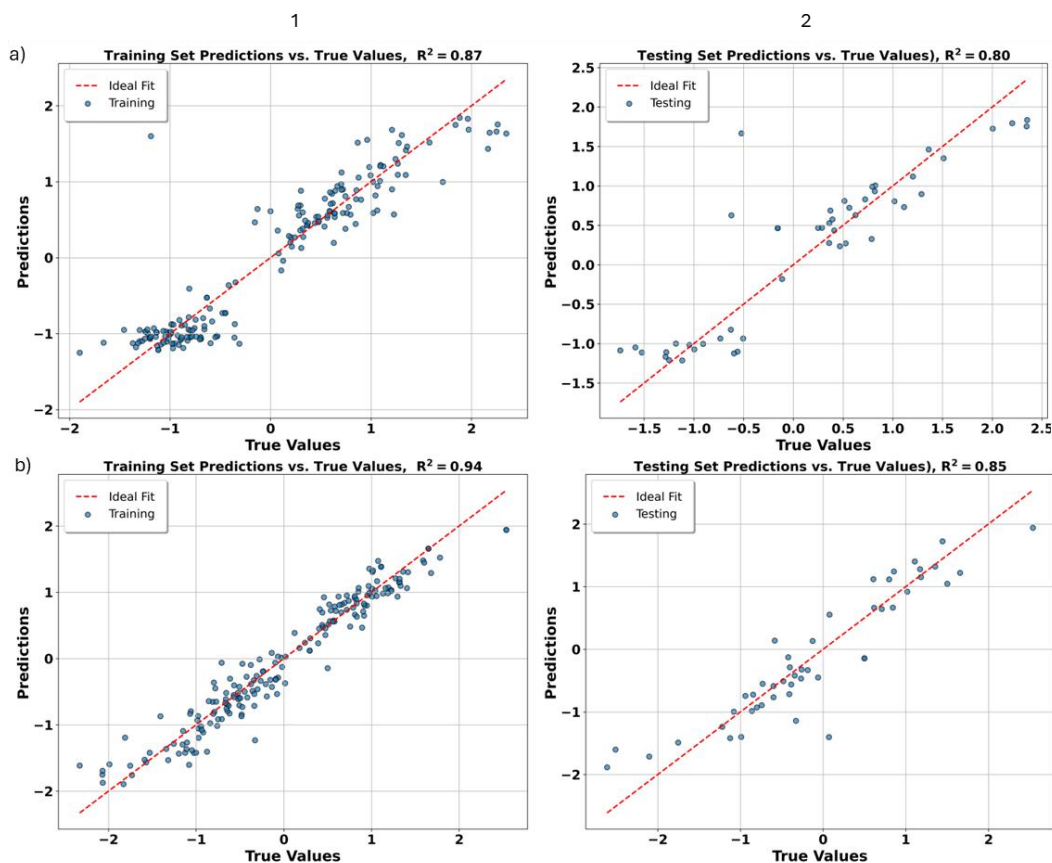
Parameters	Training Data (R^2)	Training Data (RMSE)	Testing Data (R^2)	Testing Data (RMSE)	Optimized Hyperparameters						
					model__hidden__layers	model__neurons	model__activation	model__dropout__rate	model__learning__rate	batch__size	epochs
Alpha	0.87	0.34	0.8	0.47	6	32	tanh	0.2	0.001	52	500
Beta	0.94	0.24	0.85	0.41	6	32	tanh	0.2	0.001	52	500
Gamma	0.91	0.01	0.85	0.01	3	64, 32, 16	relu, relu, relu	0.1, 0.1	0.001	38	1000
Sigma	0.88	0.33	0.82	0.46	6	32	tanh	0.2	0.001	52	500
CR-CM	0.85	0.13	0.75	0.22	3	64, 32, 16	relu, relu, relu	0.1, 0.1	0.001	38	1000
CR-Fr	0.94	0.34	0.82	0.54	3	64, 32, 16	relu, relu, relu	0.1, 0.1	0.001	38	1000

Table 6.7 Performance metrics of the DNN models for predicting sigmoidal model parameters (alpha, beta, gamma, sigma) and crossover values (CR-CM and CR-Fr) based on FTIR indices. The table presents the R^2 values and Root Mean Square Error (RMSE) for both training and testing datasets, highlighting the model's accuracy and generalization capabilities.

parameters	Training data		Testing data	
	R^2	RMSE	R^2	RMSE
Alpha	0.87	0.34	0.80	0.47
Beta	0.94	0.24	0.85	0.41
Gamma	0.91	0.01	0.85	0.01
Sigma	0.88	0.33	0.82	0.46
CR-CM	0.85	0.13	0.75	0.22
CR-Fr	0.94	0.34	0.82	0.54

These results demonstrate that the DNN models are capable of accurately predicting the sigmoidal model parameters and crossover values, offering valuable insights into the rheological properties of the material. The slight decrease in performance from training to testing data suggests that there are limitations in this work. Given the regularization techniques, such as dropout, that were already employed to prevent overfitting, the observed performance drop from training to testing can be attributed to a general limitation related to data complexity or availability rather than specific model weakness. With the current dataset, this is the best result achievable, as the model is capturing the underlying patterns effectively. However, it is important to note that the model's generalization could be further improved with a larger and more diverse dataset, which would help the model better account for variability and avoid overfitting. Additionally, factors such as noise in the data or potential model complexity could also contribute to the slight reduction in accuracy. Overall, the model performs well within the constraints of the available data, and there is room for improvement with future data expansion.

Figure 6.18 illustrates the prediction performance of the DNN models by comparing the true and predicted values for both the training and testing datasets. It can be observed that the predicted values closely follow the actual values, particularly for the training set, indicating that the models have effectively learned the underlying relationships. While some deviation is present in the testing data, the overall agreement remains acceptable, supporting the reliability of the models.



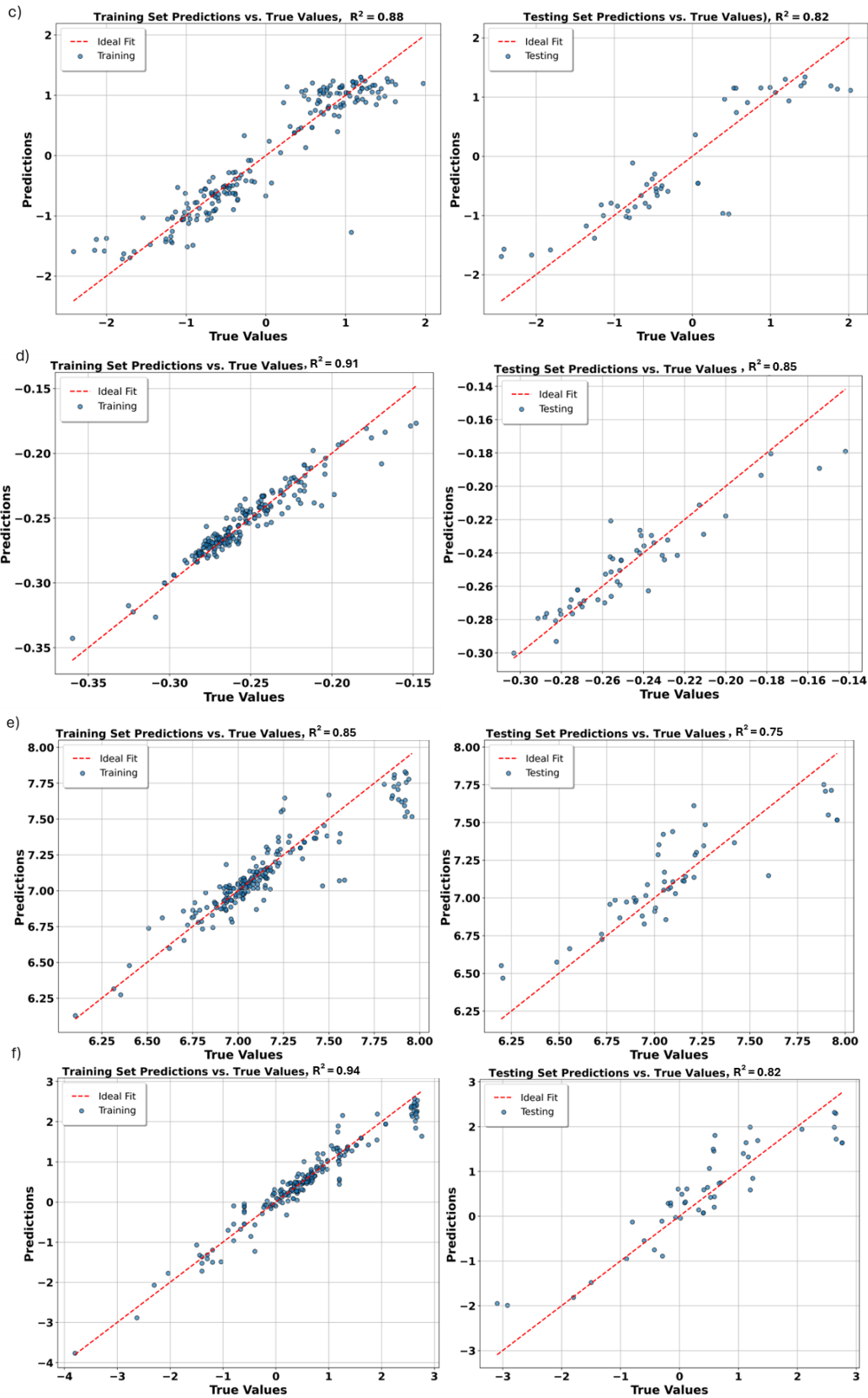


Figure 6.18 Comparison of predicted and true values for sigmoidal model parameters a) alpha, b) beta, c) gamma, d) sigma, and crossover values e) CR-CM and f) CR-Fr using DNN models. The plots illustrate the model's performance for both column 1) training and column 2) testing datasets, demonstrating the accuracy and reliability of the predictions.

Figure 6.19 illustrates the training and validation loss curves for the DNN models constructed to predict the parameters α , β , γ , σ , CR-Fr, and CR-CM. These plots serve to illustrate the learning dynamics and convergence characteristics of each model. For α , β , and σ (Figure 6.19 a–c), the loss rapidly declines and stabilizes within the first 100 epochs, with minimal discrepancy between training and validation losses, indicating efficient learning and good generalization. A similar trend is observed for γ , CR-CM, and CR-Fr (Figure 6.19 d–f), although the validation loss remains consistently above the training loss throughout the 1000 training epochs. Nonetheless, the loss curve shows clear convergence without divergence, implying that overfitting is not severe.

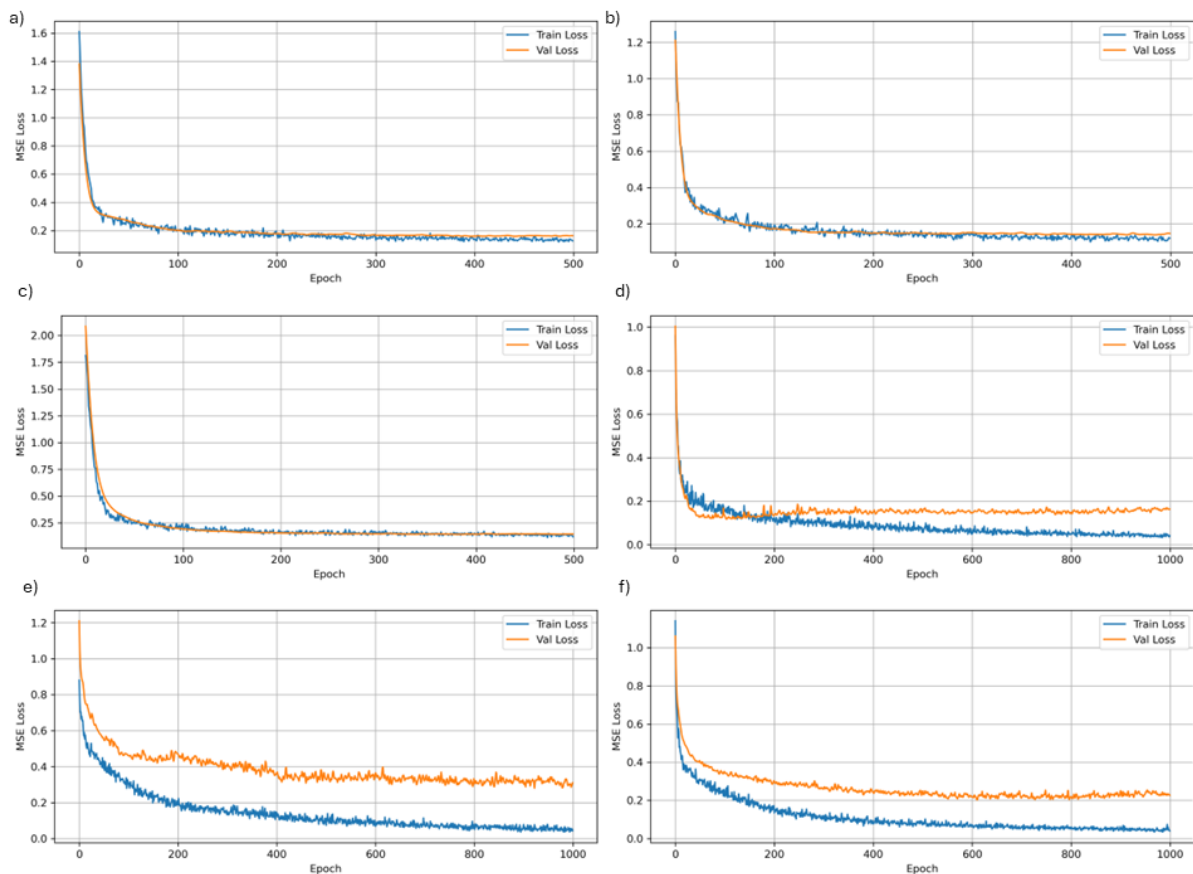


Figure 6.19 Training and validation loss curves for the ANN models predicting a) alpha, b) beta, c) sigma, d) gamma, and crossover values e) CR-CM and f) CR-Fr. The plots show the convergence behaviour of the models over epochs, indicating stability and effective learning during training without significant overfitting. A lower loss indicates a better-performing model.

The R^2 and RMSE values for both training and testing datasets, presented in the Table 6.6, align well with the qualitative trends observed in the loss plots. For instance, β and γ show the highest prediction accuracy, with testing R^2 values of 0.85 or greater and low RMSEs (0.41 and 0.01, respectively), which corresponds to the closely aligned training and validation loss curves in Figure 6.19 b and c. The strong performance of the β model is particularly noteworthy, as it is consistent with the results obtained using the SVR approach, further reinforcing its predictive robustness. Although the validation loss curve for γ plateaus slightly above the training loss, the high accuracy is maintained. CR-Fr is also predicted with satisfactory accuracy ($R^2 = 0.82$), and the corresponding loss curve in Figure 6.19 f shows convergence and stability. While the validation loss remains marginally above the training loss, this pattern is comparable to other parameters and does not indicate poor generalization.

Overall, the results affirm that DNNs are a powerful tool for predicting rheological properties of paving materials from FTIR data. Among all parameters, β , γ , and CR-Fr exhibit particularly strong predictive performance. Further improvements may be achieved through increased data availability or refined input feature design. These findings contribute significantly to the field of pavement engineering by offering a non-destructive and efficient method to estimate important rheological parameters, thus reducing the need for costly and time-consuming laboratory tests such as the Dynamic Shear Rheometer (DSR) test. While the data used in this chapter were sufficient to demonstrate the model's potential, a larger and more diverse dataset could further improve the model's accuracy and generalization.

6.4.7 Prediction of field aging for laboratory samples using SVR

To predict the equivalence of field aging duration for each laboratory aging condition, field data were used to train an SVR model, where rheological and chemical parameters served as the independent variables and the number of years of field aging as the dependent variable. The trained model was then applied to the laboratory-aged samples to estimate the corresponding duration of field aging they represent.

Two separate SVR models were trained: one using data from Stone Mastic Asphalt (SMA) field cores (referred to as the SMA-SVR model), and the other using data from Porous Asphalt (PA) field cores (the PA-SVR model). Both models employed a linear kernel, with hyperparameters optimized via GridSearchCV in combination with Leave-One-Out Cross-Validation (LOOCV), ensuring that each model's hyperparameters were fine-tuned to maximize performance. Among the kernel types tested—linear, polynomial, and radial basis function (RBF)—the linear kernel consistently yielded the best performance across both datasets, which is attributed to its reduced tendency to overfit given the limited sample sizes.

The PA-SVR model, trained on 8 data points, exhibited a relatively high R-squared value of 0.92, indicating a strong relationship between the features and the target variable. Additionally, the model achieved an RMSE of 0.59, which suggests that it performs reasonably well, with moderate variability in prediction accuracy. The balanced R-squared and RMSE values suggest that the PA-SVR model is generalizable and does not overfit the training data, making it suitable for predictive tasks beyond the specific dataset used in training. The performance of this model is robust, and its results indicate that it is capable of making accurate predictions on unseen data.

On the other hand, the SMA-SVR model, trained on just 4 data points, showed an R-squared value of 0.71. However, the high R-squared value also raises concerns about overfitting. With such a small sample size, the model may have memorized the data rather than learning generalizable patterns. The RMSE for SMA-SVR was 1.74, which is higher than that of the PA-SVR model, further suggesting that SMA-SVR is less consistent and might not generalize effectively to new data. The small training set and relatively high R-squared point to the risk that the SMA-SVR model may not be reliable when applied to broader datasets or future predictions. Consequently, the PA-SVR model was selected for further analysis in this chapter.

The PA-SVR model was employed to predict the equivalent years of field aging for all laboratory-aged samples, using chemical and rheological properties as inputs. Table 6.8 shows the most and least laboratory-aged samples with their predicted years of simulated field aging (complete table in supporting information, Table 4S in appendix of chapter 6), suggesting that the chemical and rheological properties of these samples are similar to those of field samples aged for approximately the predicted years indicated in the Table 6.8. Given the model's *RMSE*, the true field aging of these samples is expected to be within the range of the specified year ± 0.59 years, accounting for the average prediction error and variability. Based on the predicted values, Q-12%-60C-3H is the least aged sample (0.13 ± 0.59), and Q-1M-40H-RH is the most aged sample (11.16 ± 0.59). For this modelling, outlier samples such as those in clusters 1 and 3 of the PCA plot in Figure 6.13 were not

considered due to the sensitivity of the SVR algorithm to outliers. The predictions for both the least and most aged samples are consistent with the discussions in other sections, demonstrating the validity of the developed model. Consequently, this model is suitable for preliminary predicting the equivalent field aging of other laboratory-aged samples based on their chemical and rheological properties.

Table 6.8 Predicted years of field aging for select lab-aged samples subjected to extreme conditions, derived from the PA-SVR model. A comprehensive table is available in the Supporting Information as Table 4S in appendix of chapter 6.

Sample names	predicted years of field aging ± 0.59
Q-12%-60C-3H	0.13
Q-60C-9H-O	0.17
Q-12%-70C-3H	0.20
Q-85C-3H-UV	0.39
Q-3M-01B-O	0.71
...	...
Q-33%-85C-3H	9.09
Q-1M-150B-O	9.17
Q-60C-21D-RH	9.51
Q-33%-60C-9H	9.82
Q-1M-40H-RH	11.16

The SVR model predicts the equivalent field aging for various laboratory-aged samples, providing results that include decimal values. These decimal differences are informative, as they indicate the variation in the intensity of aging under different laboratory conditions. The conditions can be viewed as part of a continuous spectrum of aging intensities, with the decimal places representing the finer distinctions between them. For practical application, laboratory conditions should be chosen based on how closely they match the desired duration of field aging. While the predictions offer a spectrum of aging conditions, it is important to select the laboratory aging protocol that most closely corresponds to the required field aging duration. This decision should be guided by the limitations of the laboratory equipment, such as its limitation in controlling temperature, pressure, and humidity. Therefore, instead of rounding the predicted values, selecting the closest match to the target aging time will yield the most accurate results within the constraints of the available experimental setup.

6.5 Modelling limitations

It is important to acknowledge limitations of this work, particularly related to the size of the dataset used for training the SVR model. The current model is based on limited field-aged samples, which presents the potential risk of overfitting. However, this risk has been mitigated by performing additional validation, including PCA analysis and Euclidean distance comparisons between field-aged samples and lab-aged predictions. The close alignment between the model predictions and actual field data suggests that the SVR model is reasonably accurate, providing preliminary insights into field aging behaviour. A dataset with at least 30 field-aged samples would significantly improve the model's ability to generalize across different conditions. Therefore, while the current model offers valuable guidelines, the predictions should be considered preliminary until further validation with larger datasets is conducted.

6.6 Conclusions

This chapter presented a multivariate chemo-mechanical investigation of binder aging under various laboratory conditions, with the aim of linking chemical and rheological properties to aging variables and field performance using statistical and machine learning methods. The main conclusions are summarised below by research objective.

To classify binders by aging state and source, simplified descriptors such as FTIR indices and sigmoidal model parameters were shown to be sufficient for distinguishing binder types and aging conditions, supporting their practical use over full spectral or frequency sweep data (RSQ1). However, clear differentiation between binder films and extracted binders was not achieved, likely due to alterations introduced during extraction.

To assess whether binders could be grouped based on type and aging protocol, PCA revealed consistent clustering aligned with binder source and applied method (RSQ2). Carbonyl, sulfoxide, and the sigmoidal β parameter emerged as key indicators, confirming a chemo-mechanical relationship between oxidation and stiffening. However, overlap between binder film and extracted binder responses pointed to limitations in current sample preparation practices.

To quantify the effects of aging factors, MLR analysis showed film thickness and exposure time to be dominant factors, with humidity influencing the role of temperature and pressure (RSQ3). The model was also used to identify laboratory conditions equivalent to approximately nine years of field aging in porous and stone mastic asphalt, providing a useful basis for designing more field-representative protocols.

To evaluate the similarity between laboratory- and field-aged binders, PCA-based distances identified ROS- and thermo-oxidative aging protocols that most closely resembled field-aged conditions (RSQ4). While exact replication remains challenging, combinations of oxidation, moisture, and elevated temperature can yield realistic aging patterns.

To estimate field-equivalent aging durations, SVR models trained on field-aged data enabled direct translation between laboratory aging and years in service (RSQ5). A 1 mm film aged at 85 °C in 33% H₂O₂ for 3 hours matched the chemical and rheological condition of porous asphalt aged ~9 years, illustrating the potential of data-driven calibration.

To explore chemo-rheological relationships, SVR and DNN models successfully predicted rheological parameters from FTIR indices, with DNNs achieving higher accuracy (RSQ6). Aromatic and oxidation-related bands were the most relevant predictors. These results confirm that rheological properties can, in part, be inferred from chemical features, reducing experimental demand.

Overall, this chapter establishes key relationships between aging variables, chemical evolution, and rheological response. It supports the development of accelerated protocols and multivariate tools for predicting binder performance under realistic aging scenarios. Future studies should focus on exploring the critical FTIR regions identified in this chapter, particularly the long-chain regions associated with rheological properties, could lead to more accurate predictive models for binder performance. Expanding the dataset for the MLR model will also be essential to mitigate overfitting issues and enhance its robustness. Furthermore, investigating the interplay between hygrothermal and thermo-oxidative aging in greater detail could uncover new strategies for optimizing binder formulations and aging protocols. To improve the prediction of field aging, incorporating additional field-aged samples into the training of the formulated predictive model will allow for the development of more accurate laboratory aging protocols for various field aging durations, such as 15 or 20 years. Overall, this chapter not only contributes valuable findings but also opens multiple avenues for further exploration, ultimately aiming to improve the durability and longevity of asphalt pavements.

6.7 References

1. Prosperi, E. and E. Bocci, *A review on bitumen aging and rejuvenation chemistry: Processes, materials and analyses*. Sustainability, 2021. **13**(12): p. 6523.
2. Siroma, R.S., et al., *A literature review of bitumen aging: From laboratory procedures to field evaluation*. Journal of Testing and Evaluation, 2022. **50**(2): p. 1023-1044.
3. Khalighi, S., et al., *Multivariate chemo-rheological framework for optimizing laboratory aging protocols of paving binders*. Materials & Design, 2024: p. 113520.
4. Asemani, M. and A.R. Rabbani, *Detailed FTIR spectroscopy characterization of crude oil extracted asphaltenes: Curve resolve of overlapping bands*. Journal of Petroleum Science and Engineering, 2020. **185**: p. 106618.
5. Khalighi, S., et al., *Evaluating the impact of data pre-processing methods on classification of ATR-FTIR spectra of bituminous binders*. Fuel, 2024. **376**: p. 132701.
6. Weigel, S. and D. Stephan, *Bitumen characterization with Fourier transform infrared spectroscopy and multivariate evaluation: prediction of various physical and chemical parameters*. Energy & fuels, 2018. **32**(10): p. 10437-10442.
7. Primerano, K., et al., *Characterization of long-term aged bitumen with FTIR spectroscopy and multivariate analysis methods*. Construction and Building Materials, 2023. **409**: p. 133956.
8. Khalighi, S., S. Erkens, and A. Varveri, *Exploring the impact of humidity and water on bituminous binder aging: a multivariate analysis approach (TI CAB)*. Road Materials and Pavement Design, 2024: p. 1-25.
9. Ma, L., et al., *Chemical characterisation of bitumen type and ageing state based on FTIR spectroscopy and discriminant analysis integrated with variable selection methods*. Road Materials and Pavement Design, 2023. **24**(sup1): p. 506-520.
10. Ma, L., *Interactions of moisture and oxidative ageing mechanisms in paving binders: Towards improving durability of pavements*. 2025.
11. Khadijeh, M., et al., *Exploring the roles of numerical simulations and machine learning in multiscale paving materials analysis: Applications, challenges, best practices*. Computer Methods in Applied Mechanics and Engineering, 2025. **433**: p. 117462.
12. Tripathi, A. *A COMPLETE GUIDE TO PRINCIPAL COMPONENT ANALYSIS – PCA IN MACHINE LEARNING*. 2019; Available from: <https://ashutoshtripathi.com/2019/07/11/a-complete-guide-to-principal-component-analysis-pca-in-machine-learning/>.
13. Singh, V. *Difference Between Linear and Multiple Regression*. 2024 [cited 2025 April 2025]; Available from: <https://www.shiksha.com/online-courses/articles/linear-and-multiple-regression/>.
14. Rasifaghihi, N. *From Theory to Practice: Implementing Support Vector Regression for Predictions in Python*. 2023 [cited 2025 April 2025].
15. geeksforgeeks. *Layers in Artificial Neural Networks (ANN)*. 2025 [cited 2025 April 2025]; Available from: <https://www.geeksforgeeks.org/layers-in-artificial-neural-networks-ann/>.
16. Ma, L., et al., *Chemical characterisation of bitumen type and ageing state based on FTIR spectroscopy and discriminant analysis integrated with variable selection methods*. Road Materials and Pavement Design, 2023: p. 1-15.
17. Schölkopf, B. and A. Smola, *Support vector machines and kernel algorithms*, in *Encyclopedia of Biostatistics*. 2005, Wiley. p. 5328-5335.
18. Timilsina, M.S., et al., *Prediction of HHV of fuel by Machine learning Algorithm: Interpretability analysis using Shapley Additive Explanations (SHAP)*. Fuel, 2024. **357**: p. 129573.
19. Yeo, I.K. and R.A. Johnson, *A new family of power transformations to improve normality or symmetry*. Biometrika, 2000. **87**(4): p. 954-959.
20. Cai, J. and X. Xu, *Bayesian analysis of mixture models with Yeo-Johnson transformation*. Communications in Statistics-Theory and Methods, 2024. **53**(18): p. 6600-6613.

21. Riani, M., A.C. Atkinson, and A. Corbellini, *Automatic robust Box–Cox and extended Yeo–Johnson transformations in regression*. *Statistical Methods & Applications*, 2023. **32**(1): p. 75-102.
22. Rosenblatt, F., *The perceptron: a probabilistic model for information storage and organization in the brain*. *Psychological review*, 1958. **65**(6): p. 386.
23. Malik, A., et al., *Prediction of multi-scalar standardized precipitation index by using artificial intelligence and regression models*. *Climate*, 2021. **9**(2): p. 28.
24. Douglas, R.K., et al., *Rapid prediction of total petroleum hydrocarbons concentration in contaminated soil using vis-NIR spectroscopy and regression techniques*. *Science of the Total Environment*, 2018. **616**: p. 147-155.

7

Conclusions and Future Perspectives

This chapter presents a summary of the key findings from this thesis (Section 7.1), emphasizing the insights gained regarding the optimization of long-term aging protocols for paving binders and the development of a multivariate framework incorporating field-aged samples. These findings contribute to a more accurate simulation of in-service aging and enhance the predictive capabilities of laboratory-based protocols.

Furthermore, Section 7.2 outlines future directions for advancing aging studies. These recommendations are structured into two parts: Section 7.2.1 provides research-oriented recommendations aimed at refining experimental designs, improving algorithmic frameworks, and expanding the chemical and rheological characterization of aging processes. Section 7.2.2 addresses practice-oriented recommendations, focusing on the development of standardized protocols, incorporation of field-relevant aging factors, and validation strategies to ensure laboratory procedures align with practical pavement aging scenarios.

7.1 Conclusions

This section provides a structured synthesis of the thesis by revisiting the four Research Questions (RQs) introduced in Chapter 1. Each question is answered based on the findings presented across Chapters 3 to 6. The responses aim to concisely reflect the main contributions of the work without restating all experimental details, focusing instead on the implications and insights gained with respect to each objective.

Research Question 1

What are the chemical and rheological consequences of aging under diverse environmental factors, and how do these conditions compare to field aging?

Chemical and rheological effects of aging were systematically analysed under thermo-oxidative, hygrothermal, aqueous-thermal, and ROS-induced oxidative conditions. FTIR results demonstrated consistent increases in carbonyl and sulfoxide indices with aging severity. Hygrothermal and ROS-induced aging protocols were the most effective in accelerating oxidation, particularly under elevated pressures and temperatures, respectively. Rheological analysis confirmed stiffening and reduced phase angles under all protocols, with crossover frequency and modulus proving particularly sensitive to aging. Field-aged binders exhibited a rheological signature distinct from conventional lab-aged samples but were closely matched by specific ROS and hygrothermal protocols. Differences in oxidation rate and aging severity were strongly influenced by binder composition, film thickness, and pressure, with thinner films and higher pressures amplifying aging effects. Overall, selected laboratory protocols, particularly ROS-based methods, were able to replicate the chemo-rheological state of binders aged in service for approximately nine years.

Research Question 2

Can novel accelerated aging protocols replicate field aging more effectively than existing laboratory methods?

Yes. The UV–Peroxide Aging (UPA) protocol, which utilizes hydroxyl radicals generated via H_2O_2 and UV exposure, proved more effective than standard thermo-oxidative methods. FTIR and rheological data from binders aged under 33% H_2O_2 at 85°C for 3 hours or at 60°C for 6–9 hours were closely aligned with field-aged porous asphalt binders. Euclidean distance analysis confirmed the proximity of these samples to those extracted from long-term field-aged pavements. Rheological properties such as crossover frequency and modulus further supported this match. These results demonstrate that ROS-based protocols offer a realistic and time-efficient alternative to conventional lab aging, particularly for simulating long-term field exposure under oxidative stress.

Research Question 3

How can multivariate statistical and machine learning methods be employed to integrate chemical and rheological data for a deeper understanding of the aging process?

Multivariate methods were employed to identify key chemo-rheological descriptors and model binder aging. PCA facilitated sample grouping and feature selection, revealing carbonyl and sulfoxide indices, as well as rheological crossover parameters, as critical indicators of aging. MLR models quantified the contributions of aging variables (temperature, time, thickness, pressure, humidity), enabling calibration of lab protocols to simulate field aging durations. SVR models linked chemical indices to rheological responses and allowed the prediction of field-equivalent aging durations. DNNs outperformed SVR in predicting complex rheological parameters (e.g., sigmoidal model parameters),

providing robust, non-linear mappings between FTIR features and rheological properties. These tools enabled a unified framework for designing and validating accelerated aging protocols and for predicting binder behaviour without direct rheological testing.

Research Question 4

How can data pre-processing techniques for ATR-FTIR spectral analysis of bituminous binders be optimized to ensure reliable chemical characterization?

A systematic evaluation of data preprocessing (DP) techniques was conducted in Chapter 3. PLS-DA was used to assess the classification performance of various baseline correction and normalization methods. No single method was universally optimal; the effectiveness of DP approaches depended on the input format and analytical objective. Whole spectra and first derivative spectra yielded higher classification accuracy than indices or peak areas. Among indices, A_B/A_{TOTAL} -based metrics were preferred for detecting gradual changes due to aging. Recommended DP combinations included NTS, NMO, NCV, AS, and SNV, depending on the input data. Polynomial fitting and multiplicative correction methods were found to distort key spectral features and were not recommended. The study established that tailored preprocessing strategies, aligned with analysis goals and spectral characteristics, are essential for reliable chemometric interpretation of binder aging.

7.2 Recommendations for future work

Although this study has introduced novel accelerated aging protocols and predictive modelling strategies for bituminous binders, several limitations remain. Notably, the performance of modified binders (e.g., bio-based or polymer-modified) was not assessed, and certain environmental factors such as freeze-thaw cycles and traffic-induced stresses were not explicitly incorporated. These aspects should be addressed in future work to enhance the reliability and applicability of the proposed methodologies. To advance the understanding of aging mechanisms, optimize laboratory protocols, and improve predictive models, future work should address both scientific inquiries and practical implementations. The following recommendations are thus organized into two categories: (1) recommendations aimed at academic and scientific research, and (2) recommendations intended for practical applications relevant to contractors, road authorities, and industry stakeholders. Together, these research and practice-oriented recommendations establish a comprehensive framework for advancing the field of bituminous binder aging. By fostering methodological innovation and promoting standardized implementation, the outlined future directions aim to support the design of durable, sustainable, and high-performing materials for long-term pavement applications.

7.2.1 Recommendations for future research

Future studies should prioritize the development of adaptive algorithms capable of dynamically selecting optimal data processing (DP) methods based on specific dataset characteristics and study objectives. Coupling these optimized DP methods with advanced multivariate tools, particularly deep learning frameworks, is expected to enhance predictive accuracy and model generalizability. Extending these frameworks to chemometric studies of other complex aging-prone materials, including polymers and composites, represents a valuable direction for broadening scientific applicability.

To improve the resolution of predictive models, experimental protocols should incorporate intermediate durations for accelerated aging. This adjustment will facilitate a finer temporal mapping of chemical evolution. Comprehensive analyses of Saturates, Aromatics, Resins, and Asphaltenes (SARA) fractions are recommended to elucidate compositional changes and their mechanistic roles in

oxidative processes. Additionally, systematic variation of reactive oxygen species (ROS) concentrations, ultraviolet (UV) exposure durations, and temperature regimes should be explored to optimize ROS-driven accelerated aging methods.

Investigating the interplay between thermo-oxidative and hygrothermal aging, especially the synergistic effects of humidity and temperature, is crucial. A detailed examination of molecular changes under these coupled conditions can support the development of hybrid aging protocols that balance laboratory efficiency with field relevance. Incorporating advanced characterization techniques, including SARA fractionation and microscopy-based methods, will enable a more comprehensive understanding of the progressive chemical and mechanical evolution of bituminous binders.

Expanding datasets used in multiple linear regression (MLR) and support vector regression (SVR) models is also necessary to increase model robustness and minimize overfitting. Future studies should strategically include field-aged samples representing extended service durations (e.g., 15-20 years or more) to calibrate laboratory protocols against long-term field performance. This approach provides a crucial reference framework that directly links detailed laboratory research to real-world aging, thereby validating predictive models and accelerating test methods. Furthermore, validating predictive models through rheological evaluations will ensure that observed chemical transformations effectively correspond to meaningful changes in performance. Exploring alternative rheological indices will support the identification of subtle aging effects.

It is also essential to examine the influence of binder composition and source variability on aging behaviour. Inclusion of bio-binders, polymer-modified binders, and regenerated binders into aging studies is strongly encouraged. These materials, which are increasingly adopted due to environmental, performance, and cost-related benefits, may exhibit different chemo-rheological aging responses compared to conventional binders. Investigating their behaviour will improve the generalizability of predictive models and contribute to the formulation of tailored aging protocols.

7.2.2 Recommendations for practice

To support the implementation of more reliable and consistent laboratory protocols in practice, collaboration with industry stakeholders—including contractors, standardization agencies, and transportation departments—is essential. The development of standardized accelerated aging protocols will enable consistency in testing practices, facilitate comparability across studies, and ensure field relevance.

Future protocols should integrate a broader range of environmental factors relevant to real-world pavement service conditions. These include freeze-thaw cycles, pollutant exposure, and variations induced by traffic loading. Addressing such variables will help simulate a more realistic spectrum of aging mechanisms. For ROS-based methods in particular, refining protocol parameters to balance oxidation efficiency with field-representative outcomes is a priority.

The use of additional field-aged samples, reflecting diverse service environments and traffic-induced aging, is necessary to improve the predictive fidelity of laboratory simulations. This inclusion will help bridge the gap between laboratory aging conditions and the complex aging dynamics experienced in actual pavements.

Finally, contractors and road maintenance authorities should be encouraged to adopt protocols and predictive tools that are validated not only through chemical characterization but also through rheological performance assessments. This dual validation ensures that laboratory procedures translate effectively into actionable quality control and material selection strategies, thereby

improving pavement durability and sustainability. The term "actionable" is used here in its technical sense, meaning that the data and insights gained from these protocols are a sufficient basis for taking a specific, practical action, such as making a decision on material selection or quality control. It's not about legal recourse, but about providing a clear path forward for engineers and decision-makers. Moreover, the adoption of these tools should be driven by demonstrable economic benefits. While standardized tests like PAV and RTFOT are essential, they do not fully capture long-term performance. The validation of advanced research must clearly show how assessing a material's aging sensitivity can lead to a quantifiable improvement in expected service life. This evidence, in turn, allows for the use of a limited number of powerful tests and models, making the process cost-effective and a compelling business case for adoption. This encouragement should come from governing bodies and research institutions, who must work to establish these validated, cost-beneficial standards and promote them to the industry.

Appendix of chapter 3

Table 1S- Aging classification accuracies associated with CDPs. Each column displays accuracies for various CDPs concerning a specific peak area or chemical index calculation method or entire spectra or first derivative spectra, while each row represents the classification accuracies for a distinct CDP method but with different approaches to peak area/ chemical index calculations or entire spectra or first derivative.

Combined methods names	AB/ATO TAL	AT/ATO TAL	AB/A ALI	AT/AALI	AB	AT	Entire spectra	First derivative
asls_NTS	0.79 ± 0.02	0.75 ± 0.02	0.74 ± 0.03	0.74 ± 0.03	0.79 ± 0.03	0.79 ± 0.03	0.86 ± 0.02	0.87 ± 0.02
asls_NCV	0.79 ± 0.02	0.75 ± 0.02	0.74 ± 0.03	0.74 ± 0.03	0.74 ± 0.03	0.74 ± 0.03	0.84 ± 0.02	0.87 ± 0.02
asls_NMO	0.82 ± 0.02	0.80 ± 0.02	0.73 ± 0.01	0.74 ± 0.03	0.77 ± 0.04	0.77 ± 0.04	0.84 ± 0.03	0.86 ± 0.02
asls_MC	0.78 ± 0.02	0.77 ± 0.02	0.72 ± 0.01	0.72 ± 0.01	0.77 ± 0.03	0.77 ± 0.02	0.77 ± 0.01	0.82 ± 0.02
asls_AS	0.78 ± 0.02	0.77 ± 0.02	0.72 ± 0.01	0.72 ± 0.01	0.74 ± 0.03	0.75 ± 0.03	0.82 ± 0.02	0.87 ± 0.02
asls_PS	0.78 ± 0.02	0.77 ± 0.02	0.72 ± 0.01	0.72 ± 0.01	0.77 ± 0.03	0.78 ± 0.03	0.81 ± 0.01	0.83 ± 0.02
asls_RS	0.80 ± 0.02	0.80 ± 0.02	0.71 ± 0.02	0.72 ± 0.03	0.78 ± 0.03	0.78 ± 0.03	0.84 ± 0.02	0.86 ± 0.02
asls_SNV	0.78 ± 0.02	0.77 ± 0.02	0.72 ± 0.01	0.72 ± 0.01	0.74 ± 0.03	0.75 ± 0.03	0.82 ± 0.02	0.87 ± 0.02
asls_MSC	0.78 ± 0.02	0.77 ± 0.02	0.72 ± 0.01	0.72 ± 0.01	0.77 ± 0.04	0.75 ± 0.03	0.81 ± 0.02	0.86 ± 0.02
aspls_NTS	0.81 ± 0.04	0.81 ± 0.04	0.80 ± 0.04	0.80 ± 0.03	0.80 ± 0.03	0.81 ± 0.03	0.86 ± 0.01	0.86 ± 0.02
aspls_NCV	0.81 ± 0.04	0.81 ± 0.04	0.80 ± 0.04	0.80 ± 0.03	0.80 ± 0.04	0.80 ± 0.03	0.85 ± 0.02	0.86 ± 0.02
aspls_NMO	0.81 ± 0.03	0.81 ± 0.03	0.81 ± 0.03	0.80 ± 0.03	0.83 ± 0.04	0.83 ± 0.05	0.80 ± 0.02	0.86 ± 0.02
aspls_MC	0.80 ± 0.04	0.80 ± 0.03	0.80 ± 0.04	0.80 ± 0.03	0.81 ± 0.04	0.82 ± 0.04	0.82 ± 0.02	0.82 ± 0.02
aspls_AS	0.80 ± 0.04	0.80 ± 0.03	0.80 ± 0.04	0.80 ± 0.03	0.79 ± 0.04	0.80 ± 0.04	0.83 ± 0.02	0.87 ± 0.02
aspls_PS	0.80 ± 0.04	0.80 ± 0.03	0.80 ± 0.04	0.80 ± 0.03	0.80 ± 0.04	0.81 ± 0.04	0.81 ± 0.02	0.83 ± 0.02
aspls_RS	0.80 ± 0.04	0.80 ± 0.04	0.80 ± 0.04	0.80 ± 0.03	0.81 ± 0.03	0.82 ± 0.04	0.80 ± 0.02	0.87 ± 0.02
aspls_SNV	0.80 ± 0.04	0.80 ± 0.03	0.80 ± 0.04	0.80 ± 0.03	0.79 ± 0.04	0.80 ± 0.04	0.83 ± 0.02	0.87 ± 0.02
aspls_MSC	0.80 ± 0.04	0.80 ± 0.03	0.80 ± 0.04	0.80 ± 0.03	0.80 ± 0.04	0.79 ± 0.03	0.84 ± 0.02	0.86 ± 0.02
imodpoly_NTS	0.75 ± 0.01	0.74 ± 0.02	0.73 ± 0.02	0.72 ± 0.02	0.76 ± 0.01	0.74 ± 0.02	0.86 ± 0.02	0.87 ± 0.02

imodpoly_NCV	0.75 ± 0.01	0.74 ± 0.02	0.73 ± 0.02	0.72 ± 0.02	0.74 ± 0.03	0.75 ± 0.03	0.85 ± 0.02	0.86 ± 0.02
imodpoly_NMO	0.74 ± 0.03	0.75 ± 0.02	0.73 ± 0.01	0.73 ± 0.01	0.75 ± 0.05	0.74 ± 0.04	0.82 ± 0.02	0.85 ± 0.02
imodpoly_MC	0.76 ± 0.02	0.74 ± 0.02	0.72 ± 0.01	0.73 ± 0.01	0.75 ± 0.03	0.77 ± 0.04	0.81 ± 0.02	0.83 ± 0.02
imodpoly_AS	0.76 ± 0.02	0.74 ± 0.02	0.72 ± 0.01	0.73 ± 0.01	0.76 ± 0.03	0.75 ± 0.03	0.85 ± 0.02	0.86 ± 0.02
imodpoly_PS	0.76 ± 0.02	0.74 ± 0.02	0.72 ± 0.01	0.73 ± 0.01	0.75 ± 0.03	0.78 ± 0.03	0.84 ± 0.01	0.82 ± 0.02
imodpoly_RS	0.75 ± 0.02	0.73 ± 0.02	0.73 ± 0.02	0.73 ± 0.02	0.77 ± 0.02	0.75 ± 0.02	0.85 ± 0.01	0.87 ± 0.02
imodpoly_SNV	0.76 ± 0.02	0.74 ± 0.02	0.72 ± 0.01	0.73 ± 0.01	0.76 ± 0.03	0.75 ± 0.03	0.85 ± 0.02	0.86 ± 0.02
imodpoly_MSC	0.76 ± 0.02	0.74 ± 0.02	0.72 ± 0.01	0.73 ± 0.01	0.74 ± 0.04	0.70 ± 0.06	0.82 ± 0.02	0.85 ± 0.02
modpoly_NTS	0.78 ± 0.03	0.74 ± 0.02	0.75 ± 0.02	0.75 ± 0.02	0.78 ± 0.03	0.75 ± 0.01	0.83 ± 0.02	0.87 ± 0.02
modpoly_NCV	0.78 ± 0.03	0.74 ± 0.02	0.75 ± 0.02	0.75 ± 0.02	0.79 ± 0.03	0.77 ± 0.03	0.84 ± 0.02	0.87 ± 0.02
modpoly_NMO	0.80 ± 0.01	0.80 ± 0.02	0.73 ± 0.01	0.73 ± 0.01	0.75 ± 0.04	0.75 ± 0.04	0.80 ± 0.02	0.85 ± 0.02
modpoly_MC	0.75 ± 0.01	0.75 ± 0.01	0.73 ± 0.01	0.73 ± 0.01	0.74 ± 0.03	0.76 ± 0.04	0.77 ± 0.01	0.83 ± 0.02
modpoly_AS	0.75 ± 0.01	0.75 ± 0.01	0.73 ± 0.01	0.73 ± 0.01	0.77 ± 0.04	0.77 ± 0.03	0.83 ± 0.02	0.86 ± 0.02
modpoly_PS	0.75 ± 0.01	0.75 ± 0.01	0.73 ± 0.01	0.73 ± 0.01	0.76 ± 0.03	0.76 ± 0.03	0.79 ± 0.02	0.82 ± 0.02
modpoly_RS	0.79 ± 0.02	0.77 ± 0.02	0.73 ± 0.02	0.72 ± 0.02	0.77 ± 0.03	0.75 ± 0.03	0.84 ± 0.02	0.86 ± 0.02
modpoly_SNV	0.75 ± 0.01	0.75 ± 0.01	0.73 ± 0.01	0.73 ± 0.01	0.77 ± 0.04	0.77 ± 0.03	0.83 ± 0.02	0.86 ± 0.02
modpoly_MSC	0.75 ± 0.01	0.75 ± 0.01	0.73 ± 0.01	0.73 ± 0.01	0.73 ± 0.04	0.70 ± 0.06	0.81 ± 0.02	0.85 ± 0.02
poly_NTS	0.75 ± 0.01	0.73 ± 0.01	0.73 ± 0.00	0.73 ± 0.00	0.79 ± 0.01	0.76 ± 0.02	0.85 ± 0.02	0.86 ± 0.02
poly_NCV	0.75 ± 0.01	0.73 ± 0.01	0.73 ± 0.00	0.73 ± 0.00	0.77 ± 0.01	0.74 ± 0.03	0.86 ± 0.02	0.86 ± 0.02
poly_NMO	0.75 ± 0.03	0.79 ± 0.03	0.73 ± 0.01	0.72 ± 0.02	0.80 ± 0.05	0.77 ± 0.05	0.82 ± 0.02	0.86 ± 0.02
poly_MC	0.75 ± 0.01	0.73 ± 0.01	0.73 ± 0.00	0.73 ± 0.00	0.76 ± 0.03	0.74 ± 0.03	0.78 ± 0.02	0.82 ± 0.02
poly_AS	0.75 ± 0.01	0.73 ± 0.01	0.73 ± 0.00	0.73 ± 0.00	0.77 ± 0.01	0.74 ± 0.03	0.86 ± 0.02	0.86 ± 0.02
poly_PS	0.75 ± 0.01	0.73 ± 0.01	0.73 ± 0.00	0.73 ± 0.00	0.77 ± 0.03	0.76 ± 0.03	0.81 ± 0.01	0.83 ± 0.02
poly_RS	0.75 ± 0.02	0.74 ± 0.01	0.72 ± 0.02	0.72 ± 0.02	0.81 ± 0.02	0.76 ± 0.03	0.87 ± 0.02	0.87 ± 0.02
poly_SNV	0.75 ± 0.01	0.73 ± 0.01	0.73 ± 0.00	0.73 ± 0.00	0.77 ± 0.01	0.74 ± 0.03	0.86 ± 0.02	0.86 ± 0.02

poly_MSC	0.75 ± 0.01	0.73 ± 0.01	0.73 ± 0.00	0.73 ± 0.00	0.73 ± 0.05	0.70 ± 0.05	0.85 ± 0.02	0.85 ± 0.02
pspline_asls_NTS	0.80 ± 0.01	0.80 ± 0.02	0.76 ± 0.02	0.76 ± 0.02	0.79 ± 0.02	0.81 ± 0.02	0.86 ± 0.02	0.87 ± 0.02
pspline_asls_NCV	0.80 ± 0.01	0.80 ± 0.02	0.76 ± 0.02	0.76 ± 0.02	0.79 ± 0.03	0.79 ± 0.02	0.86 ± 0.02	0.87 ± 0.02
pspline_asls_NMO	0.79 ± 0.02	0.80 ± 0.02	0.76 ± 0.02	0.76 ± 0.02	0.78 ± 0.03	0.78 ± 0.03	0.85 ± 0.02	0.86 ± 0.02
pspline_asls_MC	0.80 ± 0.02	0.83 ± 0.02	0.79 ± 0.04	0.79 ± 0.03	0.79 ± 0.04	0.80 ± 0.04	0.84 ± 0.02	0.82 ± 0.02
pspline_asls_AS	0.80 ± 0.02	0.83 ± 0.02	0.79 ± 0.04	0.79 ± 0.03	0.81 ± 0.02	0.81 ± 0.02	0.84 ± 0.03	0.87 ± 0.02
pspline_asls_PS	0.80 ± 0.02	0.83 ± 0.02	0.79 ± 0.04	0.79 ± 0.03	0.81 ± 0.02	0.82 ± 0.04	0.86 ± 0.02	0.82 ± 0.02
pspline_asls_RS	0.79 ± 0.01	0.82 ± 0.02	0.78 ± 0.03	0.79 ± 0.03	0.73 ± 0.02	0.73 ± 0.02	0.87 ± 0.02	0.86 ± 0.02
pspline_asls_SNV	0.80 ± 0.02	0.83 ± 0.02	0.79 ± 0.04	0.79 ± 0.03	0.81 ± 0.02	0.81 ± 0.02	0.84 ± 0.03	0.87 ± 0.02
pspline_asls_MSC	0.80 ± 0.02	0.83 ± 0.02	0.79 ± 0.04	0.79 ± 0.03	0.78 ± 0.02	0.77 ± 0.04	0.82 ± 0.02	0.86 ± 0.02
pspline_airpls_NT S	0.76 ± 0.03	0.76 ± 0.02	0.78 ± 0.03	0.76 ± 0.04	0.79 ± 0.02	0.79 ± 0.03	0.85 ± 0.01	0.86 ± 0.02
pspline_airpls_NC V	0.76 ± 0.03	0.76 ± 0.02	0.78 ± 0.03	0.76 ± 0.04	0.75 ± 0.02	0.77 ± 0.03	0.85 ± 0.01	0.86 ± 0.02
pspline_airpls_N MO	0.78 ± 0.01	0.79 ± 0.01	0.77 ± 0.03	0.77 ± 0.03	0.78 ± 0.05	0.78 ± 0.05	0.79 ± 0.01	0.85 ± 0.02
pspline_airpls_MC	0.80 ± 0.02	0.79 ± 0.02	0.73 ± 0.01	0.72 ± 0.02	0.76 ± 0.04	0.77 ± 0.03	0.80 ± 0.01	0.82 ± 0.02
pspline_airpls_AS	0.80 ± 0.02	0.79 ± 0.02	0.73 ± 0.01	0.72 ± 0.02	0.78 ± 0.03	0.78 ± 0.03	0.81 ± 0.01	0.86 ± 0.02
pspline_airpls_PS	0.80 ± 0.02	0.79 ± 0.02	0.73 ± 0.01	0.72 ± 0.02	0.77 ± 0.03	0.78 ± 0.03	0.83 ± 0.01	0.83 ± 0.02
pspline_airpls_RS	0.80 ± 0.02	0.80 ± 0.02	0.80 ± 0.02	0.80 ± 0.02	0.81 ± 0.03	0.81 ± 0.03	0.82 ± 0.02	0.83 ± 0.02
pspline_airpls_SN V	0.80 ± 0.02	0.79 ± 0.02	0.73 ± 0.01	0.72 ± 0.02	0.78 ± 0.03	0.78 ± 0.03	0.81 ± 0.01	0.86 ± 0.02
pspline_airpls_MS C	0.80 ± 0.02	0.79 ± 0.02	0.73 ± 0.01	0.72 ± 0.02	0.78 ± 0.02	0.76 ± 0.03	0.80 ± 0.01	0.86 ± 0.02
airpls_NTS	0.76 ± 0.03	0.79 ± 0.03	0.76 ± 0.03	0.79 ± 0.03	0.76 ± 0.03	0.78 ± 0.03	0.84 ± 0.02	0.83 ± 0.02
airpls_NCV	0.76 ± 0.03	0.79 ± 0.03	0.76 ± 0.03	0.79 ± 0.03	0.77 ± 0.03	0.78 ± 0.03	0.84 ± 0.02	0.83 ± 0.02
airpls_NMO	0.76 ± 0.04	0.79 ± 0.03	0.76 ± 0.03	0.77 ± 0.04	0.77 ± 0.04	0.78 ± 0.04	0.82 ± 0.02	0.84 ± 0.02
airpls_MC	0.77 ± 0.03	0.78 ± 0.03	0.76 ± 0.03	0.77 ± 0.03	0.78 ± 0.03	0.79 ± 0.03	0.81 ± 0.02	0.82 ± 0.02
airpls_AS	0.77 ± 0.03	0.78 ± 0.03	0.76 ± 0.03	0.77 ± 0.03	0.77 ± 0.03	0.78 ± 0.03	0.84 ± 0.02	0.83 ± 0.02
airpls_PS	0.77 ± 0.03	0.78 ± 0.03	0.76 ± 0.03	0.77 ± 0.03	0.78 ± 0.04	0.78 ± 0.03	0.83 ± 0.02	0.83 ± 0.02

airpls_RS	0.76 ± 0.03	0.79 ± 0.02	0.76 ± 0.03	0.77 ± 0.03	0.75 ± 0.03	0.76 ± 0.03	0.83 ± 0.02	0.83 ± 0.02
airpls_SNV	0.77 ± 0.03	0.78 ± 0.03	0.76 ± 0.03	0.77 ± 0.03	0.77 ± 0.03	0.78 ± 0.03	0.84 ± 0.02	0.83 ± 0.02
airpls_MSC	0.77 ± 0.03	0.78 ± 0.03	0.76 ± 0.03	0.77 ± 0.03	0.77 ± 0.03	0.76 ± 0.03	0.80 ± 0.01	0.84 ± 0.02
8points_NTS	0.72 ± 0.01	0.73 ± 0.02	0.73 ± 0.01	0.73 ± 0.01	0.79 ± 0.03	0.79 ± 0.03	0.87 ± 0.02	0.87 ± 0.02
8points_NCV	0.72 ± 0.01	0.73 ± 0.02	0.73 ± 0.01	0.73 ± 0.01	0.75 ± 0.03	0.73 ± 0.03	0.86 ± 0.02	0.86 ± 0.02
8points_NMO	0.72 ± 0.01	0.72 ± 0.02	0.73 ± 0.01	0.74 ± 0.02	0.77 ± 0.03	0.77 ± 0.04	0.85 ± 0.02	0.86 ± 0.02
8points_MC	0.75 ± 0.02	0.74 ± 0.02	0.74 ± 0.01	0.73 ± 0.01	0.78 ± 0.03	0.76 ± 0.03	0.80 ± 0.02	0.82 ± 0.02
8points_AS	0.75 ± 0.02	0.74 ± 0.02	0.74 ± 0.01	0.73 ± 0.01	0.76 ± 0.02	0.75 ± 0.02	0.85 ± 0.02	0.86 ± 0.02
8points_PS	0.75 ± 0.02	0.74 ± 0.02	0.74 ± 0.01	0.73 ± 0.01	0.80 ± 0.03	0.77 ± 0.03	0.84 ± 0.02	0.82 ± 0.02
8points_RS	0.73 ± 0.01	0.72 ± 0.02	0.72 ± 0.01	0.73 ± 0.01	0.73 ± 0.02	0.74 ± 0.02	0.86 ± 0.02	0.86 ± 0.02
8points_SNV	0.75 ± 0.02	0.74 ± 0.02	0.74 ± 0.01	0.73 ± 0.01	0.76 ± 0.02	0.75 ± 0.02	0.85 ± 0.02	0.86 ± 0.02
8points_MSC	0.75 ± 0.02	0.74 ± 0.02	0.74 ± 0.01	0.73 ± 0.01	0.75 ± 0.02	0.75 ± 0.03	0.83 ± 0.02	0.86 ± 0.02

Appendix of chapter 4

A humidity sensor ensured that relative humidity reached 100%. The measurements were conducted at 1 bar and 3.5 bar to prevent any sensor damage, considering its maximum pressure capacity. Recorded data (Figure 3S-b) during a 115-hour span with demineralized water in the PAV revealed rapid stabilization of humidity at 99% at 1 bar and 60 °C (within approximately 15 minutes). Since 99% relative humidity was promptly achieved at 1 bar, it was inferred that humidity would approach 100% under all conditions of 1 bar or higher pressure with additional liquid water in the PAV. This hypothesis could be tested with the availability of high-pressure humidity sensors.

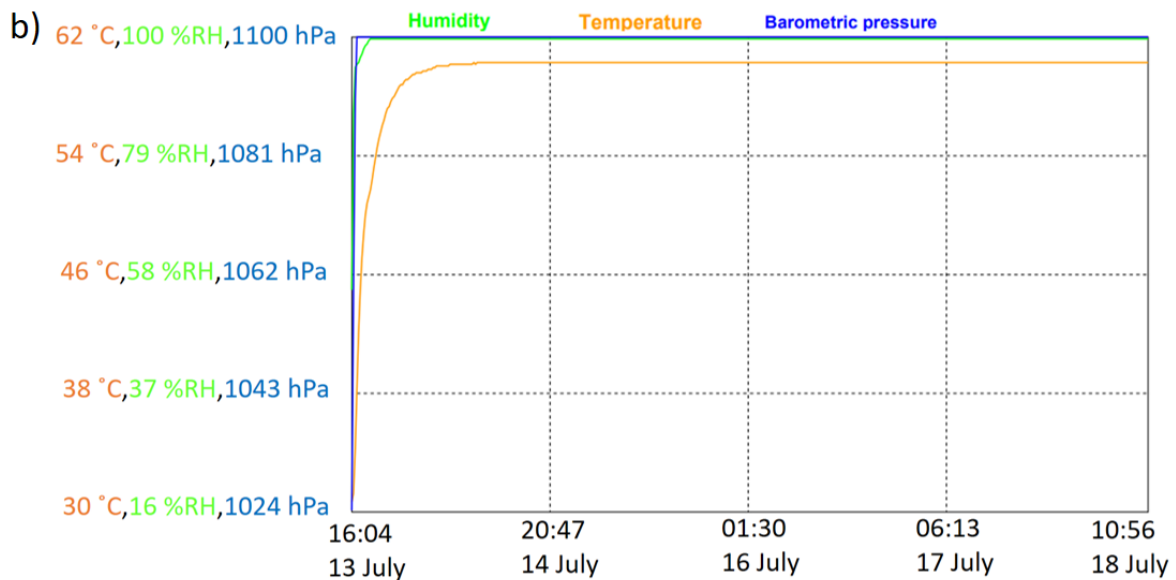


Figure 2S – a) PAV device with the demineralized water in the petri-dishes to create 100% relative humidity. b) recorded data by EXTECH sensor every 30 seconds at 60 °C and 1 bar for 115 hours. 1000 grams of demineralized water used to create humidity in PAV.

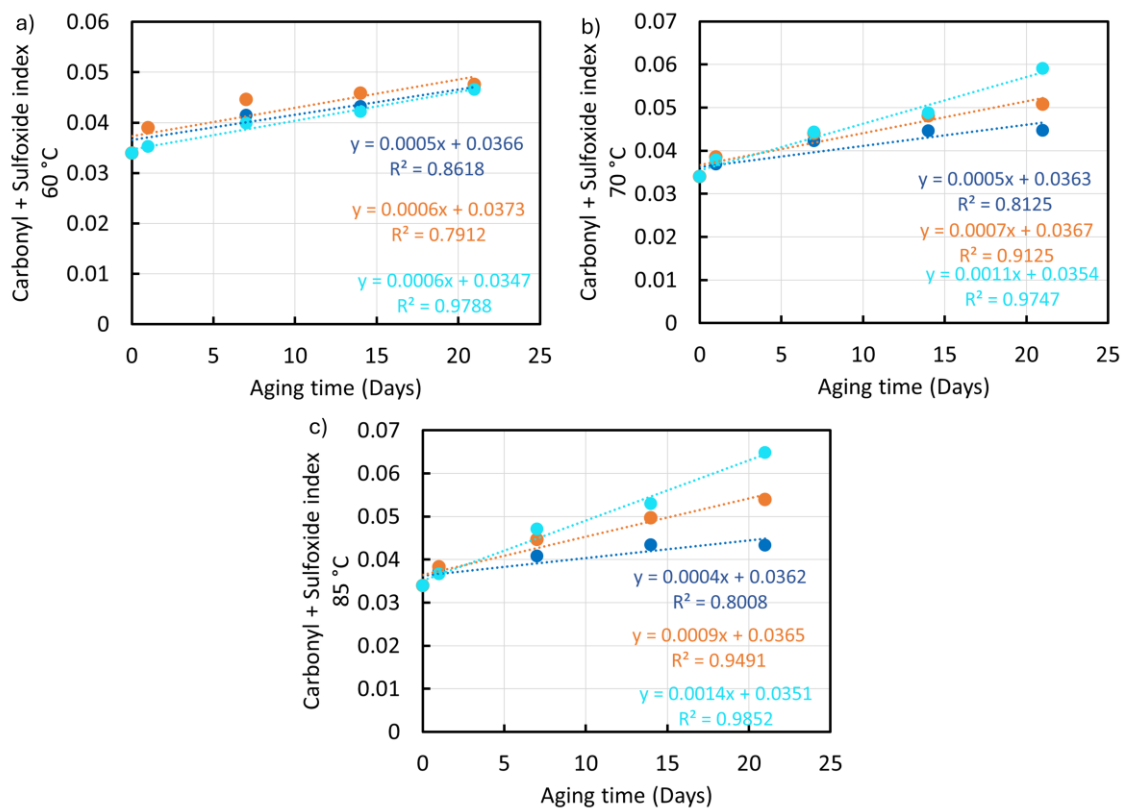


Figure 4S- Summation of carbonyl and sulfoxide indices of T binder versus aging time at a) 60 °C, b) 70 °C, c) 85 °C. Blue color represents the aqueous-thermally aged samples, orange color represents the thermo-oxidatively aged samples, and turquoise color represents the hygrothermal aged samples.

Appendix of chapter 5

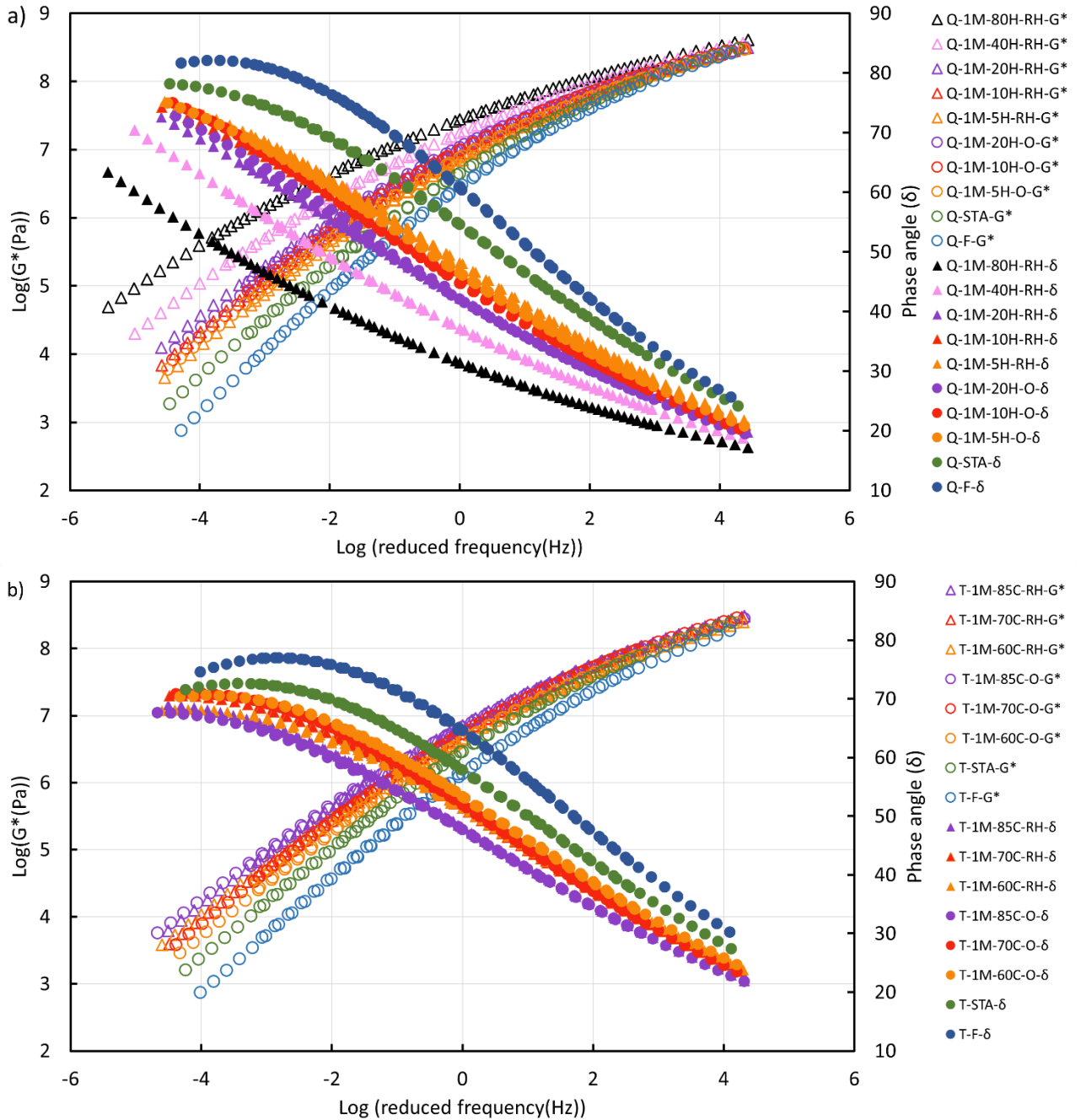


Figure 1S - Master curves (at 20 °C) of a) Q and b) T binder at different aging conditions, all temperatures (60, 70, and 85°C). Samples aged in PAV are presented by “O” and “RH” notations for thermos-oxidative and hydrothermal aged condition, respectively.

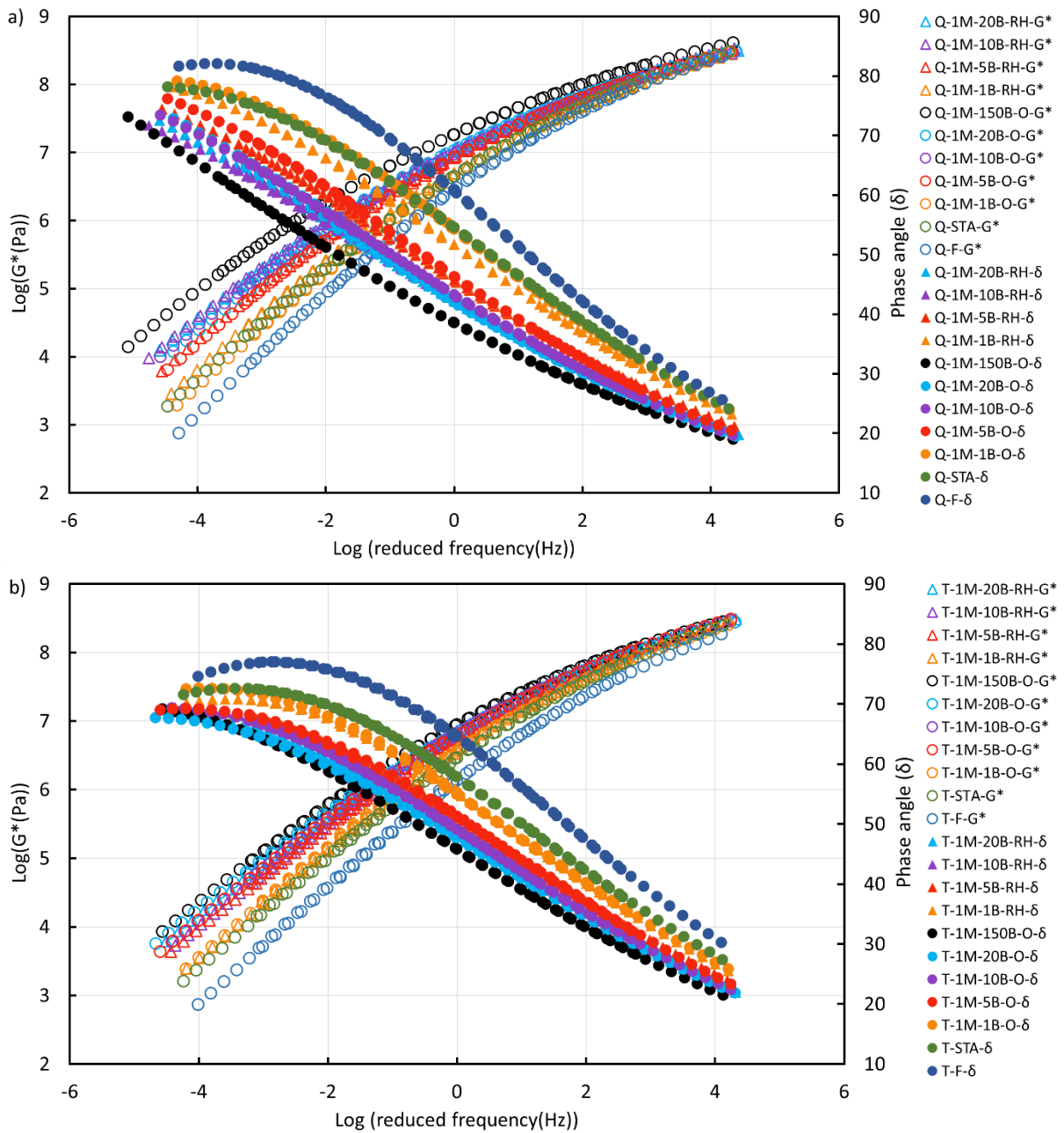


Figure 2S - Master curves (at 20 °C) of a) Q and b) T binder at different aging conditions, all pressures (1, 5, 10, 20, 150 bar). Samples aged in PAV are presented by “O” and “RH” notations for thermos-oxidative and hydrothermal aged condition, respectively.

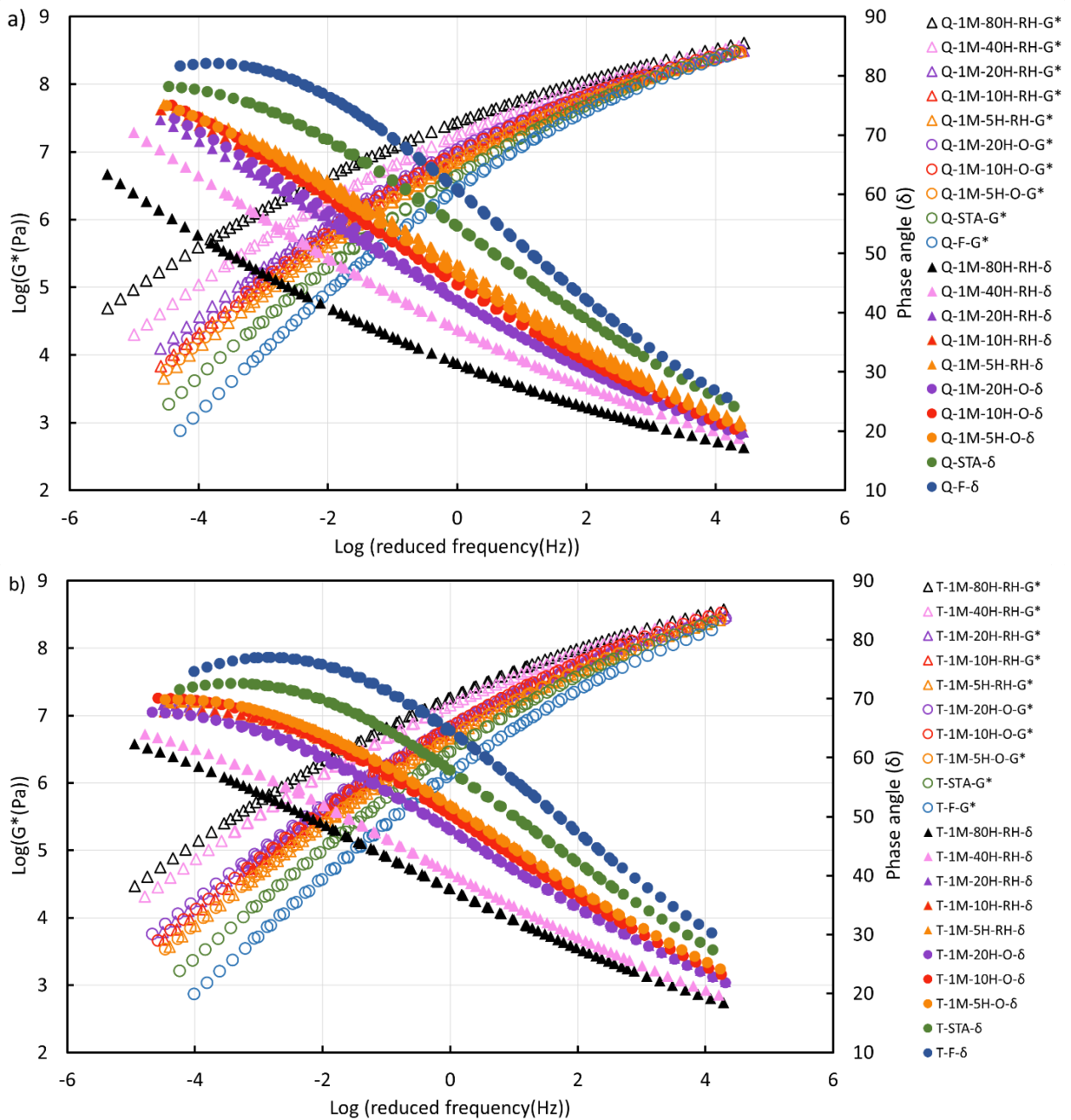


Figure 3S - Master curves (at 20 °C) of a) Q and b) T binder at different aging conditions, all durations (5, 10, 20, 40, 80 H). Samples aged in PAV are presented by “O” and “RH” notations for thermos-oxidative and hydrothermal aged condition, respectively.

Appendix of chapter 6

Table 1S- Ordered Euclidean distance of all samples from PA-2023 and SMA-2023 samples.

Sample names, ref=P_2023_T	Euclidean Distance	Sample names, ref=S_2023_T	Euclidean Distance
P-23-T	0.00	S-23-T	0.00
Q-33%-85C-3H	0.50	Q-85C-21D-O	0.22
Q-1M-40H-RH	0.94	Q-70C-21D-O	0.50
Q-1M-150B-O	1.61	Q-1M-85C-O	0.51
Q-33%-60C-9H	2.02	Q-33%-70C-3H	0.53
P-19-T	2.22	Q-70C-21D-W	0.55
P-20-T	2.32	Q-VBA-WET	0.55
Q-VBA-DRY	2.43	Q-1M-10B-O	0.61
Q-70C-21D-RH	2.71	Q-12%-60C-6H	0.66
Q-85C-7D-RH	2.90	Q-33%-60C-6H	0.70
Q-1M-85C-RH	3.13	S-20-T	0.74
Q-1M-85C-RH	3.13	Q-1M-10H-O	0.75
Q-1M-10B-RH	3.26	Q-60C-21D-RH	0.84
Q-70C-21D-W	3.66	Q-2M-85C-O	0.90
Q-85C-14D-RH	3.71	Q-1M-05B-RH	0.94
Q-1M-85C-O	3.86	Q-1M-10B-RH	1.01
Q-70C-21D-O	3.91	Q-2M-10B-RH	1.01
Q-33%-60C-6H	4.02	Q-1M-10H-RH	1.02
Q-VBA-WET	4.17	Q-60C-21D-W	1.03
S-23-T	4.18	Q-70C-14D-O	1.03
Q-85C-21D-O	4.35	Q-2M-10B-O	1.07
P-21-T	4.49	Q-1M-85C-RH	1.09
S-20-T	4.55	Q-1M-85C-RH	1.09
Q-60C-21D-RH	4.67	P-18-T	1.12
Q-33%-70C-3H	4.73	Q-70C-14D-RH	1.14
Q-1M-10B-O	4.73	S-19-T	1.16
Q-12%-60C-6H	4.81	Q-85C-14D-W	1.19
Q-1M-10H-O	4.93	Q-85C-7D-RH	1.29
Q-1M-05B-RH	4.98	Q-3M-85C-RH	1.33
Q-2M-85C-O	5.02	Q-3M-10B-RH	1.38
Q-70C-14D-RH	5.09	Q-2M-85C-RH	1.38
Q-1M-10H-RH	5.14	Q-1M-70C-O	1.40
Q-85C-14D-W	5.16	Q-60C-14D-RH	1.43
Q-2M-10B-RH	5.19	Q-70C-21D-RH	1.48
Q-70C-14D-O	5.19	Q-PAV-STD	1.51
Q-60C-21D-W	5.21	Q-1M-60C-RH	1.53
Q-2M-10B-O	5.22	Q-2M-10H-O	1.56
P-18-T	5.27	Q-1M-05B-O	1.56
Q-3M-85C-RH	5.31	Q-2M-70C-O	1.57
S-19-T	5.33	Q-70C-14D-W	1.59

Q-1M-60C-RH	5.38	Q-70C-7D-RH	1.60
Q-2M-85C-RH	5.44	Q-1M-70C-RH	1.69
Q-70C-7D-RH	5.50	Q-1M-05H-O	1.69
Q-3M-10B-RH	5.53	Q-60C-21D-O	1.73
Q-1M-70C-O	5.54	Q-12%-60C-9H	1.85
Q-60C-14D-RH	5.61	S-21-T	1.86
Q-70C-14D-W	5.62	Q-VBA-DRY	1.89
Q-PAV-STD	5.65	P-20-T	1.92
Q-2M-70C-O	5.68	Q-1M-05H-RH	1.93
Q-2M-10H-O	5.74	Q-2M-10H-RH	1.96
Q-1M-05B-O	5.74	Q-85C-7D-O	1.98
Q-1M-70C-RH	5.83	Q-70C-7D-W	1.99
Q-60C-21D-O	5.83	Q-1M-60C-O	1.99
Q-85C-21D-RH	5.84	P-19-T	2.00
Q-1M-05H-O	5.85	Q-3M-70C-O	2.10
Q-12%-60C-9H	5.97	Q-2M-70C-RH	2.10
S-21-T	6.00	Q-60C-14D-W	2.16
Q-70C-7D-W	6.07	Q-33%-60C-3H	2.16
Q-2M-10H-RH	6.09	Q-3M-85C-O	2.18
Q-1M-05H-RH	6.09	Q-1M-01B-O	2.18
Q-1M-60C-O	6.11	Q-85C-14D-O	2.21
Q-85C-7D-O	6.16	Q-2M-05B-RH	2.23
Q-2M-70C-RH	6.20	Q-2M-60C-O	2.35
Q-3M-70C-O	6.23	Q-2M-05B-O	2.36
Q-85C-1D-RH	6.29	Q-3M-10B-O	2.37
Q-33%-60C-3H	6.33	Q-2M-05H-O	2.40
Q-3M-85C-O	6.33	Q-2M-60C-RH	2.42
Q-2M-05B-RH	6.34	Q-85C-1D-RH	2.47
Q-60C-14D-W	6.34	Q-2M-05H-RH	2.48
Q-1M-01B-O	6.35	Q-3M-10H-O	2.53
Q-85C-14D-O	6.37	Q-85C-21D-W	2.53
Q-2M-60C-O	6.48	Q-60C-1D-W	2.56
Q-3M-10B-O	6.52	Q-33%-60C-9H	2.63
Q-2M-05B-O	6.53	Q-60C-14D-O	2.66
Q-2M-60C-RH	6.57	Q-70C-7D-O	2.68
Q-2M-05H-O	6.57	Q-60C-7D-W	2.72
Q-85C-21D-W	6.61	Q-60C-7D-RH	2.76
Q-2M-05H-RH	6.63	Q-3M-60C-O	2.76
Q-3M-10H-O	6.70	Q-1M-01B-RH	2.78
Q-60C-1D-W	6.73	Q-3M-60C-RH	2.82
Q-60C-14D-O	6.84	Q-3M-10H-RH	2.87
Q-70C-7D-O	6.84	Q-2M-01B-RH	2.87
Q-3M-60C-O	6.88	Q-70C-1D-W	2.89
Q-3M-60C-RH	6.89	Q-3M-05B-RH	2.90
Q-60C-7D-W	6.89	Q-12%-85C-3H	2.94
Q-70C-1D-W	6.92	Q-3M-70C-RH	2.96

Q-60C-7D-RH	6.94	Q-60C-9H-UV	3.00
Q-1M-01B-RH	6.94	Q-3M-05B-O	3.00
Q-2M-01B-RH	7.03	Q-3M-05H-RH	3.24
Q-3M-10H-RH	7.03	Q-85C-7D-W	3.26
Q-3M-05B-RH	7.05	Q-70C-1D-RH	3.27
Q-60C-9H-UV	7.09	Q-60C-9H-O	3.28
Q-12%-85C-3H	7.09	Q-60C-1D-RH	3.30
Q-3M-70C-RH	7.10	Q-3M-05H-O	3.33
Q-3M-05B-O	7.15	Q-2M-01B-O	3.34
Q-60C-9H-O	7.33	Q-60C-7D-O	3.39
Q-1M-80H-RH	7.35	Q-3M-01B-RH	3.40
Q-60C-1D-RH	7.39	Q-70C-1D-O	3.51
Q-85C-7D-W	7.39	Q-1M-150B-O	3.54
Q-70C-1D-RH	7.40	Q-3M-01B-O	3.66
Q-3M-05H-RH	7.41	Q-1M-40H-RH	3.71
Q-2M-01B-O	7.49	Q-85C-1D-W	3.75
Q-3M-05H-O	7.50	Q-85C-1D-O	3.76
Q-60C-7D-O	7.56	Q-60C-1D-O	4.06
Q-3M-01B-RH	7.57	Q-33%-85C-3H	4.08
Q-70C-1D-O	7.66	Q-12%-60C-3H	4.12
Q-3M-01B-O	7.84	P-23-T	4.18
Q-85C-1D-W	7.91	Q-12%-70C-3H	4.40
Q-85C-1D-O	7.92	Q-85C-3H-O	4.46
Q-60C-1D-O	8.24	Q-85C-3H-UV	4.53
Q-12%-60C-3H	8.26	Q-STA	5.63
Q-12%-70C-3H	8.57	Q-F	6.25
Q-85C-3H-O	8.63	Q-85C-14D-RH	7.86
Q-85C-3H-UV	8.70	P-21-T	8.64
Q-STA	9.80	Q-85C-21D-RH	10.01
Q-F	10.43	P-17-T	10.63
P-17-T	12.68	Q-1M-80H-RH	11.53
P-16-T	16.46	P-16-T	14.57
P-15-T	18.06	P-15-T	15.78
P-14-T	19.08	P-14-T	16.72

Table 2S- Pearson correlation coefficients and Variance inflation factor (VIF).

Thermo-oxidative model					Hygrothermal model				
Variable	VIF				Variable	VIF			
temperature	1.16				temperature	1.11			
pressure	1.08				pressure	1.45			
time	1.38				time	1.62			
thickness	1.21				thickness	1.24			
Pearson correlation coefficient matrix					Pearson correlation coefficient matrix				
	temperat ure	pressur e	time	thickne ss		tempera ture	pressur e	time	thickne ss

temperature	1.00	-0.11	-0.35	0.24	temperature	1.00	0.11	-0.29	0.18
pressure	-0.11	1.00	0.28	-0.10	pressure	0.11	1.00	-0.44	0.35
time	-0.35	0.28	1.00	-0.40	time	-0.29	-0.44	1.00	-0.41
thickness	0.24	-0.10	-0.40	1.00	thickness	0.18	0.35	-0.41	1.00

Table 3S- Chemo-rheological relationship analysis, R² and RMSE for calibration, prediction, cross-validation, and RPD.

<p><i>Feature: alpha, Kernel: linear</i> <i>Best Params: {'C': 100, 'epsilon': 1}</i> <i>R2 Calibration: 0.450, RMSE Calibration: 3.110, Bias Calibration: 0.337, RPD Calibration: 1.355</i> <i>R2 CV: 0.370, RMSE CV: 3.330, Bias CV: 0.330, RPD CV: 1.266</i> <i>R2 Prediction: 0.190, RMSE Prediction: 12.700, Bias Prediction: 2.027, RPD Prediction: 1.112</i></p>
<p><i>Feature: beta, Kernel: rbf</i> <i>Best Params: {'C': 1, 'epsilon': 0.01, 'gamma': 'scale'}</i> <i>R2 Calibration: 0.950, RMSE Calibration: 0.080, Bias Calibration: -0.006, RPD Calibration: 4.218</i> <i>R2 CV: 0.700, RMSE CV: 0.180, Bias CV: -0.016, RPD CV: 1.874</i> <i>R2 Prediction: 0.650, RMSE Prediction: 0.290, Bias Prediction: -0.047, RPD Prediction: 1.685</i></p>
<p><i>Feature: sigma, Kernel: linear</i> <i>Best Params: {'C': 100, 'epsilon': 1}</i> <i>R2 Calibration: 0.460, RMSE Calibration: 3.050, Bias Calibration: -0.295, RPD Calibration: 1.357</i> <i>R2 CV: 0.370, RMSE CV: 3.270, Bias CV: -0.299, RPD CV: 1.266</i> <i>R2 Prediction: 0.190, RMSE Prediction: 12.690, Bias Prediction: -2.010, RPD Prediction: 1.109</i></p>
<p><i>Feature: Gamma, Kernel: linear</i> <i>Best Params: {'C': 100, 'epsilon': 0.01}</i> <i>R2 Calibration: 0.750, RMSE Calibration: 0.010, Bias Calibration: 0.000, RPD Calibration: 2.890</i> <i>R2 CV: 0.330, RMSE CV: 0.020, Bias CV: -0.000, RPD CV: 1.445</i> <i>R2 Prediction: 0.680, RMSE Prediction: 0.020, Bias Prediction: -0.002, RPD Prediction: 1.682</i></p>
<p><i>Feature: CR-CM, Kernel: rbf</i> <i>Best Params: {'C': 1, 'epsilon': 0.01, 'gamma': 10}</i> <i>R2 Calibration: 1.000, RMSE Calibration: 0.010, Bias Calibration: -0.000, RPD Calibration: 30.841</i> <i>R2 CV: 0.360, RMSE CV: 0.250, Bias CV: -0.013, RPD CV: 1.234</i> <i>R2 Prediction: 0.330, RMSE Prediction: 0.320, Bias Prediction: 0.018, RPD Prediction: 1.232</i></p>
<p><i>Feature: CR-Fr, Kernel: linear</i> <i>Best Params: {'C': 0.1, 'epsilon': 0.01}</i> <i>R2 Calibration: 0.520, RMSE Calibration: 0.700, Bias Calibration: 0.084, RPD Calibration: 1.447</i> <i>R2 CV: 0.050, RMSE CV: 0.990, Bias CV: 0.123, RPD CV: 1.023</i> <i>R2 Prediction: 0.540, RMSE Prediction: 0.860, Bias Prediction: 0.278, RPD Prediction: 1.472</i></p>
<p><i>Feature: at0, Kernel: linear</i> <i>Best Params: {'C': 0.1, 'epsilon': 0.1}</i> <i>R2 Calibration: 0.530, RMSE Calibration: 0.090, Bias Calibration: 0.021, RPD Calibration: 1.387</i> <i>R2 CV: 0.200, RMSE CV: 0.110, Bias CV: 0.019, RPD CV: 1.135</i> <i>R2 Prediction: 0.300, RMSE Prediction: 0.120, Bias Prediction: -0.008, RPD Prediction: 1.232</i></p>

<p>Feature: at10, Kernel: rbf Best Params: {'C': 100, 'epsilon': 0.01, 'gamma': 0.01} R2 Calibration: 0.900, RMSE Calibration: 0.030, Bias Calibration: -0.002, RPD Calibration: 3.239 R2 CV: 0.560, RMSE CV: 0.060, Bias CV: 0.001, RPD CV: 1.620 R2 Prediction: 0.490, RMSE Prediction: 0.080, Bias Prediction: -0.003, RPD Prediction: 1.453</p>
<p>Feature: at30, Kernel: rbf Best Params: {'C': 10, 'epsilon': 0.01, 'gamma': 0.01} R2 Calibration: 0.820, RMSE Calibration: 0.060, Bias Calibration: -0.006, RPD Calibration: 2.489 R2 CV: 0.520, RMSE CV: 0.100, Bias CV: -0.008, RPD CV: 1.494 R2 Prediction: 0.660, RMSE Prediction: 0.090, Bias Prediction: 0.008, RPD Prediction: 1.644</p>
<p>Feature: at40, Kernel: rbf Best Params: {'C': 1, 'epsilon': 0.1, 'gamma': 'scale'} R2 Calibration: 0.810, RMSE Calibration: 0.100, Bias Calibration: -0.002, RPD Calibration: 2.330 R2 CV: 0.310, RMSE CV: 0.190, Bias CV: -0.011, RPD CV: 1.226 R2 Prediction: 0.670, RMSE Prediction: 0.140, Bias Prediction: 0.002, RPD Prediction: 1.749</p>

Table 4S- Predicted years of field aging based on PA-SVR model for all lab aged samples.

Sample names	predicted years of field aging \pm 0.59
Q_12%_60C_3H	0.13
Q_60C_9H_O	0.17
Q_12%_70C_3H	0.20
Q_85C_3H_UV	0.39
Q_3M_01B_O	0.71
Q_3M_05H_RH	0.73
Q_85C_3H_O	0.90
Q_3M_05B_RH	1.14
Q_70C_1D_W	1.15
Q_85C_1D_W	1.19
Q_3M_01B_RH	1.34
Q_85C_1D_O	1.36
Q_3M_05H_O	1.40
Q_70C_1D_RH	1.42
Q_70C_1D_O	1.42
Q_60C_1D_RH	1.43
Q_60C_9H_UV	1.44
Q_2M_01B_O	1.53
Q_3M_10H_RH	1.61
Q_3M_05B_O	1.77
Q_85C_21D_W	1.82
Q_70C_7D_RH	1.86
Q_2M_05H_RH	1.98

Q_3M_70C_RH	2.04
Q_85C_7D_W	2.08
Q_3M_60C_RH	2.21
Q_1M_01B_RH	2.28
Q_60C_1D_O	2.32
Q_3M_60C_O	2.34
Q_2M_01B_RH	2.37
Q_3M_10H_O	2.52
Q_2M_05B_O	2.55
Q_2M_05B_RH	2.57
Q_2M_85C_RH	2.58
Q_2M_05H_O	2.68
Q_2M_60C_O	2.70
Q_12%_85C_3H	2.71
Q_60C_1D_W	2.78
Q_70C_14D_RH	2.82
Q_2M_60C_RH	2.83
Q_85C_14D_O	2.83
Q_70C_7D_O	2.84
Q_2M_70C_RH	2.93
Q_1M_05H_O	3.26
Q_1M_05H_RH	3.32
Q_3M_10B_O	3.32
Q_2M_10H_RH	3.35
Q_3M_70C_O	3.43
Q_1M_60C_O	3.46
Q_70C_7D_W	3.52
Q_60C_7D_W	3.61
Q_1M_01B_O	3.65
Q_3M_10B_RH	3.72
Q_1M_70C_RH	3.75
Q_1M_05B_O	3.77
Q_3M_85C_O	3.77
Q_2M_10H_O	3.89
Q_1M_60C_RH	3.99
Q_60C_7D_O	4.04
Q_2M_70C_O	4.10
Q_60C_7D_RH	4.14
Q_33%_60C_3H	4.17
Q_3M_85C_RH	4.24
Q_70C_14D_W	4.29
Q_1M_10H_RH	4.41
Q_1M_70C_O	4.41
Q_60C_14D_W	4.50
Q_2M_10B_RH	4.69
Q_PAV_STD	4.70

Q_85C_7D_O	4.78
Q_2M_85C_O	4.85
Q_1M_10B_O	4.86
Q_1M_05B_RH	4.89
Q_85C_1D_RH	5.10
Q_60C_14D_O	5.12
Q_2M_10B_O	5.23
Q_70C_14D_O	5.54
Q_1M_10H_O	5.62
Q_12%_60C_6H	5.74
Q_12%_60C_9H	5.79
Q_1M_85C_O	6.03
Q_60C_21D_W	6.18
Q_70C_21D_O	6.69
Q_60C_21D_O	6.83
Q_33%_70C_3H	7.06
Q_60C_14D_RH	7.43
Q_85C_21D_O	7.67
Q_1M_10B_RH	7.70
Q_1M_85C_RH	7.77
Q_1M_85C_RH	7.77
Q_33%_60C_6H	8.06
Q_70C_21D_W	8.09
Q_VBA_DRY	8.42
Q_85C_7D_RH	8.69
Q_70C_21D_RH	9.02
Q_33%_85C_3H	9.09
Q_1M_150B_O	9.17
Q_85C_14D_W	9.47
Q_60C_21D_RH	9.51
Q_33%_60C_9H	9.82
Q_VBA_WET	10.83
Q_1M_40H_RH	11.16

Acknowledgment

More than four years have passed since I embarked on my PhD journey, and it has been both challenging and deeply rewarding. Throughout this time, I have been fortunate to be supported by a number of remarkable individuals who have made this experience truly memorable. I would like to take this opportunity to express my gratitude to them:

First and foremost, I extend my heartfelt thanks to my supervisor, Aikaterini Varveri. The support you've provided has gone beyond anything I could have imagined. You are an amazing supervisor who has helped me grow immensely, both academically and personally. I could not have wished for a better supervisor, and I am grateful for your constant presence and guidance.

I am also deeply grateful to my supervisor, Sandra Erkens. Your insights and guidance throughout this thesis have been invaluable. Furthermore, I would like to express my sincere thanks to Rijkswaterstaat for their financial support of this thesis. I want to thank Bernhard Hofko, my supervisor for the exchange program at TU Wien, and his team: Johannes, Kristina, Sophie, Stefan, Jan, Lucas, and Paul. Thank you for your support and for making my time there a fantastic experience. A huge thank you goes to my colleagues at TU Delft for their support and insightful discussions on both research and the philosophy of life. Thank you to my colleagues in Katerina's team: Lili, Mahmoud, Avi, Ajay, Francesca, Ion, and Ruxin. I also want to acknowledge Cor, Anupam, Xueyan, Peng, Haopeng, Panos, and Yangming. Additionally, I'm grateful for my colleagues Shisong, Chen, Mohammadjavad, Akinmade, Saranga, Zhaojie, Yi, Yunlong, Rui, Keyu, Bowen, and Georgios. Special thanks to my officemate, Eli, we have shared so many valuable moments during our PhD journey. I would also like to thank the technical and administrative staff for their kind help during my PhD journey. Thank you to our technicians Marco and Michele, and our secretary Claudia. To my colleagues at TNO, Diederik, Sayeda, Marla, Bernardo, Coen, Filippos, Dave, Mahesh, and Greet, thank you for your collaboration and support.

I want to thank my friends and family outside of the university who made my life so wonderful. Kaveh, Nasrin, Mohammad, Sara, Shahin, Maryam, Iran, Arya, Hasti, Kavian, Kaveh, Rasoul, Negar, Babak, Faezeh, Majid, Sepideh, Ashkan, Maedeh, Abbas, Sahar, Sanaz, Parviz, Zahra, Sepideh, Majid, Mohammad, Faranak, Saeedeh, Peyman, Negar, Arefeh, Fatemeh, Darya, Behrooz, Kosar, Nima, Parisa, Shadi, Bahman, Alireza, Sara, Saeed, Mina, Mehrdad, Tahmineh, Naser. I truly enjoyed our time together. You are not just friends, but my family.

My academic journey and this thesis would not have been possible without the sacrifices of my family. I miss them with every cell in my body. This thesis is dedicated to them, and I know I can never fully compensate for all their efforts. Maman, you are the strongest and kindest woman I know. I wish I could spend every moment by your side. Baba, you are my hero. I can't express how much I smile and how much easier life gets when I remember your gentle voice, warm hugs, and all of your support. Setareh, thank you for your beautiful smiles, which I miss every second of my life, and for your support and kind words when I shared things I could only tell you.

Finally, I want to express my gratitude to my husband, Arash, for his unwavering support during this journey. Your full support during my most stressful nights and the confidence you bestowed upon me, even in our most difficult moments, were truly invaluable. You cheer me up when I'm feeling down, without ever asking for anything in return. My appreciation for you extends far beyond the confines of this simple paragraph in my thesis.

Curriculum Vitae

Sadaf Khalighi

13-08-1996 Born in Kermanshah, Iran

Education

2013-2017 Bachelor in Chemical Engineering, Sharif University of Technology, Tehran, Iran

2017-2019 Master in Chemical Engineering, Sharif University of Technology, Tehran, Iran

2021-2025 PhD in Civil Engineering Delft University of Technology, Delft, the Netherland

List of Publications

Publications

1. Accelerated laboratory simulation of field aging for paving binders using hydrogen peroxide and UV light, S Khalighi, L Ma, A Varveri, *Construction and Building Materials* 476, (2025)
2. Multi-scale analysis of ageing behaviour in bituminous materials, S Khalighi, L Ma, K Primerano, J Mirwald, B Hofko, D van Lent, A Varveri, *Road Materials and Pavement Design* 26 (sup1), 654-679 (2025)
3. Exploring the impact of humidity and water on bituminous binder aging: a multivariate analysis approach (TI CAB), S Khalighi, S Erkens, A Varveri, *Road Materials and Pavement Design* 26 (4), 753-777 (2025)
4. The impact of reactive oxygen species coupled with moisture on bitumen long-term aging, S Khalighi, K Primerano, J Mirwald, B Hofko, A Varveri, *Road Materials and Pavement Design*, 1-20 (2025)
5. Evaluating the reproducibility and consistency of different sample preparation techniques used for ATR-FTIR spectroscopy from the RILEM 295-FBB TG1 round robin test, J Mirwald, S. Khalighi, A Varveri, B Hofko, *Materials and Structures*, Volume 58, article number 255, (2025)
6. Evaluating the Repeatability of Different Sample Preparation Techniques Used for ATR-FTIR Spectroscopy from the RILEM 295-FBB TG1 Round Robin Test, K Konieczna, J Mirwald, S Khalighi, *The Institute of Roads and Bridges* (2025)
7. Multivariate chemo-rheological framework for optimizing laboratory aging protocols of paving binders, S Khalighi, L Ma, Y Mosleh, D van Lent, A Varveri, *Materials & Design* 248, 113520 (2024)
8. Evaluating the impact of data pre-processing methods on classification of ATR-FTIR spectra of bituminous binders, S Khalighi, L Ma, S Ren, A Varveri, *Fuel* 376, 132701 (2024)
9. Exploring the significance of exposed surface area in the aging of bitumen films, S Khalighi, R Jing, A Varveri, S Erkens, *Bituminous Mixtures and Pavements VIII*, 71-79 (2024)
10. Identification of potential antioxidants for asphalt pavements using rheological and chemical testing, A Wouter, L Ma, A Jagadeesh, S Khalighi, A Varveri, *Bituminous Mixtures and Pavements VIII*, 183-190 (2024)
11. The Impact of Reactive Oxygen Species Coupled with Moisture on Long-Term Aging: FTIR Approach, S Khalighi, K Primerano, J Mirwald, B Hofko, S Erkens, A Varveri, *International Symposium on Asphalt Pavement & Environment*, 167-171 (2024)
12. Aging and rejuvenation effects on the rheological response and chemical parameters of bitumen, S Ren, X Liu, A Varveri, S Khalighi, R Jing, S Erkens, *journal of materials research and technology* 25, 1289-1313 (2023)
13. Water Effect on Bitumen Chemistry at Intermediate Temperature Aging Conditions, S. Khalighi, S Negenman, R Jing, & A Varveri, *Advances in Materials and Pavement Performance Prediction - Proceedings of the International AM3P Conference* (2022)
14. Hygrothermal aging of mastic samples, S Khalighi, L MA, R Koning, & A Varveri, *Advances in Materials and Pavement Performance Prediction - Proceedings of the International AM3P Conference* (2024)

Patents

1. Assessment of infrastructure comprising organic binder based composite materials, as filed 39639 G143565

Data and code

The data and code relevant to this thesis are available at DOI: <https://doi.org/10.4121/cb9b04ff-40d2-44fa-99b9-f182cee629f1>.